University of Alberta

BUCKLING AND FREE VIBRATION OF

MULTIWALL CARBON NANOTUBES

By ©

Chengyuan Wang

A thesis submitted to the Faculty of Graduate Studies and Research in partial
fulfillment of the requirements for the degree of

Doctor of Philosophy

Department of Mechanical Engineering

Edmonton, Alberta

Spring 2006

Library and
Archives Canada

Bibliothèque et
Archives Canada

Published Heritage
Branch

Direction du
Patrimoine de l'édition

395 Wellington Street
Ottawa ON K1A 0N4
Canada

395, rue Wellington
Ottawa ON K1A 0N4
Canada

NOTICE:
The author has granted a non-exclusive license allowing Library and Archives Canada to reproduce, publish, archive, preserve, conserve, communicate to the public by telecommunication or on the Internet, loan, distribute and sell theses worldwide, for commercial or non-commercial purposes, in microform, paper, electronic and/or any other formats.

The author retains copyright ownership and moral rights in this thesis. Neither the thesis nor substantial extracts from it may be printed or otherwise reproduced without the author's permission.

AVIS:
L'auteur a accordé une licence non exclusive permettant à la Bibliothèque et Archives Canada de reproduire, publier, archiver, sauvegarder, conserver, transmettre au public par télécommunication ou par l'Internet, prêter, distribuer et vendre des thèses partout dans le monde, à des fins commerciales ou autres, sur support microforme, papier, électronique et/ou autres formats.

L'auteur conserve la propriété du droit d'auteur et des droits moraux qui protège cette thèse. Ni la thèse ni des extraits substantiels de celle-ci ne doivent être imprimés ou autrement reproduits sans son autorisation.

In compliance with the Canadian Privacy Act some supporting forms may have been removed from this thesis.

While these forms may be included in the document page count, their removal does not represent any loss of content from the thesis.

Conformément à la loi canadienne sur la protection de la vie privée, quelques formulaires secondaires ont été enlevés de cette thèse.

Bien que ces formulaires aient inclus dans la pagination, il n'y aura aucun contenu manquant.

Canada

This dissertation is dedicated to my parents,
to my wife and to my son.

Abstract

The exceptional mechanical and electronic properties of carbon nanotubes (CNTs) make them a leading candidate material for nanotechnology. Since most potential applications of CNTs heavily depend on their mechanical properties, the mechanics of CNTs has become the focus of considerable research in the last decade. Among various methods, a multiple-shell model has been developed for axially compressed buckling of multiwall carbon nanotubes (MWNTs). Based on this multiple-shell model the current thesis gives a systematic study on elastic buckling and free vibration of MWNTs.

For the elastic buckling of MWNTs, the critical buckling loads and associated modes are predicted for thin, thick and (almost) solid MWNTs (the inner radius-to-thickness ratio > 4, ~ 1 and $< \frac{1}{4}$, respectively) under radial pressure, axial stress or combined load. By analyzing the numerical results, the effect of (i) the internal pressure, (ii) the possible pressure-induced interlayer locking and (iii) the interaction between axial stress and external pressure has been examined for the buckling of MWNTs. Particularly, the multiple-shell model is found to be in good agreement with available experiment in calculating the critical buckling pressure for a specific group of 20-wall CNTs.

Subsequently, the multiple-shell model is extended to free vibration of MWNTs. To demonstrate its effectiveness, the shell mode is first used for the radial breathing modes (RBMs) of CNTs, with excellent agreement with known atomistic simulations and experiments. Especially, for the very first time the pressure-dependence of RBMs

is obtained for MWNTs. Furthermore, the general vibrational behavior of MWNTs has been studied with an emphasis on the effect of the interlayer vdW interaction on free vibration of MWNTs. More recently, some special vibrational modes of MWNTs, i.e., the axisymmetric modes, beam-like modes and the lowest frequency modes have been further discussed in detail.

Moreover, to simplify analysis of MWNTs, a single-shell model is proposed for thin MWNTs to replace the multiple-shell model and the accuracy and applicability of the simplified single Donnell equation and a simplified Flugge equation have been examined for CNTs in various buckling and vibration problems.

Acknowledgements

I would like to extend my deepest gratitude and appreciation to Drs Chongqing Ru and Andrew Mioduchowski for their invaluable guidance, support and encouragement throughout my graduate years.

I am also grateful to my parents, my wife and my son for their patience, love and support throughout my studies.

<div align="right">

Chengyuan Wang

Edmonton, Alberta

June   2006

</div>

Table of Contents

List of Tables

List of Figures

Chapter 1

Introduction

1.1 Carbon Nanotubes (CNTs)

Carbon-based materials, such as diamond and graphite (Fig.1.1 (a) and (b)), have been studied and widely used for centuries. For a long time, the carbon science was thought to be a mature field until a completely new form of carbon material, i.e., fullerene (Fig. 1.1(c)), was discovered in 1985 [1]. The fullerenes or "buckyball" carbon molecules, e.g., C_{60}, C_{70} and C_{80}, are closed cages or carbon hollow spheres of 60, 70, and 80 carbon atoms arranged symmetrically in hexagons and pentagons (Fig.1(c)). The euphoria in the study on fullerenes started with the discovery of "high temperature superconductivity" of this new carbon material in 1991.

Right at this time, in TEM (transmission electron microscopy) study on fullerenes C_{60}, Japanese scientist Sumio Iijima [2] of the NEC fundamental research laboratory accidentally discovered unusual tubular, instead of sphere, carbon molecules (Fig. 1.2 (a) and (b)) in a sample of carbon soot. The observed giant fullerenes or carbon tubes, which might be $C_{1,000,000}$ or beyond, are multilayer carbon cylinders consisting of several concentric tubes (Fig. 1.2 (a) and (b)). A year later, while trying to make modified C_{60} with boron, Thomas Ebbesen and Pulickel Ajayan, also working for NEC, found, quite by chance, a highly efficient way of making large quantities of the multiwall carbon nanotubes (MWNTs) [3]. Subsequently, in 1993, carbon tubes with singlelayer structure (Fig. 1.3) were also synthesized by Iijima's group at NEC [4] and Donald Bethune's group at IBM's Almaden Research Center [5], independently. The early experimental observation showed that these carbon tubes are only a few to tens nanometers in diameter but several microns in length [2, 4-7]. Especially, carbon nanotubes (CNTs) appeared to be perfectly graphitized (i.e., the carbon atoms are in perfect hexagonal arrangement) without any defects. More important, further experimental and theoretical studies revealed that this novel carbon material exhibits exceptional rigidity, super-strong

1

strength, low density and remarkable resilience, and could be either metallic (with high conductivity) or semiconducting, depending on the structure of CNTs [6, 8]. Due to these superior mechanical and electronic properties, CNTs are highly expected to be a leading material for nanocomposites, nanodevices and nanoelectronics [9-12]. Therefore, since the discovery of CNTs, explosive research related to these tubular fullerenes has been increasingly stimulated in the fields of chemistry, physics, material science and engineering, and electrical and electronic engineering.

1.1.1 Molecular Structure of CNTs

CNTs are cylindrical molecules with aspect ratio up to 1000 or even larger [2, 4-7]. Thus, from material point of view, they can be considered as ultimate carbon fibers that are about 10,000 times thinner than human hair. Typically, there are two different categories of CNTs, i.e., singlewall carbon nanotubes (SWNTs) (Fig.1.3) and MWNTs (Fig. 1.2 (a) and (b)).

1.1.1.1 Singlewall Carbon Nanotubes (SWNTs)

As shown in Fig.1.3, SWNTs can be simply described as circular cylinders with radius usually of the order of $1nm$ [4-5]. In many cases, the two ends of a SWNT are closed by hemispherical caps.

In the cylindrical plane of a SWNT, each carbon atom is connected with three adjacent atoms via three in-plane σ – bonds separated from each other by 120^0. As a result, the carbon atoms of a SWNT are bonded together in hexagonal lattice (Fig. 1.3), like those of a graphite sheet (see Fig.1.1 (b) and 1.4). However, different from graphite, the atomic hexagons of a SWNT are arranged in a certain degree of helicity, i.e., the screw orientation with respect to the axis of a SWNT (Figs. 1.3). In view of this atomic structure, a SWNT can be visualized as a result of rolling up a graphite sheet along the screw orientation of its carbon hexagons. This process can be characterized by the rollup vector $\overrightarrow{C_h} = \overrightarrow{OA}$ in Fig. 1.4. In other words, the geometric size and helicity of a SWNT is uniquely determined by the vector $\overrightarrow{C_h}$.

In Fig. 1.4, the rollup vector $\overrightarrow{C_h}$ is expressed as a linear combination of base vectors $\overrightarrow{a_1}$ and $\overrightarrow{a_2}$, i.e., $\overrightarrow{C_h} = \overrightarrow{OA} = n_h \cdot \overrightarrow{a_1} + m_h \cdot \overrightarrow{a_2}$, which defines a SWNT (n_h, m_h), where index n_h and m_h are integers. Note that the length l of in-plane σ-bond is $0.142nm$ and the length of the two unit base vectors $\left|\overrightarrow{a_1}\right| = \left|\overrightarrow{a_2}\right| = \sqrt{3} \cdot l$ (see Fig. 1.4), the perimeter S (= $\left|\overrightarrow{C_h}\right|$) and diameter d of a SWNT (n_h, m_h) can be calculated based on simple geometry as [13-14]

$$S = 0.246 \cdot \sqrt{n_h^2 + n_h m_h + m_h^2} \quad nm$$

and
$$d = \frac{S}{\pi} = 0.0783 \cdot \sqrt{n_h^2 + n_h m_h + m_h^2} \quad nm \tag{1.1}$$

On the other hand, the helicity of SWNT (n_h, m_h) is specified in terms of the chiral angle θ, defined as the angle between base vector $\overrightarrow{a_1}$ and rollup vector $\overrightarrow{C_h}$ (Fig. 1.4). It is easy to understand that due to the hexagonal symmetry of carbon atoms, the chiral angle θ associated with different helicities of SWMTs is in the range of $0^0 \leq \theta \leq 30^0$ and determined uniquely by [13]

$$\theta = \sin^{-1}\left[\frac{\sqrt{3}m_h}{2(n_h^2 + n_h m_h + m_h^2)}\right] \tag{1.2}$$

Especially, according to different helicities or chiral angles, SWNTs are classified into the following three categories (see Figs. 1.3 and 1.4):

(1) "zig-zag" SWNTs with $\theta = 0^0$ and $m_h = 0$

(2) "chiral" SWNTs with $0^0 < \theta < 30^0$ and $n_h > m_h$

(3) "arm-chair" SWNTs with $\theta = 30^0$ and $n_h = m_h$

1.1.1.2 Multiwall Carbon Nanotubes (MWNTs)

TEM study [2] revealed that MWNTs were comprised of two to dozens of concentric SWNTs with usually different helicities. It is seen in Fig.1.2 that these concentric SWNTs are nested one upon another leading to a Russian-doll-like structure.

The interaction between two adjacent tubes of a MWNT is predominated by the normal van der Waals (vdW) interaction arising from the out-of-plane π − bond between atom-pair on neighboring tubes [13]. Since this out-of-plane π − bond is very weak as compared to strong in-plane σ − bond, the friction between two adjacent layers in tangential direction is very small [15-18]. For example, in the experiment of "shell-sliding"[15], the interlayer shear strength measured between the outermost two layers of two individual MWNTs was only $0.08MPa$ and $0.3MPa$, respectively, suggesting that the adjacent tubes of a MWNT can almost slide and twist towards each other freely.

On the other hand, using Lennard-Jones (*L-J*) potential model [19-21] for two atoms, the interlayer normal vdW interaction in MWNTs can be expressed in terms of the interlayer spacing. The repulsive or attractive interaction is present when the interlayer spacing is smaller or larger than the equilibrium value associated with zero vdW interaction. Both TEM observation [22-23] and atomistic simulation [16, 24] indicate that the equilibrium interlayer spacing of MWNTs is around $0.34nm$, close to the interlayer spacing of graphite $0.335nm$. When tube diameter decreases from the large-radius outermost few layers to the small-radius innermost few layers of MWNTs the equilibrium interlayer spacing increases monotonically from 0.342 to $0.39\,nm$ [23] or from 0.337 to $0.375\,nm$ [24]. The increase in interlayer spacing with decreasing nanotube diameter can be explained by the fact that the repulsive force increases with decreasing diameter due to strong curvature effect [23-24].

1.1.2 Mechanical and Electronic Properties of CNTs

The tiny CNTs of extremely large aspect ratio and various helicities are usually defect-free [2,7] with carbon atoms bonded together by strong in-plane σ − bond in hexagonal lattice. As a result, CNTs exhibit remarkable mechanical and electrical properties.

1.1.2.1 Mechanical Properties of CNTs

Exceptional in-plane Rigidity: Many experimental and theoretical studies have been carried out to estimate Young's modulus and shear modulus of CNTs, which, in fact, belong to the framework of continuum elasticity. By fitting the results, for example the force-deformation relation [25-30], strain energy [31-38] or vibrational deformation [39-42] obtained by experiments or atomistic simulations, to the estimate of elastic models, the effective values of these elastic constants have been calculated for CNTs. Although the scatterings of the measured results are found in different literatures, the typical values of the order of $1TPa$ [25-42] for Young's modulus and $0.5TPa$ [30, 33] for shear modulus are finally achieved for CNTs associated with the effective thickness of SWNTs $0.34nm$. Accordingly, the in-plane stiffness of SWNTs defined by the product of Young's modulus and thickness is equal to $56-59eV$ (or around $360 J / nm^2$) [32-34, 36-38]. It is noted that these exceptional values are close to the in-plane elastic constants of a graphite sheet and diamond, but much higher than those of any other existing engineering material.

Super Strong Strength and Low density: Due to the extremely high Young's modulus, CNTs are expected to have much stronger strength than conventional materials. Indeed, existing experiments show that, with the effective thickness of SWNTs $0.34 nm$, the average tensile strength of CNTs is in the range of 1.3 to $63 GPa$ [25, 27-29, 39]. On the other hand, using elastic modules of graphite Ruoff and Lorents [40] have predicted tensile strength $20 GPa$ for SWNTs of diameter $1 nm$. Moreover, based on molecular dynamic (MD) simulation, the tensile strength of SWNTs obtained by Yakobson et al. [43] and Belytschko et al. [44] is $150 GPa$, and 3.5 to $112 GPa$, respectively. These experimental measurements and theoretic predictions are generally consistent with each other, showing that CNTs about six times lighter than steel [45-46] are approximately one to two orders of magnitude stronger than the strongest steel. Obviously, this super strong strength and the low density of CNTs offer a very useful combination in engineering applications.

Remarkable Resilience: In addition to the high in-plane elastic modulus and the resulting strong axial strength, another unique feature of CNTs is their remarkable flexibility under axial compression or bending. The basic phenomenon observed in experiments [47-52] and MD simulation [32, 47] is that both SWNTs and MWNTs can be bent to a large angle in excess of 90^0 or even 110^0 (Fig. 1.5 (a)). Once the bending angle reaches a critical value, kinks or buckling pattern emerges on the inner (concave) side of bent CNTs due to high compression (see Fig. 1.5 (b)). Amazingly, it is found that, on the removing of external load, the kinks (buckling) caused by the compression are fully reversible without any damage of CNTs. In particular, Falvo et al. [48] reported up to 16% recoverable strain for MWNTs. Bower et al. [51] observed 5% buckling strain and up to 18% fracture strain of CNTs. Here, it is worth mentioning that, since the high in-plane rigidity and strong strength as well as low density of CNTs are, in fact, inherited from in-plane properties of graphite, it is this extraordinary resilience and resistance to fracture that distinguish CNTs from their predecessor (graphite) as an engineering material.

Significant Effect of The vdW Interaction: CNTs with high rigidity and remarkable resilience are usually straight carbon fibers with perfect cylindrical symmetry. However, since their diameters are only of a few nanometers, the surface area-to-volume ratio of CNTs is extremely large. As a result, the vdW interaction between adjacent CNTs or a CNT and substrate surface is significant and could result in deformation of CNTs in both axial and radial directions. The experimental evidence was first given in Rouff et al's TEM study [53], in which, the vdW interaction-induced radial deformation or flattening of cross-sections was observed for two adjacent (aligned) MWNTs. In particular, consistent with Gao et al's MD simulation [35] it was shown that the effect of the vdW interaction is strong for CNTs of outer diameter larger than $2.5nm$ but could almost be neglected for CNTs of outer diameter less than $1nm$. Hertel et al. [54] and Avouris et al. [55] further studied the effect of the vdW interaction between two crossing SWNTs (Fig.1.6 (a)) or a CNT and substrate (Fig. 1.6(b)). Both axial and radial deformations of CNTs were clearly observed due to the vdW interaction. These results indicate that the

role of the vdW interaction could be significant in determining the geometry and thus, mechanical properties of CNTs.

1.1.2.2 Electronic Properties of CNTs

In addition to exceptional mechanical properties, CNTs also possess unique electronic properties. As reviewed in Refs. 56 and 57, the electronic conductivity of a SWNT (n_h, m_h) depend sensitively on its diameter and helicity, which can be uniquely determined by index n_h and m_h in Eqs. (1.1) and (1.2). To be more specific, a SWNT (n_h, m_h) is a metallic conductor with high electrical conductivity when the following expression is satisfied [57]

$$2n_h + m_h = 3q \qquad (1.3)$$

where q is an integer. On the other hand, if condition (1.3) cannot be met SWNT (n_h, m_h) is predicted to be semiconductors with relatively low electrical conductivity. For example, all the arm-chair SWNTs with chiral angle $\theta = 30^0$ and $n_h = m_h$ are metallic SWNTs (or conductors), while zig-zag ($\theta = 0^0$ and $m_h = 0$) and chiral ($0^0 < \theta < 30^0$ and $n_h > m_h$) SWNTs can be either metallic tubes or semi-conductive tubes. For metallic SWNTs, the electrical conductivity could be even higher than that of copper. In particular, due to the nearly one-dimensional electronic structure of CNTs, the electronic transport in SWNTs occurs without scattering, which enables metallic SWNTs to carry high currents with very low heat [58]. On the other hand, the unique feature observed for semi-conductive SWNTs is that the increasing diameter of a SWNT results in decrease of its band gap, the energy needed for an electron to move from the valence band, where it is bound to an atom, into a conduction band [56]. This feature enables us to make devices that turn on and off at different voltages, which can be tailored for different applications, a versatility impossible for device made of conventional semiconductors with fixed band gap. For MWNTs, the results for the electrical

conductivity are generally analogous to those of SWNTs because of the weak coupling between individual tubes of MWNTs.

Superconductivity is another intriguing electronic property of CNTs. In 2001, this phenomenon was first reported by French and Russian researchers [59] for small bundles of SWNTs at a low temperature $0.05K$. Later, in Hong Kong, Shen et al. [60] also observed superconductivity for SWNTs of exceptionally small diameter $0.4nm$ at relatively high temperature $15K$. The later result is consistent with previous theoretical prediction that the great curvature of SWNTs is an essential property for superconductivity of CNTs.

1.1.3 Applications of CNTs

The excitement of the discovery of CNTs is greatly amplified because of the exceptional mechanical and electrical properties of CNTs. Accordingly, the expectation is running very high for practical applications of CNTs in nanotechnology. The important applications that CNTs have the most potential are briefly summarized as follows.

1.1.3.1 Super-strong Materials

The first realized application of CNTs is the nanotube-reinforced composite material. Embedding CNTs with enormous resilience and tensile strength into matrix could yield super-strong composite material with extremely high toughness. Experiments [61] showed that by adding only 1% CNTs (1% by weight) into polystyrene matrices leads to a 36-42% increase in the elastic stiffness and a 25% increase in the tensile strength. This kind super-strong and resilient material, for example, can be used to make cars that bounce in a wreck, instead of crack or buildings that sway rather than crack in an earthquake.

In addition, due to the extremely large strength-to-density ratio of CNTs, armies of these molecules could line up to form a light but strong wire that could be an unbeatable material for making light weight vehicles for space, air and ground. Particularly, it has been estimated by Harris [62] that since CNTs possess strong strength, high toughness and light density, they could be designed as the longest cable in the world, which connects space station and earth without suffering a high gravitational force.

1.1.3.2 Nano-mechanical Devices

There is no doubt that CNTs hold substantial promise as building blocks for nano-scale devices. For example, Kim and Lieber [63] have attached two thin and rigid CNTs to electrodes on a glass rod to form nano-sized tweezers, which can be opened and closed by changing voltage applied on the two tubes. Such tweezers have been used to pick up and move objects that are only 350-500 nanometers in size, which are too small for any other larger tweezers. These fine tweezers offer a useful tool to manipulate tiny objects in experiments and later can be applied to assemble nano-scale devices routinely.

In 1996, Smalley and his colleagues [64] first mounted a CNT on the tip of an atomic force microscope. They showed that the exceptional strength and dramatic flexibility of CNTs increase the probe life of the tip and minimize sample damage during repeated hard crashes into substrate. In particular, small diameter of CNTs greatly boosts the resolution of microscope by more than an order of magnitude, allowing clear views of proteins and other large molecules.

In addition to above simple nano-scale equipment, the plans to produce more complex nano-scale machines [65-67], such as molecular motors, mechanical and biological engines, or even nano-scale vehicles have also been proposed. In fact, nano-scale gears and wear-free bearings made up of CNTs, which are essential for nano-scale machines, have already been studied for years in labs. To give an example of potential applications of the molecular machines: nano-vehicles [67], which are propelled by chemical reaction, can be used as nano-medical delivery vans. This part biological and part mechanical natural machines can park there, mix the drug and deliver it right into the growth without doing any harm on the neighboring tissues.

1.1.3.3 Nano-electronic Devices

It is believed that "in the long term, the most valuable applications of CNTs will take further advantage of their unique electronic properties" [56]. As a typical example [67], to pack transistor on computer chip more densely, the already microscopic wires need to be even smaller and thinner. However, existing material on which the computer revolution has been built will begin to hit fundamental physical limits. Once further reduced, they could blow up while you are trying to send the electrical signals through

them. Thus, nano-scale carbon tubes with high electrical conductivity and low heat could be a perfect solution to this problem. It is expected that application of carbon nanotubes could make electronic circuits shrink by orders of magnitude to free up more space in microchip for more devices and at the same time, solve heat and stability problems. More important, CNTs provide orders of magnitude increase in computational power as compared to silicon. Thus this novel computer chip is an excellent successor to conventional silicon chips, and can work at a molecular scale where silicon or other semiconductors ceases to work.

1.1.3.4 Nano-electrochemical devices

The high electronically accessible surface area of porous nanotube arrays, combined with their high electronic conductivity and useful mechanical properties makes CNTs attractive electrodes for devices that use electrochemical double-layer charge injection [11]. To name a few, (1) Supercapacitors with CNT electrodes, which can offer higher power capabilities than batteries and much higher storage capacities than ordinary capacitors. (2) CNT electromechanical actuators, which can be used at just a few volts, compared with around $100V$ used for piezoelectric stacks and $\geq 1000V$ for electrostrictive actuators. Especially, because of the thermal stability of SWNTs these CNT actuators can be operated at temperature up to 350 C^0 or even over $1000C^0$, and it has been predicted [11] that if the inherent mechanical properties of CNTs can be efficiently used, the CNT actuator could be order-of-magnitude advantages over existing commercial actuators.

1.2 Recent Studies on Mechanics of CNTs

As shown in Section 1.1.3, CNTs have been identified as one of the most promising building blocks for future development of functional nano-structures. Thus, the characterization of nano-mechanics of CNTs is highly desirable for the potential applications of this novel engineering material.

1.2.1 Experimental Research

Various experimental techniques have been used to characterize the mechanical behaviors of CNTs. In particular, transmission electronic microscopy (TEM), atomic force microscopy (AFM), scanning electronic microscopy (SEM) and Raman spectroscopy as well as high external pressure are among the dominant experimental methods. The most important experiments based on these techniques are summarized as follows.

1.2.1.1 TEM, AFM and SEM Studies

Measurement of Young's modulus and strength: In 1996, Treacy et al. [39] started the first experimental investigation on Young's modulus of individual MWNTs. With the help of TEM, these authors were able to measure the intrinsic thermal vibrational amplitude of cantilevered MWNTs. By comparing the amplitudes obtained experimentally to those given by elastic beam model, the average value $1.8TPa$ was achieved for 11 examples of MWNTs. Different from TEM, the tip of AFM can be directly used to apply external forces to CNTs. Using this nano-manipulator (AFM), Wong et al. [25] performed the first direct measurement of Young's modulus and axial strength of MWNTs. The relationship between the force applied at the free end of a cantilever MWNT and resulting transverse deflection was obtained, which gave a value of $1.2TPa$ for Young's modulus and about $15GPa$ for bending strength. On the other hand, Yu et al. attached the ends of SWNT ropes [28] or an individual MWNT [29] to opposite two tips of AFM, which allowed them to apply axial tensile force to CNTs (Fig.1.7). Assuming that the axial load on SWNT rope was taken by SWNTs on its circumference, the tensile strength calculated for SWNTs ranged from 13 to $52\,GPa$ and Young's modulus ranged from 320 to $1470\,GPa$ [28]. The interesting phenomenon observed for MWNTs under tension [29] is that the outermost tube of a MWNT was fractured initially and followed by pull-out of inner tubes of the MNWT, demonstrating a "sword and sheath" fracture mechanism of MWNTs. Based on this understanding, the tensile strength obtained for the outermost tube of the MWNTs tested in [29] varied form 11 to $63\,GPa$ and Young's modulus varied from 270 to $950\,GPa$.

Observation of buckling of CNTs: In Iijima et al's TEM study [47], kinks or local buckling was first observed on the inner side of a bent CNT due to high compression. Similarly, using TEM Luroie et al. [50] and Bower et al. [51] were able to investigate buckling behaviors of MWNTs embedded within a polymer matrix. The bending [50-51] or axially compressive forces [51] acting on the MWNTs were caused by shrinkage of the polymer matrix when the composite was cooled down [50-51] or the thermal effects associated with the electron beam in the TEM cell [51]. Consistent with Iijima et al's study [47], these authors observed similar buckling patterns on the concave side of bent MWNTs. Particularly, it was noted [50-51] that buckled MWNTs could restore to their original straight and cylindrical shape when the applied force is removed by heating the polymer matrix. Another TEM study on buckling of electrically bent cantilever MWNTs was carried out by Poncharal et al. (Fig. 1.5 (b)) [52]. In this study, the elastic bending modulus of CNTs was found to decrease sharply (from about $1\,TPa$ to $0.1\,TPa$) when the outmost diameter increases from 8 to $40nm$, which indicates a crossover from a uniform elastic vibrational mode to an elastic vibrational mode that involves wavelike distortions (buckling) in the nanotube. Additionally, the reversible bending of MWNTs was also reported by Walter et al. [49] who bent MWNTs by changing the current density of the electron beam in a TEM.

On the other hand, by means of tip of AFM, Falvo et al. [48] directly applied bending force to a MWNT and repeatedly bent it through large angles in various configurations. The SEM images showed that buckling of MWNTs always occurred in the region of large curvature and was not limited to any specific location, which suggests that "the buckling is reversible, intrinsic to the nanotubes and not mediated by defects" [48]. Using similar experimental technique, the buckling under bending was also observed in Wong et al's [25] AFM study for MWNTs.

More recently, using SEM, Waters et al. [68] studied axially compressed buckling for short MWNTs of the aspect ratio only 2 or 4. The shell-like buckling mode of MWNTs, as predicted by Yakobson et al. [32] was first observed experimentally. Furthermore, under the same loading condition, the transformation between beam-like buckling for small-diameter MWNTs and local kinking for larger-diameter MWNTs was

reported in Thostenson and Chou's TEM study [69] for MWNTs as reinforcement in a nanocomposite.

1.2.1.2 Raman Spectroscopy for Vibration of CNTs

Free vibration of CNTs (see Fig.1.8) was clearly observed in TEM studies [39, 42, 52]. However, it is Raman spectroscopy that has been widely used to characterize vibrational behaviors of CNTs [14]. The typical Raman spectra for SWNTs with diameter less than $2nm$, are shown in Fig.1.9. The two most intense features are observed in the low frequency region between $120cm^{-1}$ and $250cm^{-1}$, and the high frequency region between $1550cm^{-1}$ and $1600cm^{-1}$ (Fig.1.9). With the help of theoretic modeling, Rao et al. [70] showed that the low-frequency feature observed in Raman spectra of SWNTs is associated with radial breathing (vibrational) modes (RBMs), where carbon atoms of a SWNT vibrate in radial direction as if the whole tube was breathing, while the high-frequency feature corresponds to tangential (T) stretch modes with adjacent carbon atoms stretching or squeezing towards each other inside the cylindrical plane of SWNTs. In particular, comparison of Raman spectra between CNTs and graphite indicates that the high-frequency feature, which is related to hexagonal structure of carbon atoms is shared by both graphite and SWNTs, while the low-frequency feature, resulting from the cylindrical symmetry is unique for SWNTs.

On the other hand, synthesized MWNTs usually had large innermost radius ($\geq 3nm$) [71]. As a result, for a long time the Raman spectra obtained for MWNTs closely resemble those of graphite without low-frequency features. In 1998, Jantoljak et al. [72] spotted a few peaks in low frequency region (around $205cm^{-1}$) for MWNTs. However, the authors could not exclude the possibility that the low energy modes came from SWNTs included in the samples. Three years later, by transforming a C_{60} sphere inside SWNTs into a tubular structure, Bandow et al. [73] obtained small-radius DWNTs of the inner diameter less than $1nm$ and observed the low-frequency Raman-active RBMs for these thin DWNTs. Up until 2002 when large amount of small-radius MWNTs were synthesized, for the very first time, the low-frequency Raman-active modes are unambiguously identified by Zhao et al. [71] and Benoit et al. [74], independently, for MWNTs of many layers. In particular, these Raman studies [71, 74] revealed that, similar

to the case of SWNTs, the low-frequency feature of MWNTs also represents RBMs of small-radius MWNTs and originate mainly from the innermost few tubes of diameter less than $2nm$.

1.2.1.3 High Pressure Experiment on CNTs

By means of x-ray diffraction, Tang et al. [75-76] observed the pressure-induced structural change of CNTs, such as reduction of interlayer spacing, distortion of cross-section and even breakage of intra-tube c-c bond. These experimental observations suggest that high pressure can be used as a sensitive technique to study the relationship between structure and mechanical properties of CNTs.

Pressure Dependence of Raman-active modes: For SWMT ropes and MWNTs, pressure-induced reduction of inter-tube spacing can enhance the inter-tube vdW interaction [19-21] and thus, increase their vibrational frequency. Similarly, the increase of intra-tube force constants due to the pressure-induced reduction of c-c bond length is also expected to affect the frequency of CNTs. Promoted by these ideas, efforts have been devoted to study the pressure effect on Raman-active modes of CNTs. By applying external pressure up to $10GPa$, the pressure dependence of Raman frequency is measured for RBM of SWNT ropes [77-79] and T –modes of all the CNT systems [77-78, 80-82]. As expected, these experiments unanimously showed that the frequencies of Raman active modes up shifted almost linearly with increasing external pressure. The obtained pressure derivative df/dp ranged from 5 to 11.9 cm^{-1}/GPa for RBMs of SWNT ropes and T –modes of all CNT systems. Especially, for Raman-active T –modes, the pressure derivative of MWNTs was generally smaller than that of SWNT ropes [82].

Pressure-induced structural instability: Another issue in high-pressure experiments is structural instability of CNTs. For SWNT ropes, Venkateswaran et al. [78] observed an abrupt drop of RBM intensity at pressure around $2GPa$. It is argued by the authors that the sudden decrease of Raman intensity might be a result of phase transition or structure instability of SWNT ropes. In fact, this transition model was first developed by Peters et al. [83] to explain the similar observation where RBM of SWNT ropes disappears at

pressure around $1.7GPa$. In view of this transition model [83], the distortion of cross-section of SWNTs occurs when external pressure reaches the critical value. Consequently, the axisymmetric RBM is expected to disappear because it is not an eigenmodes of distorted (non-circular) tube. This pressure-induced flattening of cross-section also served as an explanation for the sudden changes in other physical properties, such as the pressure derivative [82], electrical resistivity [84] or bragg peak position [85] for externally compressed SWNT ropes.

Sandler et al. [82] studied the pressure dependence of Raman-active T –mode for both MWNTs and SWNT ropes. The results display two distinct pressure regions characterized by different pressure derivatives df / dp. The transition pressure between the two regions is around $1.4GPa$ for MWNTs and around $2.3GPa$ for SWNT ropes. Moreover, Tang et al. [75] reported an abrupt change in electronic properties for MWNTs under pressure around $1.5GPa$. As in the case of SWNT ropes, the sudden changes occurring for MWNTs were also explained in terms of pressure-induced flattening (or polygonization) [75, 82] of the cross-sections of MWNTs. Particularly, Sandler et al. [82] showed that the cross-section flattening of CNTs are fully reversible with the transition between the flattening and restoring always occurring at the same pressure for both loading and unloading cycle. This result is consistent with the observation for buckling of CNTs under axial compression and bending [47-52], showing the remarkable resilience of CNTs.

1.2.2 Atomistic Simulations

In addition to experiments, atomistic modeling, such as classic MD simulation, ab initio model, general tight-binding model, force-constant model, lattice-dynamic model and molecular-structural-mechanics model, has been widely used to interpret experimental data and predict mechanical behaviors of CNTs.

1.2.2.1 Estimate of Young's modulus of CNTs

Fitting the bending stiffness $D = 0.85eV$ and in-plane stiffness $C = 59eV$ obtained based on Roberson et al's first principle calculation [31] to standard formula of continuum shell model, Yakobson et al. [32] obtained Young's modulus $5.5TPa$ for

SWNTs associated with effective thickness $0.066nm$. Lu [33], on the other hand, adopted an empirical force-constant model and carried out a relatively comprehensive study on elastic properties of both SWNTs and MWNTs. It is shown that the predicted Young's modulus (about $1TPa$) and shear modulus (about $0.5TPa$) associated with the assumed thickness of SWNTs $0.34nm$ are comparable with those of graphite [86] and almost independent of radius, helicity and number of layers. In particular, since elastic constants of CNTs scale with the inverse of thickness, the Young's modulus predicted by Lu is in good agreement with Yakobson et al's earlier estimate [32].

Subsequent to the above two attempts, classic MD simulations (Gao et al, 1998 and Yao et al, 1998) [35, 42], tight-binding method (Hernández et al, 1998) [34], lattice-dynamical model (Popov et al, 2000) [37], Ab *initio* calculation (Sanchez-Portal et al, 1998, and Kudin et al, 2002) [36, 38] and molecular structure-mechanics model (Li and Chou, 2003) [30] were also used to estimate the elastic properties of CNTs. Assuming that the thickness of SWNTs is $0.34nm$, most of these studies obtained almost helicity-independent value around $1TPa$ for Young's modulus [30, 36-38] and around $0.5TPa$ [30, 38] for shear modulus of CNTs. These results agree well with Lu's results [33] except that noticeable radius-dependence of the Young's modulus was reported for small-radius SWNTs (radius less than $1nm$) in Refs. 30, 36-38 and 42. In particular, Refs 30 and 36-38 predicted Young modulus of CNTs as an increase function of radius, while the opposite trend was demonstrated in Ref. 42. On the other hand, Gao et al. [35] reported relatively low Young's modulus between 0.643 and $0.673TPa$ in their MD simulation for closest-packed SWNTs. Here, it is noted that most of these atomistic simulations are in favor of Ruoff and Lorent's suggestion [40] that elastic modules of graphite can be used for CNTs by neglecting the change in the atomic structure when a piece of graphite is rolled into a SWNT.

1.2.2.2 Buckling Behavior of CNTs

In 1996, MD simulation was first performed by Iijima et al. [47] to simulate buckling behaviors of SWNTs and double-wall CNTs (DWNTs) under bending. Consistent with their own experimental observation [47], the simulation showed that buckling or kinks occurred on the concave side of a bent CNT and the number of kinks

increased with the increasing bending load. Using similar method, Yakobson et al. [32] studied buckling of SWNTs under various loading conditions, i.e., axial compression, bending and torsional loadings. The authors found that SWNTs under large deformation switch reversibly into different buckling patterns. Each shape change corresponds to an abrupt release of energy and a singularity in the stress-strain curve. In 2002, the classic MD simulation was again used by Ni et al. [87] for axially compressed buckling of SWNTs filled with C_{60}, CH_4 or Ne. This work predicted that the critical buckling force of filled SWNTs could increase by up to 50%, compared to that of empty SWNTs, depending on the density of the filling material. Besides this, the critical axial buckling stress $50GPa$ was reported in this MD simulation [87] for empty SWNT (10,10), while, using the quantum generalized tight-binding MD simulation (GTBMD), Srivastava et al. [88] obtained the critical axial buckling stress $150GPa$ for empty SWNT (8, 0). In addition to SWNTs, Li and Chou [89] studied elastic buckling for both SWNTs and DWNTs under axial compression or bending. The molecular-structural-mechanics approach [30, 89] has been employed to calculate the critical buckling force of CNTs as a function of the aspect ratio, diameter and helicity. Very recently, based on Brenner's "second generation" empirical potential, Liew et al's MD simulation [90] examined the effect of radius and number of layers on the critical buckling strain for axially compressed CNTs with up to four layers. The results show an optimum diameter for a SWNT, which corresponds to the maximum critical bucking strain.

1.2.2.3 Radial Breathing Modes (RBMs) of CNTs

Raman spectroscopy has been a dominant technique for characterization of CNTs. To interpret Raman spectra of CNTs various atomistic models have been used. In particular, the Raman-active RBMs are of major interest because it is this low frequency feature that distinguishes cylindrical CNTs from flat-plane graphite in Raman spectra.

Individual SWNTs: In 1997, Rao et al. [70] used lattice-dynamic model to simulate the Raman spectra for armchair SWNTs. Fitting the simulated results to experimental vibrational spectra they confirmed that the Raman signal in low-frequency $(120 - 250cm^{-1})$ region (see Fig.1.9) originated from RBM, which was unique to SWNTs of cylindrical symmetry. Especially, their results suggested that the frequency of RBM scaled with the inverse of the radius of the tested arm-chair SWNTs [70]. Later on, using a force-constant model Satio et al. [91] further calculated the vibrational spectra for SWNTs of various helicities. The obtained RBM frequencies are found to be sensitive to the diameter of SWNTs, but almost independent of their helicities. In particular, it was shown that, for an isolated SWNT of radius r, the RBM frequency f can be calculated by [91]

$$f = f_{(10,10)} \cdot \left(\frac{r_{(10,10)}}{r} \right)^{1.0017 \pm 0.007} \tag{1.4}$$

where $f_{(10,10)}$ and $r_{(10,10)}$ are RBM frequency and radius of SWNTs (10, 10). This relationship for RBM of SWNTs is consistent with Rao et al's earlier results [70] and later, confirmed by many other atomistic models, such as Bandow et al's force constant model [92], Kurti et al's first–principle calculation [93] and Sanchez-Portal et al's *ab initio* calculation [36]. Particularly, Bandow et al. [92] obtained

$$f = 224.5 / r \tag{1.5}$$

for RBM of SWMTs with radius r, showing that, the Raman peaks originating from low frequency RBM is a fingerprint-like signal for individual SWNTs, and thus can be effectively used in determination of radii of SWNTs.

SWNT ropes (bundles): Using GTBMD simulation, Venkateswaran et al. [77] first examined the effect of the inter-tube vdW interaction on RBM of SWNT ropes. The authors noticed that, due to the interaction between one tube and six neighboring tubes,

RBM frequency of (9, 9) SWNT ropes was about $14cm^{-1}$ (about 8%) higher than that of an isolated SWNT (9,9). Kahn and Liu [94] performed similar GTBMD calculation for (10, 10) SWNT ropes, showing $6cm^{-1}$ up-shift in RBM frequency. Moreover, a slight chiral dependence of the RBM frequency of SWNT ropes has been reported in Henrard et al's GTBMD simulation [95], which showed 10% average up-shift of the RBM frequency relative to those of isolated SWNTs. Furthermore, Popov et al. [96] and Henrard et al. [97] studied both homogeneous (made of tubes with identical radius) and inhomogeneous (made of tube with non-uniform radius) SWNT rope based on a lattice-dynamic model and a continuum model. They found that, for homogeneous ropes, the up-shift of RBM frequency increased with increasing number of SWNTs present in ropes and approached $15cm^{-1}$ for an infinite (10, 10) SWNT rope, while Raman spectra of inhomogeneous SWNT ropes cannot be considered as a superposition of signature of the constituent SWNTs. Recently, Ldfrant and his co-workers [98-99] studied the effect of the vdW interaction on RBMs of different CNT systems. The increment of RBM frequency calculated for SWNT ropes ranges from 11 to $16cm^{-1}$ [98] or 10 to $20cm^{-1}$[99], in good agreement with their experimental results [98-99].

MWNTs: In 2002, Popov and Henrard [24] conducted a comprehensive theoretical study on RBMs of MWNTs. Their MD simulation revealed that the RBMs of small-radius MWNTs (the innermost radius $0.34nm$) are radial vibrations of mainly one layer with the associated frequency slightly higher than that of the isolated tube, while for large-radius MWNTs (the innermost radius $1.36nm$), the RBMs represent collective radial motions of many layers of mixed of in-phase and counter-phase type.

Benoit et al. [74] studied the RBMs of MWNTs experimentally and theoretically. Different from Popov et al. [24], they mainly focused on small-radius MWNTs of the innermost radius less than $1nm$. Comparing experimental Raman spectra to an atomistic simulation, the authors found that the low frequency Raman peaks observed for MWNTs originated from the RBMs of the innermost few tubes with radius less than $1nm$. The associated frequency depended sensitively on the radius of the individual tube but cannot be significantly affected by the number of layers. In particular, due to the interlayer vdW interaction, the frequency of the RBM from the innermost tube(s) of the small-radius

MWNTs was found to be 5% to 10% higher than that of an isolated SWNT [74]. Similar results were also obtained in Zhao et al's experiment [71] and Popov et al's MD simulation [24]. Therefore, introducing the 5 to 10% up-shift into Eq. (1.5) for isolated SWNTs, one can easily obtain the RBM frequency-diameter relationship for small-radius MWNTs, showing that the Raman-active RBM can be as useful in the characterization of MWNTs as it is for SWNTs.

1.2.3 Elastic Models

As reviewed in Section 1.2.2, atomistic simulations are sophisticated theoretical techniques, which can be used "to guide experiment, point out the most promising avenues to explore and assist with interpretation" [26]. However, the computational resource and time needed in simulations explode exponentially for large atom systems like CNTs of thousands of carbon atoms. Thus atomistic modeling remains computationally expensive and formidable, and usually is limited to SWNTs or MWNTs of not more than four layers. Consequently, the relatively simple and cost-effective continuum models, such as beam and shell models have been widely used for nanomechanics of CNTs. It has been demonstrated that "the laws of continuum mechanics are amazingly robust and allow one to treat even intrinsically discrete object only a few atoms in diameter" [43].

This section gives an overview of elastic models for CNTs, i.e., elastic beam models and elastic shell models. To demonstrate their effectiveness and accuracy, the comparison between elastic models and available experiments or atomistic simulations is emphasized. Especially, our major attention is mainly focused on buckling and vibration of CNTs, which are closely related to the current research.

1.2.3.1 The Single-beam Model

It is known that CNTs usually have large aspect ratio up to 1000 or even larger. When this is the case the elastic beam model is adequate for overall mechanical behaviors of CNTs. The governing equation for an elastic beam under axial force F and transverse distributed pressure $p(x)$ (per unit lateral length) is governed by [100, 101]

$$p(x) + F\frac{\partial^2 w}{\partial x^2} = EI\frac{\partial^4 w}{\partial x^4} + \rho A\frac{\partial^2 w}{\partial t^2} \tag{1.6}$$

where x is the axial coordinate, t is time, $w(x,t)$ is the deflection of the beam, I and A are the moment of inertial and the area of the cross-section of the beam, and E and ρ are Young's modulus and the mass density of unit volume. Thus, for a CNT modeled as an elastic beam, the mechanical behaviors, such as static equilibrium, instability and vibration can be completely described by (1.6) with three parameters, i.e., the bending stiffness (EI), mass density per unit lateral length (ρA), and the axial stiffness (EA). Here, it is emphasized that for SWNTs, these three parameters are primarily independent of different definitions of representative thickness (e.g., $0.34\,nm$ [33], $0.066\,nm$ [4, 32] or $0.0894\,nm$ [34]).

Static Deflection: Based on Eq.(1.6), the transverse deflection y can be calculated by

$$y = \frac{pa^2}{6EI}(3x - a) \quad (a \le x \le L)$$ for a cantilevered SWNT of length L, subject to a concentrated force p at point $x = a$ measured form fixed end. The $1/a^3$ dependence of $p / y(x)\big|_{x=a}$ predicted by this formula has been found to be consistent with the results of Wong et al's AFM experiment [25]. Further, based on above beam model, Salvetat et al. [102] derived a formula for the maximum deflection of a CNT under concentrated force p acting at its midway. This formula has been used to estimate Young's modulus of CNTs. The obtained value ($0.81\,TPa$) is in reasonably good agreement with those given by other methods. Here, it is emphasized that in these studies the thickness of SWNTs is taken as $0.34\,nm$.

Column Buckling: The critical buckling force of a simply supported elastic beam under axial force is given by $p_{cr} = \frac{\pi EI}{L^2}$ [103]. This formula has been used to calculate the maximum axial force for MWNTs. With $E = 1TPa$, Dai et al. [64] obtained the Euler force around $5\,uN$ for a MWNT of length $250\,nm$ and diameter $5\,nm$. On the other hand, fitting the Euler force predicted by the above formula to MD simulation results, Garg et

al. [104] reported the estimated value of Young's modulus around $1\,TPa$, which is in good agreement with the value obtained by other studies. In addition, Euler force of clamped SWNTs was also calculated by Yakobson et al. [6] based on above formula multiplied by four to its right hand side, indicating the sensitivity of the Euler force of CNTs to the end condition.

Vibrational Frequency: Based on beam model, the n – order circular frequency of a CNT of length L can be computed by $\omega_n = \dfrac{\beta_n^2}{L^2}\sqrt{\dfrac{EI}{\rho A}}$, where β_n is a function of the number n and boundary conditions on the two ends [39, 100, 101]. Indeed, Poncharal et al. [52] showed that the value 5.68 of ratio ω_2 / ω_1 obtained in experiment for a MWNT is close to the theoretical value 6.2 given by the above formula. Moreover, the second-order vibrational mode observed in the experiment [52] gave the value of a characteristic length $0.76\,L$, in good agreement with the value $0.8\,L$ predicted by the beam model.

1.2.3.2 The Multiple-beam Model

As mentioned in Section 1.1.1.2, different from classic beam, MWNTs exhibit multiplayer structure with significant normal interlayer vdW interaction and negligible interlayer friction. However, in previous work such as those mentioned before, a MWNT was modeled as a single hollow beam, which, in fact, assumed that the repulsive and attractive intertube vdW force is always strong enough to resist the change in interlayer spacing and all the tubes of MWNTs always remain coaxial during deformation. In reality, these assumptions may not be true because an individual tube of a MWNT could deform with non-zero interlayer radial deflection while their deformations are generally coupled with each other through the interlayer vdW interaction.

Column Buckling of MWNTs: To address the issue regarding the effect of interlayer radial displacement on mechanical behaviors of MWNTs, Ru [105] has developed a multiple-beam model to study the column buckling of MWNTs embedded in an elastic medium. In contrast to existing single-beam model, the multiple-beam model assumes that each of the nested and originally concentric tubes of a MWNT is an individual elastic

beam and the radial deflections of adjacent tubes are coupled via the normal vdW interaction. The intertube interaction between two adjacent tubes can be estimated by the known vdW interaction between a carbon atom and a flat graphite sheet [19]. In particular, for infinitesimal buckling, the vdW interaction is proportional to the change in intertube spacing or radial deflection jump between two neighboring tubes. On the basis of this model, Ru [105] indicated that the nonconincidence of the deflected axes of adjacent tubes couldn't be neglected when the half wave number of buckling modes is comparable to the outermost radius of a MWNT. Thus, under this condition, the single-beam model becomes invalid for axially compressed buckling of MWNTs and has to be replaced by the multiple-beam model.

Nonconaxial Vibration of MWNTs: The multiple-beam model has also been applied to study the free vibration of MWNTs of relatively small radius (less than $1nm$) [106]. It is found that the higher order frequencies of MWNTs are associated with the unusual vibrational modes, in which some or all adjacent tubes vibrate or deform in opposite directions leading to substantial change in intertube spacing and non-coaxial geometry of MWNTs. These newly obtained modes of MWNTs are of practical interest because the non-coaxial geometry of MWNTs could significantly affect certain physical properties, e.g., electronic properties [107-110] and optical properties [111-112] of originally coaxial MWNTs. In particular, as in the case of buckling, it is concluded that for high-order modes of MWNTs whose characteristic wavelengths are only a few times that of the outermost tube, the intertube radial displacement would come to play a significant role. In this case, only multiple-beam model can be used to characterize the vibrational behaviors of MWNTs. Recently, this non-coaxial mode predicted by the multiple-beam model [106] for MWNTs has been confirmed based on an atomistic model, i.e., the molecular-structure-mechanics model [113], for DWNTs.

1.2.3.3 The Single-shell Model

Shorter CNTs of smaller aspect ratio have been used in many applications [63, 68, 114-115]. Especially, the local deformation of CNTs were observed and studied in experiments [47-52] and atomistic simulations [4, 47]. In these cases, elastic shell model

can be employed for nano-mechanics of CNTs. In particular, since the elastic properties of a two-dimensional hexagonal structure of SWNTs are almost isotropic [32], a CNT can be approximated by an isotropic shell. For instance, in the absence of tangential force, the elastic buckling or vibration of a SWNT, modeled as an isotropic cylindrical shell of radius r can be described by the Donnell equation [116-117]

$$DV^8 w = \nabla^4 p(x,\theta) + F_x \frac{\partial^2 x}{\partial x^2} \nabla^4 w + 2\frac{F_{x\theta}}{r} \cdot \frac{\partial^2}{\partial x \partial \theta} \nabla^4 w + \frac{F_\theta}{r^2} \frac{\partial^2}{\partial \theta^2} \nabla^4 w$$
$$- \frac{Eh}{r^2} \frac{\partial^4 w}{\partial x^4} - \rho h \frac{\partial^2}{\partial t^2} \nabla^4 w$$

$$(1.7)$$

where x and θ are axial coordinate and circumferential angular coordinate, respectively, t is time, w is the (inward positive) radial deflection due to buckling or vibration, $p(x,\theta)$ is the net normal (inward positive) pressure resulting from buckling or vibration. F_x and F_θ are the known uniform axial and circumferential membrane forces, D and h are effective bending stiffness and thickness of the SWNT, and E and ρ are Young's modulus and mass density per unit volume. It is seen from Eq.(1.7) that similar to the case of elastic beam, in order to use isotropic shell model, it is adequate to know three parameters, i.e., bending stiffness D, in-plane stiffness C ($= Eh$) and mass density per unit surface area ρh.

Axially Compressed Buckling of SWNTs: Shell model was used by Yakobson et al. [32] to study elastic buckling of a SWNT under axial compression. Based on the data given by [31], they obtained the value $D = 0.85eV$ and $C = 360 J/m^2$ for a SWNT as a micro-shell. Comparison showed that the elastic shell model was in accordance with the MD simulation in predicting critical buckling strain and buckling modes for SWNTs. In particular, fitting the obtained value of D and C into the formula of classic shell theory [116-118]

$$D = \frac{Eh^3}{12(1 - v^2)} \quad \text{and} \quad C = Eh \tag{1.8}$$

the authors gave $E = 5.5TPa$ associated with representative thickness $h = 0.066nm$. However, as Ru [119] pointed out, the adoption of this representative thickness " causes not only an inconsistence with the common concept of representative thickness ($0.34nm$) established for graphite sheet, but also some inconvenience in application of the elastic shell model to carbon nanotube"

On the other hand, by using the usually accepted representative thickness $0.34nm$ [33], which is equal to the interlayer spacing of MWNTs, the classic formulae (1.8) leads to bending stiffness D much larger than the obtained value $0.85eV$. Ru [119-120] realized that this discrepancy is a result of the single atom-layer structure of SWNTs, which distinguishes them from continuum shells. It is argued in [120] that the classic formula for bending stiffness in (1.8) is derived on the basis of the assumption that an elastic shell can be divided infinitesimally into thinner layers without interlayer slip, and flexural stresses and strains are linearly distributed over the thickness. However, the single atom-layer of a SWNT cannot be divided any further and therefore, the flexural stress and strain are, in fact, concentrate on a narrow region around the central line of the atom layer. In light of this discrete feature of SWNTs, Ru suggested [120] that the first formula in (1.8) could be abandoned for SWNTs and the effective bending stiffness of SWNTs can be regarded as a material parameter, not necessarily proportional to cubic of the representative thickness. Following this suggestion, the accepted representative thickness $0.34nm$ can be retained and almost all equations of elastic shell theory remain valid with small or without any modification.

Based on this modified shell model, Ru [120] derived a simple formula to calculate critical buckling strain and wave number for axially compressed SWNTs of moderate aspect ratio (not less than 4). For SWNTs of diameter $1nm$, $2.2nm$ and $3.3nm$, respectively, the critical strain predicted by this formula is 0.075, 0.034 and 0.023 [120] in good agreement with MD simulation results 0.05 [32] (or 0.08 [88]), 0.037 and 0.025 [121]. Additionally, assuming that CNTs buckle in nonaxisymmetric modes with equal axial and circumferential wave length [121-122], the wavelength about $1.2nm$ given by

the shell model for a SWNT of radius $0.67nm$ was found to be very close to value $1.3nm$ predicted by MD simulation [122]. These examples convincingly show the efficiency of the shell model for axially compressed buckling of SWNTs.

Pressure-induced Buckling of SWNT ropes: Synthesized SWNTs are usually produced in ropes consisting of aligned individual SWNTs with narrow distribution of diameter. As reviewed in Section 1.2.1.3, the abrupt changes in physical properties of externally compressed SWNT ropes have been observed in Refs. 77, 83 and 84. To explain these interesting phenomenons, Ru [123] modified the conventional honeycomb model and applied it to study the buckling of SWNT ropes under high pressure. A simple formula is given in [123] for critical pressure beyond which the instability or cross-section flattening of SWNT ropes occurs. The critical value $1.8GPa$ obtained for SWNT ropes of diameter $1.3nm$ is in excellent agreement with available experimental data ranging form 1.5 to $1.9GPa$ [77, 83-84].

Free Vibration of SWNTs: The free vibration of SWNTs with long-wavelength has also been studied based on three Donnell dynamic shell equations [124-126], instead of the single Donnell equation for radial deflection (see Eq.1.7). Here, the phonon-dispersion relations (i.e., vibrational spectra) were calculated for SWNTs of infinite length [124] or clamped SWNTs of finite length [124-126]. In particular, the axisymmetric and long-wavelength longitudinal vibration of SWNT [126] predicted by classical shell model has been directly observed in the experiment by means of inelastic light scattering measurement. Moreover, comparing the frequency of SWNTs calculated by elastic shell model to the experimental measurements leads to Young's modulus of the order of $1TPa$ for SWNTs with the assumed thickness of SWNTs of the order of $0.1nm$ [126], in accordance with other reported values.

1.2.3.4 The Multiple-shell Model

MWNTs are comprised of concentric SWNTs coupled with each other via the normal interlayer vdW interaction. Since the interlayer friction is negligible, the adjacent tubes of a MWNT can almost slide and rotate towards each other freely [15-18]. In spite

of this fact, almost all previous shell models for MWNTs ignored the interlayer slips and considered a MWNT as a single-layer elastic shell whose thickness is equal to the difference between the outermost and innermost radii. Particularly, it has been tacitly assumed that the bending stiffness of a MWNT is proportional to the cubic of such a thickness. Obviously, this oversimplified model could result in significant errors in characterizing mechanical behavior of MWNTs. In order to examine this issue, Ru [127-129] has developed a multiple-shell model to study the effect of interlayer slips on axially compressed buckling of MWNTs. This multiple-shell model [127-129] treats each of the concentric SWNTs of MWNTs as an individual elastic shell whose radial deflections are coupled through the interlayer vdW interaction without any interlayer friction.

Axially Compressed Buckling of MWNTs: Based on the multiple-shell model, Ru [127] considered a simply supported DWNT and derived an explicit formula for the axial buckling strain of the DWNT. This formula shows that for axially compressed buckling, the critical axial strain of a DWNT is the same as that of a SWNT of the same radius, in sharp contrast to the single-shell model which predicts that the critical axial strain of a DWNT should be two times that of a SWNT of the same radius. Subsequently, a DWNT embedded in an elastic medium was also studied based on the multiple-shell model [128]. The results indicated that a DWNT or a MWNT would be even more susceptible to infinitesimal axially compressed buckling than an embedded SWNT. Furthermore, Ru [129] demonstrated that for an N–wall CNT under axial compression, the critical buckling strain given by the multiple-shell model is around $5N$ times smaller than that obtained by the single-shell mode. In particular, a thin N–wall CNT (radius-to-thickness ratio larger than four) can be treated approximately as an elastic shell whose bending stiffness and effective thickness are N times those of a SWNT of the average radius. All these studies clearly reveal that the interlayer slips, which are ignored by the single-shell model, have a crucial effect on buckling behavior of MWNTs. Additionally, assuming that the interlayer vdW interaction is " infinitely strong" a simple formula [129] has been derived for the upper bound of critical buckling force of MWNTs under axial compression. Recently, this formula was used by Waters et al. [68] to estimate the upper limit of critical axial buckling force for specific 36-wall CNTs with the innermost radius

13 nm . The obtained value 3.37 μN is close to the critical axial buckling forces 2.26 μN and 2.54 μN measured experimentally for the 36-wall CNTs of the length 100 nm and 50 nm , respectively [68].

1.3   Contributions of the Present Work [130-136]

As reviewed above, the mechanical properties of SWNTs have been studied extensively in last decade. In addition, some special issues, e.g., axially compressed buckling, RBM vibration, or beam-like vibration of MWNTs have also been discussed in detail. However, comprehensive study on mechanical behavior of MWNTs has not been reported in the literature. This is because there exist major challenges in nano-scale experiments of MWNTs whose mechanical behavior is complicated and cannot be readily observed and analyzed without a theoretical guidance. Moreover, as mentioned before, computational efforts needed for atomistic modeling of MWNTs is formidable and therefore, limit the size of MWNTs that can be studied by using these discrete approaches. Additionally, due to the multiplayer structure of MWNTs and the interlayer vdW interaction, the existing (continuum) solid mechanics models, for example classic single-shell model, in general, cannot be directly employed to characterize mechanical behavior of MWNTs.

On the other hand, the cost-effective multiple-shell model [127-129], which accounts for the interlayer vdW interaction and interlayer slips of MWNTs, has been developed for the axially compressed buckling of DWNTs [127-128] or MWNTs in extreme cases [129]. Taking advantage of the multiple-shell model, the present work based on [130-136] is devoted to a systematic study on the elastic buckling and free vibration of MWNTs. The objective of this research is to catch the unique features of mechanical behavior of MWNTs and examine the role of the interlayer vdW interaction of MWNTs in nano-mechanics. Particularly, the present multiple-shell model has been compared to the available experiments and atomistic simulations to demonstrate its effectiveness and identify the accurate values of parameters used in the multiple-shell model or the multiple-beam model for CNTs [130-136].

In what follows, the detailed theoretical derivation and numerical calculation are given for buckling and vibrational analyses of MWNTs. Chapter 2 outlines the general formulations for buckling of MWNTs under axial and radial load [130-132, 133]. The single Donnell equation (1.7) [116-118] is chosen to simplify buckling analysis of MWNTs, in which radial deflection is predominant. By using the multiple-shell model and Eq. (1.7), the N coupled equations are derived for buckling of an $N-$wall CNT. The mathematical method of buckling analysis is demonstrated, in detail, for simply supported MWNTs under radial pressure, axial stress or radial–axial combined load.

Chapter 3 gives detailed analysis for elastic buckling of individual MWNTs under radial pressure [130, 133]. According to their radius-to-thickness ratios, the MWNTs discussed here are classified into three types: thin, thick, and (almost) solid. The critical buckling pressure and associated buckling modes are calculated for MWNTs under external pressure. Subsequently, the effect of an internal pressure and the possible pressure-induced interlayer locking on critical external pressure is examined for MWNTs of all the three types. In particular, the critical pressure predicted by the multiple-shell for specific group of 20-wall CNTs is in good agreement with known experimental results [75].

Chapter 4 discusses axially compressed buckling of individual MWNTs subjected to an internal or external radial pressure [131]. The emphasis is placed on new physical phenomena due to combined axial stress and radial pressure. The critical axial stress and the buckling mode of thin, thick and (almost) solid MWNTs (defined in chapter 3) are calculated for various radial pressures-to-axial stress ratios, with detailed comparison to the classic results of singlelayer elastic shells under combined loadings. It is shown that the buckling mode associated with the minimum axial stress is determined uniquely for MWNTs under combined axial stress and radial pressure, while it is not unique under pure axial stress. Especially, the present results show that the predicted increase of the critical axial stress due to an internal radial pressure appears to be in qualitative agreement with some known results for filled SWNTs obtained by MD simulations [87].

In Chapter 5, the general formulation for free vibration of MWNTs [134-136] is outlined based on the multiple-shell model [127-129]. In order to identify all the vibrational frequencies and associated modes the three exact Flugge equations [137-138]

are employed to describe the free vibration of individual tubes of MWNTs. Applying the exact Flugge equations to each individual tube of an N – wall CNT leads to $3N$ dynamic equations governing free vibration of the MWNT. The mathematical method of vibrational analysis is demonstrated, in detail, for MWNTs with two ends simply supported. It is shown that for an N – wall CNT, there exist $3N$ vibrational frequencies associated with $3N$ vibrational modes.

In order to show the relevance of the above dynamic shell model for MWNTs Chapter 6 studies the RBMs of MWNTs with or without external pressure [132, 134]. In the absence of external pressure, the RBM frequencies and vibrational modes predicted by the present shell model are found to be in good agreement with the available experimental and MD simulation results. In the presence of an external pressure, the results show that high external pressure considerably raises the vdW interaction coefficients (defined by the second derivative of potential energy between adjacent tubes with respect to the interlayer spacing), especially between the outermost few layers of MWNTs. As a result, some of the RBM frequencies of MWNTs increase significantly with increasing external pressure. The most significant pressure effect occurs for the highest-frequency mode of large-diameter MWNTs (with the innermost diameter $> 2\,nm$) or an intermediate-frequency mode of small-diameter MWNTs (with the innermost diameter $< 2\,nm$), and is always associated with those RBMs in which adjacent outermost layers vibrate in opposite directions with significant change in interlayer spacing.

In Chapter 7, the general features of free vibration of MWNTs have been investigated with an emphasis on the effect of interlayer vdW interaction on free vibrations of MWNTs [135]. The results show that the vdW interaction has a crucial effect on R-modes of large-radius MWNTs (e.g., of the innermost radius 5 nm), but is less pronounced for R-modes of small-radius MWNTs (e.g., of the innermost radius $0.65nm$), and usually negligible for T- and L-modes of MWNTs. This is attributed to the fact that the interlayer vdW interaction, characterized by a radius-independent vdW interaction coefficient, depends on radial deflections only, and is dominant only for large-radius MWNTs of lower radial rigidity but less pronounced for small-radius MWNTs of much higher radial rigidity. As a result, the R-modes of large-radius MWNTs are

typically collective motions of almost all nested tubes, while the R-modes of small-radius MWNTs, as well as the T- and L-modes of MWNTs, are basically vibrations of individual tubes.

Chapter 8 is focused on some special issues of free vibration of MWNTs [136]. First, an updated bending stiffness $(D = 2eV)$ of SWNTs is suggested based on recent data in the literature, which is in much better agreement with atomistic model for phonon dispersion relations of SWNTs than the previously adopted value $(D = 0.85eV)$ [32]. Using the multiple-shell model with $D = 2eV$, this chapter gives a comprehensive study on axisymmetric modes $(n = 0)$ of MWNTs. The major attention is focused on the unique features of axisymmetric modes of MWNTs and the effect of the Poisson-ratio of SWNTs on coupling between R - and L - modes of MWNTs. Furthermore, the present shell model is employed to study beam-like vibrational modes $(n = 1)$ of MWNTs and examine the accuracy and applicability of the multiple-beam model [106]. In addition, the lowest frequency and associated modes of MWNTs are also studied in detail.

Finally, Chapter 9 suggests some simplifications on the multiple-shell model [130-131, 132]. For buckling or the lowest-frequency vibration, a thin N-wall CNT (defined by the radius-to-thickness ratio around or larger than 4) is found to be approximately equivalent to a singlelayer elastic shell whose effective bending stiffness and thickness are N times those of SWNTs [130-131, 135]. Based on this single-shell model for a thin MWNT, an approximate method is suggested for the buckling problem of a thick or almost solid MWNT of many layers [130-131]. The accuracy of these approximate methods has been examined with specific examples. On the other hand, the applicability and limitations of Donnell equation [116-118] and a simplified Flugge equation [139] has been investigated systematically for SWNTs in various problems of static buckling and free vibration [132]. It is shown that the simplified Flugge model, which retains the mathematical simplicity of the Donnell model, enjoys improved accuracy and enlarged range of applicability as compared to the Donnell model, and thus is recommended for static and dynamic problems of CNTs [132]. Subsequently, the simplified Flugge equation has been further used for the radial vibration frequencies of MWNTs in good agreement with the three exact Flugge equations [135].
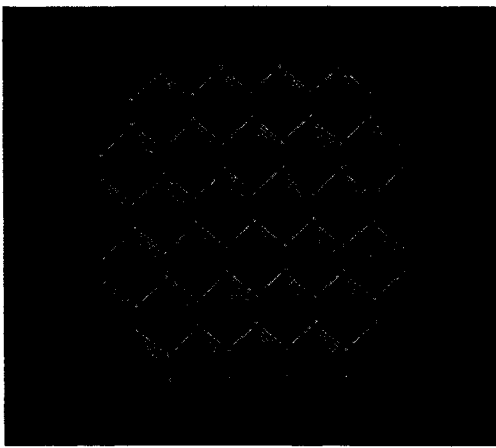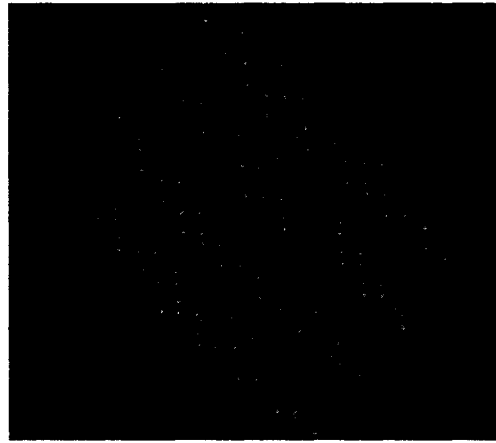
(a) Diamond   (b) Graphite
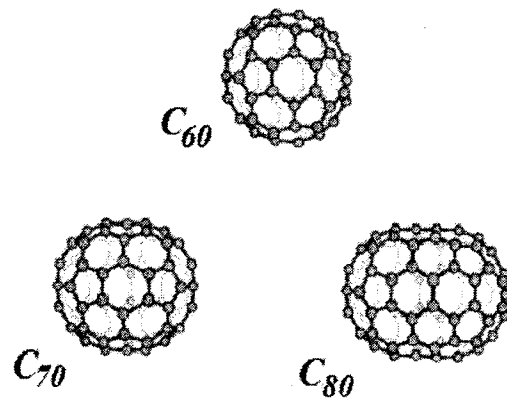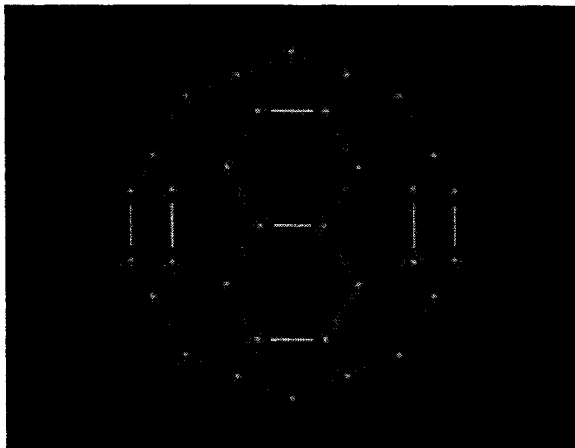
(c) Fullerenes

Fig.1.1 Molecular structures of (a) diamond, (b) graphite and (c) fullerenes (e.g., C_{60},

C_{70} and C_{80}).

(a)   (b)
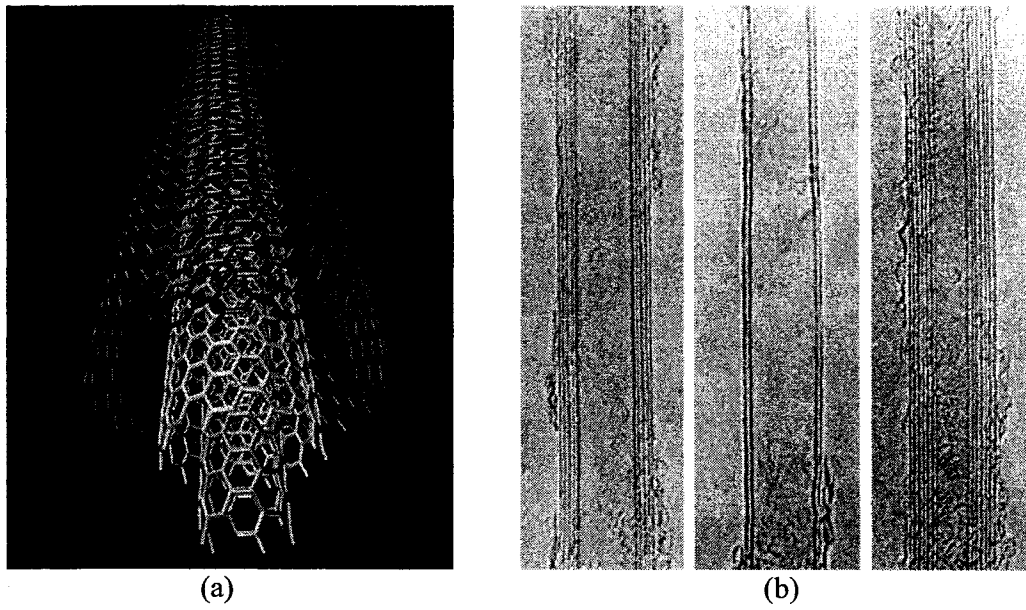
Fig. 1.2 (a) Simulation model of a MWNT and (b) High-resolution electron micrographs

of MWNTs [2] (from left to right: 5-, 2- and 7-wall CNTs).

(a)   (b)   (c)
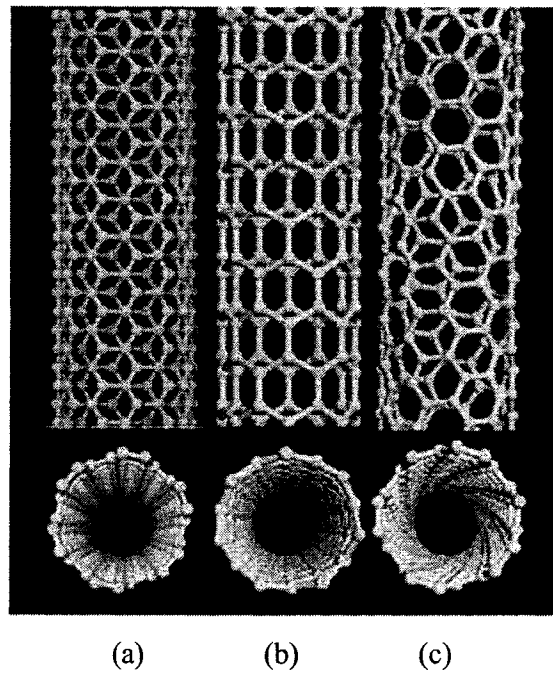
Fig. 1.3 (a) Arm-chair, (b) Zig-zag and (c) Chiral SWNTs [11].
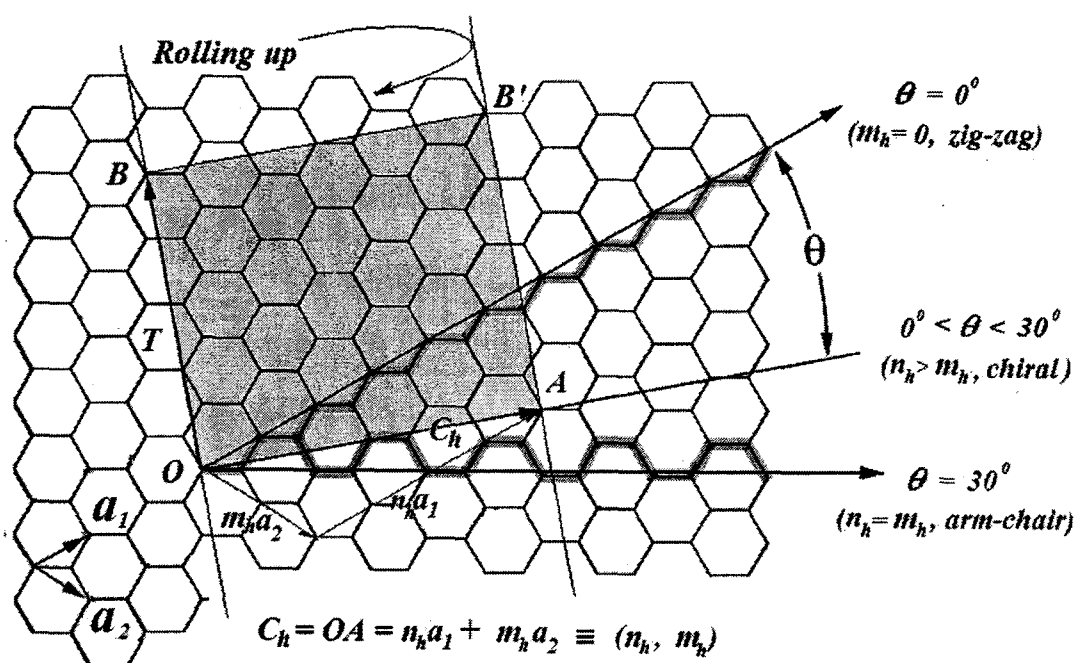
Fig.1.4 Schematic diagram showing how a hexagonal sheet of graphite is "rolled" to form SWNTs of different helicities shown in Fig.1.3.

(a)   (b)
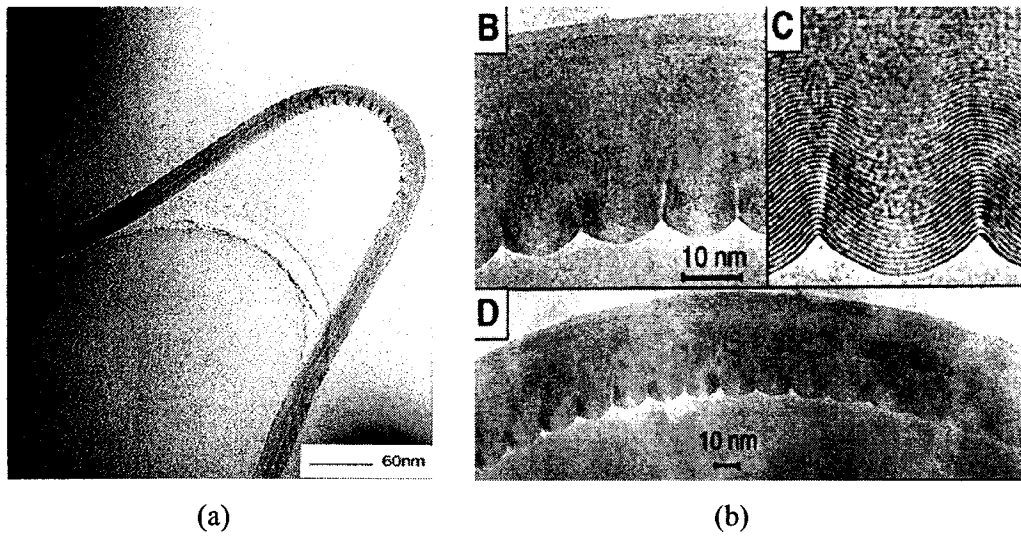
Fig 1.5 (a) A MWNT is bent into a large angle with removable kinks occurring on
concave side due to high compression [50]. (b) Enlarged images of local
buckling patterns on concave side of bent MWNTs [52].

(a)   (b)
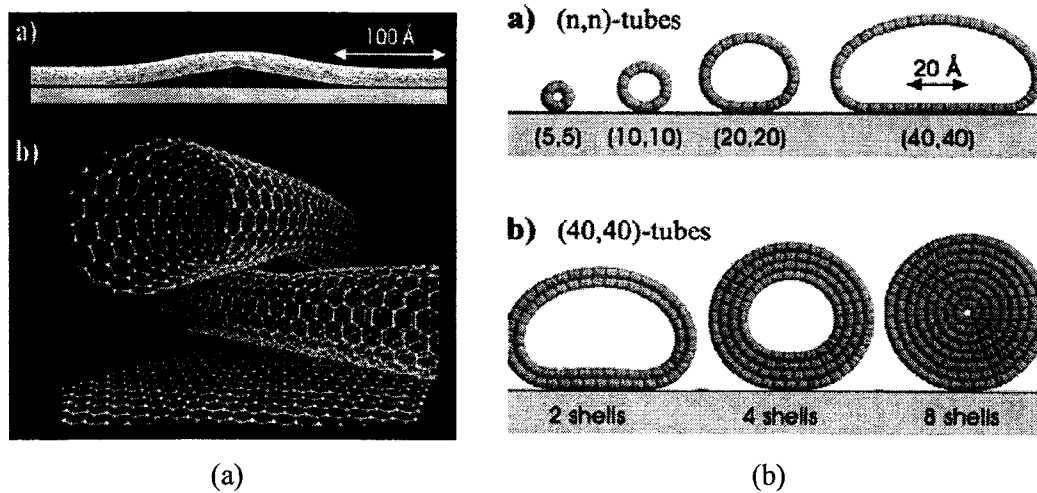
Fig. 1.6 The surface vdW interaction-induced (a) axial deformation and (b) radial
deformation of SWNTs and MWNTs [54].
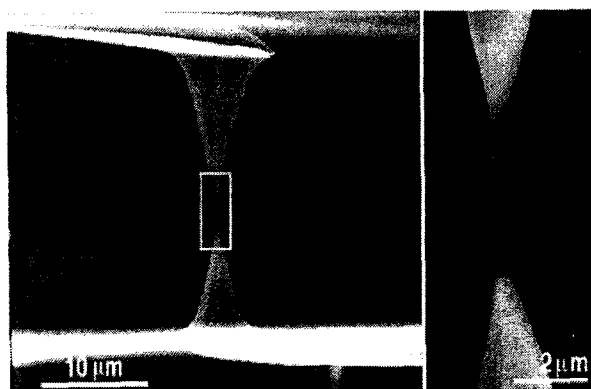
Fig. 1.7 SEM Image of a CNT with two ends   1.8 Free vibration of MWNTs [52]

attached to two AFM tips before tensile loading [29].
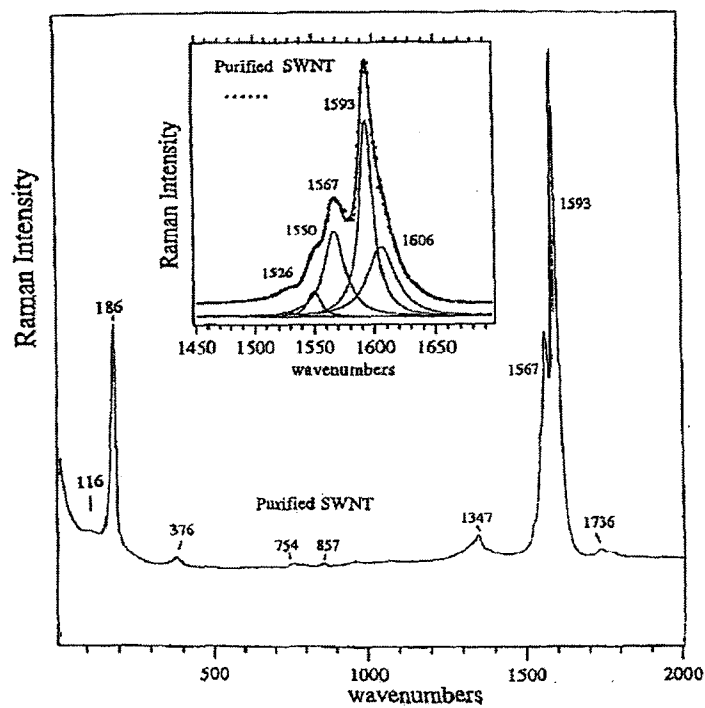
Fig. 1.9 Experimental Raman spectrum for ropes of SWNT (10, 10) [14].

Chapter 2

Basic Formulations for Buckling of MWNTs

2.1 Introduction

Elastic buckling of CNTs has received considerable attention in recent research [47-52]. It has been shown that the buckling of CNTs could significantly affect their performance as reinforcing fibers in super-strong nano-composite material [50-51], which is the most potential application of CNTs. Especially, the buckling-induced structure-instability of CNTs could lead to substantial changes in other mechanical or physical properties of CNTs, e.g., vibrational modes [78, 82-83], electrical resistance/capacitance [75] and optical properties [145]. Thus, thorough understanding of buckling behavior is crucial for the potential applications of CNTs in nanotechnology

Among various theoretical methods, the elastic shell models have been effectively used in buckling analysis of SWNTs under axial force [32, 120], radial pressure [123] or bending [48]. The critical buckling load and associated modes predicted by the shell model agree very well with known MD simulation [32, 120] and experimental data [123]. However, for MWNTs some previous shell models have tacitly assumed that no sliding occurs between any two adjacent tubes in a MWNT and thus a MWNT can be described as a single-layer elastic shell whose thickness is equal to the difference between the innermost and the outermost radii. Such a simplified model has ignored the fact that the interlayer friction between adjacent tubes is usually so low that free-sliding could take place between adjacent tubes. Based on this idea, a multiple-elastic shell model [127-129] has been developed, in which each of the concentric tubes of MWNTs is modeled as an individual elastic shell coupled with adjacent tubes through the interlayer vdW interaction, and the interlayer friction is ignored. This multiple-shell model [127-129] has been effectively used for axially compressed buckling of DWNTs or MWNTs in extreme cases.

To conduct a systematical study on buckling of MWNTs in more general cases, this chapter further utilizes the multiple-shell model [127-129] to derive the general

37

formulations for elastic buckling of MWNTs under both axial stress and radial pressure. For simplification, the single Donnell shell equation (2.1) for radial deflection is used in the multiple-shell model to describe elastic buckling of each individual tube of MWNTs. Therefore, the buckling of an N-wall CNT is governed by N equations coupled with each other through the vdW interaction terms. Subsequently, the mathematical methods for both pre-buckling and buckling analyses are demonstrated, in detail, for MWNTs with two ends simply supported.

2.2 The Multiple-shell Model for Elastic Buckling

The elastic-shell models have been effectively applied to CNTs [32, 48, 120, 123, 127-129]. In particular, for MWNTs, a multiple-elastic shell model [127-129] has been developed for axially compressed buckling of MWNTs in extreme cases. In the present work, we shall further extend the multiple-shell model to general buckling behavior of MWNTs subjected to axial stress combined with radial pressures.

2.2.1 Basic Equations

The multiple-shell model [127-129] assumes that each of the concentric tubes of MWNTs can be described as an individual elastic shell. The adjacent two tubes are coupled with each other via the interlayer normal vdW interaction and the interlayer friction is negligible. In the absence of any tangential external force, elastic buckling of a cylindrical shell (of radius r) under axial stress and radial pressures is governed by [116-119, 127-129].

$$DV^8 w = V^4 p(x,\theta) + F_x \frac{\partial^2}{\partial x^2} V^4 w + \frac{F_\theta}{r^2} \frac{\partial^2}{\partial \theta^2} V^4 w - \frac{Eh}{r^2} \frac{\partial^4 w}{\partial x^4} \qquad (2.1)$$

In fact, the buckling equation (2.1) can be obtained directly from general equation (1.7) with $F_{x\theta} = 0$ and $\rho h \frac{\partial^2}{\partial t^2} V^4 w = 0$. In particular, for a SWNT the effective bending

stiffness D can be treated as a material constant independent of the thickness h, and thus not necessarily proportional to h^3.

The present work studies elastic buckling of individual MWNTs under combined axial stress and radial pressures, as shown in Fig. 2.1. Applying Eq. (2.1) to each of the concentric tubes of a MWNT, elastic buckling of a MWNT is governed by the N coupled equations

$$D_1\nabla_1^8 w_1 = \nabla_1^4 p_{12} + F_x^{(1)}\frac{\partial^2}{\partial x^2}\nabla_1^4 w_1 + \frac{F_\theta^{(1)}}{r_1^2}\frac{\partial^2}{\partial\theta^2}\nabla_1^4 w_1 - \frac{Eh_1}{r_1^2}\frac{\partial^4 w_1}{\partial x^4},$$

$$D_2\nabla_2^8 w_2 = \nabla_2^4\left[p_{23} - \frac{r_1}{r_2}p_{12}\right] + F_x^{(2)}\frac{\partial^2}{\partial x^2}\nabla_2^4 w_2 + \frac{F_\theta^{(2)}}{r_2^2}\frac{\partial^2}{\partial\theta^2}\nabla_2^4 w_2 - \frac{Eh_2}{r_2^2}\frac{\partial^4 w_2}{\partial x^4},$$

$$\cdots$$

$$D_N\nabla_N^8 w_N = -\frac{r_{N-1}}{r_N}\nabla_N^4 p_{(N-1)N} + F_x^{(N)}\frac{\partial^2}{\partial x^2}\nabla_N^4 w_N + \frac{F_\theta^{(N)}}{r_N^2}\frac{\partial^2}{\partial\theta^2}\nabla_N^4 w_N - \frac{Eh_N}{r_N^2}\frac{\partial^4 w_N}{\partial x^4}.$$

$$(2.2)$$

Where w_k ($k = 1,2,\cdots N$) is the (inward) deflection of the k-th tube, D_k and h_k are the bending stiffness and thickness of the k-th tube, the subscripts $1, 2,\cdots N$ denote the quantities of the innermost tube, its adjacent tube, ... and the outermost tube, respectively, r_k is the radius of the k-th tube, $F_x^{(k)}$ and $F_\theta^{(k)}$ ($k = 1,2,\cdots N$) are the uniform axial and circumferential membrane forces of the k-th tube prior to buckling, and

$$\nabla_k^2 = \frac{\partial^2}{\partial x^2} + \frac{1}{r_k^2}\frac{\partial^2}{\partial\theta^2}, (k = 1,2,\cdots N)$$

$$(2.3)$$

In addition, $p_{k(k+1)}$ is the (inward) pressure on tube k due to tube $k+1$, $p_{(k+1)k}$ is the (inward) pressure on tube ($k+1$) due to tube k. Since the action and reaction are equal but opposite, they are related by

$$r_k p_{k(k+1)} = -r_{k+1} p_{(k+1)k}, \quad (k = 1,2,\cdots N)$$ (2.4)

Here, the pressure $p_{k(k+1)}$ in Eqs.(2.2) is the (inward) pressure exerted on the tube k by the tube $(k+1)$ due to buckling, thus $p_{01} = 0$ and $p_{N(N+1)} = 0$. In addition, it should be mentioned that the net (inward) pressure for each layer is obtained simply as the sum of the outer (inward) pressure and the inner (inward) pressure. This will not cause any significant error when the radius of each layer is much bigger than its thickness.

Since all nested tubes are originally concentric and the initial interlayer spacing is equal or very close to the equilibrium spacing, the initial vdW interaction pressure between any two adjacent tubes of undeformed MWNTs is negligible. When the axial stress and radial pressure are applied, the interlayer spacing changes, and the vdW interaction pressure (per unit area) at any point between any two adjacent tubes depends linearly on the difference of the radial deflections at that point. Thus, the pressure $p_{k(k+1)}$ due to buckling (see Eqs. (2.2)) is related to the deflections of tube k and tube $(k+1)$ due to buckling by

$$p_{12} = c[w_2 - w_1], \, p_{23} = c[w_3 - w_2], \, \dots \, p_{(N-1)N} = c[w_N - w_{N-1}],$$ (2.5)

Here, the vdW interaction coefficient c can be estimated as the second derivative of the energy–interlayer spacing relation of MWNTs using recent data given by Saito et al. [146]

$$c = \frac{320 \times erg / cm^2}{0.16d^2} = 99.18 GPa / nm \quad (d = 1.42 \times 10^{-8} cm)$$ (2.6)

This value, which is slightly bigger than those suggested in [129], is used in [130-136]. Here, because the present analysis is limited to infinitesimal buckling, the coefficient c is calculated at the initial interlayer spacing (about 0.34nm). The curvature-dependency of

the coefficient c is neglected here because it is small for relatively larger innermost radii as compared to 0.6 nm [86, 147].

Substitution of (2.5) into (2.2) leads to N coupled linear equations for N deflections w_k ($k = 1,2,\cdots N$). The condition for existence of a non-zero solution will determine the critical values for elastic buckling of MWNTs under combined axial stress and radial pressure. To this end, one has to first determine all membrane forces $F_x^{(k)}$ and $F_\theta^{(k)}$ ($k = 1,2,\cdots N$) prior to buckling for given external load.

2.2.2 Pre-buckling Analysis

Constraints for the ends of cylindrical shell are usually ignored in pre-buckling analysis [148-149]. As a result, under uniform axial stress and radial external or internal pressure, the axial and circumferential membrane forces $F_x^{(k)}$ and $F_\theta^{(k)}$ ($k = 1,2,\cdots N$) prior to buckling are some constants. The equilibrium conditions prior to buckling give

$$\sigma_\theta^{(k)} = \frac{F_\theta^{(k)}}{h_k} = -\frac{p_k^0 r_k}{h_k} \;, \quad \sigma_x^{(k)} = \frac{F_x^{(k)}}{h_k} = \sigma_{axial}, (k = 1,2,\cdots N) \tag{2.7}$$

where $\sigma_\theta^{(k)}$ and $\sigma_x^{(k)}$ are the pre-buckling axial and circumferential membrane stresses in the k-th tube, p_k^0 is the pre-buckling net (inward) pressure to the k-th tube, and σ_{axial} is the axial stress applied to the MWNT. Note that (Hook's relation)

$$\varepsilon_\theta^{(k)} = \frac{\Delta r_k}{r_k} = \frac{1}{E}(\sigma_\theta^{(k)} - v\sigma_x^{(k)}), \quad (k = 1,2,\cdots N) \tag{2.8}$$

where Δr_k is the radial (inward) deflection of the k-th tube prior to buckling, or the difference between the initial radius r_k and the deformed radius of the k-th tube prior to buckling, and v is Poisson's ratio. Thus, prior to buckling, we have

$$\frac{\Delta r_k}{r_k} = -\frac{1}{E}(\frac{p_k^0 \cdot r_k}{h_k} + v \cdot \sigma_{axial}), \quad (k = 1,2,\cdots N)$$ (2.9)

For pre-buckling analysis

$$p_1^0 = p_{12}^0 + p_{10}^0 = c(\Delta r_2 - \Delta r_1) - P_{int},$$

$$p_2^0 = p_{23}^0 + p_{21}^0 = p_{23}^0 - \frac{r_1}{r_2} \cdot p_{12}^0 = c \cdot [(\Delta r_3 - \Delta r_2) - \frac{r_1}{r_2}(\Delta r_2 - \Delta r_1)]$$

$$\cdots\cdots$$

$$p_N^0 = p_{N(N+1)}^0 + p_{N(N-1)}^0 = p_{N(N+1)}^0 - \frac{r_{N-1}}{r_N} p_{(N-1)N}^0 = P_{ext} - c\frac{r_{N-1}}{r_N}(\Delta r_N - \Delta r_{N-1})$$ (2.10)

where $p_{k(k+1)}^0$ represents pre-buckling outer pressure on tube k due to tube $k+1$ and $p_{k(k-1)}^0$ denotes the pre-buckling inner pressure on tube k due to tube $k-1$. In particular, $P_{int}(=-p_{10}^0)$ is the applied internal pressure, and P_{ext} $(= p_{N(N+1)}^0)$ is the applied external pressure. Substituting (2.10) to (2.9) gives N conditions, which allow us to determine Δr_k $(k=1, 2,\ldots, N)$

$$(\frac{1}{r_1^2} + \frac{c}{Eh}) \cdot \Delta r_1 - \frac{c}{Eh} \cdot \Delta r_2 = -\frac{P_{int}}{Eh} + \frac{v}{Er_1} \cdot \sigma_{axial}$$

$$-\frac{c}{Eh} \cdot \frac{r_1}{r_2} \cdot \Delta r_1 + [\frac{1}{r_2^2} + (1 + \frac{r_1}{r_2}) \cdot \frac{c}{Eh}] \cdot \Delta r_2 - \frac{c}{Eh} \cdot \Delta r_3 = \frac{v}{Er_2} \cdot \sigma_{axial}$$

$$\cdots\cdots$$

$$-\frac{c}{Eh} \cdot \frac{r_{N-1}}{r_N} \cdot \Delta r_{N-1} + (\frac{1}{r_N^2} + \frac{r_{N-1}}{r_N} \cdot \frac{c}{Eh}) \cdot \Delta r_N = \frac{P_{ext}}{Eh} + \frac{v}{Er_N} \cdot \sigma_{axial}$$ (2.11)

Once the constants Δr_k $(k = 1,2,\cdots,N)$ are known, the net pressure (p_k^0) and outer pressure $(p_{k(k+1)}^0)$ distribution can be determined by Eqs. (2.10). Substituting obtained p_k^0

into Eq. (2.7), one can calculate the circumferential membrane force $F_\theta^{(k)}$. In addition, the axial membrane force $F_x^{(k)}$ in Eqs. (2.7) can be calculated directly as $\sigma_{axial} \cdot h_k$.

2.2.3 Buckling Analysis

With the known net pressure distribution or pre-buckling membrane forces, it is now possible to study elastic buckling of MWNTs under combined axial stress and radial pressures. Here, the simply supported boundary condition will be considered for the two ends of all the constituent tubes of MWNTs. which is given by $w_k = 0, v_k = 0$, $F_x = 0$ and $M_x = 0$ ($k = 1, 2, ..., N$) at two ends of each constituent tube. Here, F_X and M_X represent membrane force and bending moment (defined per unit length of circumference) in axial direction. Thus, the buckling mode that satisfies the above-mentioned boundary condition is as follows

$$w_k = W_k \sin\frac{m\pi}{L}x\cos n\theta, \quad (m \geq 1) \tag{2.12}$$

where W_k ($k = 1,2,\cdots\cdots,N$) are some real coefficients; L is the length of the MWNT; m is the axial half wave number, and n is the circumferential wave number. Introducing (2.12), together with the known net pressure distribution (see Section 2.2.2), into Eqs. (2.2) gives

$$\left\{-\frac{r_1}{r_2}\left[\left(\frac{m\pi}{L}\right)^2+\left(\frac{n}{r_2}\right)^2\right]^2\right\}\cdot W_1 +$$

$$\left\{\begin{array}{l}\dfrac{D}{c}\left[\left(\dfrac{m\pi}{L}\right)^2+\left(\dfrac{n}{r_2}\right)^2\right]^4+\left[1+\left(\dfrac{m\pi}{L}\right)^2 h\cdot\left(\dfrac{\sigma_{axial}}{c}\right)-\psi_2\cdot\dfrac{n^2}{r_2}\cdot\left(\dfrac{P}{c}\right)+\dfrac{r_1}{r_2}\right]\cdot\left[\left(\dfrac{m\pi}{L}\right)^2+\left(\dfrac{n}{r_2}\right)^2\right]^2 \\ +\dfrac{Eh}{cr_2^2}\left(\dfrac{m\pi}{L}\right)^4 \end{array}\right\}\cdot W_2$$

$$+\left\{-\left[\left(\frac{m\pi}{L}\right)^2+\left(\frac{n}{r_2}\right)^2\right]^2\right\}\cdot W_3 = 0$$

$$\left\{\frac{D}{c}\left[\left(\frac{m\pi}{L}\right)^2+\left(\frac{n}{r_1}\right)^2\right]^4+\left[1+\left(\frac{m\pi}{L}\right)^2 h\cdot\left(\frac{\sigma_{axial}}{c}\right)-\psi_1\cdot\frac{n^2}{r_1}\cdot\left(\frac{P}{c}\right)\right]\cdot\left[\left(\frac{m\pi}{L}\right)^2+\left(\frac{n}{r_1}\right)^2\right]^2\right.$$
$$\left.+\frac{Eh}{cr_1^2}\left(\frac{m\pi}{L}\right)^4\right\}\cdot W_1+$$

$$\left\{-\left[\left(\frac{m\pi}{L}\right)^2+\left(\frac{n}{r_1}\right)^2\right]^2\right\}\cdot W_2=0$$

$$\cdots\cdots$$

$$\left\{-\frac{r_{N-1}}{r_N}\left[\left(\frac{m\pi}{L}\right)^2+\left(\frac{n}{r_N}\right)^2\right]^2\right\}\cdot W_{N-1}+$$

$$\left\{\frac{D}{c}\left[\left(\frac{m\pi}{L}\right)^2+\left(\frac{n}{r_N}\right)^2\right]^4+\left[\left(\frac{m\pi}{L}\right)^2 h\cdot\left(\frac{\sigma_{axial}}{c}\right)-\psi_N\cdot\frac{n^2}{r_N}\cdot\left(\frac{P}{c}\right)\right.\right.$$
$$\left.\left.+\frac{r_{N-1}}{r_N}\right]\cdot\left[\left(\frac{m\pi}{L}\right)^2+\left(\frac{n}{r_N}\right)^2\right]^2\right.$$
$$\left.+\frac{Eh}{cr_N^2}\left(\frac{m\pi}{L}\right)^4\right\}\cdot W_N=0$$

(2.13)

where P represents radial external pressure (or internal pressure when external pressure is zero). ψ_k $(k=1,2,\cdots,N)$ denotes net pressure p_k^0 normalized by the external (or internal pressure). As will be shown in Chapters 3 and 4, for a specific MWNT, ψ_k $(k=1,2,\cdots,N)$ are some constants determined in pre-buckling analysis. In particular, for MWNTs under pure axial stress, $P=0$ and $\psi_k=0$ $(k=1,2,\cdots,N)$. Eqs. (2.13) can be written into

$$M(m,n,P,\sigma_{axial})_{N\times N}\begin{bmatrix}W_1\\W_2\\\cdots\cdots\\W_N\end{bmatrix}=0$$

(2.14)

Thus, the existence condition of a nonzero solution of $W_k (k = 1,2,....N)$ is:

$$\det M = 0 \qquad (2.15)$$

This condition determines a relationship between the applied external load and associated buckling mode (m,n). Thus, with each pair (m, n), one can identify the corresponding (i) external pressure P for a MWNT under radial pressure, (ii) axial stress σ_{axial} for a MWNT under pure axial stress, or (iii) axial stress σ_{axial} and corresponding external (or internal) pressure P when combined axial stress and external (or internal) pressure are applied with given external (or internal) pressure-to-axial stress ratio. In particular, the critical buckling pressure of a MWNT under pure radial pressure is defined by the lowest external pressure P with $n \geq 2$ [148-149].

Throughout the buckling analysis of MWNTs (see Chapters 3 and 4), we shall assume that $L = 12r_N$ (the outermost radius of an N-wall CNT), and for each constituent SWNT Poisson-ratio $v = 0.3$ [48], bending stiffness $D = 0.85eV$ and in-plane stiffness $Eh = 360J/m^2$ [32]. In addition, according to the radius-to-thickness ratios of MWNTs, all examples of MWNTs will be classified into the following three typical cases:

a) thin MWNTs (the innermost radius-to-thickness ratio is around or larger than four);

b) thick MWNTs (the innermost radius-to-thickness ratio is around unity);

c) (almost) solid MWNTs (the innermost radius-to-thickness ratio is around or smaller than 1/4).
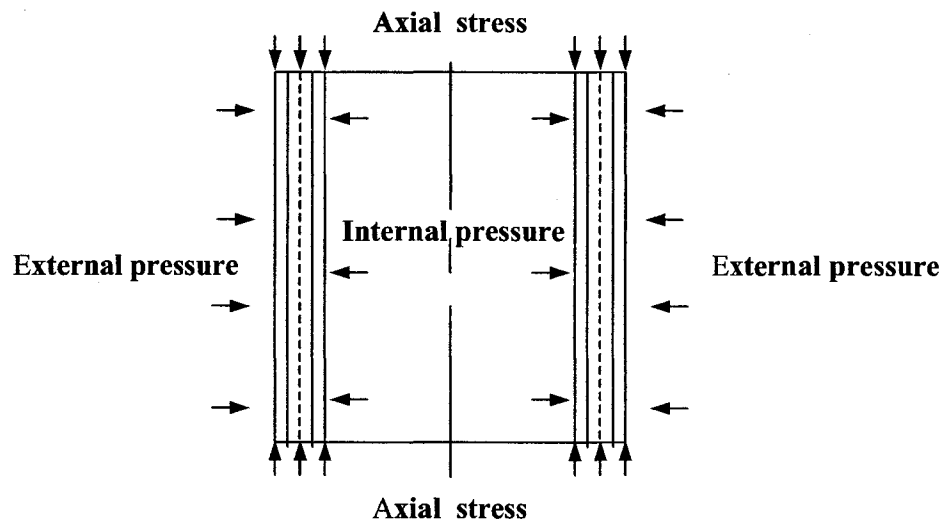
Axial stress

Fig.2.1 Elastic buckling of a MWNT under axial stress and radial pressures.

Chapter 3

Elastic Buckling of MWNTs under Radial Pressure

3.1 Introduction

SWNTs under external high pressure have been the subject of numerous researches [77-85, 123, 150-152]. An interesting phenomenon is pressure-dependent abnormalities observed for vibration modes and electric resistivity of SWNT ropes when the applied external pressure reaches a critical value ranging from 1.5 to 1.9 GPa [77, 83-84]. To explain these phenomena in terms of pressure-induced elastic buckling of SWNT ropes, an elastic honeycomb model has been developed by Ru [123] which leads to a simple critical pressure formula in good agreement with known experimental data for SWNTs of diameters around 1.4 nm. Remarkably, this model can also explain pressure-induced abnormalities of optical properties of SWNT ropes observed for very small diameters around 0.8 nm [145]. These results make us believe that elastic shell models can be used to predict the main features of mechanical behavior of CNTs under high pressure.

More recently, MWNTs under high pressure have been studied [75-76, 78, 80-82]. In addition, considerable effort has been devoted to MWNTs embedded in a polymer or metal matrix [50-51, 153-154], where hydrostatic compressive stress due to thermal mismatch and specimen cooling is identified as a major factor affecting physical properties of embedded MWNTs. Therefore, buckling behavior of MWNTs under external radial pressure are of practical interest. To study MWNTs with elastic shell models, it is crucial to notice that MWNTs are distinguished from conventional singlelayer elastic shells due to their multilayer structure and the interlayer vdW forces. On one hand, interlayer friction of undeformed MWNTs is usually so low that adjacent layers can slide to each other almost freely [15-18]. On the other hand, some studies have revealed that interlayer friction in MWNTs largely depends on interlayer commensurability and could lead to significant interlayer locking for commensurate

47

adjacent layers [15, 155-158]. In addition, pressure-induced interlayer friction and interlocking have been suggested [105] to explain the observed wavelength of bending buckling of relatively thin MWNTs [48]. Furthermore, we believe that pressure-induced partial interlayer locking (only for the outermost few layers) could be responsible for unexplained wavelengths of thick MWNTs [51]. Hence, it is of greater interest to study the possibility of interlayer locking for MWNTs under high pressure.

Using the governing equations (2.1) this chapter gives a theoretical analysis of elastic buckling of individual MWNTs under high pressure. The critical buckling pressure and associated buckling modes have been first calculated for thin, thick and (almost) solid MWNTs under pure external pressure. Then the effect of internal pressure on the critical external pressure for MWNTs subject to both internal and external pressure has been examined. In particular, the critical pressure predicted by the present shell model is found to be in good agreement with known experimental result [75], which to our best knowledge is probably the only experimental result available in the literature for critical pressure of MWNTs. In addition, the present model shows that critical pressure will increase drastically if an interlayer locking occurs even only in few layers. Therefore, the agreement between theoretical predictions (without any interlayer locking) and experimental data suggests that elastic buckling will take place prior to any significant interlayer locking in MWNTs under increasing external pressure.

3.2 Elastic Buckling of MWNTs under an External Pressure

Now, let us first examine elastic buckling of MWNTs under an external pressure, as shown in Fig. 3.1(a). To this end, seven examples shown in Table 3.1 will be considered. Obviously, examples 1, 2 and 3 are thin MWNTs, examples 4, 5 and 6 are thick MWNTs, and example 7 is a(n) (almost) solid MWNT.

3.2.1 Pre-buckling Pressure Distribution

By using Eqs. (2.10) and (2.11) with zero σ_{axial} and P_{int}, the pre-buckling outer pressure $p^0_{k(k+1)}$ ($k = 1,2,\cdots,N$) and the net pressure p^0_k (normalized by external pressure $P_{ext} = P$) for five examples (examples 1, 2, 4, 5, and 7) are calculated and shown in Figs. 3.2 and 3.3, respectively. Here, the external pressure P is the only applied pressure, and all pressures are normalized by the applied external pressure P. It is seen that both the net pressure p^0_k and the outer pressure $p^0_{k(k+1)}$ decrease monotonically from the outermost tube to the innermost tube, and are very low for the innermost few tubes of a thick or solid MWNT. In particular, for thin MWNTs (examples 1 and 2), the outer pressure is almost linearly distributed, and the net pressure is nearly constant. This means that all concentric tubes of a thin MWNT almost equally share the applied external pressure. In this case, as will be shown below, the critical pressure for a thin N−wall CNT is approximately N times the critical pressure of a SWNT of the average radius of the MWNT.

3.2.2 Critical Buckling Pressure

With known net pressure distribution, we are now able to study elastic buckling for simply supported MWNTs under external pressure alone. By following the approach demonstrated in Section 2.2.3 with $\sigma_{axial} = 0$ and $\psi_k = \dfrac{p^0_k}{P}$ ($k = 1,2,\cdots,N$) in (2.13) the critical buckling pressure and associated buckling modes are calculated for examples 1-7. Since the results for examples 1 and 4 are found to be very similar to those for examples 2 and 5, we shall only focus on five examples (examples 2, 3, 5, 6 and 7). The dependency on the pair (m,n) of the external pressure P is plotted in Figs. 3.4 to 3.8 for the five examples, respectively. In addition, it is easy to understand that the results for free ends are equivalent to the results for simply supported end with $m = 0$ and the corresponding solution takes the form $w_k = A_k \cos n\theta$ ($k = 1,2,\cdots\cdots,N$).

It is seen from Figs.3.4 to 3.7 that the pressure P is an increasing function of n for thin or thick MWNTs with free end ($m = 0$), thus the critical pressure is determined by

$n = 2$. However, for solid MWNT (example 7) shown in Fig. 3.8, P is found to be a non-monotonic function of n for $m = 0$ and has an internal minimum at around $n = 5$ or 6. On the other hand, P is an increasing function of m for simply supported end ($m \geq 1$), thus the critical pressure is determined by $m = 1$. The circumferential wave number n corresponding to the lowest pressure varies between 2 and 4 for these examples. The critical pressure for the five 8-wall CNTs (see Table. 3.1) are summarized in Table 3.2, and are compared to the critical pressure of a SWNT whose radius is equal to the average radius, the innermost radius, or the outermost radius of the MWNTs. In particular, for thin MWNTs (examples 2 and 3), it is seen from Table 3.2 that the critical pressure of a thin N − wall CNT is approximately N times that of a SWNT of the average radius of the N − wall CNT.

A similar conclusion has been drawn for axially compressed buckling of thin MWNTs [129]. Based on these results, it is expected that a thin N − wall MWNT can be approximately treated as a singlelayer elastic shell with the equivalent bending stiffness ND and the thickness Nh. This issue will be further examined in detail in Chapter 9.

3.3 Elastic Buckling of MWNTs under Internal and External Pressures

In this Section, we shall further consider elastic buckling of MWNTs under both internal and external pressures, as shown in Fig.3.1(b). The emphasis will be placed on the effect of an internal pressure on critical external pressure and associated buckling modes of MWNTs. Here, two MWNTs in Table 3.1 are used as representative examples, i.e., a thick 8-wall CNT (example 5) and a(n) (almost) solid 8-wall CNT (example 7). This is because the effect of internal pressure is very similar for both thin and thick MWNTs with the innermost radius-to-thickness ratio larger than unity but significantly different for (almost) solid MWNTs with the innermost radius-to-thickness smaller than ¼.

3.3.1 Pre-buckling Pressure Distribution

Based on Eqs. (2.10) and (2.11) with zero σ_{axial}, the pre-buckling pressure distributions for p_k^0 and $p_{k(k+1)}^0$ (normalized by external pressure P) are calculated for examples 5 and 7 in Figs. 3.9 and 3.10, respectively, with various internal-to-external pressure ratios α $(=P_{int}/P_{ext})$. Here, to cover different cases of physical interest, we assume that the internal pressure may be different from the external pressure. Of course, $\alpha = 1$ when the internal pressure is kept exactly the same as the external pressure.

As seen in Figs. 3.9 and 3.10, with increasing internal pressure, the (inward) outer pressure on each tube of MWNTs increases while the (inward) net pressure, which is crucial for the critical external pressure of MWNTs, decreases. These results indicate that an internal pressure leads to stronger interlayer vdW interaction between adjacent tubes, while it reduces the (inward) net pressure or the external pressure-induced compression on each concentric tube of MWNTs. In particular, a high internal pressure can even cause an outward (negative) net pressure and an increase in the radius of almost all tubes of a thick MWNT (Fig.3.9) and of the innermost few tubes of a solid MWNT (Fig.3.10). Moreover, it is seen that for a thick MWNT (Fig.3.9), the effect of an internal pressure on pressure distribution is significant from the innermost tube to the outermost few tubes, while for a(n) (almost) solid MWNT (Fig.3.10), the internal pressure only affects pressure distribution on the innermost few tubes.

3.3.2 The Internal Pressure Effect on Critical External Pressure

Next, let us examine the effect of an internal pressure on buckling behaviors of MWNTs. Here, we first consider MWNTs of free ends ($m = 0$) as an illustration. Solving (2.15) with known pre-buckling net pressure distribution and $m = 0$, external pressure P and the associated circumferential wave number n are obtained in Fig. 3.11 and 3.12 for examples 5 and 7, respectively, with α $(=P_{int}/P_{ext})$ increasing from 0 to 2 for example 5 and from 0 to 5 for example 7.

An interesting phenomenon observed in Figs.3.11 and 3.12 is that when α is relatively small, an increasing internal pressure leads to an increase in the critical external pressure while the buckling mode remains unchanged with the circumferential wave

number $n = 2$. However, when the pressure ratio α reaches a certain critical value, for instance, $\alpha = 1.3$ in Fig.3.11 for the thick 8-wall CNT, example 5, and $\alpha = 0.2$ in Fig.3.12 for a solid 8-wall CNT, example 7, an abrupt change of buckling mode occurs, where the circumferential wave number n jumps from 2 to 9 and 6 for example 5 and 7, respectively. Furthermore, it is noticed in Fig.3.11 that when α increases from 0 to 2, the critical external pressure of the thick MWNT increases by more than an order of magnitude. In contrast, for the (almost) solid MWNT (see Fig.3.12), when α increases from 0 to 0.2 the critical external pressure increases slightly. Beyond $\alpha = 0.2$, no significant increase in the critical external pressure can be achieved by raising the internal pressure with α up to 5 or even larger. For thin MWNTs, our results indicate that the effect of an internal pressure on buckling behaviors is very similar to that for thick MWNTs. The different effect of an internal pressure on the critical external pressure of thick (or thin) and (almost) solid MWNTs can be explained by the fact that an internal pressure can effectively reduce the (inward) net pressure on each concentric tube of a thick (or thin) MWNT with the innermost radius-to-thickness ratio larger than unity, while its effect on a(n) (almost) solid MWNT with the innermost radius-to-thickness much less than unity, is limited only to the innermost few tubes. Analogous effect of an internal pressure on buckling behavior can also be obtained for simply supported MWNTs.

3.4 Comparison with an Experiment

The above buckling analyses of MWNTs are based on the multiple-elastic shell model [127-129]. Thus, it is of great interest to compare the present shell model to available experiments or atomistic simulations. In Table 3.1, the data for example 8 are taken from [75], which to our best knowledge, is probably the only experiment reported in the literature for the critical radial pressure of MWNTs. We have been informed that helium was used in [75] as a medium to apply an external pressure on MWNTs, and there were some helium molecules in the interior of MWNTs tested in [75]. Thus, as suggested by Thomsen & Reich [81], it is assumed that an internal pressure, not higher than the

external pressure, exists in the interior of the MWNTs tested in [75]. Hence, To make a comparison between the present model and the experiment [75], we study the elastic buckling for example 8, a(n) (almost) solid 20-wall CNT under both internal and external pressures.

The net pressure p_k^0 and the outer pressure $p_{k(k+1)}^0$ (normalized by external pressure P) for example 8 are shown in Fig.3.13 with the internal pressure-to-external pressure ratio $\alpha = 0$, 0.6 and 1, respectively. Then, an approximate method (see details in Section 9.1.2) is employed to simplify the calculation in the buckling analysis of the 20-wall CNT. With this approximate method, example 8, consisting of twenty concentric SWNTs, can be effectively reduced to a nine-layer shell coupled with each other through the vdW interaction, the data for each layer of which are shown in Table 3.3. It is seen from Table 3.3 that the radius-to-thickness ratios for all new layers are larger than 4.5. As will be shown in Section 9.1.2, each of these new layers can be modeled as a single-layer thin shell whose radius, effective bending stiffness and thickness as well as pre-buckling net pressure can be determined based on the approximate method (see Section 9.1.2). In particular, MWNTs used in high-pressure experiments usually have free ends and are characterized by a very large aspect ratio. Thus, in this section we only consider example 8 with free ends or infinite axial wavelength, which corresponds to $m = 0$. Applying the buckling shell equation (2.1) to each of the new nine layers with possibly different effective bending stiffness and thickness, one can obtain nine coupled equations for nine deflections of these new layers. Following a similar procedure demonstrated in Section 2.2.3, the relation between the external pressure P and n can be obtained with the internal pressure-to-external pressure ratio α as a parameter. The dependency of P on circumferential wave number n is presented in Fig.3.14, for example 8 with $m = 0$ and $\alpha = 0$, 0.3, 0.4, 0.6 and 1, respectively.

As seen from Figs.3.13 and 3.14, pre-buckling (Fig. 3.13) and buckling behaviors (Fig.3.14) of example 8 are qualitatively similar to those of the (almost) solid 8-wall CNT, example 7, shown in Figs. 3.10 and 3.12. When pressure ratio α changes from 0 to 0.3, the lowest pressure P with $n \geq 2$ is obtained with $n = 2$. Thus the critical pressure is determined by $n = 2$. On the other hand, when α is greater than 0.4, the lowest pressure

P with $n \geq 2$ corresponds to $n=11$. Thus, the critical pressure is determined by $n=11$. The critical pressures of example 8 for various pressure ratios α are given in Table 3.4.

From Table 3.4, it is seen that when internal pressure P_{int} increases from 0 to $0.3 P_{ext}$ (external pressure), the critical external pressure of example 8 increases from $0.567 GPa$ to $0.860 GPa$ with $n=2$. Further, when pressure ratio varies from 0.3 to 0.4, the critical external pressure changes slightly from $0.860 GPa$ to 0.944 GPa while the circumferential wave number n jumps form 2 to 11. If we further raise the internal pressure from $0.4 P_{ext}$ to P_{ext}, the critical external pressure remains about 0.944 GPa with $n = 11$. Therefore for example 8, the critical pressure of $0.944 GPa$ is obtained in the wide range of pressure ratio α $(0.4 \leq \alpha \leq 1)$. As explained before, because there were some helium molecules inside the MWNTs tested in [75], it seems reasonable [81] to assume that an internal pressure has existed within the interior of the MWNTs used in [75]. Hence, the critical pressure predicted by the present model for example 8 should be close to 1 GPa, which is in reasonable agreement with the critical pressure about 1.48 GPa, observed for the first structural change of the MWNT [75].

It is noticed that there is about 30% difference between the theoretical prediction and the experimental value. This discrepancy was first explained by the increase of the vdW interaction coefficient c due to pressure-induced reduction of interlayer spacing of a MWNT, which has not been considered in the above analysis. In Fig.3.15, it is shown that if all c's from the innermost few tubes to the outermost few tubes of a MWNT are equally affected by radial internal and external pressure and increases to 2 to $3 c_0$ (c_0 is given by (2.6)), the critical buckling pressure of 1.36-$1.64 GPa$ can be obtained based on the present shell model. However, our results [134] (also see Chapter 6) for pressure dependence of c indicates that, for external pressure up to $1.5 GPa$, only c's between outermost few layers (or the innermost few layers if an internal pressure is introduced) reach the maximum value around $1.5 c_0$, while others c's are smaller or much smaller than $1.5 c_0$. It is seen from Fig.3.15 that, when $c \leq 1.5 c_0$ the critical pressure of example 8 is only about 1 GPa. Thus it is believed that the pressure-induced increase of c cannot significantly increase the critical buckling pressure of MWNTs.

On the other hand, based on recent data in the literatures [36, 38, 147], an updated bending stiffness $D=2eV$ has been suggested for SWNTs in our latest work [136], offering a much better agreement between the multiple-shell model and an atomistic model in vibrational analysis of SWNTs than the value $0.85eV$ used in the present buckling analysis (also see Chapter 8). With this updated value of bending stiffness [136] combined with the pressure effect on the vdW interaction coefficient c [134], the critical buckling pressure predicted for example 8 under both internal and external pressure is $1.32GPa$ [159] very close to the experimental value $1.48GPa$ [75]. This result offers convincing evidence of the relevance of multiple-shell model for buckling analysis of MWNTs.

3.5 The Effect of Interlayer Locking on Elastic Buckling of MWNTs

In the present multiple-shell model [127-129], the interlayer friction of MWNTs is ignored because of the reported low friction between two adjacent layers [15-18]. On the other hand, there is a possibility that under high external pressure the interlayer friction could substantially increase and the adjacent two layers of MWNTs could be partially or even completely interlocked [15, 155-158]. It is known that the interlocked layers behave like a singlelayer shell, and the overall bending stiffness of interlocked layers could increase by a few orders of magnitude [105]. As a result, it is expected that even partial interlayer locking could have a significant effect on critical pressure of MWNTs. In fact, this pressure-induced interlayer locking has already been used [105] to explain observed wavelengths for bending buckling of relatively thin MWNTs [48]. Furthermore, pressure-induced partial interlayer locking (only for the outermost few layers) could probably offer an plausible explanation for the experimental results of Bower et al. [51] about the wavelengths of thick MWNTs embedded within a polymer matrix.

Here, let us briefly examine the possibility of the interlayer locking and its effect on critical pressure of MWNTs under high external pressure. It is seen from Fig.3.12 that, for MWNTs under external pressure, the maximum interlayer vdW interaction pressure

occurs in the outermost few tubes. Hence, it is reasonable to assume that, if interlayer locking occurs, it will most likely occur in the outermost few layers. Here, we calculate the critical pressure for examples 1, 2, 4, 5 and 7, under the assumption that the outermost few layers are interlocked as a singlelayer shell. The predicted critical pressure are shown in Figs.3.16 and 3.17, as a function of the number of interlocked layers, for free end and simply supported end, respectively (where Q is the ratio of critical pressure with interlayer locking to critical pressure without interlayer locking). It is seen that the critical pressure will increases drastically when even only the outermost few layers are intercloked. Since theoretical predictions without any interlayer locking are in good agreement with experimental results [75], it is believed that no significant interlayer locking occurs prior to the onset of elastic buckling.

(a)

(b)
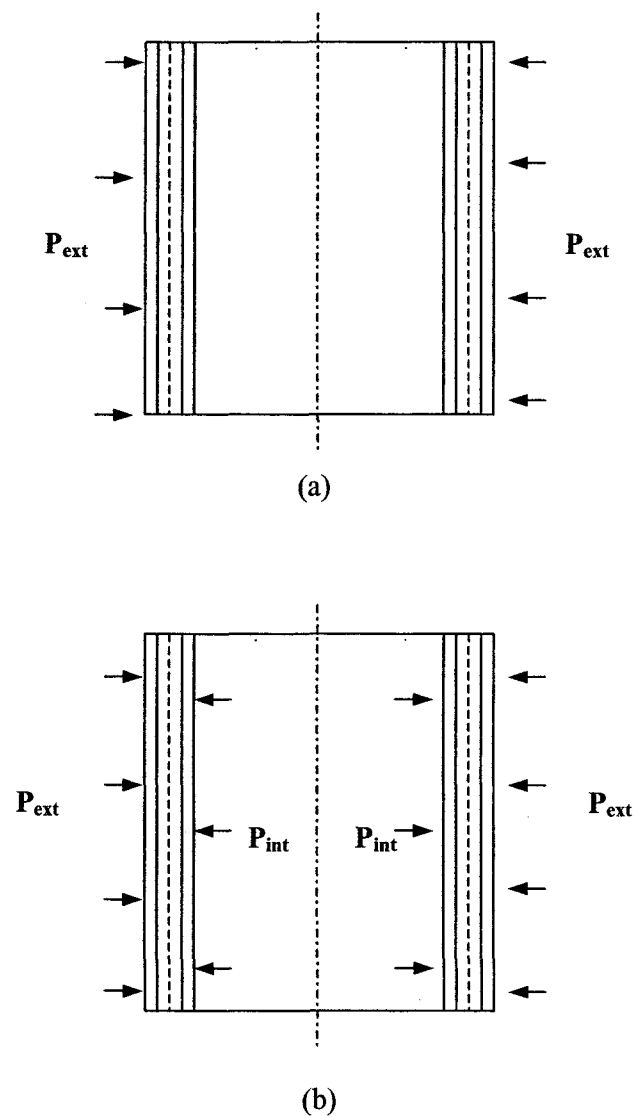
Fig.3.1 Elastic buckling of a MWNT under (a) external pressure and

(b) both external pressure and internal pressure.
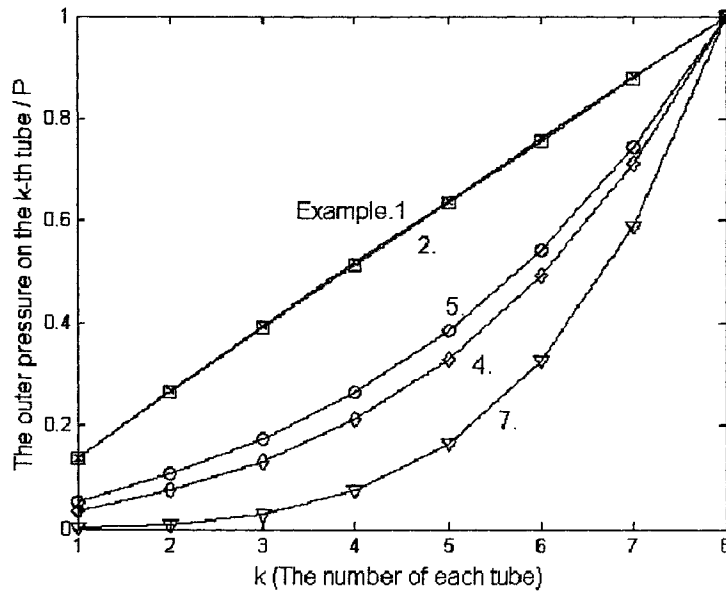
Fig. 3.2. The pre-buckling outer pressure distribution for examples 1, 2, 4, 5 and 7

(in Table 3.1) under an external pressure P.
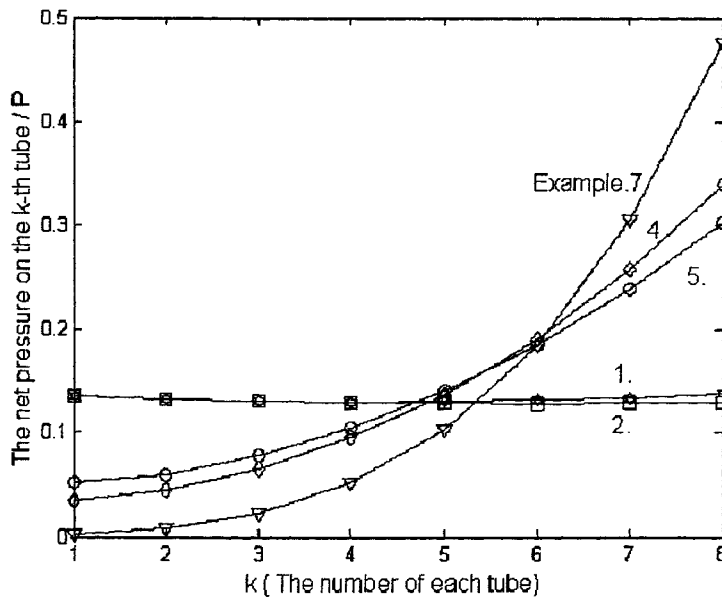
Fig.3.3. The pre-buckling net pressure distribution for examples1, 2, 4, 5 and 7

(in Table 3.1) under an external pressure P.
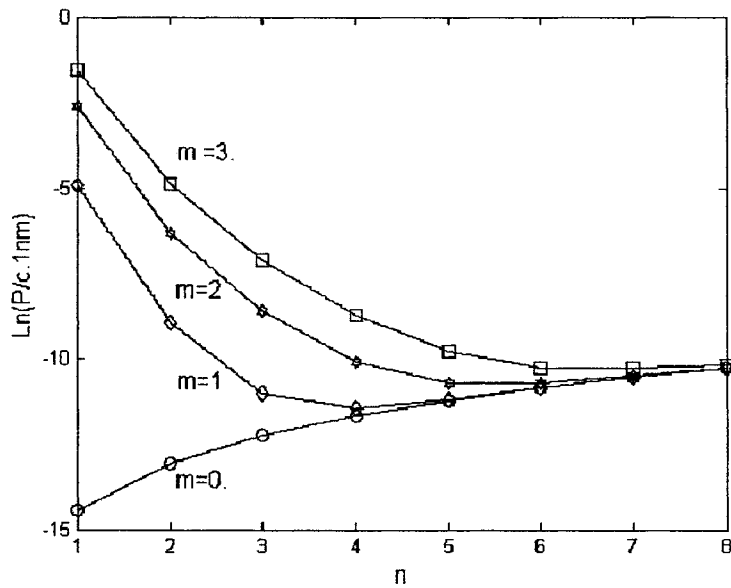
Fig.3.4. The dependency of the external pressure P on (m,n) for example 2

(in Table 3.1) under an external pressure.
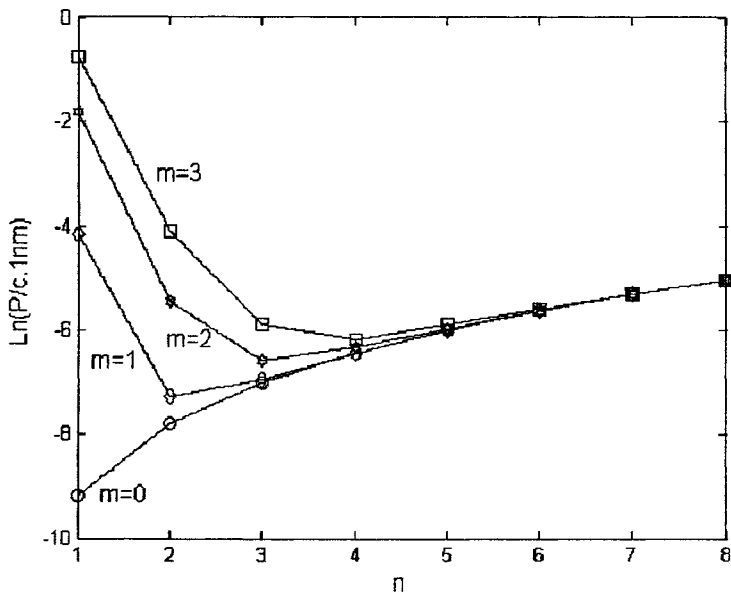
Fig.3.5. The dependency of the external pressure P on (m,n) for example 3

(in Table 3.1) under an external pressure.
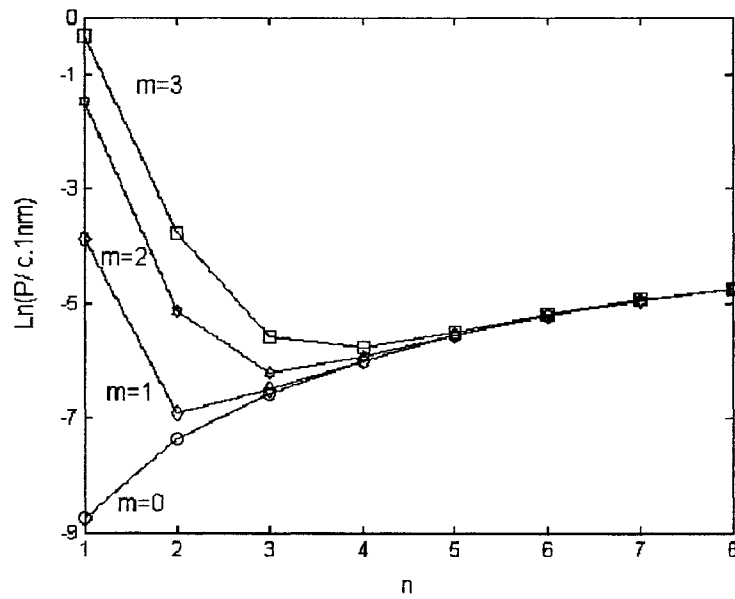
Fig.3.6. The dependency of the external pressure P on (m,n) for example 5

(in Table 3.1) under an external pressure.
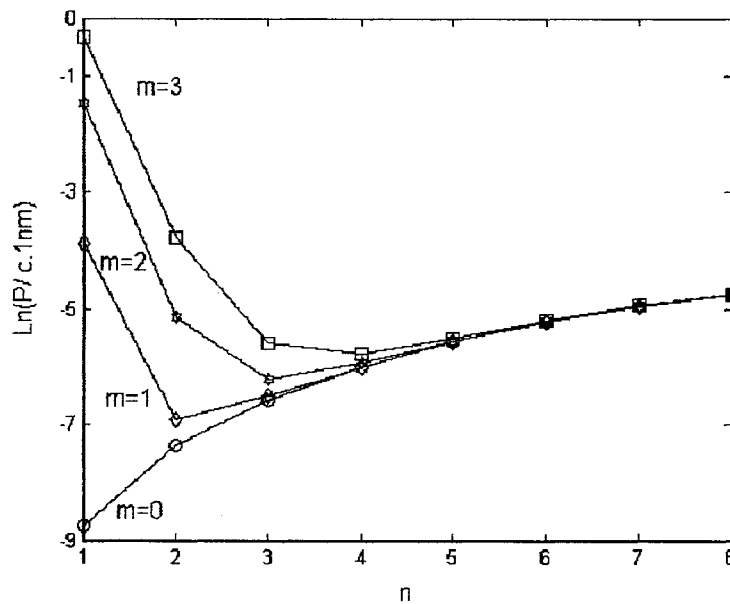
Fig.3.7. The dependency of the external pressure P on (m,n) for example 6

(in Table 3.1) under an external pressure.
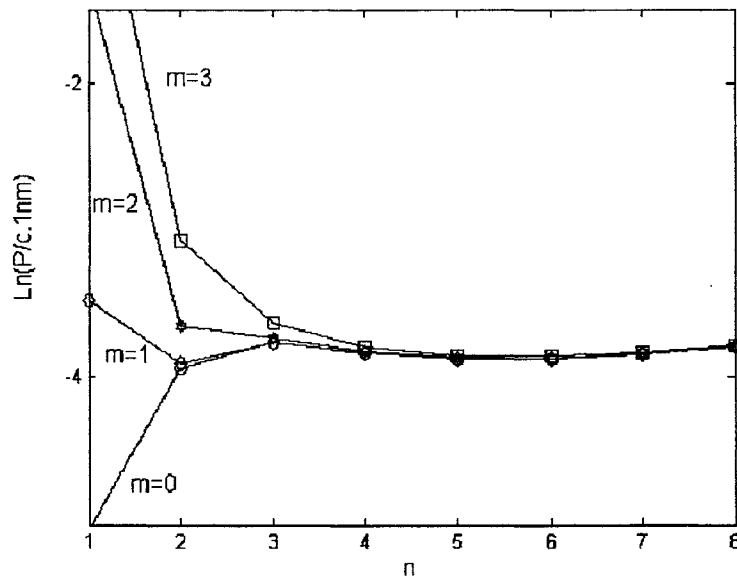
Fig.3.8. The dependency of the external pressure P on (m,n) for example 7

(in Table 3.1) under an external pressure.
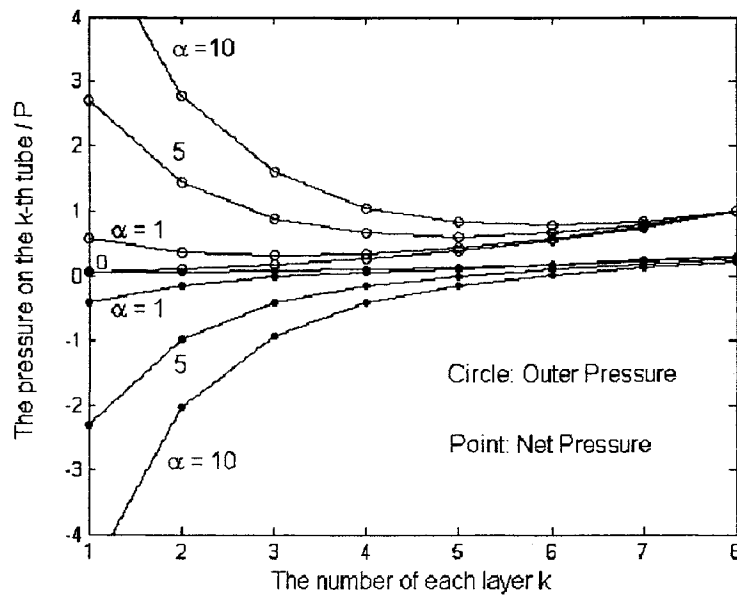
Fig.3.9 Pre-buckling pressure distribution for example 5 (in Table 3.1) under both

internal and external pressure. Here, α is the internal pressure-to-external
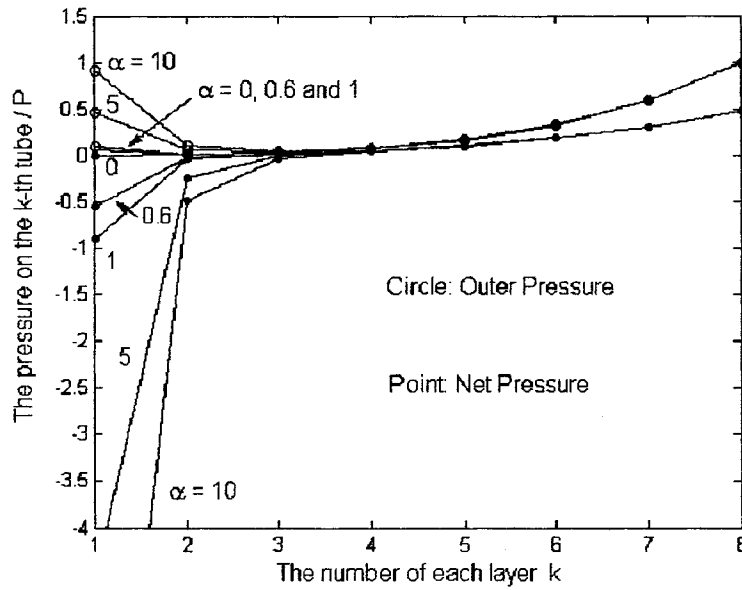
pressure ratio.

Fig.3.10 Pre-buckling pressure distribution for example 7 (in Table 3.1) under both internal and external pressure. Here, α is the internal pressure-to-external pressure ratio.
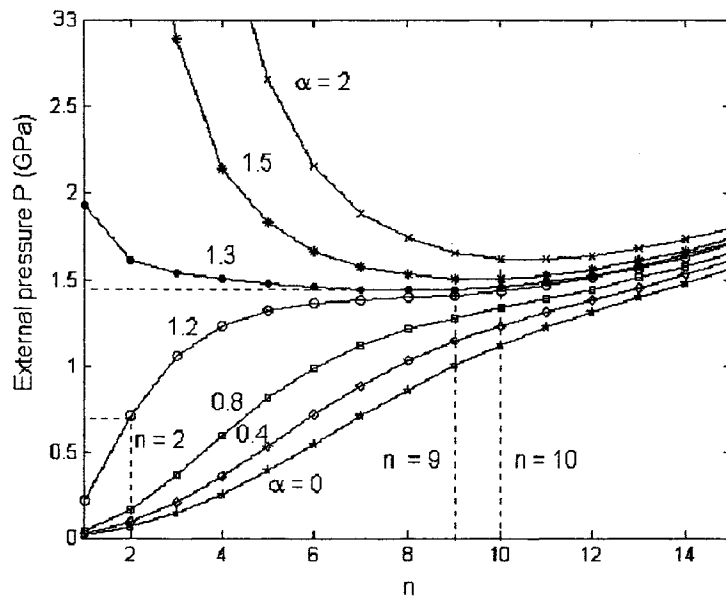
Fig.3.11 The dependency of external pressure P on the internal pressure-to-external pressure ratio α and n for example 5 (in Table 3.1).
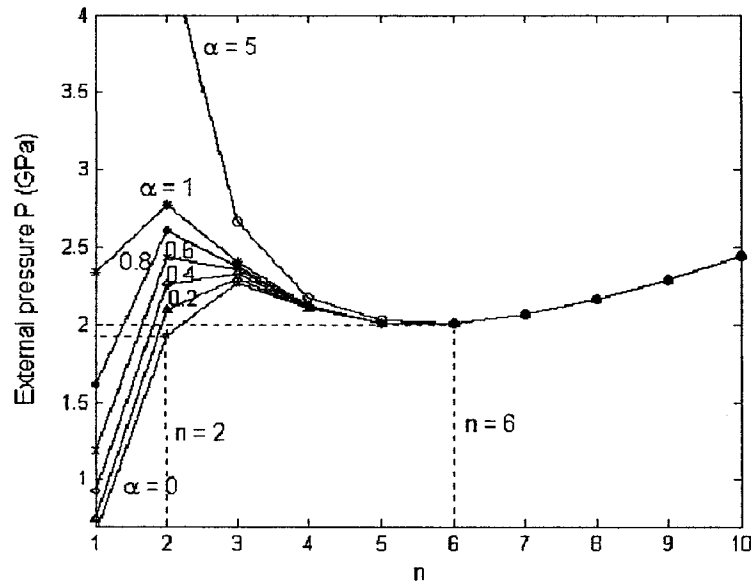
Fig.3.12 The dependency of external pressure P on the internal pressure-to-external pressure ratio α and n for example 7 (in Table 3.1).
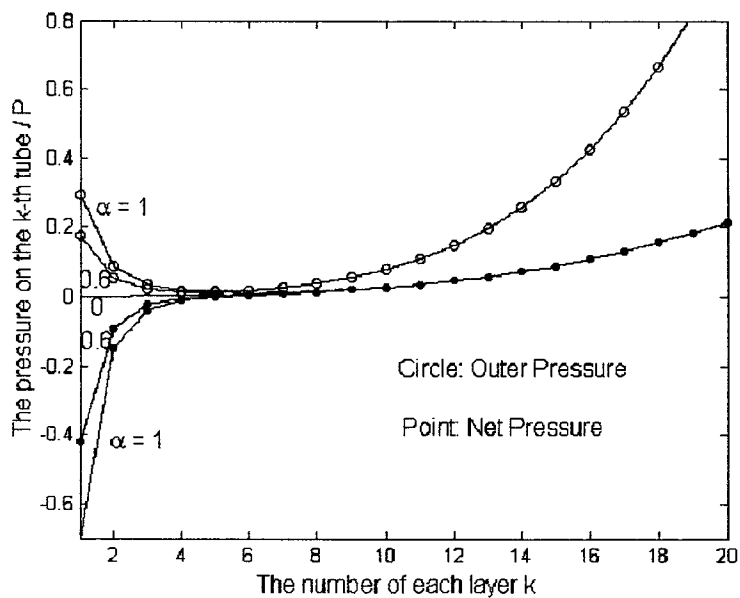
Fig.3.13 Pre-buckling pressure distribution for example 8 (in Table 3.1) under both internal and external pressure. Here, α is the internal pressure-to-external pressure ratio.
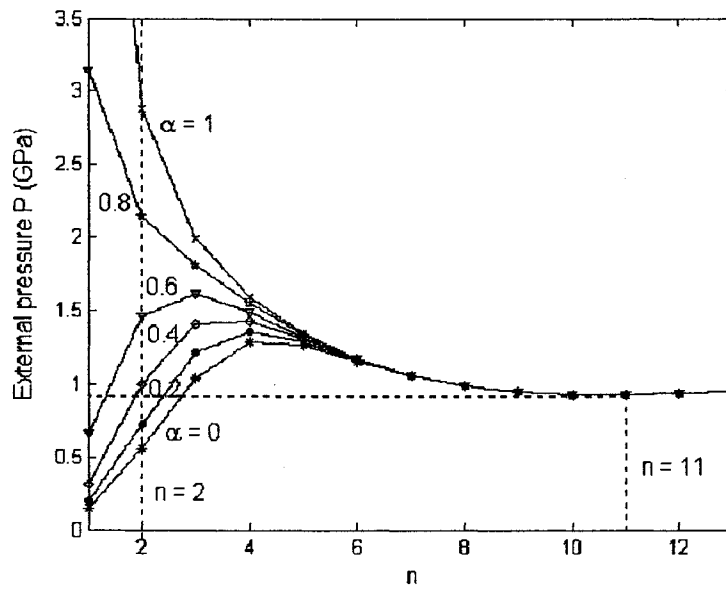
Fig.3.14 The dependency of external pressure P on the internal pressure-to-external pressure ratio α and n for example 8 in Table 3.1.
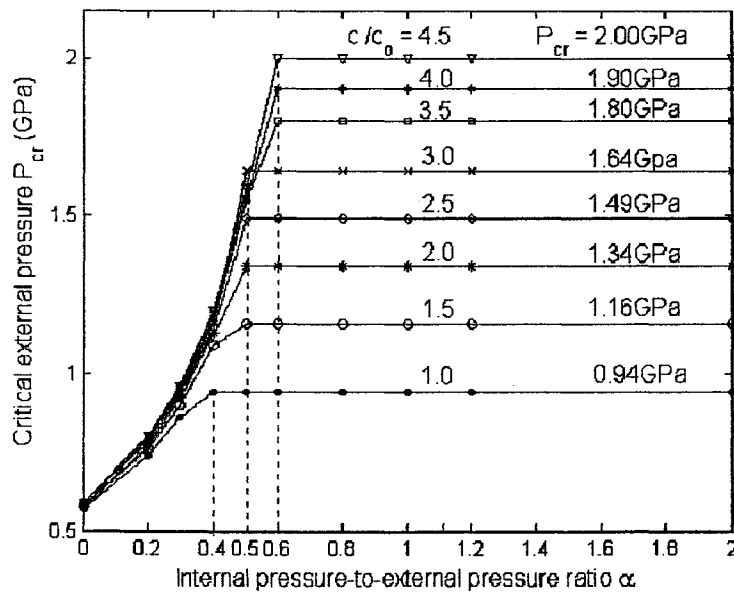
Fig.3.15 The dependency of P_{cr} on α and c/c_0 for example 8 in Table 3.1.
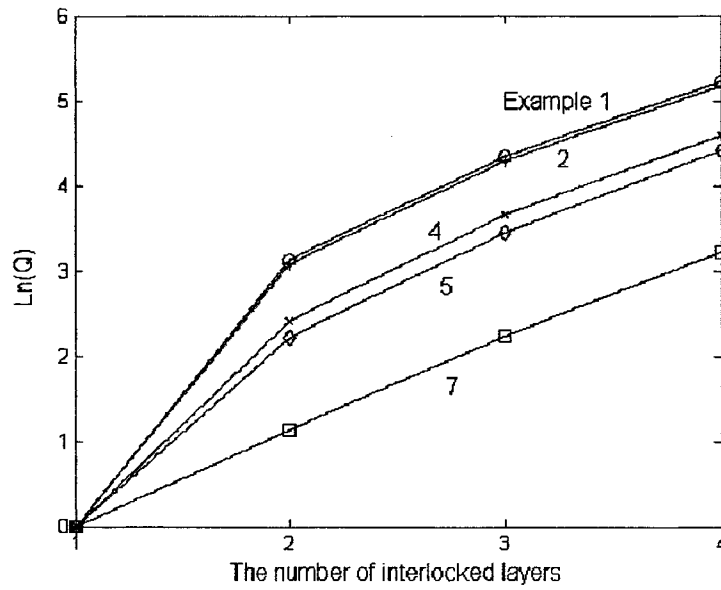
Fig.3.16. The effect on critical pressure of interlayer locking (free end).
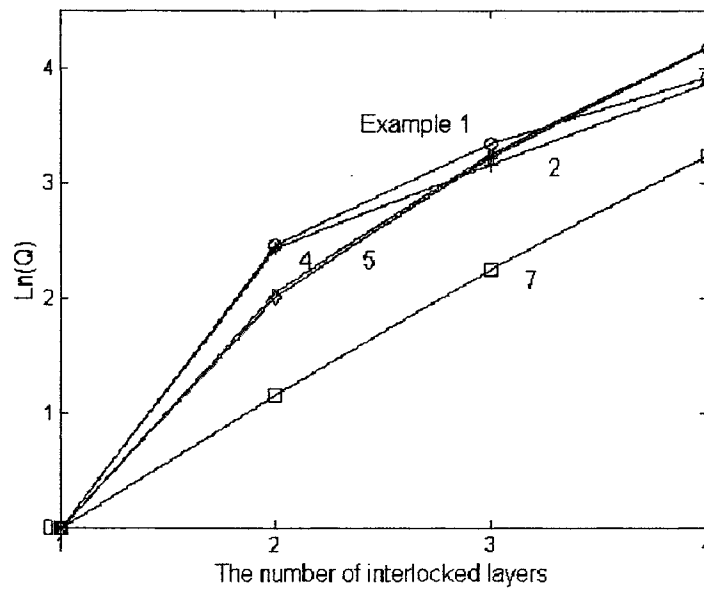
Fig. 3.17. The effect of interlayer locking on critical pressure (simply supported end).

Table 3.1.The geometrical data for eight examples of MWNTs. Here, N is the number of tubes of a MWNT and h is the effective thickness of a SWMT.

Example	Thin MWNTs			Thick MWNTs			Solid MWNTs	
Number	1	2	3	4	5	6	7	8
r_1 (nm)	18	26	2.8	2.3	3.0	0.68	0.65	1.5
r_1 / Nh	6.62	9.56	4.12	0.85	1.10	1.00	0.24	0.22
N	8	8	2	8	8	2	8	20

Table 3.2. Comparison of the critical pressures between MWNTs and SWNTs. Here P_{cr} is critical pressure of a MWNT, P_{cr}^o is the critical pressure of a SWNT of the outermost radius, P_{cr}^i is the critical pressure of a SWNT of the innermost radius, and P_{cr}^a is the critical pressure of a SWNT of the average radius. The unit of P_{cr} is GPa.

Boundary condition \ MWNT		Thin MWNTs		Thick MWNTs		Solid MWNT
		Example 1	Example 2	Example 4	Example 5	Example 7
$m=0$	P_{cr}	5.85×10^{-4}	2.08×10^{-4}	1.21×10^{-1}	6.32×10^{-2}	1.95
$m=1$	P_{cr}	2.05×10^{-3}	9.38×10^{-4}	1.41×10^{-1}	8.17×10^{-2}	1.98
$m=0$	P_{cr}/P_{cr}^o	--	--	22.8	18.1	100
	P_{cr}/P_{cr}^i	--	--	2.7	3.1	0.98
	P_{cr}/P_{cr}^a	7.6	7.7	--	--	--
$m=1$	P_{cr}/P_{cr}^o	--	--	12.2	11.2	52.9
	P_{cr}/P_{cr}^i	--	--	2.3	3.0	0.93
	P_{cr}/P_{cr}^a	7.4	7.5	--	--	--

Table 3.3. Substitution of a nine-layer elastic shell for a MWNT of twenty layers (example 8 in Table 3.1). Here K is the number of concentric tubes in each new layer, and r_{out} and H are the outermost radius and the thickness of each new layer.

Number of new layer	I	II	III	IV	V	VI	VII	VIII	IX
r_{out}	1.5	1.84	2.18	2.52	3.2	3.88	4.90	6.26	7.96
K	1	1	1	1	2	2	3	4	5
H	0.34	0.34	0.34	0.34	0.68	0.68	1.02	1.36	1.70
r_{out}/H					4.71	5.72	4.8	4.60	4.68

Table 3.4 The critical buckling pressure for example 8 with $m = 0$.

α	0	0.2	0.3	0.4	0.6	0.8	1
n	2	2	2	11	11	11	11
$P_{cr}(GPa)$	0.568	0.738	0.860	0.944	0.944	0.944	0.944

Chapter 4

Elastic Buckling of MWNTs under Axial Stress and Radial Pressure

4.1 Introduction

Axially compressed elastic buckling of CNTs has been one of recent topics of considerable interest [25, 32, 39, 48, 52, 120, 127-129]. Especially, detailed comparison has shown [32, 120] that the critical stress and buckling wavelength predicted by isotropic elastic shell model are in good agreement with the results of axially compressed SWNTs obtained by MD simulations. It is believed that isotropic elastic shell model can be used to catch main features of buckling of SWNTs under axial compression. On the other hand, axially compressed buckling of MWNTs of larger radius-to-thickness ratio has been studied based on a multiple-elastic shell model [127-129], although a comparison is still not available due to the lack of relevant experimental results or molecular MD simulations for MWNTs.

Recently, SWNTs [77-79, 83-84] and MWNTs [76-82] under external radial pressure have been the subject of numerous researches. A remarkable phenomenon is the pressure-induced abrupt change of physical properties of SWNTs and MWNTs when the applied pressure reaches a critical value. In an effort to explain these phenomena in terms of pressure-induced elastic buckling, an elastic honeycomb model for SWNT ropes has been developed by Ru [123], which leads to a simple critical pressure formula in excellent agreement with known experimental data [77, 82, 83]. Furthermore, Wang et al [130] have recently studied elastic buckling of individual MWNTs under external radial pressure based on the multiple-elastic shell model [127-129]. Wang et al's results showed that the predicted critical pressure, about 1 GPa, is in reasonably good agreement with the experimental results (about 1.48 GPa, which, to the present author's best knowledge, is probably the only available experimental data for critical radial pressure of MWNTs) of [75] for a

68

specific group of MWNTs of about twenty layers. This agreement offers an evidence for the relevance of the multiple-elastic shell model [127-129] to MWNTs, which suggests that the multiple-elastic shell model can be used to study buckling behavior of MWNTs. Here, it should be mentioned that MWNTs under radial internal pressure has been suggested by Thomsen & Reich [81] as a simplified model for MWNTs filled with some other molecules.

To our knowledge, elastic buckling of CNTs under combined axial and radial loadings remains an open topic in the literature. Recently, axially compressed buckling of SWNTs filled with other molecules has been studied by Ni et al. [87]. These authors found that the critical axial strain increases by 10-20% for different filling molecules at low density, and up to 45% for filling molecules at high density. As shown in chapter 3, following Thomsen & Reich [81] the role of filling molecules can be modeled approximately as an internal pressure. Although the value of this equivalent internal pressure depends on the filling molecules and the density, and thus cannot be determined exactly, its magnitude can be assumed to be the order of magnitude of the critical radial external pressure [81] (the latter is about 5% of the critical axial stress for SWNTs [120]). Therefore, filled SWNTs can be approximately modeled as SWNTs subjected to an internal radial pressure not much higher than 5% of the critical axial stress. Motivated by all of the above ideas, this chapter is devoted to a systematic study on axially compressed buckling of MWNTs subjected to an internal or external radial pressure, with an emphasis on new physical phenomena due to combined radial pressure and axial stress. The analysis is based on the multiple-elastic shell model [127-129]. The representative MWNTs considered in Chapter 4 are listed in Table 4.1, where examples 1 and 2 are thin MWNTs, examples 4 and 5 are thick MWNTs, while example 6 is a(n) (almost) solid MWNT. In particular, example 3 for SWNTs is included here, as a special case $N = 1$, for a comparison with [87] which, to our knowledge, is probably the only available result regarding the effect of filling molecules on the critical axial stress of CNTs. Among other results, the present analysis shows that the predicted increase of critical axial stress due to an internal radial pressure is in qualitative agreement with the results for filled CNTs obtained by MD simulations [87].

4.2 Elastic Buckling of MWNTs under Pure Axial Stress

First, let us examine elastic buckling of MWNTs under pure axial stress, as shown in Fig. 4.1(a). Prior related works have been essentially limited to SWNTs [32, 120] and thin MWNTs of larger radius-to-thickness ratio [127-129]. Here, instead, we shall consider all three types of MWNTs, including thick and solid MWNTs as shown in Table 4.1. Under pure axial stress, the pre-buckling radial deformation of individual tubes of MWNTs is negligibly small and thus the pre-buckling radial pressure on individual tubes can be ignored. Applying Eqs. (2.13) to (2.15) with $p_k^0 = 0$ and $\psi_k = 0$ $(k = 1,2,\cdots,N)$, the dependency of axial buckling stress on the wave numbers (m,n) is shown in Figs. 4.2 to 4.6 for thin (examples 1 and 2 in Table 4.1), thick (examples 4 and 5 in Table 4.1) and a(n) (almost) solid MWNT (example 6 in Table 4.1), respectively. An interesting general result is that, similar to classic results of axially compressed buckling of elastic thin shells [118, 148], the wave-numbers corresponding to the minimum axial stress are not unique for all three types of MWNTs. More precisely, there always is more than one combination of (m,n) which corresponds to the same minimum (critical) axial stress. As a result, the wave-numbers of the buckling mode of MWNTs under pure axial stress cannot be determined uniquely.

It was mentioned in Chapter 3 that a thin N – wall CNT under external pressure can be approximated by an equivalent singlelayer shell whose effective bending stiffness and thickness are N times the effective bending stiffness and thickness of SWNTs. Indeed, as will be shown in Section 9.1.2, this conclusion still holds true for thin MWNTs (e.g., examples 1 and 2 in Table 4.1) under pure axial load. As a result, the critical axial stress of a thin MWNT under pure axial stress is approximately equal to the critical axial stress of a SWNT of the average radius of the MWNT, as stated in [129].

On the other hand, the critical axial stresses for three thick or solid MWNTs (examples 4, 5, and 6 in Table 4.1) are summarized in Table 4.2, with a comparison to the critical axial stress of a SWNT whose radius is equal to the innermost or the outermost radius of the MWNT. For these examples, the critical axial stress for

MWNT is bounded, from above and from below, respectively, by the critical axial stress of a SWNT of the innermost radius of the MWNT, and the critical axial stress of a SWNT of the outermost radius of the MWNT. Here, the results for example 5 of sixteen layers are obtained with an approximate method (See details in Section 9.1.3), which has been used in Section 3.4 for buckling of a 20-wall CNT (example 8 in Table 3.1) under radial pressure. Based on this approximate method the original 16-wall CNT can be reduced to a multiplayer shell of only five thin layers, whose data are shown in Table 4.3.

4.3 Elastic Buckling of MWNTs under Combined Axial Stress and Radial Pressure

Next, let us further consider elastic buckling of MWNTs subjected to both axial stress and internal or external pressure, as illustrated in Fig.4.1(b) and (c), respectively. Here, our attention is focused on the interaction between radial pressure and axial stress in elastic buckling of MWNTs.

4.3.1 Pre-buckling Radial Pressure Distribution

As shown in Section 2.2.2, before the buckling analysis, the radial pressure distribution must be determined for MWNTs under both axial stress and radial pressure. Using (2.10) and (2.11) with known external (or internal) pressure-to-axial stress ratio β (or γ), the distributions of pre-buckling outer pressure $p^0_{k(k+1)}$ and net pressure p^0_k ($k = 1,2,\cdots N$) normalized by the axial stress σ_{axial} for three representative examples (examples 1, 4 and 6 in Table 4.1) are shown in Figs. 4.7 to 4.12 for combined axial stress and external or internal pressure, respectively. In Figs.4.7 to 4.9, the pressure distribution under combined axial stress and external pressure is given for various external pressure-to-axial stress ratios β. Similar to the case of MWNTs under radial pressure alone, both the net pressure p^0_k and the outer pressure $p^0_{k(k+1)}$ ($k = 1,2\cdots N$) decrease monotonically from the outermost tube to the

innermost tube, and are very low for the innermost few tubes of a thick (example 4 in Table 4.1) or solid (example 6 in Table 4.1) MWNT. For thin MWNTs (example 1 in Table 4.1), the outer pressure is almost linearly distributed, and the net pressure is almost constant, showing that the applied external pressure are almost equally shared by all concentric tubes of a thin MWNT.

In addition, the pre-buckling net pressure p_k^0 and outer pressure $p_{k(k+1)}^0$ ($k = 1,2 \cdots N$) for combined axial stress and internal pressure are shown in Figs. 4.10 to 4.12 for various internal pressure-to-axial stress ratios γ. In contrast to the case of MWNTs under external pressure, as seen from Figs. 4.10 to 4.12, both the net pressure p_k^0 and the outer pressure $p_{k(k+1)}^0$ decrease monotonically from the innermost tube to the outermost tube, and are very low for the outermost few tubes of a thick (example 4 in Table 4.1) or solid (example 6 in Table 4.1) MWNT. Therefore, the applied internal pressure only significantly affects the innermost few tubes, and has little influence on the pressure distributions of the outermost tubes of thick or solid MWNTs. On the other hand, for thin MWNTs (example 1 in Table 4.1), it is seen from Fig. 4.10 that the outer pressure can be considered to be nearly linearly distributed and the net pressure be nearly constant.

4.3.2 The Effect of an Internal Pressure on Critical Axial Stress

Now, let us consider buckling of the combined axial stress and internal pressure. The main objective is to examine the effect of internal pressure on the critical axial stress of thin, thick and (almost) solid MWNTs. In particular, for sake of a comparison with [87] regarding the effect of filling molecules on the critical axial stress of CNTs, we start with the SWNT, example 3 in Table 4.1, which was also considered in Ni et al's MD simulation [87].

One of main results for elastic singlelayer shells under combined axial stress and internal pressure [118, 148] is that the internal pressure has no effect on axisymmetric buckling mode, but has a significant effect on non-axisymmetric buckling modes. First, for SWNTs, it has been argued [120] that, due to some

unidentified reasons (such as non-axisymmetric atomic structure of SWNT), the actual buckling mode of SWNTs under pure axial stress is non-axisymmetric, and can be approximately determined by the condition that the circumferential wave-length is equal to the axial wave-length. Based on this assumption, the relative change of the critical axial stress for example 3 (a SWNT of diameter 1.3 nm) due to an internal pressure is shown in Fig.4.13, as a function of the internal pressure-to-axial stress ratio γ. It is seen from Fig.4.13 that the critical axial stress increases 10%, 20%, and 45% when the internal pressure-to-axial stress ratio is around 0.04, 0.07 and 0.14, respectively. Therefore, the relative increase of the critical axial stress due to filling molecules observed by Ni et al. [87], which is about 10-20% at low density or 45% at high density, could be explained by an equivalent internal pressure about 5% or 14% of the critical axial stress (or equivalently, by an equivalent internal pressure which is about the critical external pressure or 2-3 times the critical external pressure). Since the internal pressure due to filling molecules can be reasonably assumed to be of the order of magnitude of the critical external pressure [81, 130], the present theoretical results appear to be in qualitative agreement with Ni et al.'s results [87] obtained by MD simulations.

For MWNTs, we consider three representative examples 1, 4 and 6 (in Table 4.1). Here, the minimum axial stresses of MWNTs are calculated as functions of the circumferential wave-number n, for various internal pressure-to-axial stress ratios γ. The results are shown in Figs. 4.14 to 4.16 for examples 1, 4 and 6, respectively. It is seen from these figures that the internal pressure has no effect on the axisymmetric buckling mode ($n = 0$), but significantly promotes the critical axial stress for non-axisymmetric modes. In particular, for non-axisymmetric modes, the effect of internal pressure on the critical axial stress is strong for thin MWNTs (Fig. 4.14), moderate for thick MWNTs (Fig.4.15), and negligible for solid MWNTs (Fig.4.16). We noticed that the last conclusion is different from the results in Chapter 3 combined internal and external pressures (without axial stress) where the internal pressure has a moderate effect on the critical external pressure even for solid MWNTs. This can be explained by the fact that under axial stress the individual tubes of MWNTs become much stiffer in radial direction than they are when the axial stress is absent.

4.3.3 The Interaction between Axial Stress and External Pressure

Next, let us examine elastic buckling of MWNTs under combined axial stress and external pressure to investigate the interaction between critical axial stress and external pressure. Here, we consider all examples 1 to 6 of MWNTs in Table 4.1, as well as an additional thin SWNT of radius $5.3\,nm$. The critical axial stress (under pure axial stress) for these seven examples is $4.481\,GPa$, $2.172\,GPa$, $63.962\,GPa$, $9.911\,GPa$, $4.460\,GPa$, $16.300\,GPa$ and $8.153\,GPa$, and the critical external pressure (under pure external pressure) is $0.0083\,GPa$, $0.0021\,GPa$, $2.098\,GPa$, $0.102\,GPa$, $0.0297\,GPa$, $1.8805\,GPa$ and $0.0093\,GPa$, respectively. These critical axial stresses (for pure axial stress) and critical external pressures (for pure external pressure) are obtained by following the procedures demonstrated in Chapter 2. Two main results for elastic thin shells under combined axial stress and external pressure [118, 148] are that 1) the buckling mode can be determined uniquely and is characterized by $m=1$; 2) the critical condition expressed by a relation between the axial stress and the external pressure is nearly linear. For all examples discussed here, the conclusion that the buckling mode can be determined uniquely remains true, although the buckling mode is not always characterized by $m=1$. To further examine the interaction between the axial stress and external pressure, the critical values of the axial stress and corresponding external pressure are calculated with various external pressure-to-axial stress ratios β, and the critical condition given in terms of the above two critical values, together with the corresponding wave-numbers (m,n), is shown in Fig.4.17 and Fig. 4.18 for a SWNT (example 3 in Table 4.1) and MWNTs (all other examples in Table 4.1), respectively.

It is seen from Figs. 4.17 and 4.18 that, the critical condition as a relation between the axial stress and the external pressure is apparently nonlinear for all six examples given in Table 4.1. This discrepancy with the classic results of elastic thin shells is due to the fact that the radius-to-thickness ratio for these examples is too small compared to that of conventional elastic thin shells [118, 148]. In other words, the critical condition is expected to be nearly linear when the radius-to-thickness ratio

of CNTs is sufficiently large. In Fig.4.17, this is demonstrated by the critical condition for a thin SWNT of radius $5.3\,nm$, in which the critical condition is indeed nearly linear, because of the sufficient large ratio-to-thickness ratio.
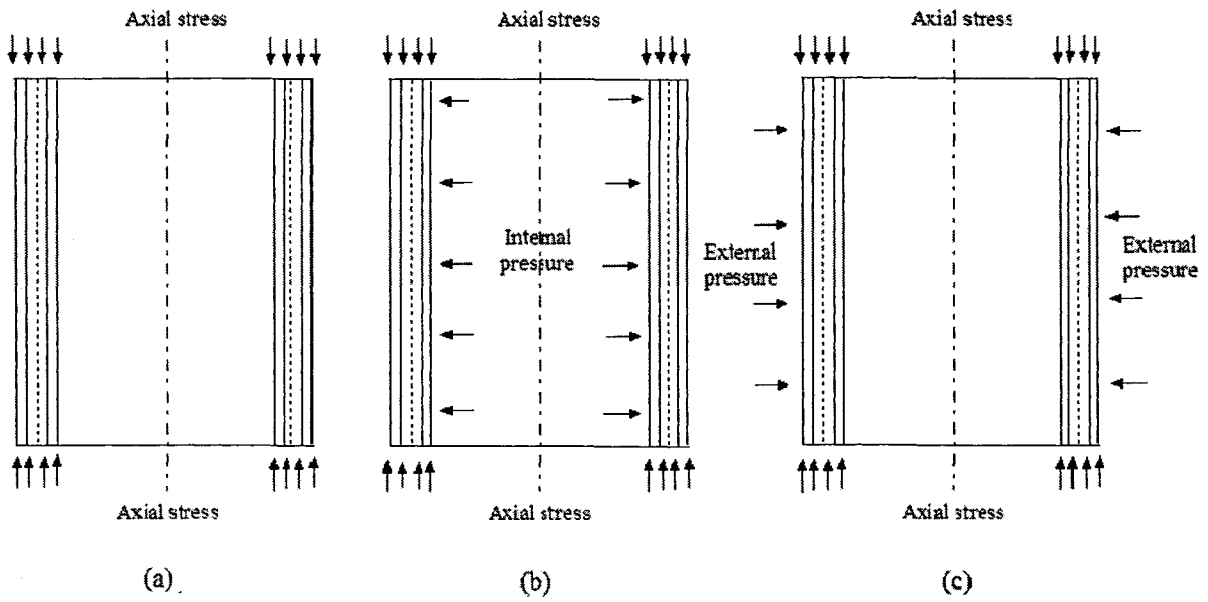
Fig. 4.1 Buckling of a MWNT under (a) axial stress (b) axial stress and internal pressure and (c) axial stress and external pressure.
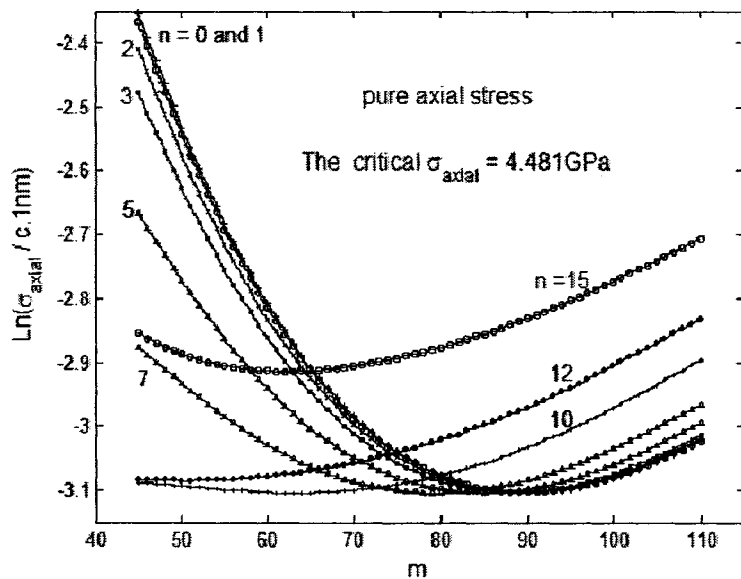
Fig.4.2 The dependency of axial stress on the wave-numbers (m,n) for example 1

(in Table 4.1) under pure axial stress.
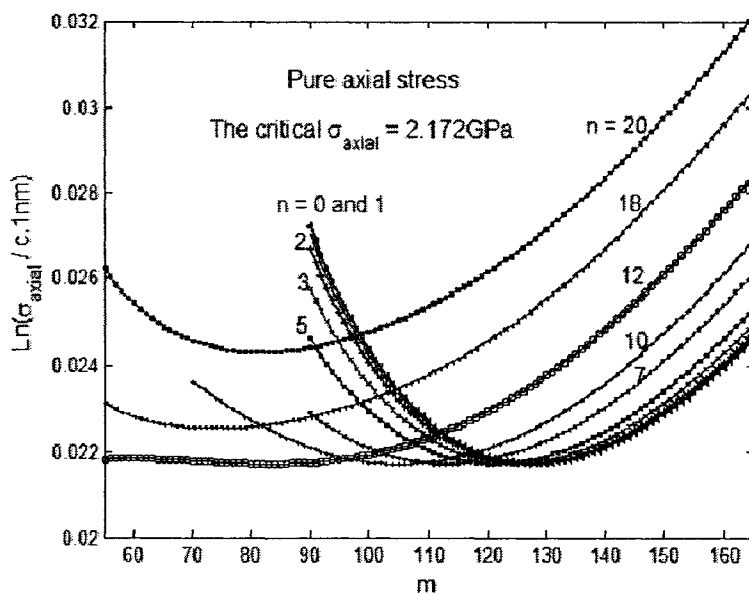
Fig.4.3 The dependency of axial stress on the wave-numbers (m,n) for example 2

(in Table 4.1) under pure axial stress.
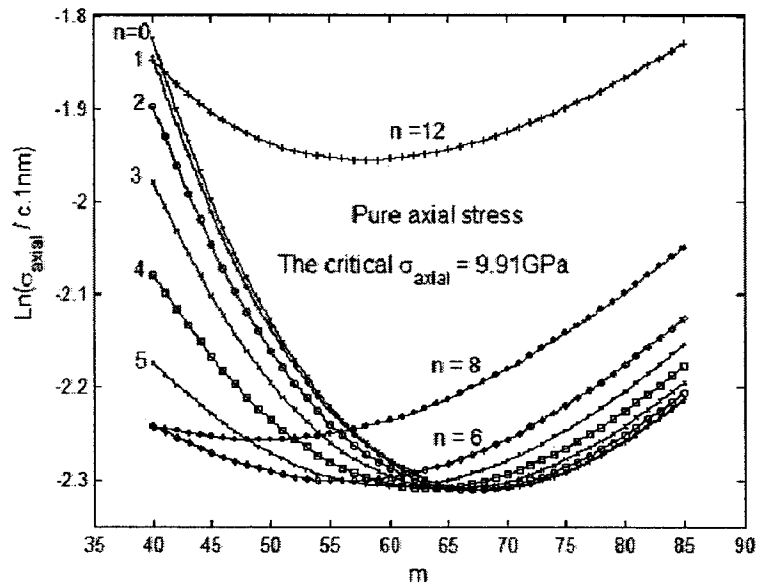
Fig.4.4 The dependency of axial stress on the wave-numbers (m,n) for example 4

(in Table 4.1) under pure axial stress.
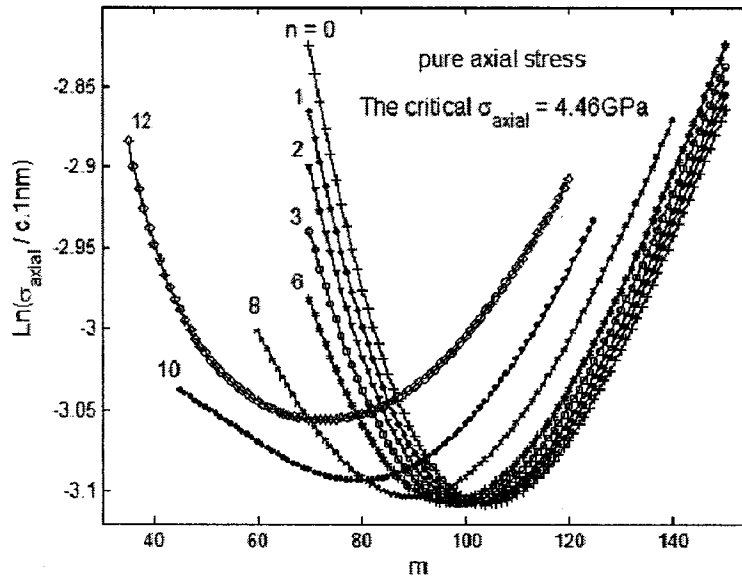
Fig.4.5 The dependency of axial stress on the wave-numbers (m,n) for example 5

(in Table 4.1) under pure axial stress.
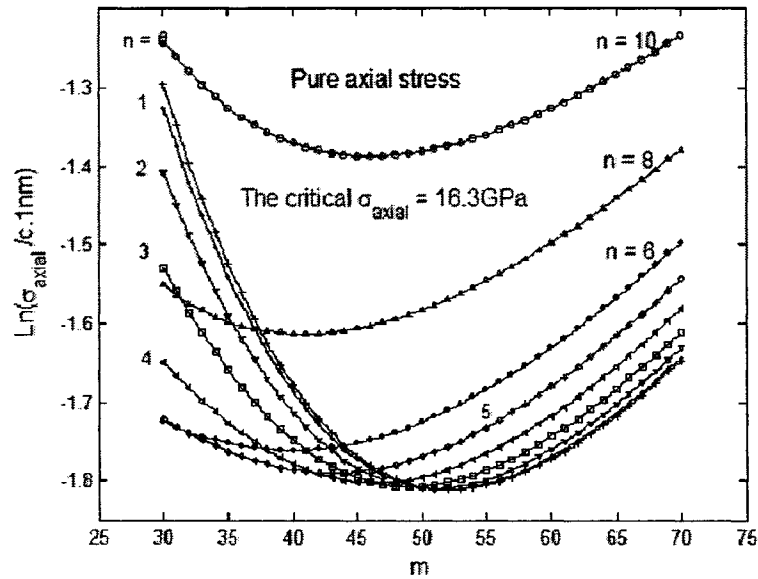
Fig.4.6 The dependency of axial stress on the wave-numbers (m, n) for example 6

(in Table 4.1) under pure axial stress.
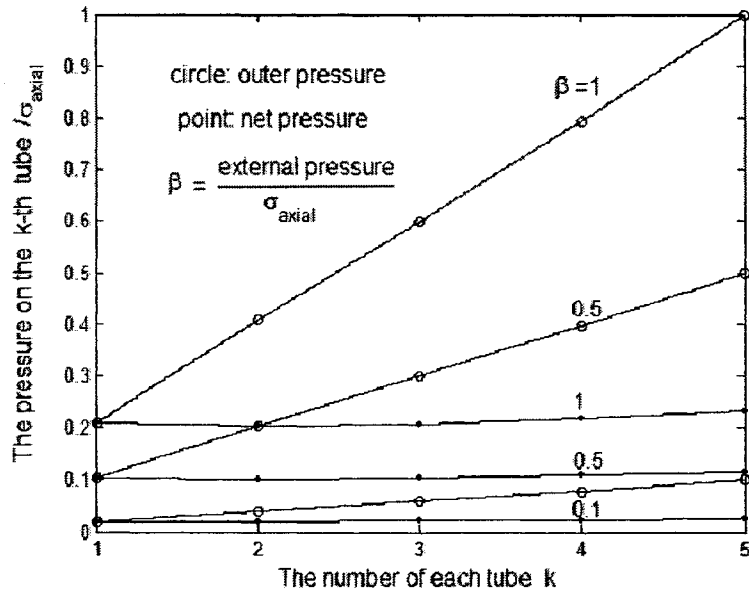
Fig. 4.7 Pre-buckling pressure distribution for example 1 (in Table 4.1)

under combined axial stress and external pressure.
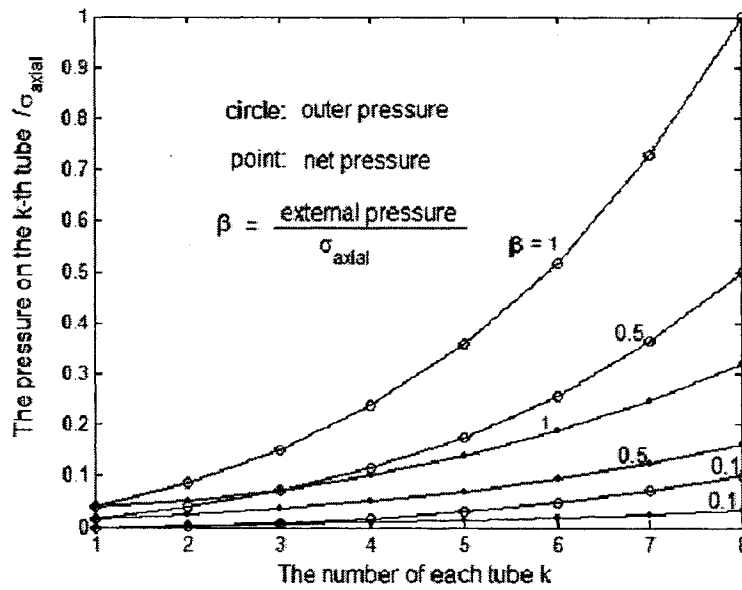
Fig. 4.8 Pre-buckling pressure distribution for example 4 (in Table 4.1) under combined axial stress and external pressure.
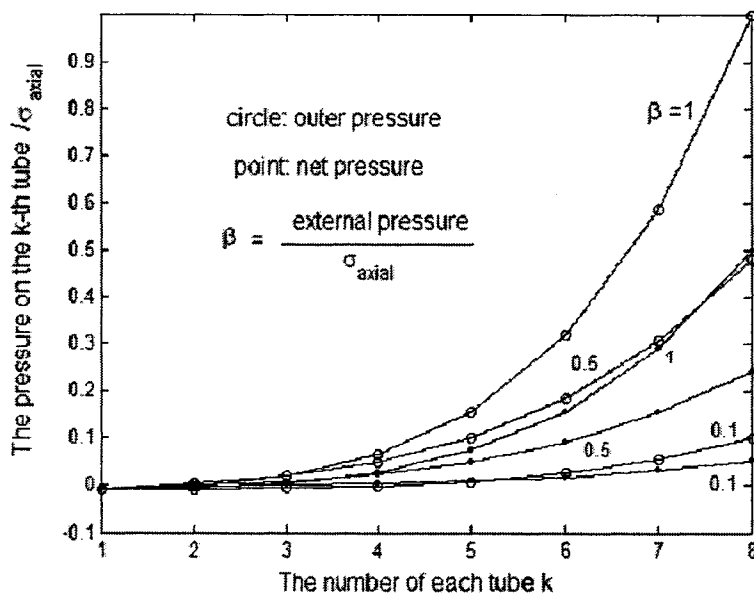
Fig.4.9 Pre-buckling pressure distribution for example 6 (in Table 4.1) under combined axial stress and external pressure.
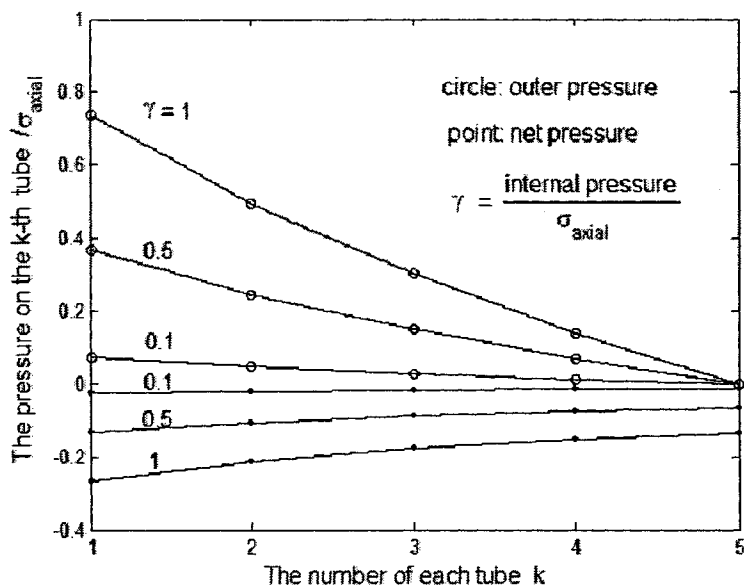
Fig. 4.10 Pre-buckling pressure distribution for example 1 (in Table 4.1)

under combined axial stress and internal pressure.
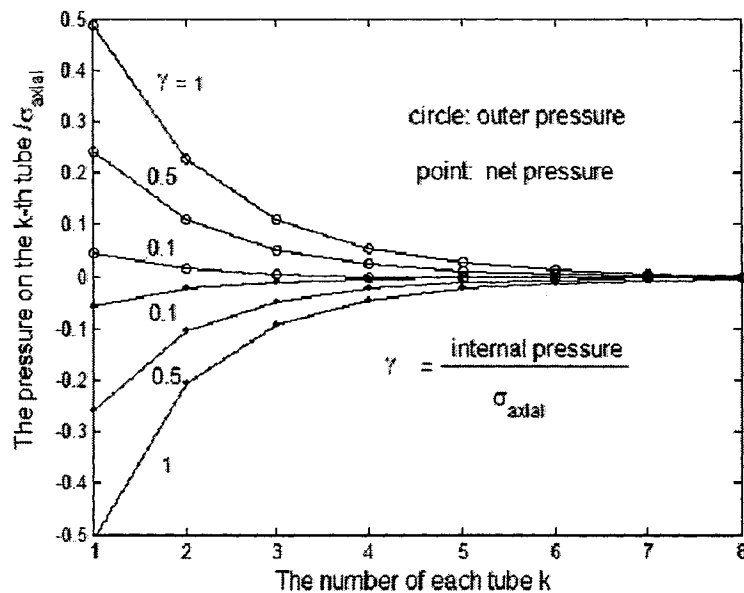
Fig.4.11 Pre-buckling pressure distribution for example 4 (in Table 4.1)

under combined axial stress and internal pressure.
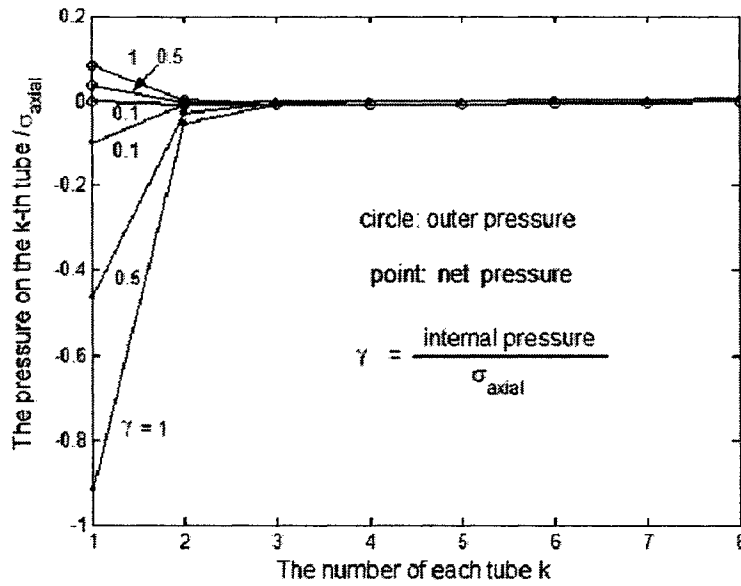
Fig.4.12 Pre-buckling pressure distribution for example 6 (in Table 4.1)

under combined axial stress and internal pressure.
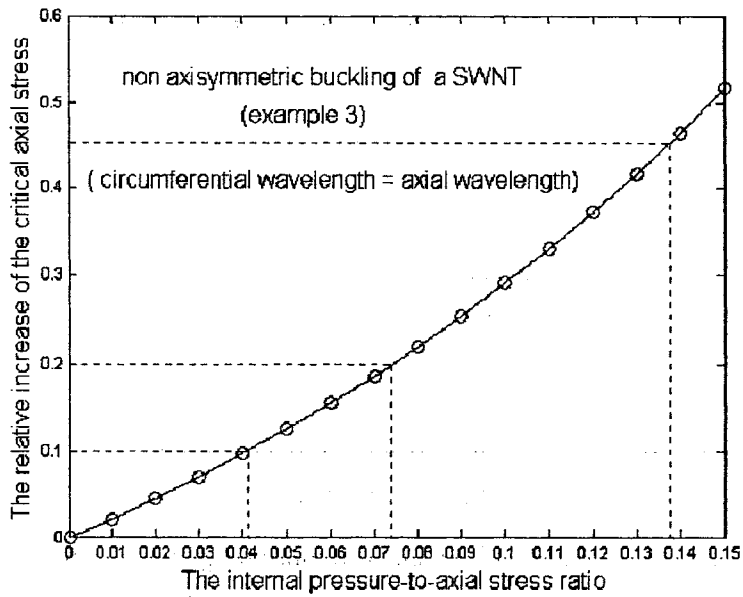
Fig.4.13 The effect of an internal pressure on the critical axial stress of

a SWNT (example 3 in Table 4.1).
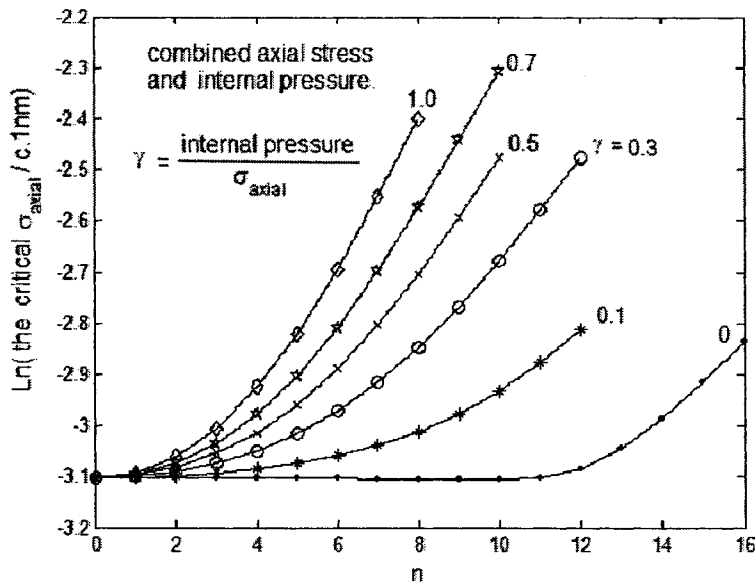
Fig.4.14 The effect of an internal pressure on the critical axial stress for various circumferential wave-number (example 1 in Table 4.1)
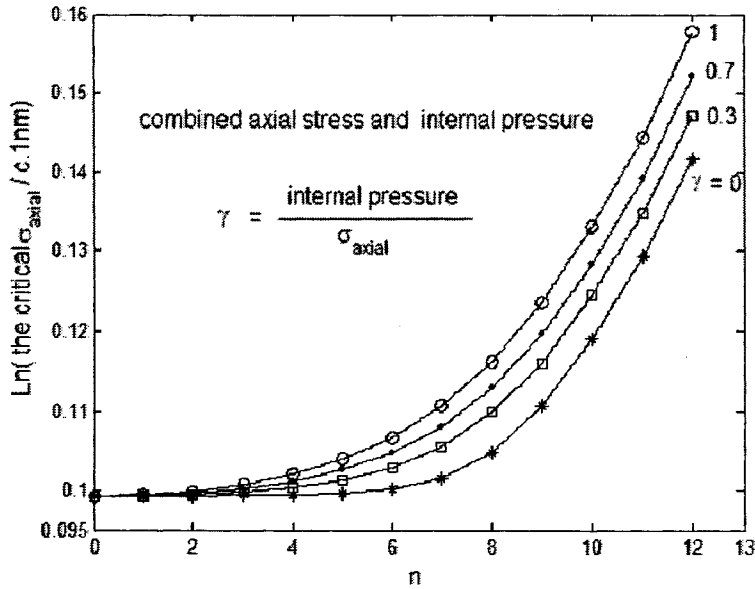
Fig.4.15 The effect of an internal pressure on the critical axial stress for various circumferential wave-number (example 4 in Table 4.1)
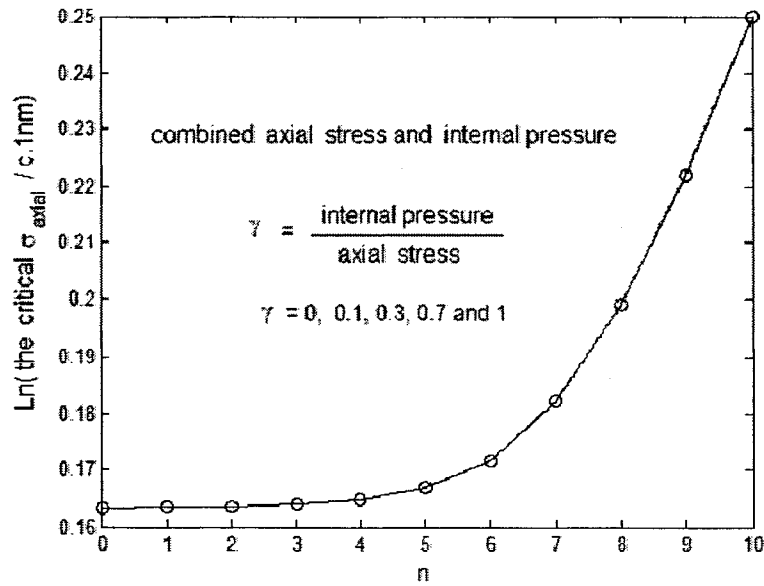
Fig.4.16 The effect of an internal pressure on the critical axial stress for various circumferential wave-number (example 6 in Table 4.1)
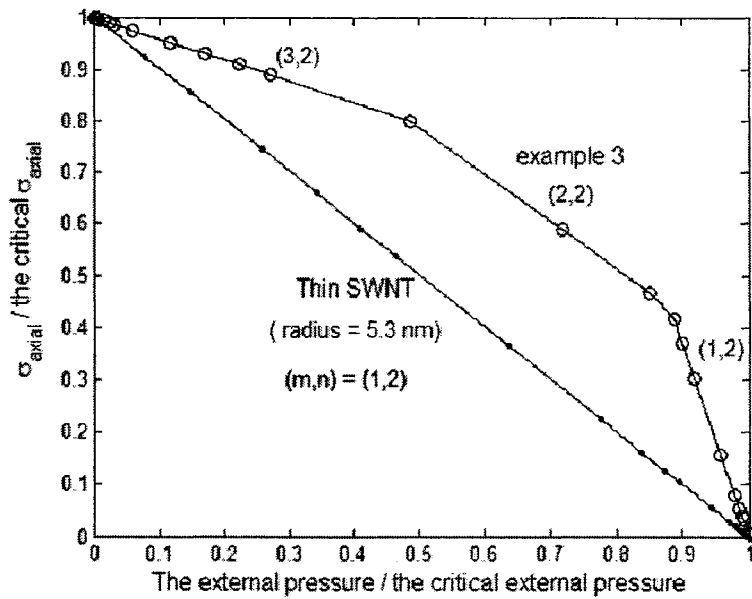
Fig.4.17 The critical condition under combined axial stress and external pressure for a thin SWNT of radius $5.3nm$ and example 3 in Table 4.1.
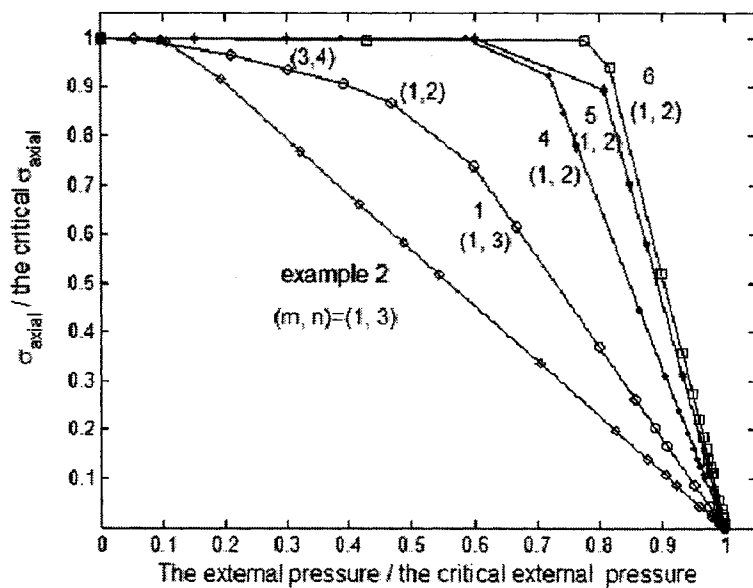
Fig. 4.18 The critical condition under combined axial stress and external pressure for examples 1, 2, 4, 5 and 6 in Table 4.1.

Table 4.1. The geometrical data for examples of MWNTs considered in Chapter 4. Here r_1 is the innermost radius of a MWNT, N is the number of layers of the MWNT, and h (= $0.34\,nm$) is the effective thickness of a SWNT.

Example	Thin MWNTs			Thick MWNTs		Solid MWNTs
The example number	1	2	3	4	5	6
r_1 (nm)	8.5	18	0.65	2.7	6.5	0.65
r_1 / Nh	5.00	6.62	1.9	0.99	1.20	0.24
N	5	8	1	8	16	8

Table 4.2. Critical axial stress for thick or solid MWNTs (examples 4-6 in Table 4.1) with comparison to the critical axial stress of a related SWNT. Here σ_{MWNT} is the critical axial stress for a MWNT under axial stress, and σ_{inner} and σ_{outer} are critical axial stresses for related SWNTs with the innermost radius or outermost radius of the MWNT.

Example	Thick MWNTs		Solid MWNTs
Example number	4	5	6
σ_{MWNT} (GPa)	9.91	4.46	16.30
σ_{inner} (GPa)	15.40	6.40	64.00
σ_{outer} (GPa)	8.18	3.58	13.72

Table 4.3. Substitution of a five-layer elastic shell for a MWNT of sixteen layers (example 5 in Table 4.1). Here K is the number of concentric tubes in each new layer, and r_{inner} and H are the inner radius and thickness and of each new layer.

The new layer number	I	II	III	IV	VI
K	1	3	3	4	5
$H\,(nm)$	0.34	1.02	1.02	1.36	1.70
$r_{inner}\,(nm)$	6.5	6.84	7.86	8.88	10.24
$r_{inner}\,/\,H$		6.71	7.71	6.53	6.02

Chapter 5

Basic Formulations for Free Vibration of MWNTs

5.1 Introduction

Free vibration of CNTs is a current topic of great interest [14, 70-74, 91-99]. In particular, Raman spectroscopy is the dominant experimental technique for characterization of vibrational behavior of CNTs [14]. The obtained results showed that due to extremely small size and distinctive molecular structure, CNTs, especially MWNTs exhibit complex vibrational behaviors, which are difficult to be observed and analyzed directly in experiments. For example, the data obtained by Raman scattering can only be understood on the basis of theoretical predictions [14, 70-71, 74]. Hence sophisticated theoretical models are particularly important in predicting vibrational properties of CNTs, and in guiding and interpreting experiments.

Atomistic approaches are standard way to study objects, like CNTs. Thus, atomistic simulations, for instance first principles [36, 93], force-constant [91], tight binding [160] and zone folding [161] models, are first employed to predict vibrational properties of CNTs. However, in many cases, these discrete approaches remain computationally prohibitive for large-scale atom system like CNTs, in particular, MWNTs of many layers. Thus continuum models, such as elastic beam models [106, 162-164], elastic shell models [124-126] and other continuum models [165-170] have been widely used to catch the main features of free vibration of CNTs. As an evidence of the effectiveness of the continuum models for CNTs, for example, non-coaxial vibration modes of MWNTs were first predicted based on a multiple-beam model [106] and later, confirmed by recent atomistic simulation [113]. On the other hand, it is noted that most of previous studies are mainly focused on vibration of SWNTs [124-126, 165-170] or beam-like vibration of MWNTs [106, 163-164].The systematic theoretical study on general vibrational behavior of MWNTs has not been addressed in the literature primarily due to the lack of reliable and efficient theoretical dynamic models for MWNTs.

88

Recently, to study mechanical behaviors of MWNTs, a multiple-elastic shell model has been developed by Ru [127-129] and effectively used to study elastic buckling of CNTs under axial compression [127-129], radial pressure [123, 130], or combined loadings [131], with good agreement to available experiments and atomistic simulations of SWNTs [123] and MWNTs of as many as twenty layers [130]. Thus it is expected that the multiple-shell model can be further employed to study the vibrational behavior of MWNTs.

Based on the multiple-shell model [127-129], this chapter derives the general dynamic equations and formulations for the free vibration of MWNTs. To obtain more accurate results and retain all the possible vibrational frequencies and associated vibrational modes of MWNTs, three Flugge dynamic shell equations [137-138], instead of simplified single Donnell shell equation [116], are used for the free vibration of each individual tube of MWNTs. Using the multiple-shell model based on Flugge dynamic equations, the analytical method for free vibration of MWNTs is demonstrated, in detail, for MWNTs with simply supported ends.

5.2 The Multiple-Shell Model for Free Vibration of MWNTs

In view of the multiple-elastic shell model [127-129], each of the nested tubes of a MWNT is an individual elastic shell, and the adjacent tubes are coupled with each other through the normal vdW interaction without the interlayer friction. It is known that free vibration of a cylindrical thin shell can be described by three Flugge dynamic equations, which are derived from the basic assumptions of linear elastic thin shell without other further simplifications [137-138]. Applying the three dynamic equations to each nested tube of an N-wall CNT, in the absence of tangential force, yields the following $3N$ equations governing the free vibration of the N-wall CNT ($k = 1,2,\cdots,N$).

$$\frac{r_k}{2}(1+v)\frac{\partial^2 u_k}{\partial x \partial \theta} + \frac{r_k^2}{2}(1-v)\frac{\partial^2 v_k}{\partial x^2} + \frac{\partial^2 v_k}{\partial \theta^2} + \frac{\partial w_k}{\partial \theta} + (1-v^2)\frac{D}{Ehr_k^2}\left[\begin{array}{c} \frac{3r_k^2}{2}(1-v)\frac{\partial^2 v_k}{\partial x^2} \\ -\frac{r_k^2}{2}(3-v)\frac{\partial^3 w_k}{\partial x^2 \partial \theta} \end{array}\right]$$

$$= \frac{\rho h}{Eh}(1-v^2)r_k^2\frac{\partial^2 v_k}{\partial t^2},$$

$$r_k^2\frac{\partial^2 u_k}{\partial x^2} + \frac{1}{2}(1-v)\frac{\partial^2 u_k}{\partial \theta^2} + \frac{r_k}{2}(1+v)\frac{\partial^2 v_k}{\partial x \partial \theta} + vr_k\frac{\partial w_k}{\partial x} + (1-v^2)\frac{D}{Ehr_k^2}\left[\begin{array}{c} \frac{1}{2}(1-v)\frac{\partial^2 u_k}{\partial \theta^2} \\ -r_k^3\frac{\partial^3 w_k}{\partial x^3} \\ +\frac{r_k}{2}(1-v)\frac{\partial^3 w_k}{\partial x \partial \theta^2} \end{array}\right]$$

$$= \frac{\rho h}{Eh}(1-v^2)r_k^2\frac{\partial^2 u_k}{\partial t^2},$$

$$vr_k\frac{\partial u_k}{\partial x} + \frac{\partial v_k}{\partial \theta} + w_k + (1-v^2)\frac{D}{Eh}r_k^2\cdot\nabla^4 w_k + (1-v^2)\frac{D}{Ehr_k^2}\left[\begin{array}{c} -r_k^3\frac{\partial^3 u_k}{\partial x^3} + \frac{r_k}{2}(1-v)\frac{\partial^3 u_k}{\partial x \partial \theta^2} \\ -\frac{r_k^2}{2}(3-v)\frac{\partial^3 v_k}{\partial x^2 \partial \theta} + w_k \\ +2\frac{\partial^2 w_k}{\partial \theta^2} \end{array}\right]$$

$$= -\frac{1}{Eh}(1-v^2)r_k^2\left[\rho h\frac{\partial^2 w_k}{\partial t^2} + p_k\right]$$

(5.1)

where t is time; u_k, v_k and w_k are longitudinal, circumferential and (inward positive) radial vibration displacements of tube k; r_k is the radius of tube k; the subscribe 1, 2, ..., N denotes the quantities of the innermost tube, its adjacent tube,..., and the outermost tube; In particular, for a SWNT, the effective bending stiffness D, in-plane stiffness Eh and mass density per unit lateral area on the surface of each tube ρh are treated as three material constants, independent of the specific definition of thickness h.

In other words, for different definitions of thickness h, Eh and ρh are defined in such way that the products of Eh and ρh keep the same for different definitions of h. The effective values of D and Eh are given in Chapter 2 (page 45) and $\rho h = (2.27g/cm^3) \times 0.34nm$ [126, 132,134-136]. In addition, as in the case of buckling analysis (see Section 2.2.1) the net radial pressure p_k ($k = 1,2,3,\cdots,N$) on tube k due to vibration are obtained as the sum of the (inward positive) outer pressure $p_{k(k+1)}$ and the (inward positive) inner pressure $p_{k(k-1)}$ exerted on tube k by tube $k+1$ and tube $k-1$, respectively. According to above definitions, $p_{10} = 0$ and $p_{N(N+1)} = 0$. Moreover, keeping in mind that all pressures and radial deflections result from vibration, instead of buckling, one can directly use Eqs. (2.4) and (2.5) to calculate $p_{k(k+1)}$ and $p_{k(k-1)}$ ($k = 1,2,3,\cdots,N$) for free vibration of MWNTs. Accordingly, the net pressure p_k ($k = 1,2,3,\cdots,N$) in Eqs.(5.1) can be expressed as follows [127-129, 130-136]:

$$p_1 = p_{12} + p_{10} = c_1.(w_2 - w_1)$$

$$p_2 = p_{23} + p_{21} = c_2.(w_3 - w_2) - c_1 \frac{r_1}{r_2}(w_2 - w_1)$$

$$\cdots\cdots$$

$$p_N = p_{N(N+1)} + p_{N(N-1)} = -c_{N-1}.\frac{r_{N-1}}{r_N}(w_N - w_{N-1}) \tag{5.2}$$

where $c_k(k = 1,2,\cdots,N-1)$ represents the vdW interaction coefficient between tube k and tube $k+1$. In the presence of a high external pressure, $c_k(k = 1,2,\cdots,N-1)$ could significantly increase due to pressure-induced reduction of the interlayer spacing (see Section 6.4.1). On the other hand, in the absence of an external pressure, which is the case that will be discussed in Chapters 7 and 8, or when the pressure effect on the vdW interaction coefficients is neglected, which is the case in Chapters 2 to 4, the vdW interaction coefficient $c_k(k = 1,2,\cdots,N-1)$ associated with equilibrium interlayer spacing ($0.34nm$) is a constant given by Eq. (2.6). In addition, it is noted in Eqs.(5.1) that the N

dynamic equations in radial direction are coupled with each other through the vdW interaction terms p_k ($k = 1,2,\cdots,N$).

5.3 Analysis Method for Free Vibration of MWNTs

To catch main features of free vibration of MWNTs, let us consider individual MWNTs with simply supported ends. To satisfy the specific boundary condition, the solution to Eqs. (5.1) are given by ($k = 1,2,\cdots,N$)

$$u_k(x,\theta,t) = U_k \cos\frac{m\pi}{L}x \cdot \cos n\theta \cdot e^{i\omega t}$$

$$v_k(x,\theta,t) = V_k \sin\frac{m\pi}{L}x \cdot \sin n\theta \cdot e^{i\omega t}$$

$$w_k(x,\theta,t) = W_k \sin\frac{m\pi}{L}x \cdot \cos n\theta \cdot e^{i\omega t} \tag{5.3}$$

where real numbers U_k, V_k and W_k denote the longitudinal, circumferential and radial displacement amplitudes of tube k, L is the length of an N – wall CNT, ω ($\omega = 2\pi f$, f is frequency) represents the angular frequency, m is the axial half wave number and n is the circumferential wave number. Substituting Eqs. (5.2) and (5.3) into (5.1) leads to the following $3N$ equations ($k = 1,2,\cdots,N$).

$$\left\{-r_k \cdot (\frac{m\pi}{L})^2 - \frac{1+\bar{k}}{2} \cdot (1-v^2) \cdot n^2 + \frac{\rho h}{Eh} \cdot (1-v^2) \cdot \omega^2\right\} \cdot U_k + \left\{\frac{r_k}{2} \cdot (1-v) \cdot (\frac{m\pi}{L})\right\} \cdot V_k +$$

$$\left\{v \cdot r_k n + \bar{k} \cdot \left[-r_k^3 \cdot (\frac{m\pi}{L})^3 + \frac{r_k}{2} \cdot (1-v) \cdot (\frac{m\pi}{L}) \cdot n^2\right]\right\} \cdot W_k = 0$$

$$\left\{ \frac{r_k}{2} \cdot (1+v) \cdot (\frac{m\pi}{L}) \cdot n \right\} \cdot U_k - \left\{ \begin{matrix} \frac{r_k^2}{2} \cdot (1-v^2) \cdot (\frac{m\pi}{L})^2 + n^2 + \bar{k} \cdot \frac{3r_k}{2} \cdot (1-v^2) \cdot (\frac{m\pi}{L}) \\ + \frac{\rho h}{Eh} \cdot (1-v^2) \cdot \omega^2 \end{matrix} \right\} \cdot V_k +$$

$$\left\{ n + \bar{k} \cdot \frac{r_k^2}{2} \cdot (3-v) \cdot (\frac{m\pi}{L})^2 \cdot n \right\} \cdot W_k = 0$$

$$\left\{ -v \cdot r_k \cdot (\frac{m\pi}{L}) + \bar{k} \cdot \left[-r_k^3 \cdot (\frac{m\pi}{L})^3 + \frac{r_k}{2} \cdot (1-v) \cdot (\frac{m\pi}{L}) \cdot n \right] \right\} \cdot U_k + \left\{ \begin{matrix} n + \bar{k} \cdot \frac{r_k^3}{2} \cdot (3-v) \\ \cdot (\frac{m\pi}{L})^2 \cdot n \end{matrix} \right\} \cdot V_k$$

$$\left\{ -1 - \bar{k} \cdot \left\{ r_k^4 \cdot \left((\frac{m\pi}{L})^2 + (\frac{n}{r_k})^2 \right)^2 - 1 + 2n^2 \right\} + c \cdot (\bar{\lambda} + \frac{r_{k-1}}{r_k}) + \frac{\rho h}{Eh} \cdot (1-v^2) \cdot \omega^2 \right\} \cdot W_k$$

$$-\frac{r_{k-1}}{r_k} \cdot W_{k-1} - c \cdot W_{k+1} = 0$$

(5.4)

where $\bar{k} = (1-v^2) \cdot \frac{D}{Eh} \cdot \frac{1}{r_k^2}$, $r_0 = r_{N+1} = 0$ and $W_0 = W_{N+1} = 0$. In addition, in the third

equation of (5.4), $\bar{\lambda} = 1$ for $k = 1,2,\cdots,N-1$, while $\bar{\lambda} = 0$ for $k = N$. It is easy to see

that (5.4) can be written in the following form

$$M\{(n,m),\omega\}_{3N\times3N} \begin{bmatrix} U_1 \\ V_1 \\ W_1 \\ \cdots \\ U_N \\ V_N \\ W_N \end{bmatrix} = 0$$

(5.5)

where $M_{3N \times 3N}$ is a $3N \times 3N$ matrix, whose elements are functions of (m, n) and ω. The condition for existence of non-zero solutions U_k, V_k and W_k ($k = 1, 2, \cdots, N$) is

$$\det M = 0 \tag{5.6}$$

Since the key parameters of free vibration modes are the normalized axial wavelength $L/(r_N m)$ (normalized by the outermost diameter $2 r_N$) and the circumferential wave number n, our results for MWNTs will be given in terms of ($L/(r_N m)$, n). With given $L/(r_N m)$ and n, condition (5.6) determines $3N$ frequencies for an N − wall CNT. Substitution of a frequency into (5.5) yields amplitude ratios $\dfrac{U_k}{W_N}$, $\dfrac{V_k}{W_N}$ and $\dfrac{W_k}{W_N}$ ($k = 1, 2, \cdots, N$), defining the associated mode of the N − wall CNT. Therefore, for each combination of ($L/(r_N m), n$), the multiple-shell model gives $3N$ vibration frequencies associated with $3N$ vibration modes for an N − wall CNT.

Chapter 6

Radial Breathing Vibration of MWNTs

6.1 Introduction

Raman-active radial breathing modes (RBMs) of CNTs have been studied extensively in last decade [24, 36, 70-74, 91-99]. It has been shown that for an isolated SWNT, RBM frequency is inversely proportional to its diameter [36, 70, 91-93]. A similar conclusion has also been drawn for the RBMs of SWNT ropes [77, 94-99, 170] and MWNTs of very small innermost diameter ($< 2\,nm$) [24, 71, 73-74], with RBM frequencies up-shifted around 5% to 10% (compared to isolated SWNTs) due to the intertube vdW interaction. This simple diameter dependence of RBM frequency and its sensitivity to the intertube vdW interaction make RBM a valuable probe for the structure and properties of CNTs.

Recently, the pressure effect on Raman-active modes of CNTs [77-83] is of great interest, especially for SWNT ropes and MWNTs. This is because an externally applied pressure can effectively enhance the intertube vdW interaction and the intra-tube carbon-carbon ($c - c$) interaction and thus provides a useful method to study both the intertube and intra-tube interactions occurring in SWNT ropes and MWNTs. Previous studies are mainly focused on RBMs of SWNT ropes [77-79, 82-83] and $T-$modes of both SWNTs ropes and MWNTs [77-78, 80-82], showing that the vibrational frequencies increase monotonically with the external pressure. The pressure effects on $T-$modes or RBM of an isolated SWNT are shown as a result of the pressure-induced in-plane compressive strains [80-82], which cause a reduction of the intra-tube $c - c$ distance and a small change in the intra-tube force constants [171], elastic constants, mass density and diameter [79]. On the other hand, for RBMs of SWNT ropes the most significant pressure effect is attributed to the increased intertube vdW interaction due to external pressure [77, 79], while the small changes in the material constants and the diameter of individual SWNTs play only a relatively minor role. So far, to our the present author's knowledge, the pressure effect on RBMs of MWNTs is almost absent from the literature. This is

95

partly due to the fact that RBMs of MWNTs exhibit complex frequency spectrum and cannot be easily observed and analyzed without a theoretical guidance. In addition, only the RBMs associated with very thin innermost tube of MWNTs (with the innermost diameter $< 2\,nm$) have high enough frequencies and could be observed in Raman spectra [71-74]. Unfortunately, as shown in the present work, the significant pressure effect occurs only for those RBMs in which the outermost few layers are substantially involved and adjacent outermost layers vibrate in opposite directions (counter-phase) with significant change in interlayer spacing. This can explain why the pressure effect on RBMs of MWNTs in Raman spectra remains almost absent in the literature.

In this chapter, the dynamic Eqs. (5.1) are used first to explain the main features of RBMs of CNTs observed in experiments and atomistic simulations. This offers a good opportunity to examine the effectiveness of the present shell model in studying free vibrational of CNTs. Then, we shall further investigate the pressure effect on RBMs of MWNTs for which detailed experimental data or MD simulations are not yet available in the literature. Here, the pressure dependence of RBMs of MWNTs is mainly attributed to an increase of the interlayer vdW interaction coefficients due to pressure-induced reduction of the interlayer spacing. The results show that in the absence of external pressure, the present shell model is in excellent agreement with experiments and atomistic modeling in calculating the RBM frequencies of CNTs. In particular, all the main features of RBMs of MWNTs obtained by experiments and atomistic simulations can be clearly explained by the present shell model. In the presence of an external pressure, RBM frequencies of MWNTs generally increase with increasing external pressure, and the most significant pressure effect is associated with the highest-frequency RBM for large-diameter MWNTs (the innermost diameter $> 2nm$), or an intermediate frequency RBM for small-diameter MWNTs (the innermost diameter $< 2\,nm$).

6.2 Basic Equations for Radial Breathing Vibration

Based on the present elastic shell model [127-129], let us first derive the governing equations for RBMs of MWNTs. To this end, we start with SWNTs, whose vibrational behaviors are governed by Eqs. (5.1) with $k = 1$.

6.2.1 Basic Equation for SWNTs

It is known that RBM of SWNTs is characterized by the only nonzero radial displacement, which is spatially uniform and thus independent of x and θ. In this special case, dynamic Eqs. (5.1) with $k = 1$ reduce to the following one equation for the (inward positive) radial deflection $w(t)$ of an individual SWNT.

$$\frac{w(t)}{r^2} + \frac{\rho h}{Eh}(1 - v^2)\frac{\partial^2 w(t)}{\partial t^2} = -\frac{1}{Eh}(1 - v^2) \cdot p \tag{6.1}$$

Here, p represents a net (inward positive) radial pressure exerted on the SWNT. It should be pointed out that a small term $\bar{k} = (1 - v^2) \cdot \dfrac{D}{Eh} \cdot \dfrac{1}{r^2}$ in Eqs. (5.1) with $k = 1$ has been neglected as compared to unity. Thus, for RBMs of CNTs, only two material constants are needed, i.e., in-plane stiffness Eh and mass density per unit lateral surface ρh. Bending stiffness D of SWNTs does not appear because RBM does not involve bending deformation. In addition, as will be explained later, the pressure dependence of the two material constants ($Eh, \rho h$) is negligibly small compared to the pressure dependence of the interlayer vdW interaction of MWNTs and thus is ignored in the present work. For RBM of SWNTs in the absence of net radial pressure p, Eq.(6.1) gives the RBM frequency

$$f = 230cm^{-1}(nm/2r) \tag{6.2}$$

which is in good agreement with experimental result $f = 224cm^{-1}(nm/2r)$ [92], or Mahan's 3D elasticity result $f = 227cm^{-1}(nm/2r)$ [165].

6.2.2 Basic Equations for MWNTs

In the present work, we study the RBMs of an N-wall CNT subjected to an external pressure P, as shown in Fig.6.1. Applying Eq (6.1) to each of the N tubes of an N-wall CNT leads to N coupled dynamic equations, and the total radial deflection of

tube k $(k = 1,2,\cdots,N)$ is equal to $w_k^0 + w_k(t)$, where w_k^0 is the initial equilibrium deflection due to the external pressure P prior to vibration and $w_k(t)$ is the time-dependent deflection due to RB vibration. Accordingly, the total net pressure p_k $(k = 1,2,\cdots,N)$ acting on tube k has two components: one is the initial net pressure p_k^0 due to external pressure P without vibration, which is a constant independent of time t. The other is the additional net pressure due to RB vibration, which can be calculated by using Eqs.(5.2). Thus, the total net pressures acting on tube 1, tube 2, ..., and tube N are given as follows:

$$p_1 = c_1(w_2 - w_1) + p_1^0,$$

$$p_2 = \left(c_2(w_3 - w_2) - c_1 \cdot \frac{r_1}{r_2}(w_2 - w_1) \right) + p_2^0$$

$$\cdots\cdots$$

$$p_N = \left(-c_{N-1} \cdot \frac{r_{N-1}}{r_N}(w_N - w_{N-1}) \right) + p_N^0 \tag{6.3}$$

To determine the initial equilibrium deflections $w_k^0 (k = 1,2,\cdots,N)$, the equilibrium equations for N concentric tubes of an N-wall CNT prior to vibration give:

$$\frac{w_1^0}{r_1^2} = \frac{1}{Eh}(1-v^2) \cdot p_1^0, \quad \frac{w_2^0}{r_2^2} = \frac{1}{Eh}(1-v^2) \cdot p_2^0, \quad \cdots, \quad \frac{w_N^0}{r_N^2} = \frac{1}{Eh}(1-v^2) \cdot p_N^0 \tag{6.4}$$

Recall that the total radial deflection of tube k $(k = 1,2,\cdots,N)$ in Eq.(6.1) is equal to $w_k^0 + w_k(t)$, the following N dynamic equations for RBMs of an N-wall CNT can be obtained from Eqs.(6.1), (6.3) and (6.4) as follows.

$$\left(\frac{1}{r_1^2(1-v^2)} - \frac{c_1(P)}{Eh} \right) \cdot w_1 + \frac{\rho h}{Eh} \cdot \frac{\partial^2 w_1}{\partial t^2} + \frac{c_1(P)}{Eh} \cdot w_2 = 0$$

$$\frac{c_1(P)}{Eh} \cdot \frac{r_1}{r_2} \cdot w_1 + \left(\frac{1}{r_2^2(1-v^2)} - \frac{c_2(P)}{Eh} - \frac{c_1(P)}{Eh} \cdot \frac{r_1}{r_2} \right) \cdot w_2 + \frac{\rho h}{Eh} \cdot \frac{\partial^2 w_2}{\partial t^2} + \frac{c_2(P)}{Eh} \cdot w_3 = 0$$

. . . . . .

$$\frac{c_{N-1}(P)}{Eh} \cdot \frac{r_{N-1}}{r_N} \cdot w_{N-1} + \left(\frac{1}{r_N^2(1-v^2)} - \frac{c_{N-1}(P)}{Eh} \cdot \frac{r_{N-1}}{r_N} \right) \cdot w_N + \frac{\rho h}{Eh} \cdot \frac{\partial^2 w_N}{\partial t^2} = 0$$

(6.5)

As mentioned before, the interlayer vdW interaction coefficient $c_k(P)$ $(k = 1,2,\cdots,N-1)$ between tube k and tube $k+1$ is generally a function of externally applied radial pressure P. In particular, when $P = 0$, $c_k(0) = c_0$ given by (2.6). In Chapter 6, we shall classify MWNTs into two types, i.e., large-diameter MWNTs defined by the innermost diameter larger than $2\,nm$, and small-diameter MWNTs defined by the innermost diameter smaller than $2\,nm$.

6.3 Radial Breathing Vibration without External Pressure

In order to identify the main features of RBMs of MWNTs and to demonstrate the accuracy and effectiveness of the multiple-shell model, let us first study RBMs of MWNTs in the absence of external pressure, and compare our results to available experimental data and atomistic simulations. In the absence of external pressure, $w_k^0 = 0$ $(k = 1,2,\cdots,N)$ and $c_1 = c_2 = \cdots = c_{N-1} = c_0$, where c_0 is given by Eq.(2.6), and RBMs of an $N-$ wall CNT governed by (6.5) are of the form $(k = 1,2,...,N)$

$$w_k(t) = W_k \cdot e^{-i\omega t}$$

(6.6)

where real number W_k $(k = 1,2,...,N)$ represents the radial displacement amplitude of tube k and ω denotes the angular frequency of the RBMs. Introducing (6.6), together with $c_1 = c_2 = \cdots = c_{N-1} = c_0$ into Eqs. (6.5) gives N equations:

$$
M(\omega)_{N\times N} \cdot \begin{bmatrix} W_1 \\ W_2 \\ \cdots \\ W_N \end{bmatrix} = 0 \tag{6.7}
$$

where $M(\omega)$ is an $N \times N$ coefficient matrix. The existence condition of a non-zero solution of W_k $(k = 1,2,...,N)$ is

$$
\det M = 0 \tag{6.8}
$$

This condition determines the N RBM frequencies of an N-wall CNT. Substituting each of the N frequencies into Eqs. (6.5), one can determine the associated amplitude ratios $A_1 / A_N, A_2 / A_N, \cdots, A_N / A_N$ for each frequency. Thus, for an N-wall CNT, there are a total of N RBM frequencies, corresponding to N different RB vibrational patterns. Following other authors [74], the highest-frequency RBM is referred to as mode 1, the second highest-frequency RBM as mode 2, ..., and the lowest-frequency RBM as mode N.

6.3.1 Radial Breathing Frequencies

Let us first compare RBM frequencies of MWNTs given by the present multiple-shell model with atomistic models and experiments. Following the procedure shown above, RBM frequencies of DWNTs and three-wall CNTs with the innermost radius ranging from $0.34\,nm$ to $1.36\,nm$ are calculated and shown graphically in Figs. 6.2 and 6.3, with comparison to Popov et al.'s MD simulation results [24]. It is seen that the present shell model is in excellent agreement with the MD simulations of RMBs for DWNTs and three-wall CNTs, with relative errors less than 5%.

Furthermore, to examine the c_0 value of the vdW interaction coefficient given by Eq.(2.6), we study the sensitiveness of frequencies on the vdW coefficient c. Since the interlayer interaction has little influence on the RBM frequencies of small-radius DWNTs or 3-wall CNTs (such as the innermost radius equal to $0.34nm$), the RBM frequencies are insensitive to the coefficient c for small-radius DWNTs or 3-wall CNTs. Thus, to

identify the best value of the coefficient c, we consider a DWMT and a three-wall CNT of relatively large innermost radius $1.36\,nm$ and $1.02\,nm$, respectively. Moreover, because the lowest RBM frequency of large-radius MWNTs (the innermost radius larger than $1\,nm$) is associated with an in-phase mode, which does not sensitively depend on the vdW interaction, the dependency on the vdW interaction coefficient c is shown in Fig. 6.4 only for the higher RBM frequencies of the large-radius DWNT and 3-wall CNT. It is seen from Fig.6.4 that a relative change of 20% occurs when the coefficient c_0 increases or decreases by a factor of two. Therefore, the excellent agreement given in Figs.6.2 and 6.3 between the multiple-shell model based on the coefficient c_0 (2.6) and the MD simulations [24] suggests that the coefficient c_0 given by Eq. (2.6) can be regarded as a good value at least for CNTs of larger radii (the innermost radius is not smaller than 1 nm). This offers an evidence for the accuracy of the coefficient (2.6), which was suggested in Section 2.2 and applied to buckling analysis of MWNTs in Chapters 2 to 4.

Moreover, existing studies [71, 73-74] show that only mode 1 (with the highest frequency) of small-radius MWNTs has a considerable Raman intensity and can be easily observed in Raman spectra. Thus, to further compare the present shell model with available experiments and atomistic simulation we shall focus on RB mode 1 of MWNTs of small innermost diameter varying from $0.41\,nm$ to $1.7\,nm$ and the number of layers ranging from 5 to 50. The obtained results for the mode 1 (or 2 and 3) of all these small-radius MWNTs are shown in Table 6.1, in comparison with the experimental data [71] and the atomistic simulation [74].

As seen in Table 6.1, the frequency of mode 1 given by the present shell model decreases monotonically with increasing innermost diameter of MWNTs. This frequency-diameter relation is consistent with the results obtained by the experimental data [71] and the atomistic model [74] for the same examples as shown in Table 6.1. On the other hand, the highest frequency (mode 1) given by the present shell model remains almost constant when the number of layers increases from 5 to 50. In particular, for the MWNT of innermost diameter $1.2\,nm$, both the present shell model and the atomistic model [74] show that all three highest frequencies associated with modes 1, 2 and 3 are affected only slightly by the number of layers varying from 5 to 50. In fact, as will be explained later, for small-radius MWNTs of many layers, mode 1 (or even mode 2 and mode 3) is

basically associated with the RBM of the individual innermost tube (or the second and third innermost tube), and its frequency is primarily determined by the innermost diameter and almost independent of the number of layers of MWNTs. This result explains why Raman study on RBMs of small-diameter MWNTs can be used to determine the innermost diameter of MWNTs [71, 74] regardless of the number of layers. Furthermore, it is seen in Table 6.1 that the highest RBM frequency for mode 1 (or the highest three frequencies for mode 1 to mode 3) predicted by the present shell model for MWNTs of the innermost diameter ranging from $0.41\,nm$ to $1.7\,nm$ are consistently in excellent agreement with those obtained by experiment [71] and atomistic model [74] with relative errors less than 5%.

6.3.2 Radial Breathing Modes

Next, let us further discuss N RBMs of an N-wall CNT for four illustrative examples, i.e., DWNTs (5,5)@(10, 10) and (20,20)@(25, 25), and 3-wall CNTs (5,5)@(10, 10)@(15,15) and (15,15)@(20,20)@(25,25). Here, (20,20)@(25, 25) and (15,15)@(20,20)@(25,25) are MWNTs of large innermost diameter $2.72\,nm$ and $2.04\,nm$, respectively, while (5,5)@(10, 10) and (5,5)@(10, 10)@(15,15) are MWNTs of small innermost diameter $0.68\,nm$. By following the procedure described above, the vibrational amplitude ratios of individual tubes are calculated in Table 6.2 for the four examples, and the associated RBMs are illustrated in Figs. 6.5 and 6.6, for the DWNTs and 3-wall CNTs, respectively.

It is noted in Figs. 6.5 and 6.6 that, for DWNT (20, 20)@(25, 25) and 3-wall CNT (15,15)@(20,20)@(25, 25) of larger innermost diameter $2.72\,nm$ and $2.04\,nm$, all of the constituent tubes are substantially involved in the RB vibration. In particular, the counter-phase mode, characterized by opposite vibration directions of adjacent tubes, has the highest frequency, the in-phase mode in which all tubes vibrate in the same direction has the lowest frequency, and the mixed-phase mode for the 3-wall CNT has an intermediate frequency. Based on the present shell model, this conclusion is generally true even for large-diameter MWNTs of many layers.

On the other hand, it is also seen in Figs. 6.5 and 6.6 that for DWNT (5,5)@(10, 10) and 3-wall CNT (5,5)@(10, 10)@(15,15) of very small innermost diameter $0.68\,nm$, the RBMs are characterized almost by the RBMs of individual tubes. For example, mode 1 is

basically the RBM of tube 1; mode 2 is from tube 2, and mode 3 is from tube 3. Similarly, for small-diameter MWNTs of many layers, the present shell model shows that mode 1 is always essentially the RBM of the innermost tube 1. When the innermost tube 1 is very thin (for example, with diameter < $1.2\,nm$), mode 2 and mode 3 are also essentially the RBMs of the second and third innermost tube, respectively. However, other modes (with mode number larger than 3) with lower frequencies are usually more or less associated with collective RB vibration of many tubes. In particular, similar to large-diameter MWNTs, the in-phase RBM of small-diameter MWNTs in which all tubes vibrate in the same direction is always associated with the lowest frequency.

In summary, all distinctive features of RBMs of MWNTs obtained by the present shell model agree well with the results of MD simulation [24] and atomistic model [74], and are consistent with the experiment [71]. Therefore the multiple-elastic shell model does offer a simple and effective method for RBMs of MWNTs and can be used to study more complex vibrational behavior of MWNTs for which detailed experiments or MD simulations are not yet available in the literature.

6.4 Radial Breathing Vibration under External Pressure

In this section, the pressure effect on RBMs of MWNTs will be further studied. For atomic systems like SWNT ropes and MWNTs, high external pressure results in a reduction of intertube spacing [75-76] and a compression of intratube $c - c$ distance of individual SWNTs [169]. The reduction of intertube spacing could cause significant increase in the intertube force constant or the vdW interaction coefficient c, while the compression of intratube $c - c$ distance usually leads to only slight decrease in diameter and small increase in the mass density and the in-plane elastic constants [79]. Previous studies [77-82] showed that T-mode frequency of all CNT systems and the RBM frequency of SWNT ropes increase monotonically with increasing external pressure. In particular, for the RBM of SWNT ropes of diameter not smaller than $1.3\,nm$, the pressure effect on the up-shift of RBM frequency due to increase of the intertube force constant is found to be about an order of magnitude larger than the pressure effects due to the compression of individual SWNTs [79]. Therefore it is expected that for MWNTs

(usually, of innermost diameter 1.3 *nm* or larger), the pressure effect due to the pressure-induced increase in the vdW interaction coefficients is dominant over other pressure effects due to the pressure-induced small changes in material constants (Eh and ρh) and the radius. Based on this understanding, this section focuses on the pressure effect due to the increased vdW interaction coefficients, while the in-plane stiffness Eh and the mass density ρh for individual tubes are treated as constants, independent of the external pressure. In what follows, we shall consider 8 examples, as shown in Table 6.3, namely DWNT, 5-wall, 10-wall and 20-wall CNTs of innermost diameter 1.3 *nm* and 3.0 *nm*, respectively.

6.4.1 The Pressure effect on the vdW interaction coefficient

It is seen from Eqs. (6.5) that, to calculated the pressure dependence of RBM frequencies for MWNTs, we have to determine the vdW interaction coefficients c_1, c_2 $\cdots c_{N-1}$ as functions of external pressure P.

6.4.1.1 Analysis Method

By using the continuum Lennard-Jone (L-J) model [20], the potential energies of interaction between two adjacent tubes of a MWNT can be expressed approximately in terms of the interlayer spacing s as [20]

$$U(s) = A \cdot [(\frac{0.34}{s})^4 - 0.4 \cdot (\frac{0.34}{s})^{10}]$$

(6.9)

where $U(s)$ denotes the potential energies of interaction per carbon atom (the average area of a carbon atom on the surface of SWNTs is $(0.142nm)^2$) between two concentric SWNTs; 0.34 is the value of equilibrium interlayer spacing in nanometer and A is a constant. Substitution of the data obtained in [146] for two concentric SWNTs into Eq. (6.9) yields

$$A = -61.665 mev / atom$$

(6.10)

Based on Eqs. (6.9) and (6.10), the potential energy $U(s)$ is calculated and plotted in Fig.6.7 vs. the interlayer spacing s. Furthermore, the second derivative of (6.9) gives the vdW interaction coefficient c as a function of the interlayer spacing s

$$c(s) = -\alpha \cdot s^{-6} + \beta \cdot s^{-12} \; GPa/nm \qquad (6.11)$$

where $\alpha = 0.131 GPa \cdot nm^5$ and $\beta = 4.445 \times 10^{-4} GPa \cdot nm^{11}$. The relation between c and s given by Eq. (6.11) is displayed in Fig.6.8. In particular, it is noted that the value of vdW interaction coefficient associated with $s_0 = 0.34nm$ is $c_0 = 101.59 GPa/nm$, in good agreement with the value $c_0 = 99.18 GPa/nm$ (see Eq. 2.6) used in our previous work. Consistent with the result obtained in Section 6.3.1 for the accuracy of the value c_0 (2.6), this calculation offers a further confirmation that c_0 given by Eq.(2.6) is accurate for characterization of the interlayer vdW interaction in MWNTs

Next let us use Eq.(6.11) to determine the vdW coefficient c_k $(k = 1,2,...,N-1)$ of an N-wall CNT under an external pressure P. For tube k $(k = 1,2,...,N)$, the pre-vibration uniform circumferential membrane force F_k is related to the pre-vibration net (inward) pressure p_k^o by $F_k = -p_k^o \cdot r_k$. This relation combined with the radial equilibrium condition of a thin cylindrical shell [141] gives

$$p_k^o = \frac{Eh}{1-v^2} \cdot \frac{\Delta r_k}{r_k^2} \qquad (6.12)$$

where $\Delta r_k (= w_k^o)$ is the pressure-induced uniform radial displacement or reduction of r_k prior to vibration. On the other hand, the multiple-elastic shell model [127-129] gives

$$p_k^o = p_{k(k+1)}^o - \frac{r_{k-1}}{r_k} \cdot p_{(k-1)k}^o \qquad (6.13)$$

where $p^o_{k(k+1)}$ represents the pressure acting on tube k due to tube $k+1$ prior to vibration. In particular, p^0_{01} is the applied internal pressure, which is zero in the present analysis, and $p^0_{N(N+1)}$ is the applied external pressure P. Based on Eq. (6.9)

$$p^0_{k(k+1)} = \frac{dU(s)}{ds}\bigg|_{s=s_k} \tag{6.14}$$

where s_k ($k=1,2,...,N-1$) denotes the initial or pre-vibration interlayer spacing between tube k and tube $k+1$. In the presence of an external pressure, we have

$$s_k = 0.34nm - (\Delta r_{k+1} - \Delta r_k) \tag{6.15}$$

Using Eqs. (6.9), (6.12), (6.14) and (6.15) to eliminate all p^o_k, $p^o_{k(k+1)}$ and s_k in Eq. (6.13) gives N equations to determine the N unknowns $\Delta r_1, \Delta r_2,...,$ and Δr_{N-1}. Substituting $\Delta r_1, \Delta r_2,...,$ and Δr_N into Eq. (6.15) and then (6.11), one can calculate ($N-1$) vdW interaction coefficients, $c_1, c_2,...,$ and c_{N-1} for any given external pressure P. In this section, the pressure-induced relative increase of vdW interaction coefficient $\frac{\Delta c_k}{c_0}$

($\Delta c_k = c_k - c_0$, $k = 1,2,...,N-1$) and the relative reduction of radius $\frac{\Delta r_k}{r_k}$ ($k=1,2,..,N$) are calculated for the eight examples in Table 6.3, for an external pressure increasing from $1\,GPa$ to $5\,GPa$.

6.4.1.2 Results and Discussion

The relative increases of the vdW interaction coefficients are shown in Figs.6.9 and 6.10 for the large-diameter MWNTs, examples 1-4 and the small-diameter MWNTs, examples 5-8 (in Table 6.3), respectively. It is evident in these two figures that the relative increase of the vdW coefficient decreases from the outermost tube to the innermost tube and is most significant only for the outermost few tubes. For 20-wall CNTs, examples 4 and 8, when the applied pressure increases from $1\,GPa$ to $5\,GPa$, c_{19},

the vdW interaction coefficient between the tube 19 and the outermost tube 20, is increased by a factor of 1.4 to 3, while c_1, c_2, c_3 and c_4 remain almost unchanged. Analogous results are also obtained for 5-wall CNTs, examples 2 and 6, and 10-wall CNTs, examples 3 and 7. Therefore, it is concluded that the high external pressure can considerably increase the vdW interaction coefficients between the outermost few tubes but has little effect on those between the innermost few tubes. On the other hand, when the number of layers decreases, the vdW interaction coefficients between the outermost few tubes become less sensitive to the external pressure. For example, in Figs.6.9 and 6.10, it is seen that, regardless of the innermost diameter and the applied external pressure, the relative increase of the vdW interaction coefficient between the outermost two tubes decreases from about 40% ~ 200% to 20% ~ 160% when the number of layers drops from 20, to 10 and to 5. In addition, comparison between Figs.6.9 and 6.10 shows that the pressure effects on the vdW interaction coefficients for the large-diameter MWNTs, examples 1-4 (see Fig.6.9), are more significant than those for the small-diameter MWNTs, example 5-8 (see.Fig.6.10). The qualitatively similar results can be obtained for the relative reduction of the radii of the large-diameter MWNTs, examples 1-4 and the small-diameter MWNTs, examples 5-8, as shown in Figs.6.11 and 6.12, respectively. Because the vdW interaction coefficient is very sensitive to even a small change in the interlayer spacing, the relative changes in the vdW coefficients are usually about 2 orders of magnitudes larger than the relative changes in the radii.

6.4.2 The Pressure Effect on Radial Breathing Modes

In Section 6.4.1, the distribution of the vdW interaction coefficients of a MWNT is determined as a function of an external pressure. Then, in a similar way as shown in Section 6.3, we are able to calculate RBM frequencies of a MWNT under the external pressure. Here we shall consider 6 examples in Table 6.3: the large-diameter MWNTs, examples 1-3 and the small-diameter MWNTs, examples 5-7. The pressure dependences of RBM frequencies obtained for all these examples are plotted in Figs. 6.13 to 6.17, respectively. As expected, all these figures show that RBM frequencies of a MWNT increase almost linearly with increasing external pressure up to $5\,GPa$. Thus, the pressure derivative df_{RBM}/dP can be approximately calculated over the pressure range. This

offers a simple method to evaluate the pressure effect on RBMs. Here, it is noted that for a MWNT, the pressure dependence of RBM frequency varies for different RBMs, and also changes with the innermost diameter of the MWNT. The pressure derivatives for all RBMs of the above six examples are shown in Fig. 6.18.

6.4.2.1 Large-diameter MWNTs

Here, let us first examine the pressure effect on RBMs of the large-diameter MWNTs, examples 1-3 (in Table 6.3). For example, in example 1 in which mode 1 is counter-phase and mode 2 is in-phase, as seen in Fig. 6.18 (a), the pressure derivative for mode 1 $(5.77 cm^{-1} / GPa)$ is more than an order of magnitude larger than the pressure derivative for mode 2 $(0.11 cm^{-1} / GPa)$, although both modes are associated with the same vdW interaction coefficient. This provides clear evidence that the external pressure-induced increase in the vdW interaction coefficient has a pronounced effect only on counter-phase modes, but not on in-phase modes. Further, it is seen in Figs. 6.18 (b) and (c) that for examples 2 and 3, the largest pressure derivatives, $7.66 cm^{-1} / GPa$ and $9.76 cm^{-1} / GPa$ respectively, are obtained for mode 1 of highest frequency. Then the pressure derivative decreases almost monotonically with the mode number and reaches the minimum for the mode of lowest frequency, i.e., $0.34 cm^{-1} / GPa$ for mode 5 of example 2 and $0.24 cm^{-1} / GPa$ for mode 10 of example 3, respectively. As mentioned before, for a large-diameter $N-$wall CNT, the RBMs are essentially collective vibrations of all concentric tubes, among which mode 1 is always a completely counter-phase RB vibration (that is, any two adjacent tubes vibrate in opposite direction). From mode 2 to mode $N-1$, the RB vibration is mixed-phase in the sense that some adjacent tubes vibrate counter-phase and other adjacent tubes vibrate in-phase. A completely in-phase RB vibration (that is, all tubes vibrate in the same direction) is achieved for mode N of the lowest frequency. Indeed, the pressure effect on RBMs of large-diameter MWNTs increases monotonically from lower-frequency to higher-frequency modes, and the maximum pressure derivative is always associated with the completely counter-phase mode 1 of highest frequency.

6.4.2.2 Small-diameter MWNTs

Next let us study the pressure effect on RBMs of the small-diameter MWNTs, examples 5-7 (in Table 6.3). First, it is shown in Fig.6.18 (a) that the pressure effect on mode 1 of example 5 is very small as compared to that for mode 1 of example 1 (large-diameter). The small pressure effect for mode 1 of example 5 can be explained by the fact that mode 1 of the small-diameter DWNT is basically the RBM of the individual tube 1 (see Fig.6-5), which is not significantly affected by an external pressure. In this case, the vdW interaction between adjacent tubes has much less effect on RBM frequency than it does in large-diameter DWNTs. Thus intensifying the vdW interaction by applying an external pressure cannot considerably affect mode 1 of a small-diameter DWNT as efficiently as it does for mode 1 of a large-diameter DWNT. Moreover, it is seen in Figs.6.18 (b) and (c) that for examples 6 and 7, very small pressure effect is obtained not only for mode 1 but also for the lowest-frequency mode (mode 5 and mode 10, respectively), with the pressure derivatives between $0.01\,cm^{-1}\,/\,GPa$ and $0.51\,cm^{-1}\,/\,GPa$. On the other hand, the pressure derivatives of some intermediate-frequency modes can be a few times or more than an order of magnitude larger. For example, the maximum pressure derivative $4.13\,cm^{-1}\,/\,GPa$ or $8.25\,cm^{-1}\,/\,GPa$ is attained for mode 3 of example 6 or 7, respectively. In fact, as pointed out before, for a small-diameter MWNT, mode 1 is almost the RBM of the individual innermost tube 1. Therefore, mode 1 of the individual innermost tube 1 is affected only by the vdW interaction coefficient c_1 which, as shown before, is not significantly affected by the external pressure. In addition, as shown for example 5, this RBM of the individual innermost tube of a small-diameter MWNT is not sensitive to even significant change in the vdW interaction coefficient c_1. This explains why very small pressure effect occurs for mode 1 of examples 6 and 7. On the other hand, because the lowest-frequency mode, such as mode 5 of example 6 (5-wall) or mode 10 of example 7 (10-wall), is completely in-phase RBM without significant change in the interlayer spacing, it will not be significantly affected by the pressure-induced increase in the vdW interaction coefficients. Therefore, for small-diameter MWNTs, the most significant pressure effect occurs only for a few intermediate-frequency modes in which many outermost tubes are involved substantially and vibrate in opposite directions (counter-phase).

Finally, it is seen in Fig.6.18 that when the number of layers increases from 2 to 5 or to 10, the maximum pressure derivative for a MWNT of innermost diameter $1.3\,nm$ increases from $1.46\,cm^{-1}/GPa$ to $4.13\ cm^{-1}/GPa$ or to $8.25\,cm^{-1}/GPa$, while the maximum pressure derivative predicted for a $3\,nm$ - innermost diameter MWNT of the same number of layers is $5.77\,cm^{-1}/GPa$, $7.66\,cm^{-1}/GPa$ and $9.76\,cm^{-1}/GPa$, respectively. This indicates that the pressure effect is usually more significant for the RBMs of large-diameter MWNTs than for small-diameter MWNTs. In addition, for MWNTs of the same innermost diameter, the pressure effect increases with the increasing number of layers for both large-diameter and small-diameter MWNTs.
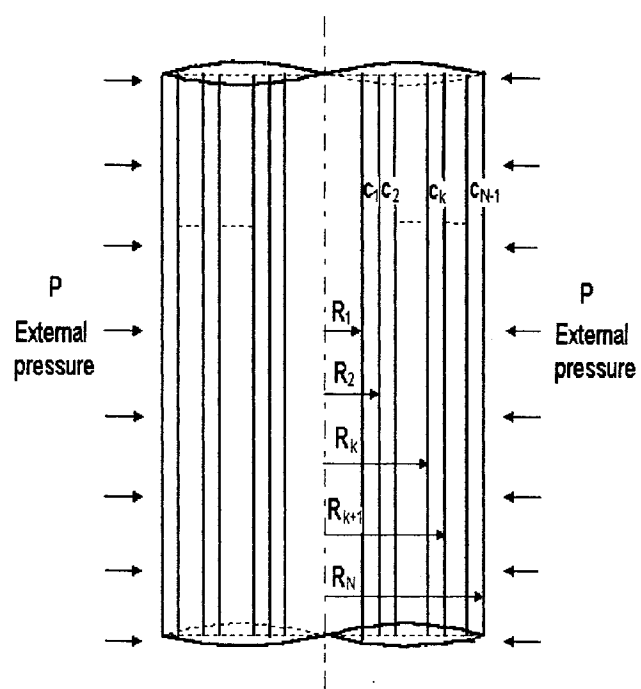
Fig.6.1 RBM vibration of an N-wall CNT subjected to an external pressure P.
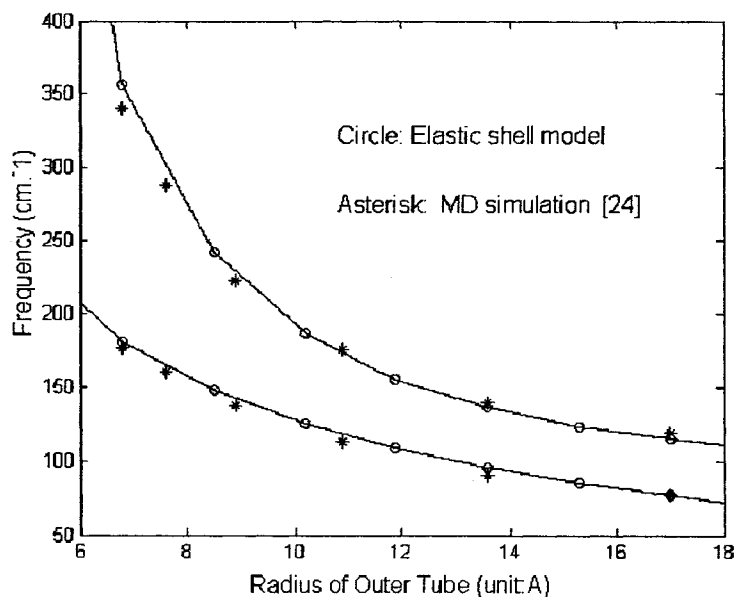
Fig.6.2 RBM frequencies predicted by the multiple-shell model and MD

simulation [24] for DWNTs of various outer radii.
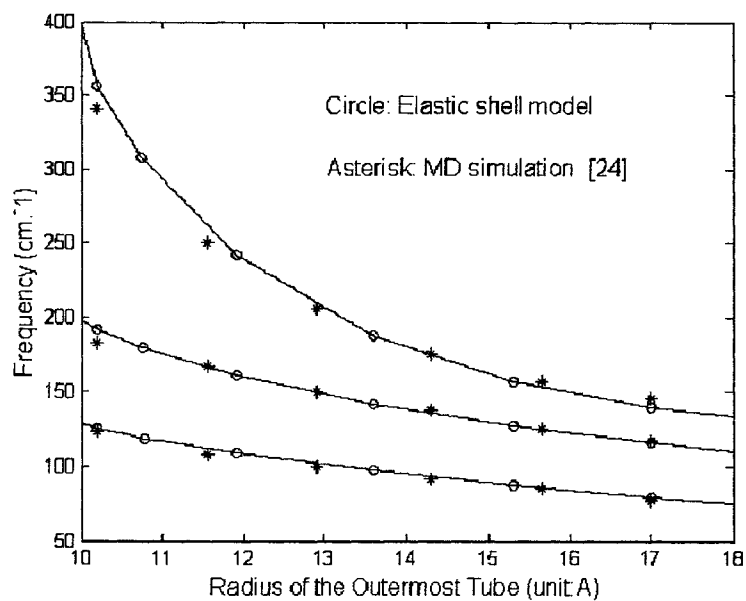
Fig.6.3 RBM frequencies predicted by the multiple-shell model and MD

simulation [24] for three-wall CNTs of various outermost radii.
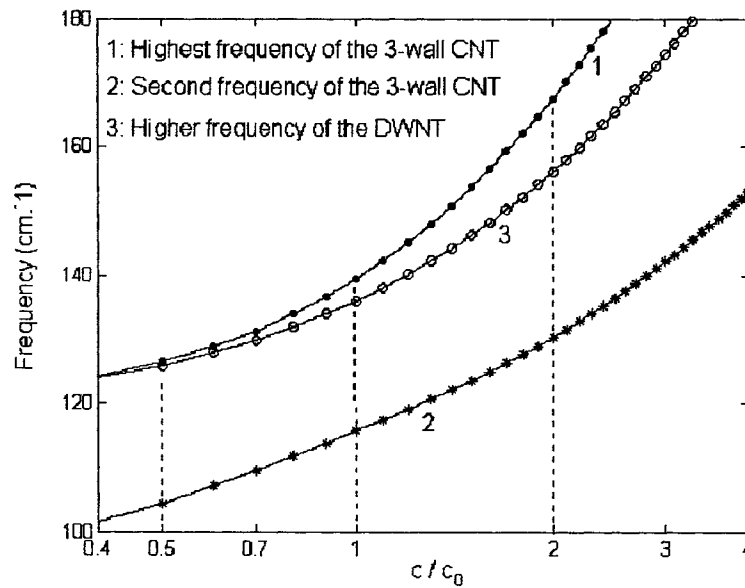
Fig. 6.4 Dependence of the RBM frequencies of a DWNT of inner radius
$1.36nm$ and a three-wall CNT of the innermost radius $1.02nm$ on
the vdW interaction coefficient.
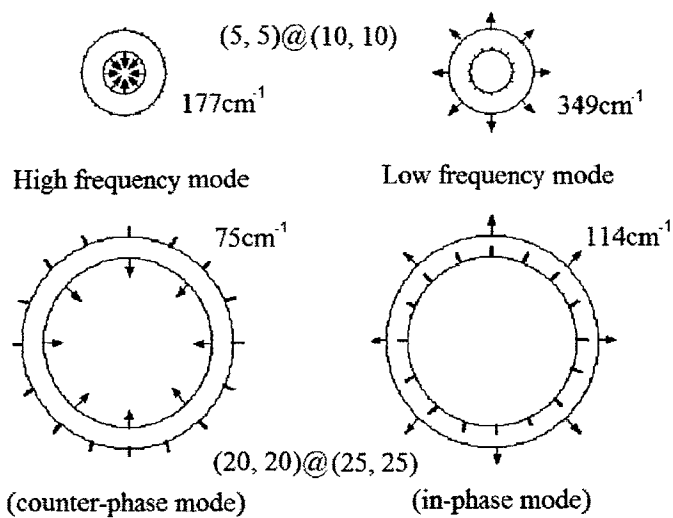
Fig.6.5 The RBMs of DWNTs (5,5)@(10, 10) and (20,20)@(25, 25) with amplitude ratios shown in Table 6.2.
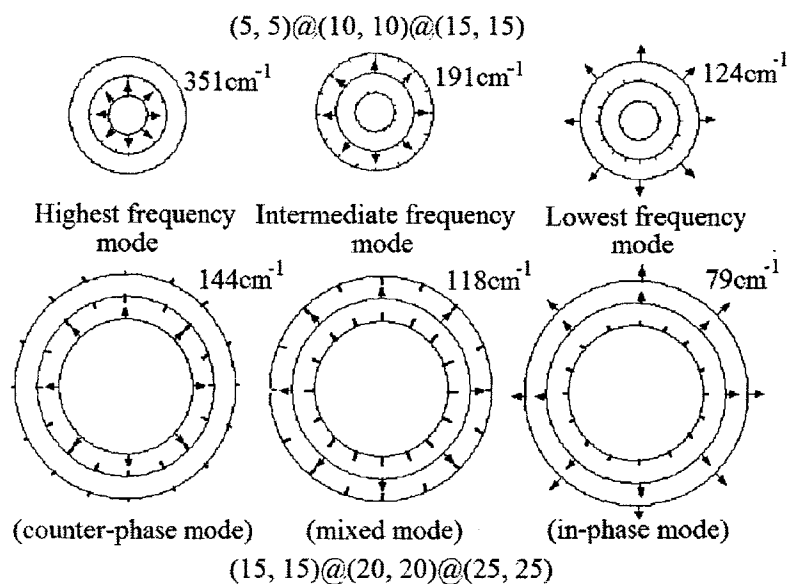
Fig.6.6 The RBMs of three-wall CNTs (5,5)@(10, 10)@(15,15) and (15,15)@(20,20)@(25,25) with amplitude ratios shown in Table 6.2.
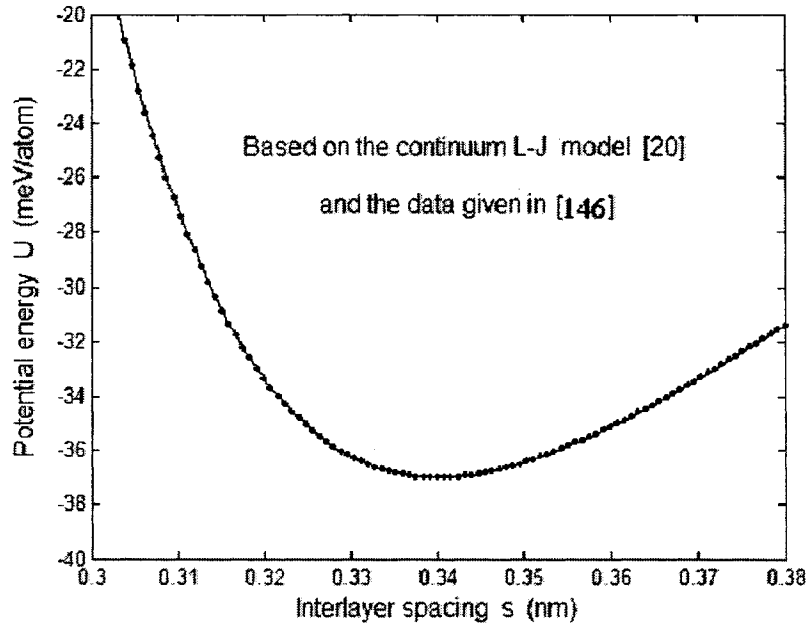
Fig.6.7 Potential energy of the vdW interaction between two concentric
SWNTs as a function of interlayer spacing.
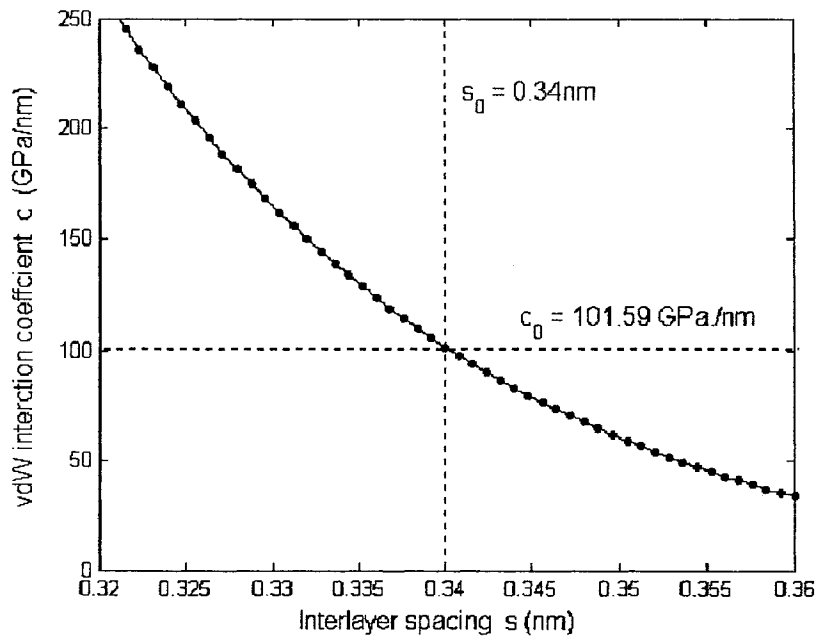
Fig. 6.8 The vdW interaction coefficient between two concentric SWNTs
as a function of interlayer spacing.
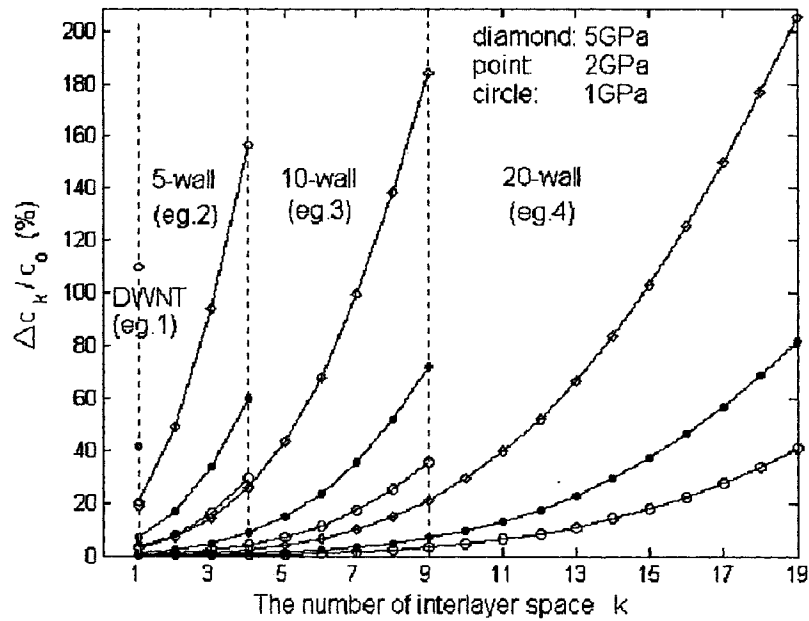
Fig.6.9 The relative increase of the vdW coefficient as a function of external
pressure for large-diameter MWNTs (examples 1-4 in Table 6.3).
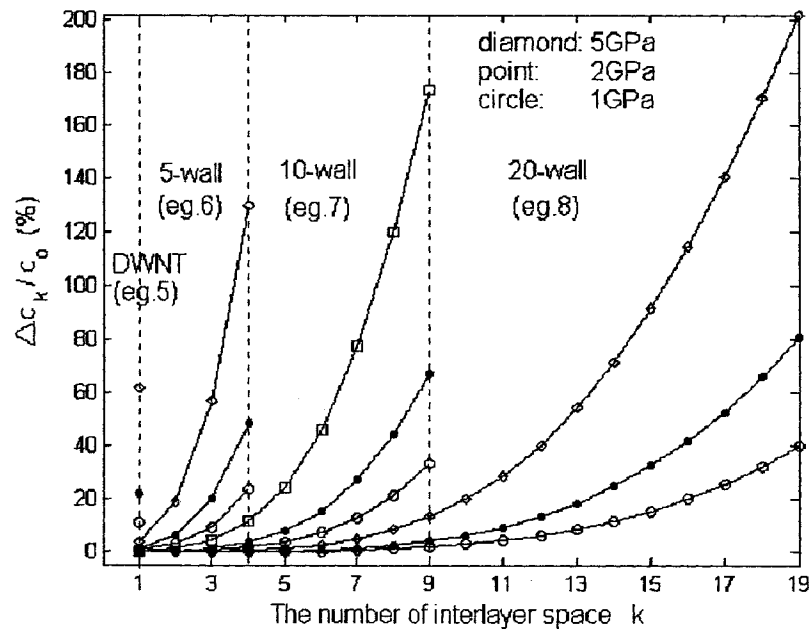
Fig.6.10 The relative increase of the vdW coefficient as a function of external
pressure for small-diameter MWNTs (examples 5-8 in Table 6.3).
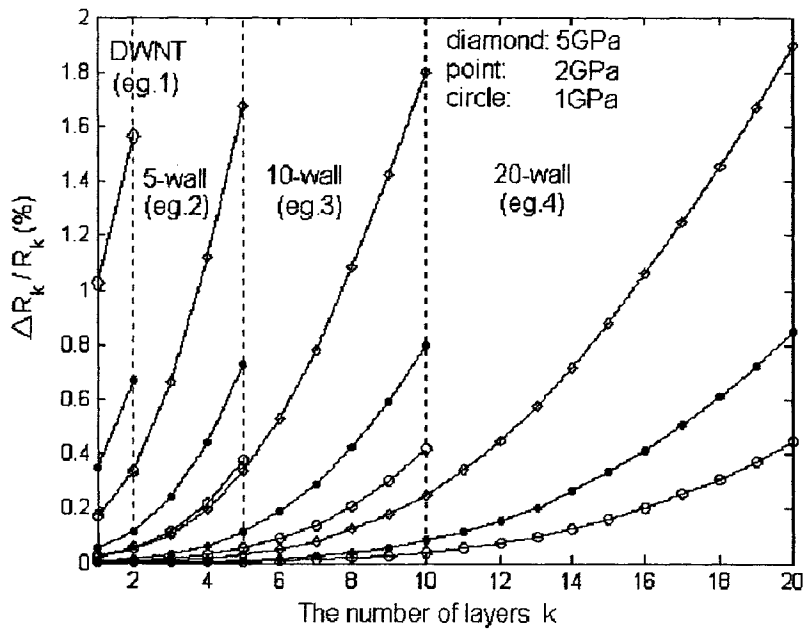
Fig.6.11 The relative reduction of radius as a function of external pressure

for large-diameter MWNTs (examples 1-4 in Table 6.3).
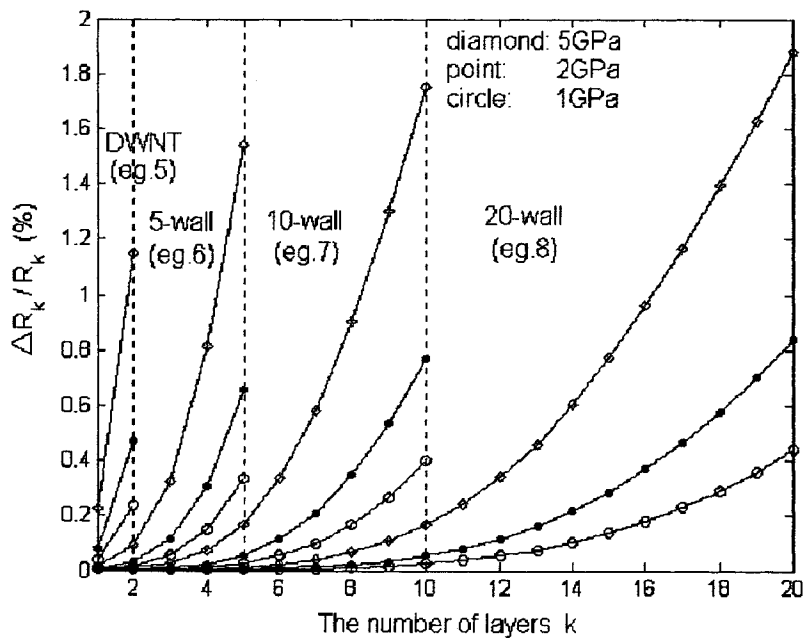
Fig.6.12 The relative reduction of radius as a function of external pressure

for small-diameter MWNTs (examples 5-8 in Table 6.3)..
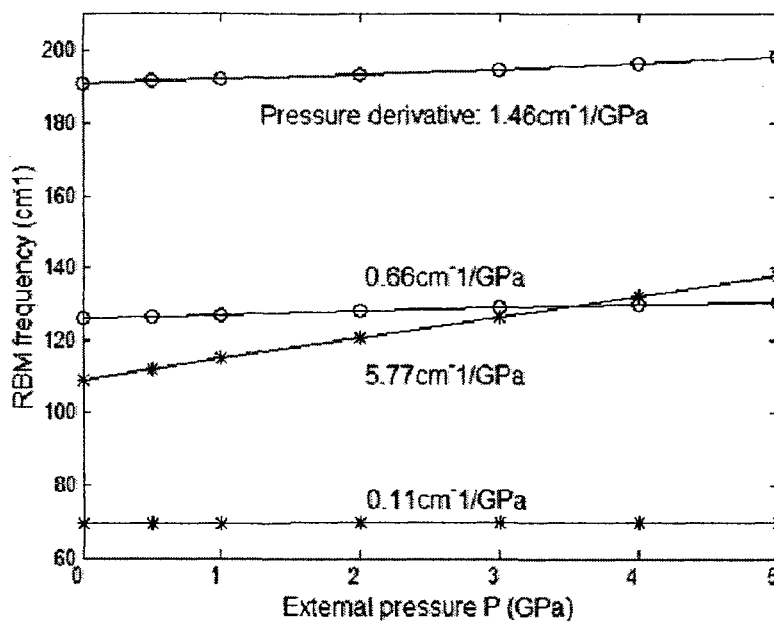
Fig.6.13 Pressure dependence of RBM frequencies for example 1(asterisk, large-diameter) and example 5 (circle, small-diameter) in Table 6.3.
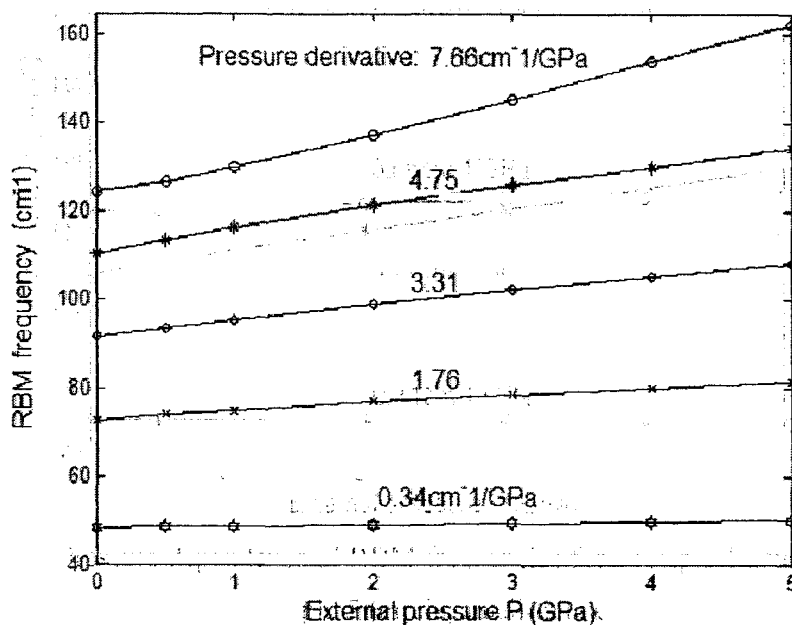
Fig. 6.14 Pressure dependence of RBM frequencies for example 2 (large-diameter) in Table 6.3.
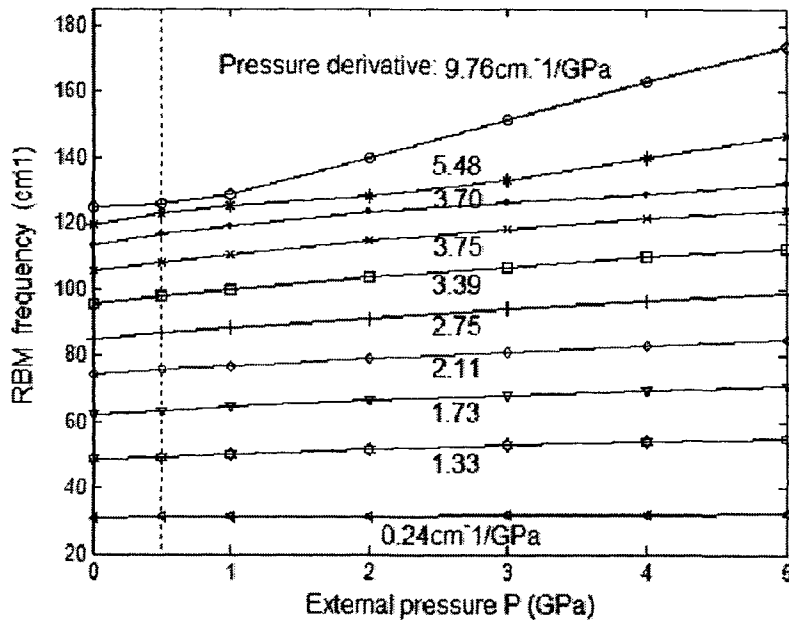
Fig. 6.15 Pressure dependence of RBM frequencies for example 3 (large-diameter) in Table 6.3.
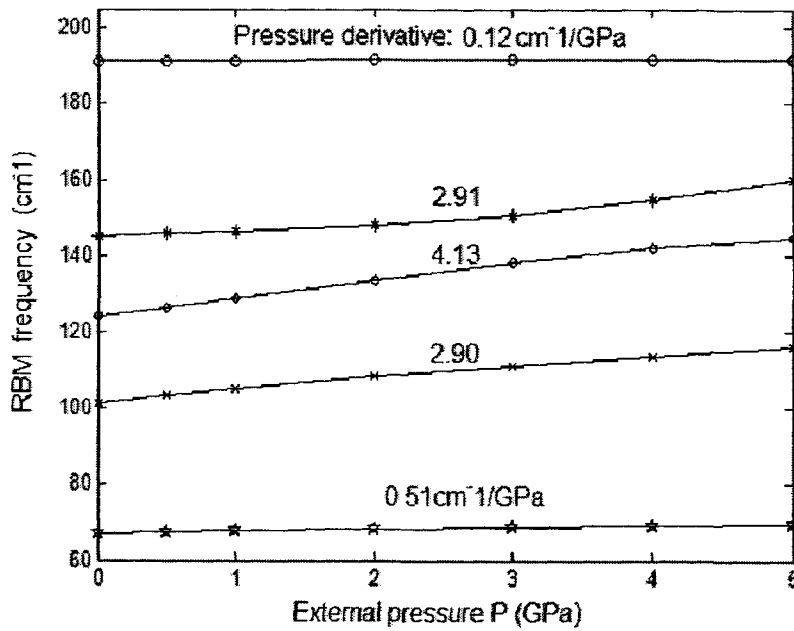
Fig.6.16 Pressure dependence of RBM frequencies for example 6 (small-diameter) in Table 6.3.
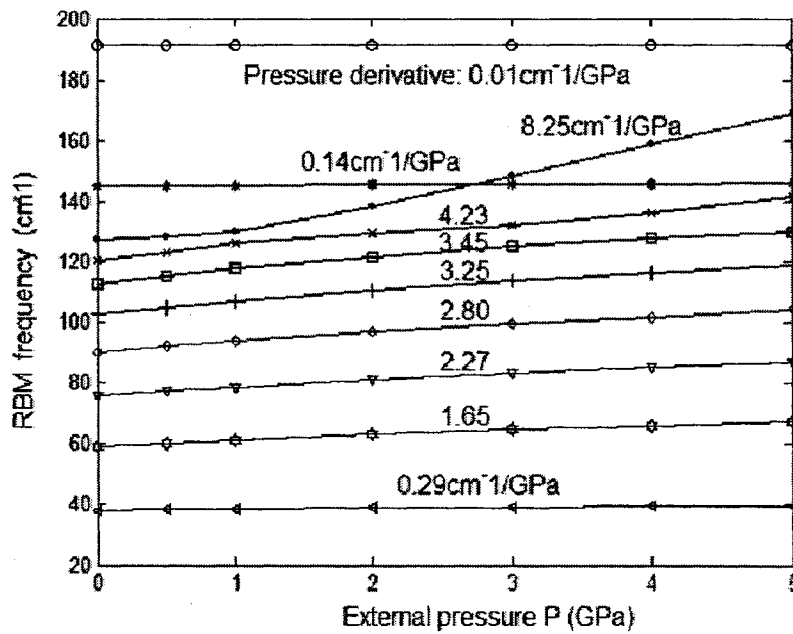
Fig.6.17 Pressure dependence of RBM frequencies for example 7 (small-
diameter) in Table 6.3.
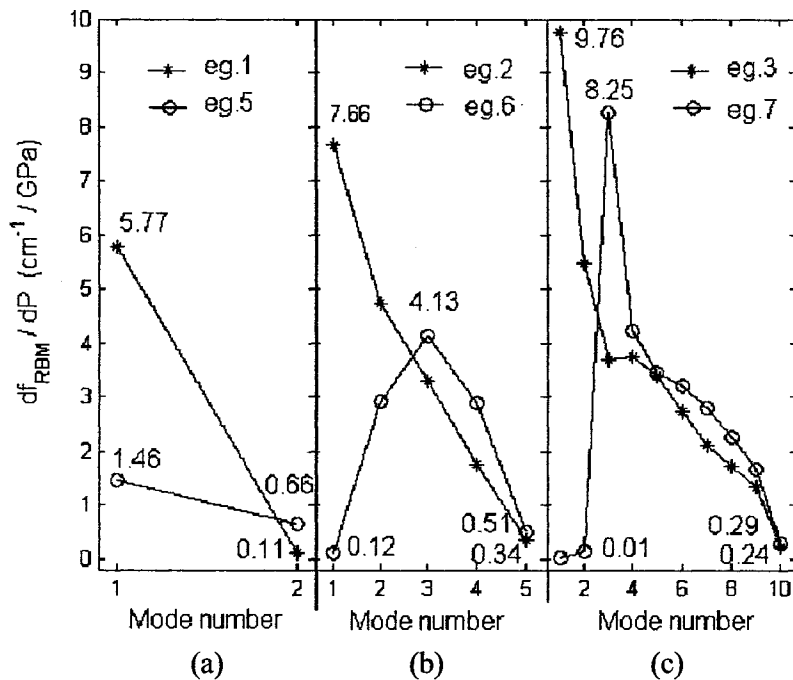
Fig.6.18 Pressure derivatives df_{RBM}/dP of RBM frequencies for (a) DWNTs, examples 1
and 5, (b) five-wall CNTs, examples 2 and 6 and (c) ten-wall CNTs, examples 3 and
7 in Table 6.3.

Table 6.1 The RBM frequencies $f_{RBM}(= \omega/2\pi v$, v is the speed of light) predicted by the multiple-shell model for N-wall CNTs of small innermost diameter d_1 in comparison with the results of experiment [71] and atomistic model [74].

d_1	Mode	Experiment [71] or Atomistic model [74]		The multiple- elastic shell model	
		N	$f_{RBM}(cm^{-1})$	N	$f_{RBM}(cm^{-1})$
0.41	1	~15	570 [71]	5-50	576
0.60	1	~15	392 [71]	5-50	395
0.84	1	~15	279 [71]	5-50	286
1.08	1	~15	217 [71]	5-50	226
1.20	1	5-50	~199 [74]	5-50	205
	2		~146 [74]		150
	3		~125 [74]		126-129
1.36	1	20	180 [74]	5-50	184
1.54	1	20	162 [74]	5-50	166
1.70	1	20	149 [74]	5-50	154

Table 6.2 Amplitude ratios predicted by the multiple-shell model for the RBMs of four examples. Here A_k ($k = 1,2,\cdots,N$) is the amplitude of tube k of MWNTs.

MWNTs	Highest frequency	Intermediate frequency	Lowest frequency
(5,5)@(10, 10)	$A_1/A_2 = -51$		$A_2/A_1 = 25$
(20,20)@(25, 25)	$A_1/A_2 = -1.9$		$A_2/A_1 = 1.4$
(5,5)@(10, 10)@(15,15)	$A_1/A_2 = -44$	$A_2/A_1 = 21$	$A_3/A_1 = 138$
	$A_1/A_3 = 1.8\times10^3$	$A_2/A_3 = -7.6$	$A_3/A_1 = 5.1$
(15,15)@(20, 20)@(25,25)	$A_1/A_2 = -1.6$	$A_2/A_1 = 1.0$	$A_3/A_1 = 5.5$
	$A_1/A_3 = 6.3$	$A_2/A_3 = -1.9$	$A_3/A_2 = 1.9$

Table 6.3 Geometric data for eight examples of MWNTs used in Section 6.4.

Example	1	2	3	4	5	6	7	8
Number of layers	2	5	10	20	2	5	10	20
The innermost diameter (nm)	3.0				1.3			

Chapter 7

General Features of Free Vibration of MWNTs

7.1 Introduction

Free vibration of CNTs, as cantilever beams, has been clearly observed in TEM studies [39, 42, 52]. In particular, due to the high stiffness and strength, low density, and large aspect ratio, cantilevered or bridged CNTs [172-173] are expected to be a good candidate for nanomechanical resonators, a key component in signal processing systems [174]. On the other hand, as reviewed in Chapter 1, CNTs also exhibit strong potential to be structure elements, e.g., micro-shells and beams in nanomechanical and nanoelectronic devices, whose performance could be significantly affected by dynamic behaviors of CNTs. For example, the vibration of CNTs as building blocks in nanostructure could threaten structural integrity, impair performance and introduce positional uncertainty. Thus successful nano-scale engineering will depend crucially on the ability to reliably predict vibrational properties of CNTs. All these ideas provide the impetus for investigation on general vibrational behavior of individual CNTs, as nano-scale shells [124-126] or beams [106, 162].

Previously, free vibration of SWNTs, modeled as beams [162] or cylindrical shells [124-126, 165-166] has been studied extensively. The general vibrational spectra are calculated and associated vibrational modes, i.e., L (longitudinal) modes, T (tosional) modes and R (radial) modes as well as beam-like bending (B) modes are identified for SWNTs. Furthermore, the multiple-beam model [106] and multiple-shell model [127-129] developed for MWNTs have also been effectively used for the unique non-coaxial B-modes [106] or RBMs [132, 134] of MWNTs in good agreement with atomistic simulations and experiment. These results demonstrate that the continuum models, especially the multiple-shell model offer a reliable and cost-effective method for vibrational analysis of CNTs.

122

In Chapter 7, the multiple-shell model [127-129] will be further applied for general vibrational behavior of MWNTs, which still remains challenging for nano-scale experiments and atomistic simulations. The primary goal of the present work is to identify the unique features of MWNTs arising from the multilayer-structure with an emphasis on the role of the interlayer vdW interaction in free vibration of MWNTs. It is found that torsional and longitudinal modes of MWNTs are essentially motions of individual tubes, while the radial modes of MWNTs of large innermost radius (e.g., $5\,nm$) involve all the nested tubes. In other words, the interlayer vdW interaction exerts the most significant effect on radial vibration of large-radius MWNTs (eg. of the innermost radius $5\,nm$) but has little influence on torsional and longitudinal modes. For radial modes of small-radius MWNTs (e.g., of the innermost radius $0.65\,nm$) the effect of the vdW interaction is noticeable only when the circumferential wave number n is nonzero but relatively small (e.g., $2 < n < 7$).

7.2 Free Vibration Frequency and Associated Modes

In this section, our goal is to identify the distinct vibrational behaviors of individual MWNTs. To this end, four examples of MWNTs given in Table 7.1 are considered, among which examples 1 and 2 are large-radius MWNTs of the innermost radius $5\,nm$ and examples 3 and 4 are small-radius MWNTs of the innermost radius $0.65\,nm$. To be specific, we consider the cases when $L/(r_N \cdot m) = 10$, 5 or 1, respectively.

7.2.1 Large-radius MWNTs (the innermost radius $5\,nm$)

First let us consider large-radius MWNTs of the innermost radius $5\,nm$. For illustration, we start with the DWNT, example 1 (see Table 7.1). The frequencies are calculated in Fig.7.1(a) for the DWNT with $n = 0$ to 20 and $L/(r_2 \cdot m) = 10$. As seen from Fig.7.1(a), there exist three groups of curves, such as $T_2 \& T_1$, $L_2 \& L_1$, and $R_2 \& R_1$, indicating six frequencies of the DWNT for each combination of n and $L/(r_2 \cdot m)$. To identify the vibration modes of example 1, the amplitude ratios associated with each frequency are calculated in Figs. 7.2, 7.3 and 7.4, respectively.

It is noted in Fig.7.2(a) that when $n \geq 5$, the circumferential amplitude V_1 of the inner tube 1 is 10 to 1000 times larger than any other amplitude of the two nested tubes. Thus, for $n \geq 5$ frequency T_2 is associated with the torsional (T) vibration primarily of the inner tube 1. Correspondingly, Fig.7.2(b) indicates that when $n \geq 5$ frequency T_1 results in the T – vibration primarily of the outer tube 2. Furthermore, it is seen from Fig.7.3 that when $n > 1$ the longitudinal amplitude U_1 of the inner tube 1 (see Fig.7.3(a)) or U_2 of the outer tube 2 (see Fig.7.3(b)) is predominant, which implies that frequency L_2 and L_1 basically correspond to the longitudinal (L) vibrations of tube 1 and 2, respectively. On the other hand, as seen from the inset in Fig.7.2(a) for frequency R_2 at $n < 3$ and the inset in Fig.7.4(a) for frequency R_2 at $n > 5$, the radial amplitude ratio W_1 / W_2 is almost equal to minus one while other amplitude ratios $(U_1, V_1, U_2$ and $V_2)/W_2$ are close to zero. These results show that frequency R_2 leads to a counter-phase radial ($R-$) mode in which the two tubes of the DWNT vibrate in opposite directions (see Fig.7.5(a)). At the same time, based on the results in Fig.7.4(b) frequency R_1 are essentially associated with an in-phase R – mode with the two individual tubes moving in the same direction (see Fig.7.5(b)). In addition to the modes that are predominant in one direction, the DWNT exhibits more complicated modes with comparable displacements in different directions. Particularly, when $n = 1$ Fig.7.4(b) gives $W_1 = V_1 = W_2 = V_2$, leading to a $B-$ mode with only a rigid body motion of the cross-section (see Fig.7.5(c)).

Next, let us further consider the 5-wall CNT, example 2 (see Table 7.1). Here, to examine the role of $L/(r_5 \cdot m)$ the frequencies and the associated modes of example 2 are calculated as functions of n for $L/(r_5 \cdot m) = 10$, 5 and 1, respectively. When $L/(r_5 \cdot m) = 10$ Fig. 7.6(a) shows that frequencies T_5 to T_1 at $n > 5$ and L_5 to L_1 at $n > 1$ essentially correspond to T – and L – vibration of individual tubes, while frequencies R_5 to R_1 result in five R – vibrations involving all the five individual tubes, among which an in-phase mode is associated with the lowest frequency R_1; a counter-phase mode is associated with the highest frequency R_5, and the modes with intermediate frequencies

R_2 to R_4 are of mixed phases. For $L/(r_5 \cdot m) = 5$ and 1 the results are presented in Fig.7.7(a) and (b), respectively and it turns out that the features of $T-$, $L-$ and $R-$modes of the 5-wall CNT remain essentially unchanged when $L/(r_5 \cdot m)$ drops from 10 to 5 and to 1.

It follows from the above results that for the large-radius MWNTs of the innermost radius $5\,nm$, $T-$ and $L-$modes are characterized by vibration of individual tubes. The associated frequencies of $T-$ and $L-$modes, shown in Figs.7.1(a), 7.6(a) and 7.7 increase considerably with increasing n, and decrease gradually from the innermost to the outermost tube with increasing radius. On the contrary, R-modes are essentially collective vibrations of all the nested tubes. Thus, the R-mode frequencies depend mainly on the corresponding $R-$vibration patterns, but, as shown in Figs. 7.1(a), 7.6(a) and 7.7, are insensitive to n and $L/(r_N \cdot m)$ ($N = 2$ or 5). Additionally, it is also noticed in Figs. 7.1(a), 7.6(a) and 7.7 that when n is small (say $n < 3$) the highest few frequencies correspond to $R-$mode vibrations. However, for sufficiently large n (say $n > 5$), $R-$modes show the lowest frequencies, $T-$modes exhibit the highest frequencies, while $L-$modes are associated with intermediate ones.

7.2.2 Small-radius MWNTs (the innermost radius 0.65 nm)

Next, let us deal with small-radius MWNTs of the innermost radius $0.65\,nm$, i.e., example 3 (DWNT) and example 4 (5-wall CNT) in Table 7.1. The frequencies and the associated amplitude ratios are calculated for the two examples with $n = 0$ to 20 and $L/(r_N \cdot m) = 10$ or 5 or 1 ($N = 2$ or 5). For example 3 with $L/(r_2 \cdot m) = 10$, the frequencies are shown in Fig.7.8(a) and the amplitude ratios associated with frequencies T_2 & T_1, L_2 & L_1 and R_2 & R_1 in Fig. 7.8(a) are displayed in Figs. 7.9, 7.10 and 7.11, respectively. Similar to the large-radius MWNTs, the predominant amplitude ratio V_1/W_2 in Fig.7.9(a), V_2/W_2 in Fig.7.9(b), U_1/W_2 in Fig.7.10(a) and U_2/W_2 in Fig.7.10(b) indicate that the corresponding frequencies T_2 & T_1 and L_2 & L_1 in Fig.7.8(a) are basically associated with $T-$ and $L-$ vibrations of tube 1 or tube 2. On the other hand, Fig.7.11 shows that frequencies R_2 and R_1 in Fig.7.8(a) are primarily associated with $R-$modes

of the DWNT. For $3 < n < 7$ the two R – vibrations are generally collective motions of both tubes, which are similar to the modes shown in Figs.7.5(a) and 7.5(b) for example 1, while for $n > 7$ the R – vibration of tube 1 or tube 2 is predominant. Additionally, Fig.7.11 indicates that when $n = 1$, $W_1 \approx V_1 \approx -W_2 \approx -V_2$ (see the inset in Fig.7.11(a)) or $W_1 = V_1 = W_2 = V_2$ (see Fig.7.11(b)), showing noncoaxial and coaxial (bending) B – modes for the small-radius DWNT. To demonstrate the vibrating cross-sections of MWNTs the R – modes characterized by motion of inner tube or outer tube, and the noncoaxial and coaxial B – modes are illustrated in Figs.7.12 (a) to (d), respectively.

For the 5-wall CNT, example 4, analogous results are shown in Fig.7.13(a) with $L/(r_5 \cdot m) = 10$, Fig.7.14(a) with $L/(r_5 \cdot m) = 5$ and Fig.7.14(b) with $L/(r_5 \cdot m) = 1$. It is found that just like the large-radius MWNTs the small-radius MWNTs also exhibit T – and L – vibrations primarily of individual tubes. For small but nonzero n (say $3 < n < 7$) the R – modes of the small-radius MWNTs are essentially collective motions of all the nested tubes. However, when $n = 0$ or sufficiently large (say $n > 7$ or 8) R – motions of individual tubes dominate. Thus, as shown in Figs.7.8 (a), 7.13(a) and 7.14 for the small-radius MWNTs, the frequencies associated with all three modes generally increase with increasing n but decrease with increasing radius of the individual tube. When n is relatively small (say $2 < n < 14$ for example 3 or $2 < n < 8$ for example 4), all the R – modes are associated with the lowest few frequencies. However, when n becomes large (say $n \geq 14$ for example 3 or $n \geq 8$ for example 4) the highest R -mode frequency could be even higher than L – or T – frequencies.

7.3 The Effect of the Interlayer vdW Interaction

To understand the unique vibrational behavior of MWNTs, let us further examine the role of the interlayer vdW interaction in free vibrations of MWNTs. In doing this, the vibrational behaviors of MWNTs will be compared to those of individual nested tubes. Assuming that $c = 0$ in Eqs.(5.1) and following the procedure shown in Chapter 5, one can calculate vibration frequencies for all individual nested tubes of a MWNT without the interlayer vdW interaction. For an isolated tube as an elastic shell there exist three

frequencies associated essentially with T–mode, L–mode and R–mode. In the absence of the vdW interaction ($c = 0$), the three vibration frequencies are obtained for individual tubes of examples 1 to 4 with $L/(r_N \cdot m)$=10, 5 and 1 ($N = 2$ or 5), respectively. In particular, when $L/(r_N \cdot m)$=10 the results for example 1 to 4 are displayed in Figs. 7.1(b), 7.6(b), 7.8(b) and 7.13(b), respectively with comparison to the corresponding frequencies in Figs. 7.1(a), 7.6 (a), 7.8(a) and 7.13(a) with $c = c_0$.

7.3.1 Torsional and Longitudinal Modes

To study the effect of the interlayer vdW interaction on T– and L–modes of MWNTs, we again start with the large-radius DWNT, example 1. It is noted in Fig.7.1 that when $n > 5$ frequencies T_2 and T_1 in Fig.7.1(a), associated with T–motion primarily of tube 2 or tube 1 are nearly equal to T_2 and T_1 in Fig.7.1(b), representing the T–mode frequencies of the isolated inner tube 1 and outer tube 2, respectively. At the same time, L–mode frequencies L_2 and L_1 in Fig. 7.1 (a), associated with L–modes basically of the two individual tubes almost coincide with L_2 and L_1 in Fig. 7.1(b), denoting the L–mode frequencies of isolated tube 1 and 2, respectively. From these results, it is seen that when T– or L–modes are considered the two nested tubes of the DWNT vibrate almost independently as if they were two isolated SWNTs. In other words, the normal interlayer vdW interaction does not exert significant influence on T– and L–modes of the DWNT. Correspondingly, the comparison between Figs.7.6(a) and 7.6 (b), 7.8(a) and 7.8(b), and 7.13(a) and 7.13(b) leads to similar results for T– and L–modes of large-radius example 2, and small-radius examples 3 and 4 with $L/(r_N \cdot m) = 10$. In addition, for all the examples considered here the comparison results associated with $L/(r_N \cdot m)$= 5 or 1 ($N = 2$ or 5) are found very similar to the above results corresponding to $L/(r_N \cdot m)$= 10. Therefore, it is concluded that regardless of the innermost radius of MWNTs, the effect of the normal interlayer vdW interaction is generally negligible for T– and L–modes of MWNTs. As a result, T– and L–modes of a MWNT are usually the collection of T– and L–motions of individual nested tubes of the MWNT.

7.3.2 Radial Modes

Large-radius MWNTs (examples 1 and 2): It has already been shown in Section 7.2.1 that for large-radius MWNTs, e.g., examples 1 (DWNT) and 2 (5-wall CNT) in Table 7.1, R – modes are collective motions of all the nested tubes of the smallest radius $5\,nm$, showing that the R – motions of the large-radius individual tubes are strongly coupled through the interlayer vdW interaction. The frequency R_2 in Fig.7.1(a) for the counter-phase R – mode of example 1 and frequencies R_2, R_3, R_4 and R_5 in Fig.7.6 (a) for three mixed and one counter-phase R – modes of example 2 are up-shifted considerably compared to the R – mode frequencies in Figs.7.1(b) and 7.6(b) for the individual tubes of the two MWNTs. In particular, as mentioned in Section 7.2.1, the frequencies of example 2 increase significantly from R_2 to R_5 (see Fig.7.6(a)) with increasing number of adjacent tubes vibrating counter phase. All these results indicate that the interlayer vdW interaction considerably raises frequencies of R – modes of large-radius MWNTs associated with counter-phase vibrational modes.

On the other hand, for example 1, a thin DWNT (with inner radius-to-thickness ratio larger than four), the lowest frequency R_1 in Fig.7.1(a) is close to the average of R_1 and R_2 in Fig.7.1(b) for the isolated outer tube 2 and inner tube 1. As shown in Fig.7.4(b), this frequency is primarily associated with the in-phase R – mode of the DWNT in which the two nested tubes vibrate with almost identical radial deflections ($W_1 = W_2$). These results indicate that for the lowest frequency mode of example 1, the thin DWNT is approximately equivalent to a single layer shell of the average radius of the DWNT. In fact, as will be shown later in Chapter 9, this phenomenon is also observed for thin MWNTs of many layers.

Small-radius MWNTs (example 3 and 4): As shown in Section 7.2.2, for small-radius MWNTs, i.e., examples 3 (DWNT) and 4 (5-wall CNT) in Table 7.1, when $3 < n < 7$, frequencies R_1 and R_2 of example 3 (see Fig.7.8(a)), and R_1 to R_5 of example 4 (see Fig.7.13(a)) are basically associated with collective R – vibrations of all the nested tubes, while when $n = 0$ or $n > 7$ or 8, the associated modes are primarily R – vibrations

of individual tubes. Correspondingly, R − mode frequencies shown in Figs.7.8(a) and 7.13(a) for $c = c_o$ and $3 < n < 7$ are only slightly higher than R − mode frequencies of individual tubes displayed in Figs.7.8(b) and 7.13(b) with $c = 0$, while both are almost the same for $n = 0$ or $n > 7$ or 8. Based on these results, it is concluded that the interlayer vdW interaction plays a less significant role in R − modes for small-radius MWNTs than for large-radius MWNTs. Indeed, the effect of the vdW interaction on R − modes of small-radius MWNTs is moderate only when $3 < n < 7$ and can almost be ignored when $n = 0$ or $n > 7$ or 8.

The different effect of the interlayer vdW interaction on R − modes of the large- and small-radius MWNTs can be explained by the facts that the interlayer vdW interaction, characterized by a radius-independent constant c, is dominant compared to the low radial rigidity of the large-radius individual tubes, but negligible compared to the much higher radial rigidity of the small-radius individual tubes. In fact, it is seen from Figs.7.1, 7.6 and 7.7 and Figs.7.8, 7.13 and 7.14 that the R − frequencies of small-radius MWNTs are one order of magnitude higher than the R − frequencies of large-radius MWNTs, indicating that the radial rigidity of small-radius MWNTs is much higher than that of large-radius MWNTs.

(a) $c = c_0$ (b) $c = 0$
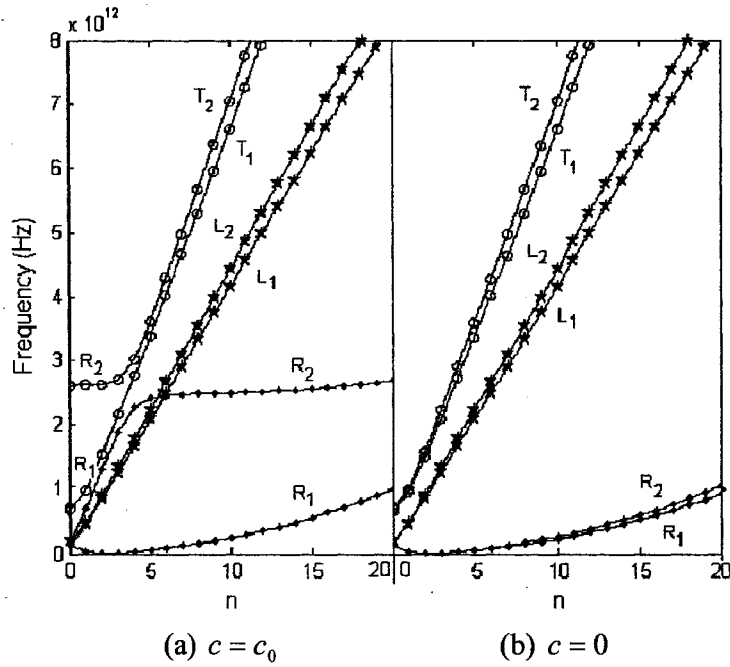
Fig.7.1 The dependence of frequency on circumferential wave number n for

example 1 (in Table 7.1) with $L/(r_2 m) = 10$, and (a) $c = c_0$ and (b)

$c = 0$.

(a)   (b)
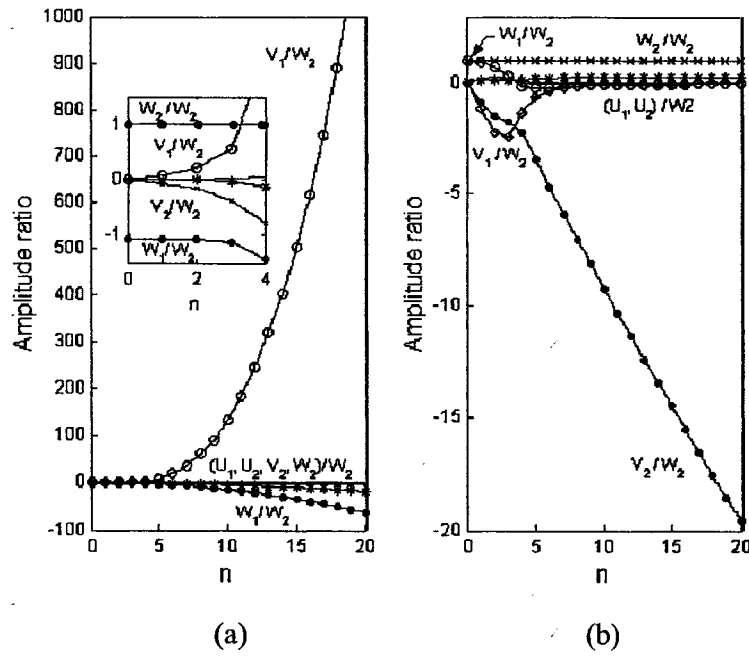
Fig.7.2 The amplitude ratios associated with frequency (a) T_2 (the inset for R_2 at

$n < 3$) and (b) T_1 shown in Fig.7.1(a) for example 1 in Table 7.1.

(a)   (b)
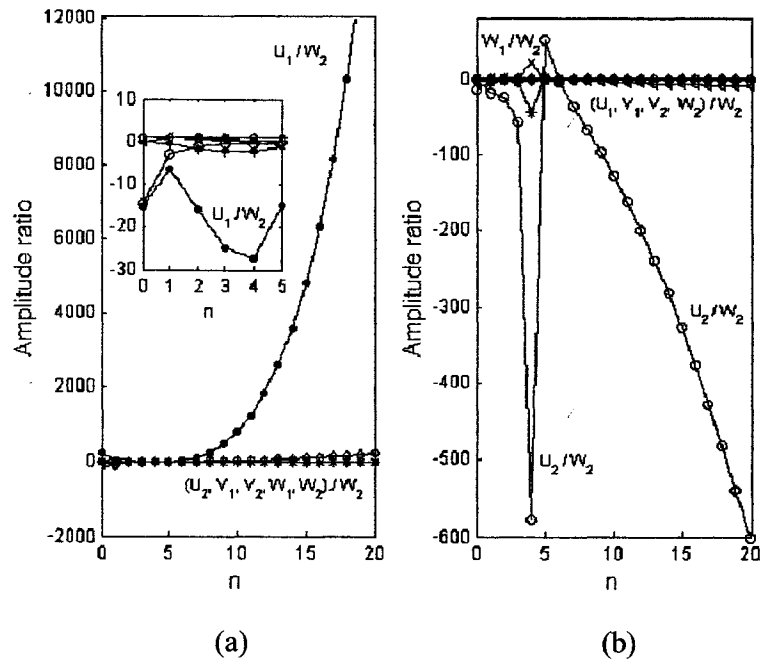
Fig.7.3 The amplitude ratios associated with frequency (a) L_2 and (b) L_1 shown

in Fig.7.1(a) for example 1 in Table 7.1.
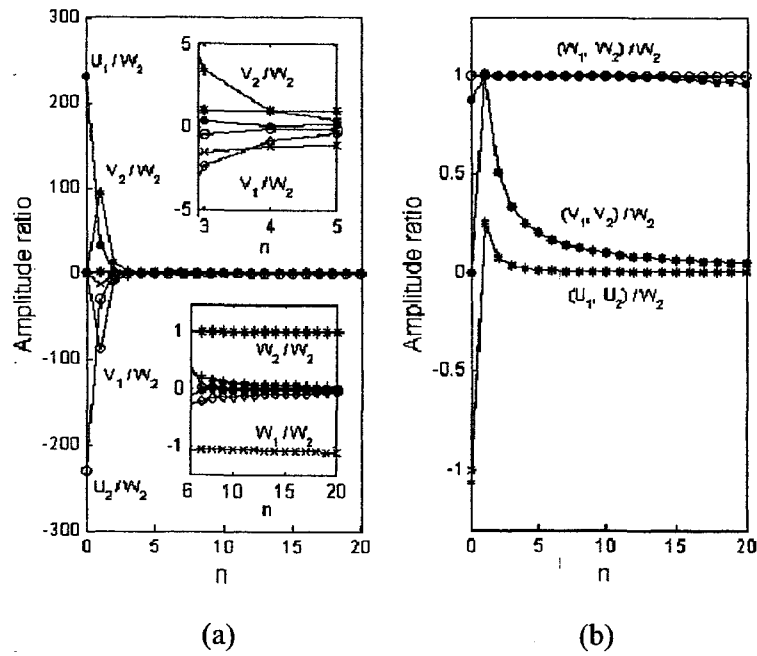
Fig.7.4 The amplitude ratios associated with frequency (a) R_2 and (b) R_1 shown

in Fig.7.1(a) for example 1 in Table 7.1.

(a) Counter-phase R-mode   (b) In-phase R-mode   (c) Coaxial B-mode (n = 1)
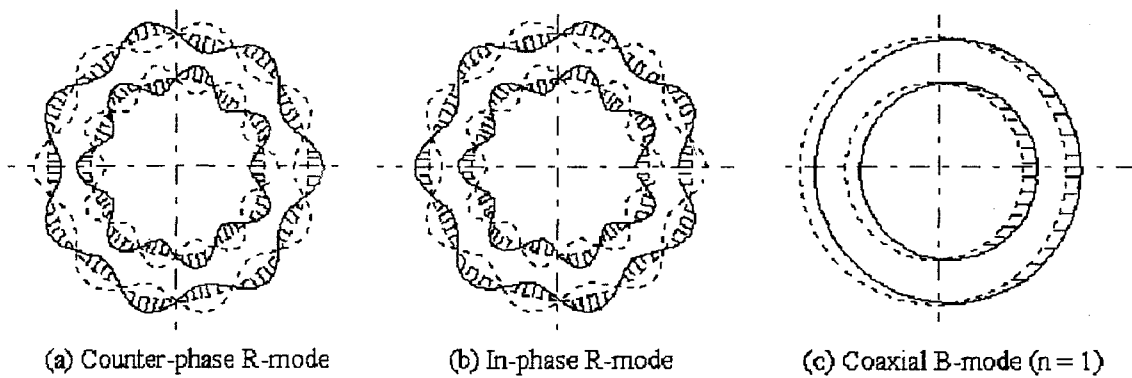
Fig.7.5 Top view of $R-$ and $B-$ modes of example 1 in Table 7.1.

(a) $c = c_0$ (b) $c = 0$
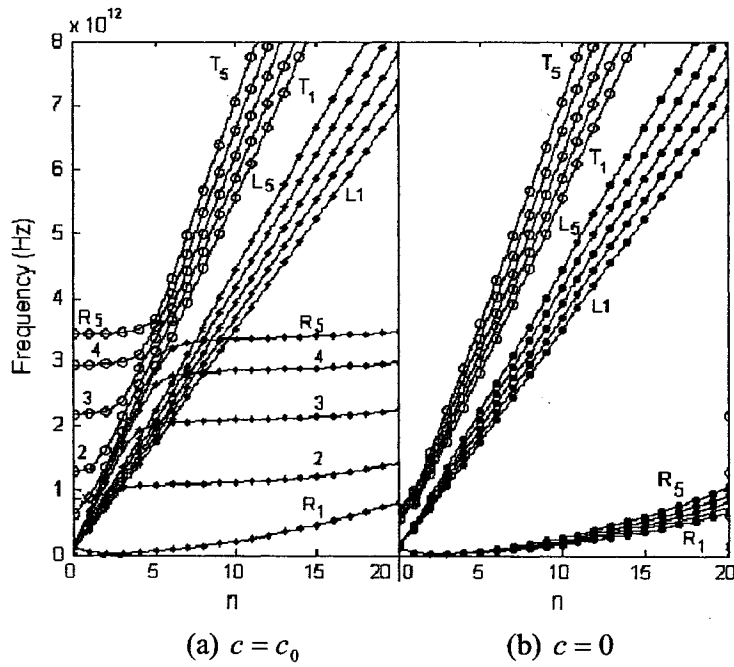
Fig.7.6 The dependence of frequency on circumferential wave number n for example

2   (in Table 7.1) with $L/(r_5m) = 10$, and (a) $c = c_0$ and (b) $c = 0$.

(a) $L/(r_5m) = 5$ (b) $L/(r_5m) = 1$
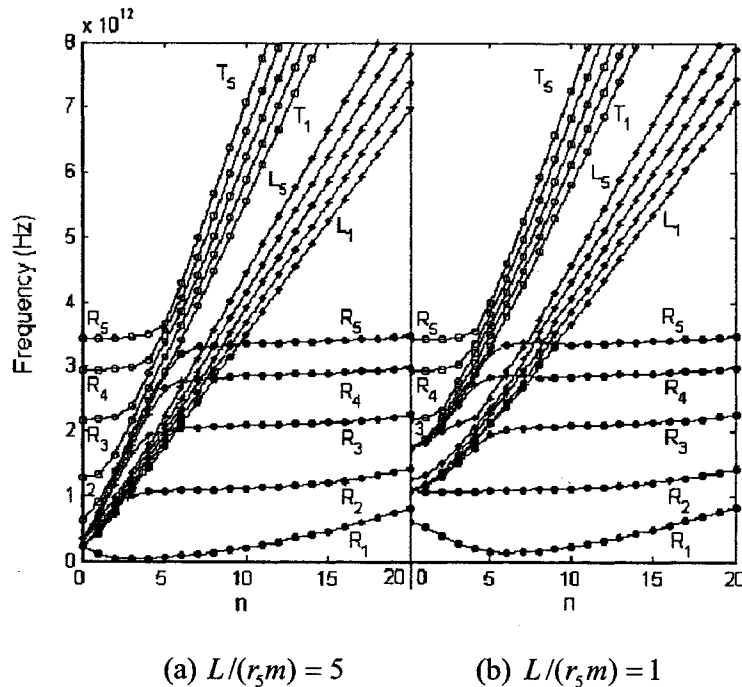
Fig.7.7 The dependence of frequency on circumferential wave number n for example 2

(in Table 7.1) with $c = c_0$, and (a) $L/(r_5m) = 5$ and (b) $L/(r_5m) = 1$.

(a) $c = c_0$ (b) $c = 0$
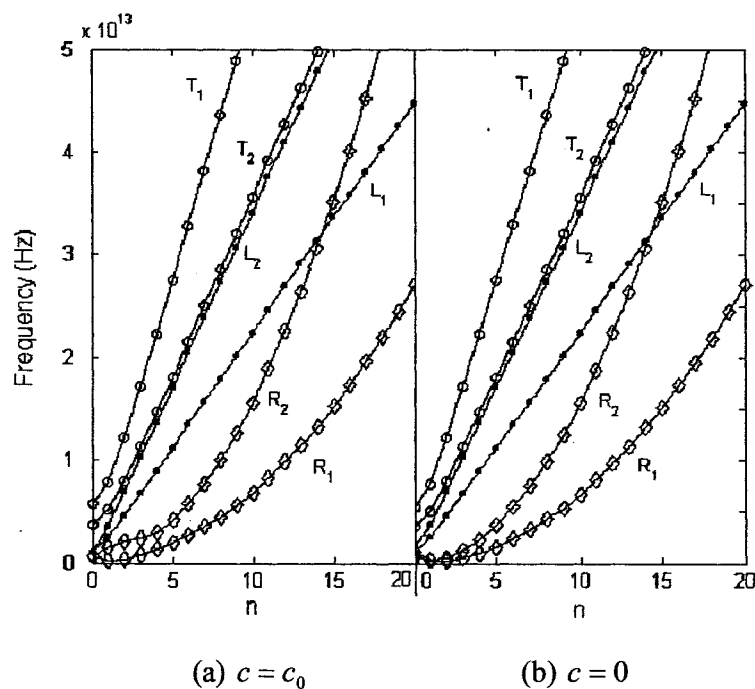
Fig.7.8 The dependence of frequency on circumferential wave number n for example

3   (in Table 7.1) with $L/(r_2 m) = 10$, and (a) $c = c_0$ and (b) $c = 0$.

(a)   (b)
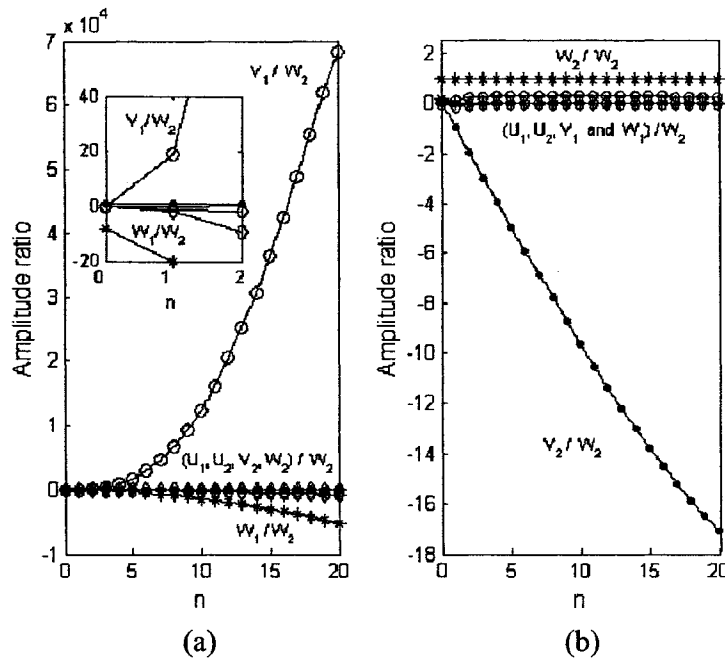
Fig.7.9 The amplitude ratios associated with frequency (a) T_2 and (b) T_1

shown in Fig.7.8(a) for example 3 in Table 7.1.

(a)   (b)
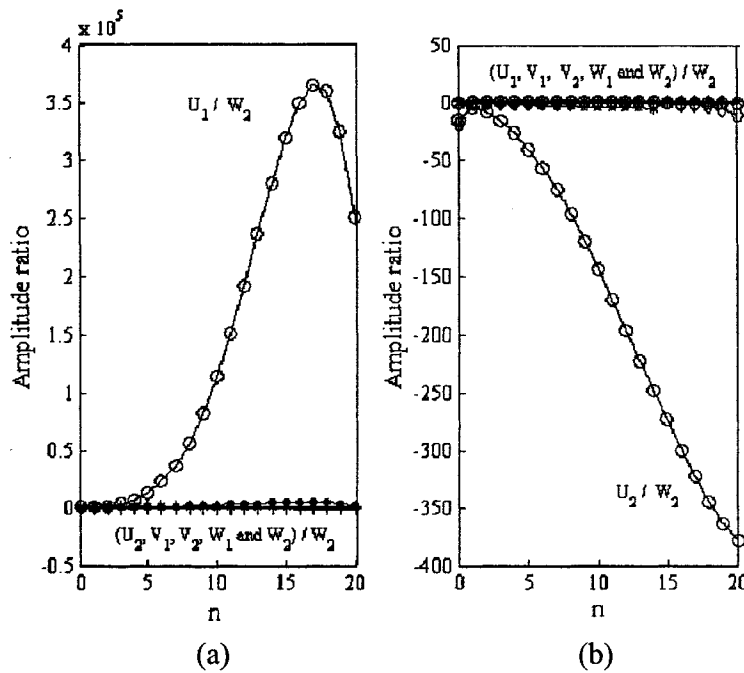
Fig.7.10 The amplitude ratios associated with frequency (a) L_2 and (b) L_1

shown in Fig. 7.8(a) for example 3 in Table 7.1.
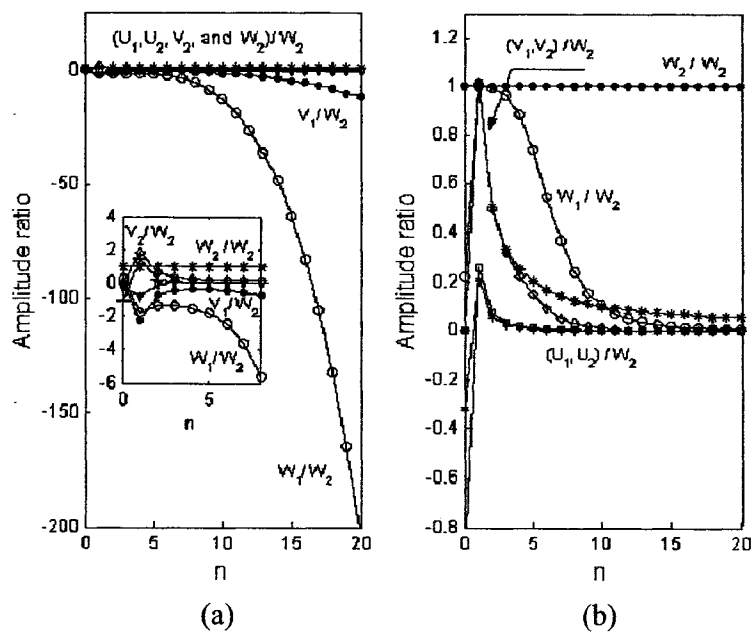
Fig.7.11 The amplitude ratios associated with frequency (a) R_2 and (b) R_1 shown

in Fig.7.8(a) for example 3 in Table 7.1.

(a) R-mode (mainly of inner tube)   (b) R-mode (mainly of outer tube)

(c) Non-coaxial B-mode (n = 1)   (d) Coaxial B-mode (n = 1)
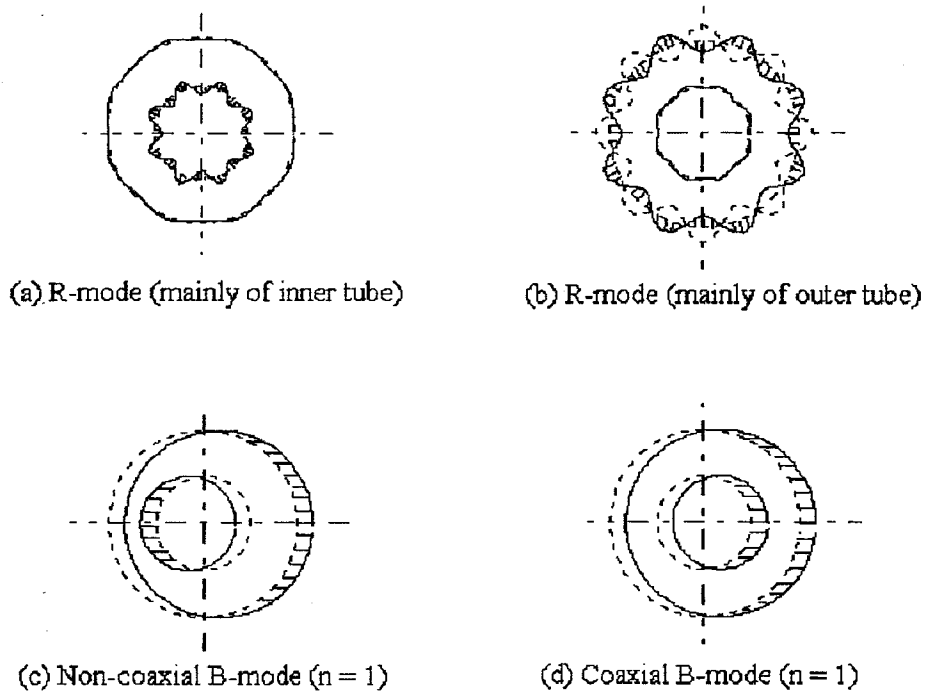
Fig.7.12 Top view of $R-$ and $B-$ modes of example 3 in Table 7.1.

(a) $c = c_0$

(b) $c = 0$
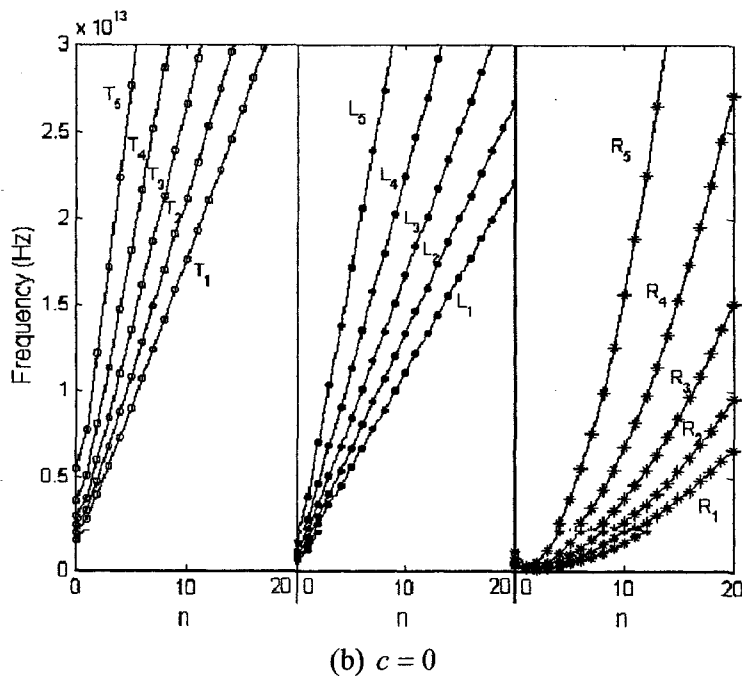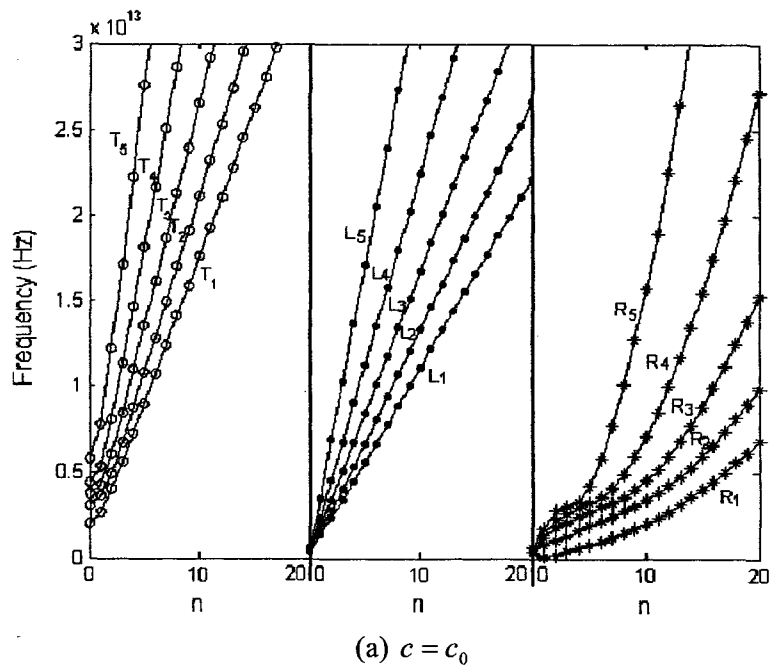
Fig.7.13 The dependence of frequency on circumferential wave number n

for example 4 (in Table 7.1) with $L/(r_5 m) = 10$, and (a) $c = c_0$

and

(b) $c = 0$.

(a) $L/(r_5 m) = 5$

(b) $L/(r_5 m) = 1$
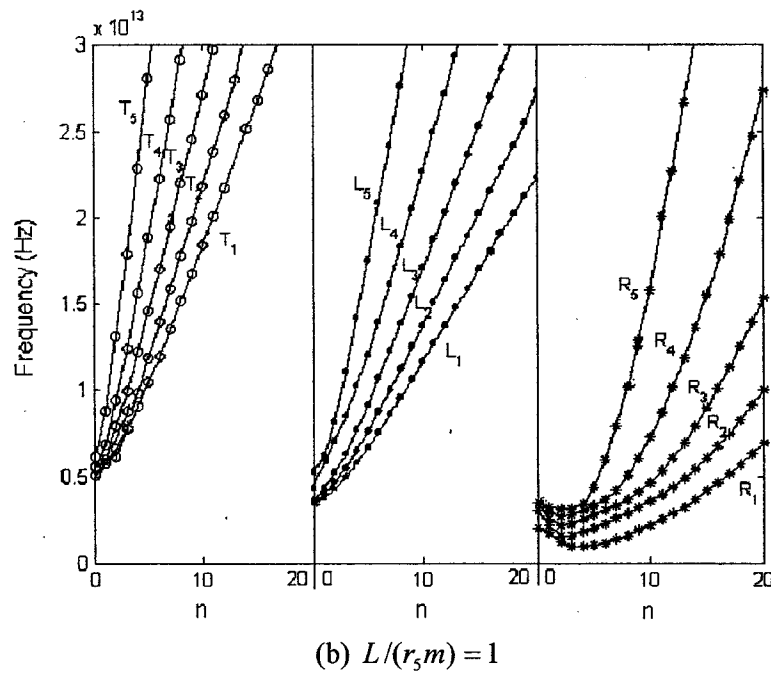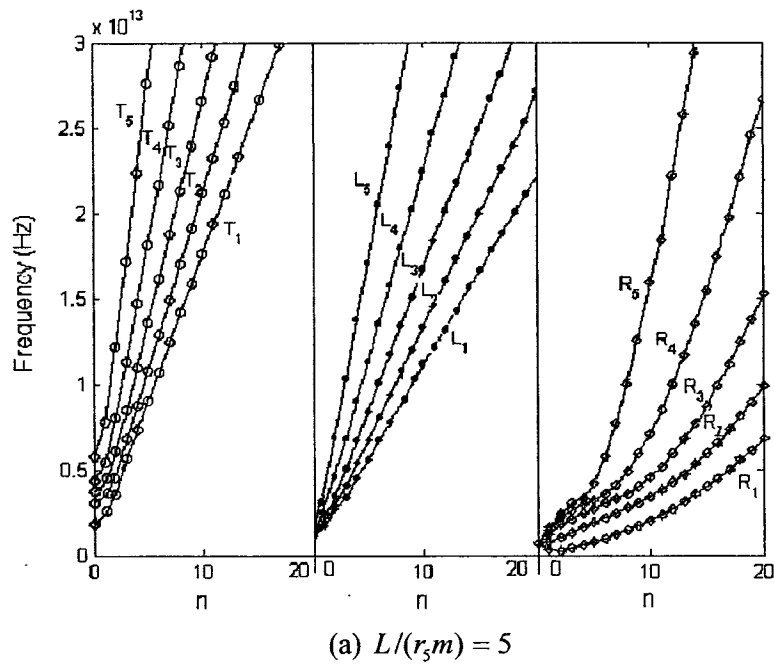
Fig.7.14 The dependence of frequency on circumferential wave number n for

example 4 (in Table 7.1) with $c = c_0$, and (a) $L/(r_5 m) = 5$ and (b)

$L/(r_5 m) = 1$.

Table 7.1 The data of geometry of four MWNTs considered in Chapter 7.

Example	1	2	3	4
$r_1(nm)$	5	5	0.65	0.65
Number of layers N	2	5	2	5

Chapter 8

Special Issues of Free Vibration of MWNTs

8.1 Introduction

Raman-active radial breathing modes (RBMs) of both SWNTs [36, 70, 91-93] and MWNTs [24, 71-74] are of major interest in previous studies. These axially uniform axisymmetric modes (with axial half wave number $m = 0$ and circumferential wave number $n = 0$) provide a useful tool to investigate structure-vibrational property relation for CNTs. More recently, other axisymmetric radial ($R-$), Longitudinal ($L-$) and torsional ($T-$) modes, which are not necessarily uniform in axial direction, have also been examined for SWNTs [167], where strong $R-L$ coupling is observed as a unique feature for SWNTs of cylindrical symmetry. However, axisymmetric vibrations of MWNTs have not been studied in the literature. On the other hand, beam-like vibrations of MWNTs have been the topic of numerous recent researches. For example, based on a multiple-beam model [106], beam-like vibrations of MWNTs have been examined for MWNTs of small innermost diameter. It is predicted that the interlayer vdW interaction results in non-coaxial intertube vibration of MWNTs. This unique phenomenon has later been confirmed for DWNTs by a more accurate molecular-structure-mechanics model [113], although the accuracy and limitations of the multiple-beam model remain unexplored in the literature.

In this Chapter, first, an updated bending stiffness ($D = 2eV$) of SWNTs is suggested based on recent data in the literature, which is in much better agreement with atomistic model for phonon dispersion relations of SWNTs than the previously adopted value ($D = 0.85eV$) estimated by Yakobson et al [32] based on earlier data of Roberson et al [31]. Using the multiple-shell model with $D = 2eV$, this Chapter gives a comprehensive study on axisymmetric modes ($n = 0$) of MWNTs, with an emphasis on the unique features of axisymmetric modes for MWNTs and the effect of the Poisson-ratio of SWNTs on coupling between $R-$ and $L-$ modes of MWNTs. Furthermore, the present shell model is employed to study beam-like vibrational modes ($n = 1$) of

141

MWNTs and examine the accuracy and applicability of the multiple-beam model [106]. Finally, the lowest frequency and associated modes of MWNTs are also studied in detail.

8.2 Comparison between Shell Model and an Atomistic Model

To further demonstrate the relevance of the elastic shell model for free vibration of CNTs, phonon-dispersion relations are calculated in Figs.8.1 and 8.2 based on Eqs. (5.1) and (5.3) for SWNT (10, 10). It is known that the bending stiffness D of SWNTs is related to the elastic strain energy per unit area g by the relationship $g = D/2r^2$ where r is the radius of SWNTs. The value $D = 0.85eV$, used in our previous work [130-135] and Chapters 2 to 7, was suggested by Yakobson et al [32] based on Robertson et al.'s data [31] published in 1992. However, recent data obtained by ab

$initio$ calculations yield $2g \cdot r^2 = 4 - 4.32$ eV $(\overset{0}{A}{}^2/atom)$ in Ref.36 (1999),

$3.9–4.32 eV (\overset{0}{A}{}^2/atom)$ in Ref. 38 (2001) and $4.28 eV (\overset{0}{A}{}^2/atom)$ in Ref.147 (2002), which suggest an effective value $D = 1.95 - 2.16$ eV. It is seen from Fig.8.1 and 8.2(a) that, overall, the present shell model with $D = 2eV$ is in good agreement with a continuum elastic model [166] and a force-constant model [91] with maximum relative errors usually less than 10%. Particularly, for $n = 1 - 3$ and smaller normalized wave

vector Kr or KT/π ($K = \dfrac{m\pi}{L}$ is wave vector, r is the radius of SWNT (10, 10), T is

the vector representing the shortest repeat distance between two unit atomic cells along the axis of SWNTs, the magnitude of which is $0.246 nm$ for SWNT (10, 10)), the present shell model with $D = 2eV$ almost coincides with the continuum model [166] while the two continuum models are a little different from the force constant model [91]. As mentioned in [166], this discrepancy is probably due to "an inappropriate choice of force-constant value" in [91]. In fact, the phonon dispersion relations of SWNT (10, 10) are also obtained by initio ab calculation and a lattice-dynamic model in [36] and [37], respectively. Different from [91] which gives an almost linear

frequency-K (wave vector) relation for long-wavelength bending modes ($n = 1$), the results of [36] and [37] show an approximate K^2 dispersion for the long-wavelength bending mode, which is in favor of our results shown in Figs.8.1 and 8.2(a). Since the figures shown in [36] and [37] are too small for detailed comparison, the present shell model has been compared to the atomistic model used in [91] only. On the other hand, it is seen in Fig.8.2(b) that the shell model with $D = 0.85eV$ leads to much larger relative errors as compared to the force-constant model, especially for larger n and the normalized wave vector KT / π. Here, it should be stated that the continuum model [166] and the force-constant model [91] are limited to SWNTs. Indeed, because no detailed experimental or atomistic simulation results are available for phonon-dispersion relation of MWNTs, similar comparison for the present multiple-shell model cannot be made for MWNTs.

In this Chapter, we shall apply the multiple-shell model with $D = 2eV$ to study axisymmetric and beam-like vibrations of MWNTs. Here, we still focus on the four examples of MWNTs in Table 7.1, i.e., large-radius MWNTs, examples 1 and 2 with the innermost radius $5nm$, and small-radius MWNTs, examples 3 and 4 with the innermost radius $0.65nm$.

8.3 Axisymmetric Vibration

In axisymmetric vibration ($n = 0$), solution (5.3) takes the form ($k = 1,2,\cdots,N$)

$$u_k(x,\theta,t) = U_k \cos\frac{m\pi x}{L} \cdot e^{i\omega t}$$
$$v_k(x,\theta,t) = 0$$
$$w_k(x,\theta,t) = W_k \sin\frac{m\pi x}{L} \cdot e^{i\omega t}$$

(8.1)

With this solution the N circumferential dynamic equations in Eqs.(5.1) are satisfied automatically. As a result, the $3N$ equations in (5.1) reduce to $2N$ equations for an $N-$wall CNT ($k = 1,2,\cdots,N$)

$$r_k^2 \frac{\partial^2 u_k}{\partial x^2} - v r_k \frac{\partial w_k}{\partial x} + (1-v^2)\frac{D}{Eh} r_k \frac{\partial^3 w_k}{\partial x^3} = \frac{\rho h}{Eh}(1-v^2) r_k^2 \frac{\partial^2 u_k}{\partial t^2},$$

$$v r_k \frac{\partial u_k}{\partial x} - w_k - (1-v^2)\frac{D}{Eh} r_k^2 \cdot \frac{\partial^4 w_k}{\partial x^4} + (1-v^2)\frac{D}{Ehr_k^2}\left[\begin{array}{c} -r_k^3 \frac{\partial^3 u_k}{\partial x^3} \\ -w_k \end{array}\right]$$

$$= \frac{1}{Eh}(1-v^2) r_k^2 \left[\rho h \frac{\partial^2 w_k}{\partial t^2} - p_k\right]$$

(8.2)

When the axial wavelength-to-diameter ratio $L/(r_N m)$ is much larger than one, the bending stiffness D-related coupled terms in (8.2) are negligible. In this case, the axial displacement and radial displacement are coupled through the Poisson-ratio $v \neq 0$. Hence, the Poisson-ratio plays a crucial role in $R-L$ coupling. On the other hand, if an θ-independent circumferential vibration is considered, one should consider the solution given by [138]

$$u_k(x,\theta,t) = 0$$

$$v_k(x,\theta,t) = V_k \sin\frac{m\pi x}{L} \cdot e^{i\omega t}$$

$$w_k(x,\theta,t) = 0$$

(8.3)

It is readily verified that the following N uncoupled equations can be derived from (5.1), for N uncoupled torsional (T) modes ($k = 1,2,\cdots,N$)

$$\frac{r_k^2}{2} \cdot \frac{\partial^2 v_k}{\partial x^2} + (1-v^2) \cdot \frac{3D}{2Eh} \cdot \frac{\partial^2 v_k}{\partial x^2} = \frac{\rho h}{Eh}(1+v) \cdot r_k^2 \cdot \frac{\partial^2 v_k}{\partial t^2}$$

(8.4)

Here, it should be stated that such decoupled equations are not available for θ-dependent circumferential vibration. Obviously, for θ-independent pure T-modes of a MWNT, each constituent tube behaves exactly like an isolated SWNT without coupling with adjacent tubes. In particular, the second term is much smaller than the first term on LHS of (8.4), indicating that T-mode frequencies will be radius-insensitive. Thus, T-modes of MWNTs will not be further discussed in much detail. In the following, we will focus on $R-$ and $L-$modes of MWNTs for examples1-4 in Table 7.1.

8.3.1 Axisymmetric Radial Modes

First, let us consider DWNTs, i.e., examples 1 and 3 of inner radius $5nm$ and $0.65nm$, respectively. When $n = 0$, frequencies R_1 and R_2 of R – modes, frequencies L_1 and L_2 of L – modes, and frequencies T_1 and T_2 of T – modes are displayed in Figs.8.3(a) and (b) for examples 1 and 3, respectively. The amplitude ratios associated with R – and L – modes of examples 1 and 3 are shown in Figs.8.4 and 8.5. In particular, as stated before, two T – mode frequencies for the inner and outer tubes are almost indistinguishable.

As seen from the insets in Fig.8.4, frequencies R_1 and R_2 in Fig.8.3(a) for large-radius DWNT of example 1, are associated with an in-phase $(W_1 / W_2 = 1)$ and a counter-phase $(W_1 / W_2 = -1)$ R – mode, respectively. Differently, Fig.8.5 (see the insets) shows that frequency R_1 or R_2 in Fig.8.3(b) for small-radius DWNT of example 3, is basically associated with R – mode of individual tube 2 or 1.

It is seen in Fig.8.3 for the two DWNTs that the frequencies associated with pure R – modes are usually insensitive to axial wavelength, i.e., $L/(r_2 m)$, when $L/(r_2 m) > 1$, due to negligible effect of bending stiffness, and approach the RBM frequencies as axial wavelength tends to infinity. They significantly decrease with increasing axial wavelength $L/(r_2 m)$ only in the range of $L/(r_2 m) < 1$ due to strong effect of bending stiffness D. On the other hand, in the transition zone between R – and L – modes where their frequencies are very close to each other, R – and L – modes of the DWNTs are generally coupled through Poisson-ratio effect (where $L/(r_2 m) > 1$ and the effect of bending stiffness is negligible). In Fig. 8.3(b) for small-radius DWNT of example 3, this $R - L$ coupling (or transition) zone is relatively wide for both R – modes. However, in Fig.8.3(a) for the large-radius DWNT of example 1, the $R - L$ coupling (or transition) zone is relatively wide only for the in-phase R – mode of lower frequency R_1, and almost vanishes for the counter-phase R – mode of higher frequency R_2. In other words, in the latter case, there is almost an abrupt transition between the counter-phase R – mode and the L – mode, and the $R - L$ coupling zone is very narrow and thus can be actually ignored. This unique feature of large—radius DWNT can be attributed to the dominant interlayer vdW interaction

associated with counter-phase R – modes of large-radius MWNTs. For large- and small-radius 5-wall CNTs, examples 2 and 4, qualitatively similar results are shown in Fig.8.6 (a) and (b), respectively.

8.3.2 Axisymmetric Longitudinal Modes

First, it is seen from Fig.8.3 for both large- and small-radius DWNTs, the two L – mode frequencies for $n = 0$ are almost indistinguishable, implying that L – mode of one tube could be stimulated by L – modes of adjacent tubes through an even very weak coupling effect. It is noted in Figs.8.4 (a) and (c) that, when the longitudinal wavelength is not very short, say $L/(r_2 m) > 1$ or 2, example 1 (DWNT) exhibits coupled axisymmetric L – vibrations involving both tubes, among which the in-phase one ($U_1 \approx U_2$, see Fig.8.4(a)) is associated with frequency L_1 in Fig.8.3(a), and the counter-phase one ($U_1 \approx -U_2$, see Fig.8-4(c)) is associated with frequency L_2 in Fig.8-3(a). This phenomenon is in sharp contrast to the axisymmetric T – modes and non-axisymmetric L – modes (with larger n), which are almost uncoupled vibrations of individual tubes.

In fact, it is known for elastic shells [141] that, when $n = 0$, longitudinal vibration is always accompanied by a small but usually non-negligible radial vibration due to the $R - L$ coupling effect of Poisson-ratio. Therefore, once an individual tube of the DWNT first vibrates in axisymmetric L – mode, the associated R – vibration induced by Poisson-ratio effect could stimulate a small R – vibration combined with a predominant L – vibration of adjacent tubes through the interlayer vdW interaction. Here, almost identical L – mode frequencies of adjacent tubes are likely responsible for the strong coupling of axisymmetric L – modes. For the same reasons, the strong coupling between L – vibrations of individual tubes can also be observed for the small-radius DWNT, example 3 (see Figs. 8.5(a) and (c)), and the 5-wall CNTs, examples 2 and 4. Indeed, when Poisson-ratio v is set to zero, Eqs.(8.2) break into two systems for pure L – vibrations of individual tubes and collective R – vibrations of all individual tubes provided that the axial wavelength is not very small, say $L/(r_N m) > 1$ and thus the effect of bending stiffness is negligible. Thus, for MWNTs, coupling between L – vibrations of concentric tubes is a result of the Poisson-ratio effect and the

interlayer radial vdW interaction. This coupling effect becomes significant when $n = 0$ due to the fact that L – mode frequencies of individual tubes are almost identical. It is expected that similar concept can be used to explain the observed coupled resonant axisymmetric L – modes of aligned SWNT ropes [126].

8.4 Beam-like Vibration

For MWNTs, non-coaxial vibrational modes are predicted based on a multiple-(Euler) beam model [106], in which each nested tube of MWNTs is treated as an individual elastic (Euler) beam coupled with adjacent tubes through the interlayer vdW interaction. The intertube interaction per unit length along the axial direction is given by $\delta \cdot r(c\Delta w)$, where δ represents the intertube vdW interaction effective length between two adjacent tubes, r is the radius of inner tube, Δw is transverse deflection jump between the two tubes, and c is given by (2.6). In particular, $\delta = 2$ is used in Ref. 106. In this section, we shall compare the more accurate multiple-shell model with the multiple-beam model to further study the beam-like modes, especially non-coaxial modes [106, 113] for MWNTs and identify a better value of δ.

8.4.1 Large-radius MWNTs (the innermost radius 5 nm)

Let us start with the large-radius DWNT, example 1 in Table 7.1. Following the procedure demonstrated in Chapter 5, six frequencies can be obtained for the DWNT with $n = 1$ and $0.1 \leq L/(r_2 m) \leq 50$. For a comparison to the beam model [106] which gives two frequencies for a DWNT, the lowest frequency (corresponding to a beam-like bending mode) and the highest frequency R (of a radial mode) are identified from six frequencies and shown in Fig.8.7(a), with associated amplitude ratios displayed in Figs. 8.8(a) and (b), respectively.

Beam-like bending of a shell is defined by $n = 1$ and $w = u$, where w and v represent radial and circumferential displacements of the shell, respectively. It is seen in Fig. 8.8(a) that, when $L/(r_2 m) < 1$, the lowest frequency for $n = 1$ corresponds to an in-phase R – mode of the DWNT having $W_1 \approx W_2$ and $(U_1, V_1, U_2$ and $V_2) << W_2$. The circumferential amplitudes V_1 and V_2 increase with increasing axial wavelength

$L/(r_2 m)$. When $L/(r_2 m)$ exceeds 5, we have $W_1 = V_1 = V_2 = W_2$ and $U_1 = U_2 \ll W_2$, showing a coaxial bending $(B-)$ mode characterized by a translation of the circular cross-section. In Fig.8.7(a), this frequency (B) is compared to the coaxial mode frequency given by the beam model. As expected, when $L/(r_2 m) > 15$, the beam model agrees very well with the shell model with relative errors less than 5%.

On the other hand, the amplitude ratios in Fig. 8.8(b) for the frequency R indicate $W_1 \approx -W_2$ and $(U_1, V_1, U_2$ and $V_2) \ll W_2$, which gives a non-coaxial $R-$ mode with non-beam-like deformation of the cross-section. In particular, this result $(W_1 \approx -W_2)$ predicted by the present shell model is the same as that predicted by the beam model for example 1. On the other hand, as seen from Fig. 8.7 (a), the higher non-coaxial mode frequency obtained by the beam model with $\delta = 2$ differs from frequency R given by the present shell model by around 50%. Similar results are obtained in Fig. 8.9 (a) for coaxial $B-$ mode of the lowest frequency and four non-coaxial $R-$ modes of large-radius 5-wall CNT, example 2 in Table 7.1. The relative errors of the beam model with $\delta = 3$ (which, as will be shown later, is more accurate than $\delta = 2$) range from 30 to 50% for the four non-coaxial $R-$ modes. This discrepancy between the shell model and the (Euler) beam model is due to non-beam-like deformation of the cross-section caused by the interlayer vdW interaction. This non-beam-like deformation is negligible for small-radius MWNTs, but could be significant for large-radius MWNTs due to their low radial rigidity. Therefore, consistent with the recent results [163], the present work also suggests that the multiple-beam model is more accurate for small-radius MWNTs than large-radius MWNTs.

8.4.2 Small-radius MWNTs (the innermost radius $0.65\,nm$)

Next, let us consider small-radius MWNTs, example 3 (DWNT) and 4 (5-wall CNT) in Table 7.1. When $n = 1$, the (lowest) two frequencies B_1 and B_2 of example 3, both of which correspond to beam-like bending modes, are identified from six frequencies and displayed in Fig.8.7(b). The amplitude ratios associated with frequencies B_1 and B_2 are shown in Figs. 8.10(a) and (b), respectively.

We see from Fig.8.10 that the lowest frequency B_1 when $L/(r_2 m) > 10$ is associated with the coaxial beam-like $B-$mode, while frequency B_2 corresponds to $W_1 \approx V_1 \approx -1.7W_2$ and $W_2 \approx V_2$, showing a non-coaxial $B-$mode in which the inner and outer tubes are bent in opposite directions with individual circular cross-sections. It follows from Fig. 8.7(b) that, when $L/(r_2 m) > 15$, the beam model agrees well with the shell model for both coaxial and non-coaxial $B-$modes with relative errors less than 20% when $\delta = 2$. Our results showed that, for the non-coaxial $B-$modes, the beam model with $\delta = 3$ is in better agreement with the shell model with relative errors less than 10%. In particular, $\delta = 3$, selected by the best comparison to the shell model, is quite close to the value of $\delta = \pi$ obtained by a simple theoretical calculation (omitted here).

For 5-wall CNT, example 4 in Table 7.1 (of the outermost radius $2 nm$), similar results are obtained in Fig. 8.9(b). Accordingly, when $L/(r_5 m) > 15$, the beam model with $\delta = 3$ is adequate for both coaxial and non-coaxial $B-$modes of the small-radius MWNTs (example 4 in Table 7.1) with relative errors less than 5% and for the three higher-order non-coaxial modes with relative errors less than 20%. Moreover, considering small-radius MWNTs, e.g., 3, 4, and 5-wall CNTs of the outermost radius $1.45 nm$, $1.65 nm$ and $1.9 nm$, we find that the beam model is in good agreement with the shell model for all coaxial and non-coaxial modes with maximum relative errors less than 10%. In these cases, due to high radial rigidity of small-radius individual tubes, all non-coaxial modes are associated with nearly beam-like bending modes with smaller cross-sectional deformation. Hence, the (Euler) beam model is relevant for MWNTs of smaller outermost radius (e.g., less than $2 nm$).

8.5 The Lowest Frequency Vibration

CNTs are expected to be the potential building blocks in nano-devices. Thus the lowest frequency and the associated modes of CNTs are of practical interest. Here, based on the multiple-shell model, the lowest frequency and the associated modes are calculated for MWNTs.

First, let us consider DWNTs, example 1 and 3 in Table 7.1. The dependence of six frequencies on axial wavelength $L/(r_2 m)$ are displayed in Figs.8.11 and 8.12 for example 1 and 3, respectively, with $0 \le n \le 10$ and $0.1 \le L/(r_2 m) \le 50$. For a given $n(n \ge 1)$, the lowest frequency, the second lowest frequency, ..., and the highest frequency are presented in (a) to (f) of Figs.8.11 and 8.12 for the two DWNTs.

It is noted that, when the circumferential number n is sufficiently large, e.g., $n > 5$ for large-radius example 1 and $n > 2$ for small-radius example 3, the two lowest frequencies R_1 and R_2, shown in (a) and (b) of Figs.8.11 and 8.12, are mainly associated with R − modes, the highest two frequencies T_1 and T_2, shown in (e) and (f) of Figs.8.11 and 8.12, are primarily associated with T − modes, while the two intermediate frequencies L_1 and L_2 , shown in (c) and (d) of Figs.8.11 and 8.12, correspond to L − modes of the two DWNTs. On the other hand, for given axial wavelength $L/(r_2 m)$, the lowest frequencies of the two DWNTs are represented by the envelope curves in Figs.8.11(a) and 8.12(a), respectively. Obviously, the lowest frequency of the two DWNTs decreases monotonically with increasing $L/(r_2 m)$, showing that, for any given ratio L/r_2, the lowest frequency of the two DWNT with simply supported ends always corresponds to the minimum axial half wave number $m = 1$.

Proceeding in the same way, analogous features are also obtained for large-and small-radius 5-wall CNTs, examples 2 and 4 in Table 7.1. Especially, the lowest frequency is also consistently associated with $m = 1$. In view of this result, the "L/r_N" dependence of the lowest frequency is plotted in Fig. 8.13 for all the N − wall CNTs considered here. It is clearly seen from Fig.8.13 that, when L/r_N ($N = 2$ or 5) increases up to 50, the lowest frequencies of examples 1-4 in Table 7.1 decrease form around $10^{12} - 10^{13} Hz$ to about $10^9 Hz$ and the associated modes shift from an in-phase R − mode with relatively larger n ($n = 3 - 6$) to a combined R − and T − mode with $n = 2 - 3$, and finally, to a coaxial B − mode with $n = 1$.
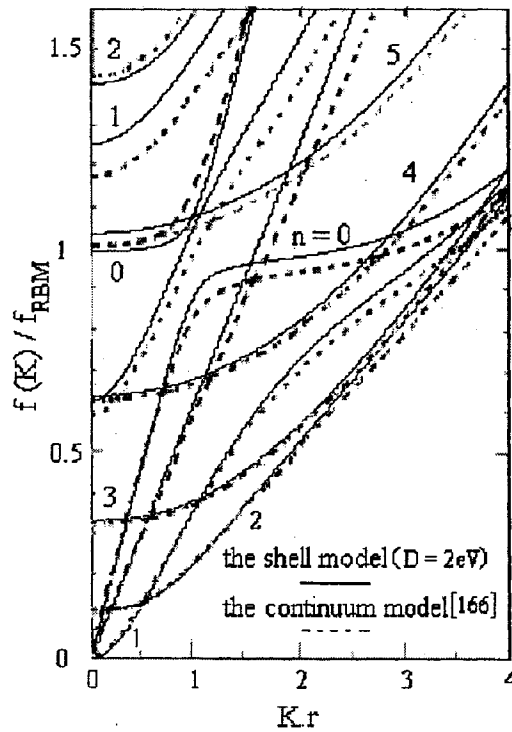
Fig.8.1 The comparison between the continuum model [166]
and the multiple-shell model with $D = 2eV$ for
phonon-dispersion relations of SWNT (10, 10). Here

K $(=\dfrac{m\pi}{L})$ is wave vector, r is the radius of SWNT

(10, 10) and f_{RBM} is RBM frequency of the SWNT.
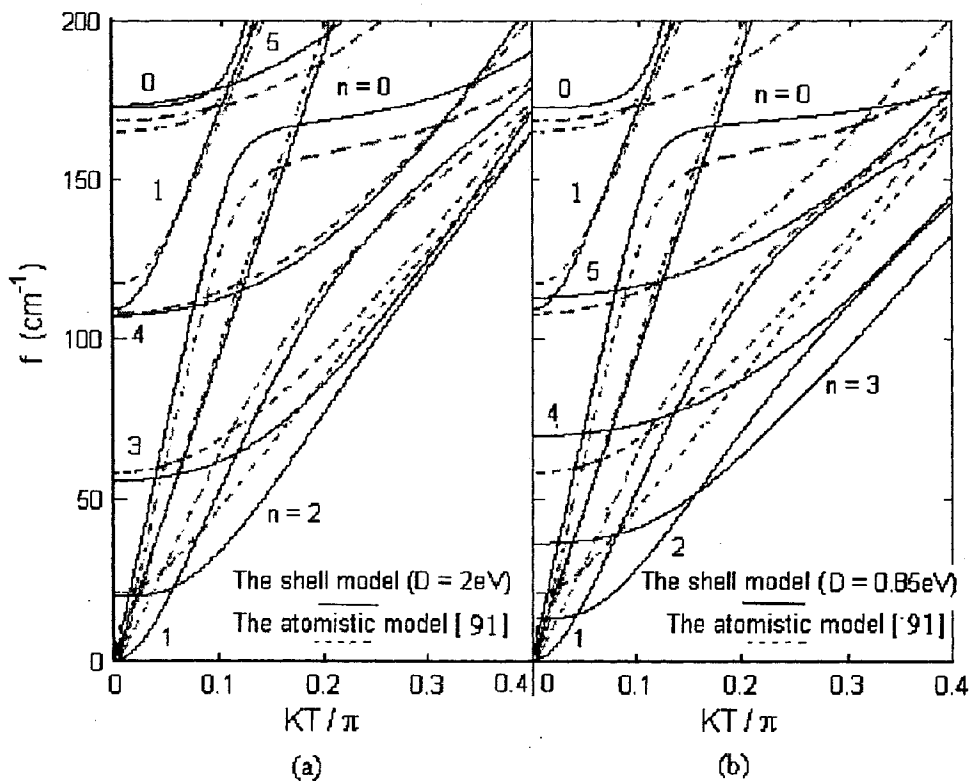
Fig.8.2. The comparison between the atomistic model [91] and the multiple-shell model with (a) $D = 2eV$ and (b) $D = 0.85eV$ for phonon-dispersion relations of SWNT (10, 10). Here K $(=\dfrac{m\pi}{L})$ is wave vector and T is the vector representing the shortest repeat distance between two atomic cells along the axis of the SWNT.
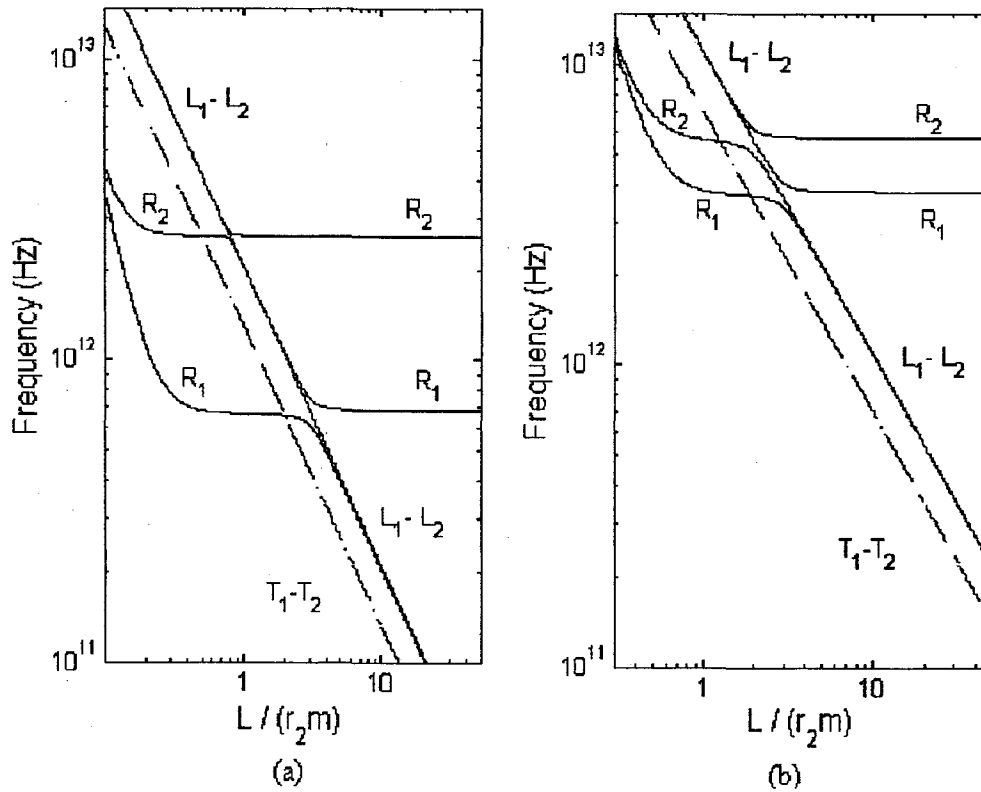
Fig.8.3 Axisymmetric mode frequencies ($n = 0$) of (a) example 1 and (b) example 3

in Table 7.1.
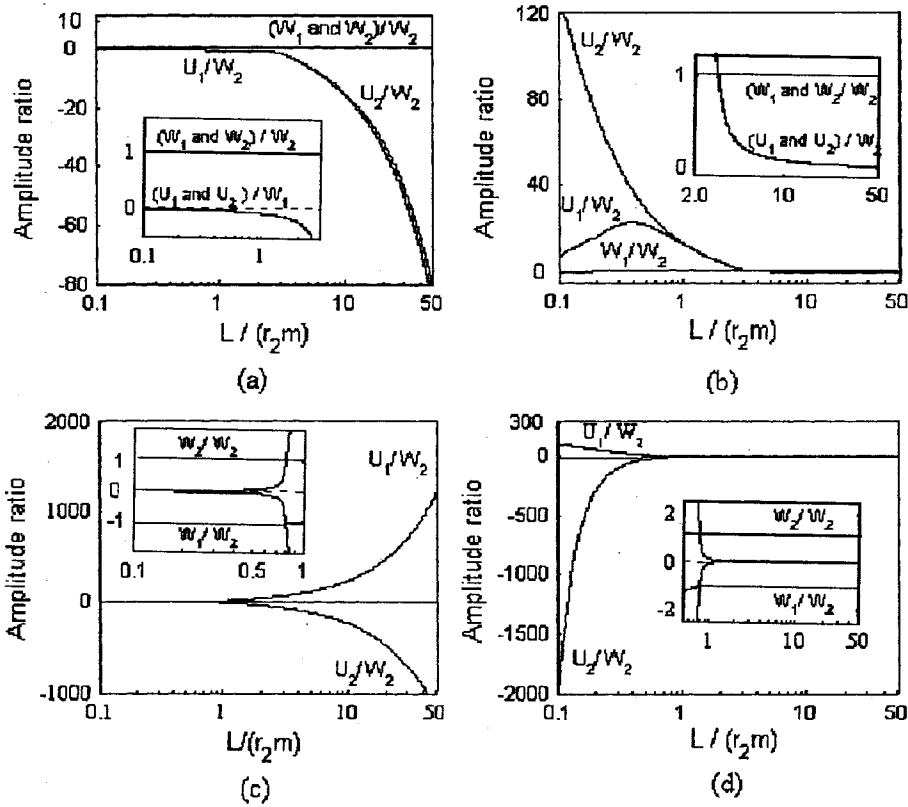
Fig.8.4 Amplitude ratios associated with frequencies (a) R_1 (inset)& L_1, (b)

L_1 & R_1 (inset), (c) R_2 (inset) & L_2 and (d) L_2 & R_2 (inset) shown

in Fig.8.3 (a) for example 1 in Table 7.1.
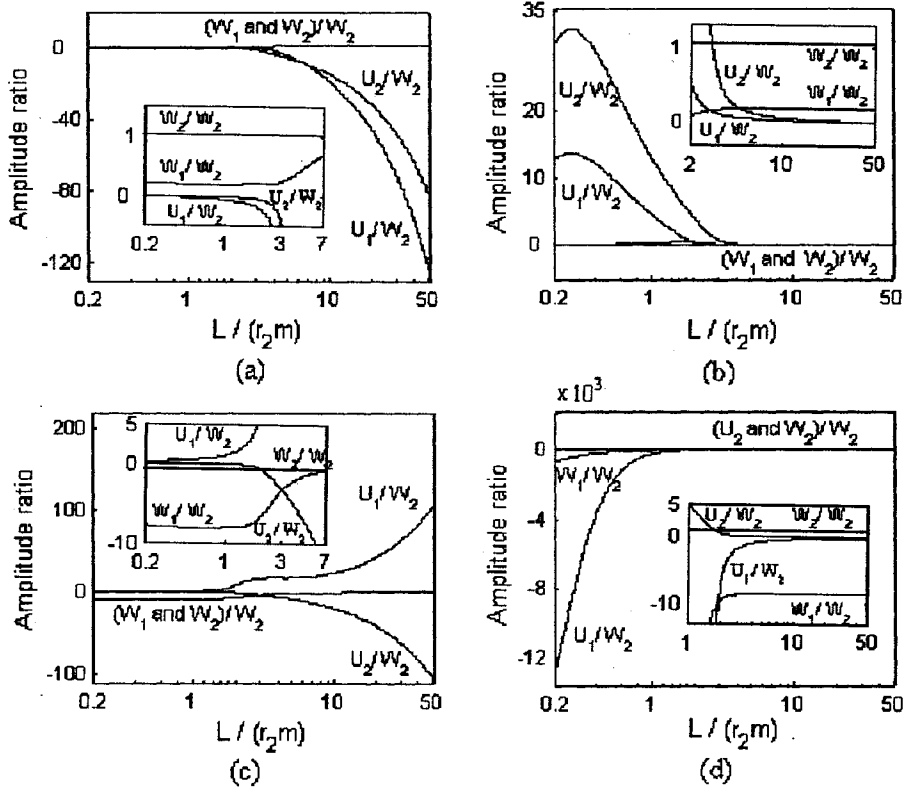
Fig.8.5 Amplitude ratios associated with frequencies (a) R_1 (inset)& L_1, (b) L_1 & R_1 (inset), (c) R_2 (inset)& L_2 and (d) L_2 & R_2 (inset) shown in Fig.8.3 (b) for example 3 in Table 7.1.
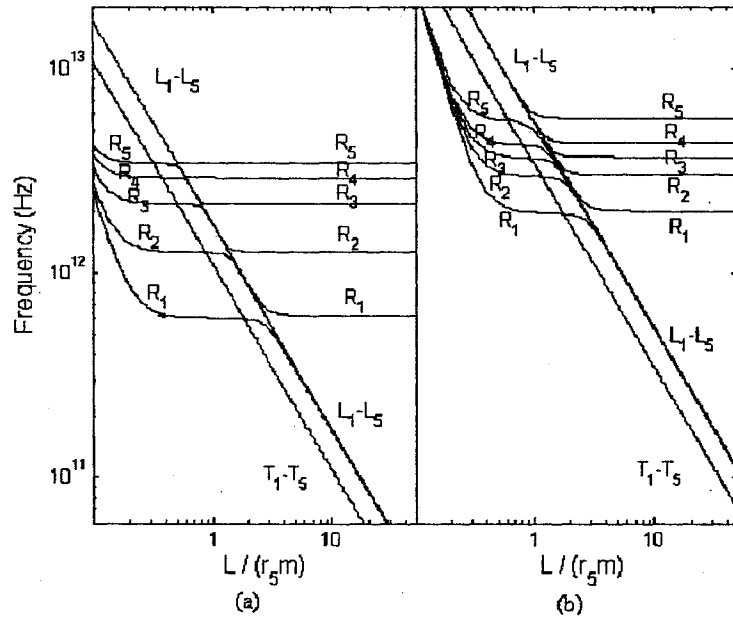
Fig.8.6 Axisymmetric mode frequencies ($n = 0$) of (a) example 2 and (b) example 4 in Table 7.1.
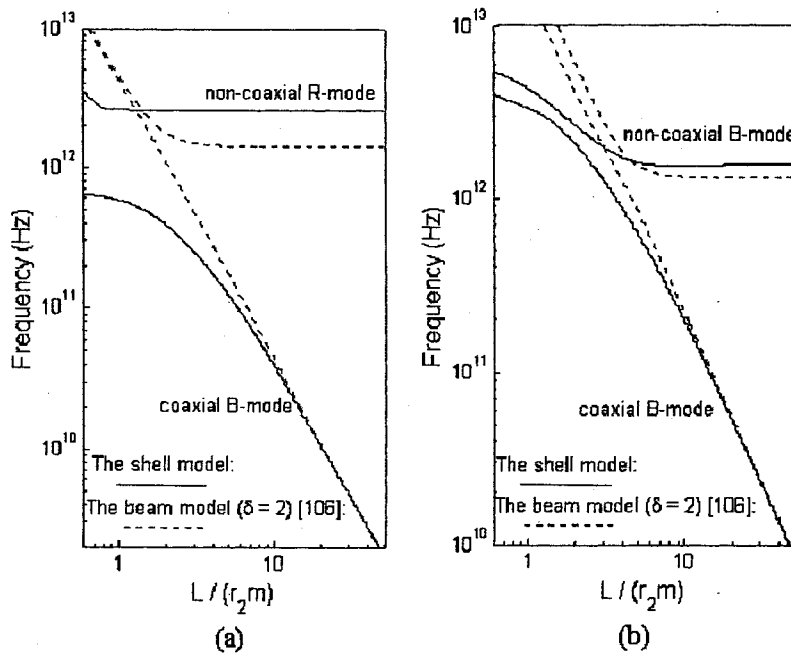
Fig.8.7 Comparison between the multiple-shell model and the multiple-beam model with $\delta = 2$ [106] when $n = 1$ for (a) coaxial B – mode and non-coaxial R – mode of example 1 in Table 7.1 and (b) coaxial and non-coaxial B – modes of example 3 in Table 7.1.
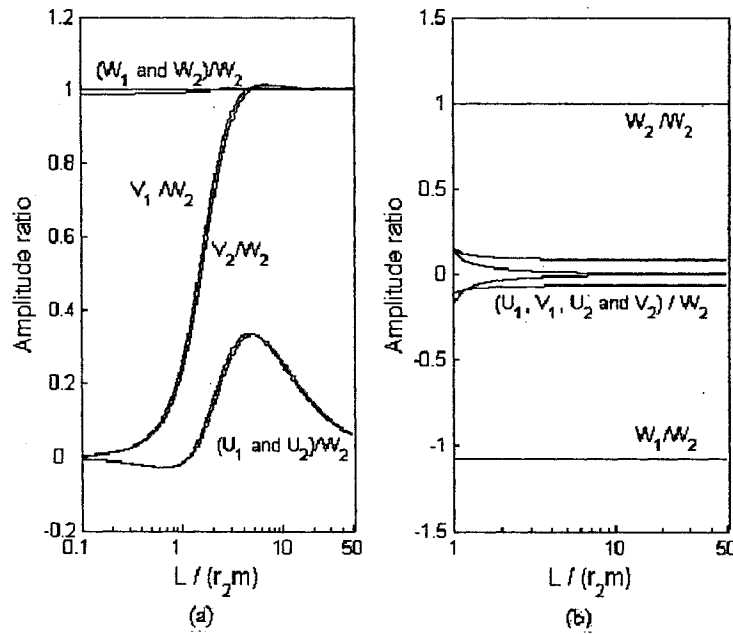
Fig.8.8 Amplitude ratios associated with frequencies (a) B and (b) R shown in Fig.8.7(a) for example 1 in Table 7.1.
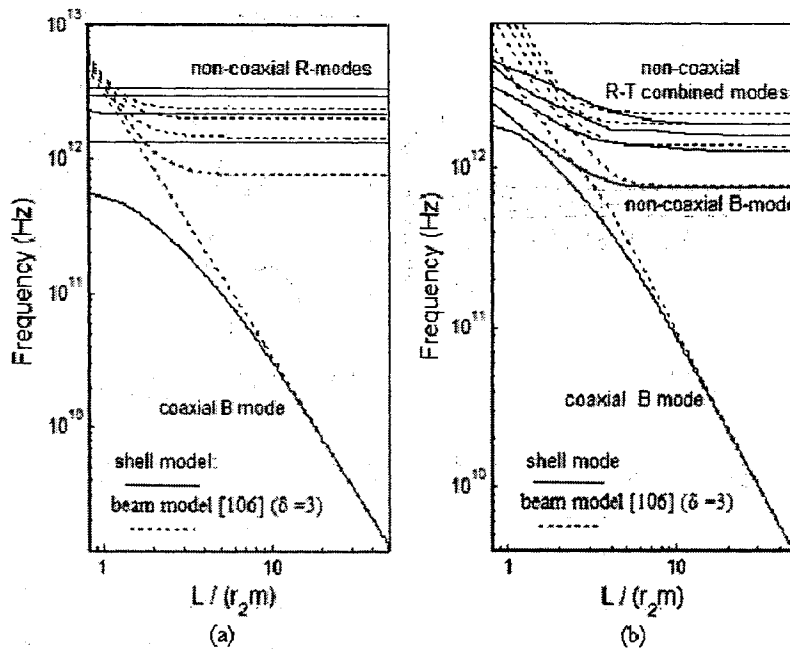
Fig.8.9 Comparison between the multiple-shell model and the multiple-beam model [106] with $\delta = 3$ when $n = 1$ for (a) coaxial B − mode and non-coaxial R − modes of example 2 in Table 7.1 and (b) coaxial and non-coaxial B − modes, and non-coaxial $R - T$ combined modes of example 4 in Table 7.1.
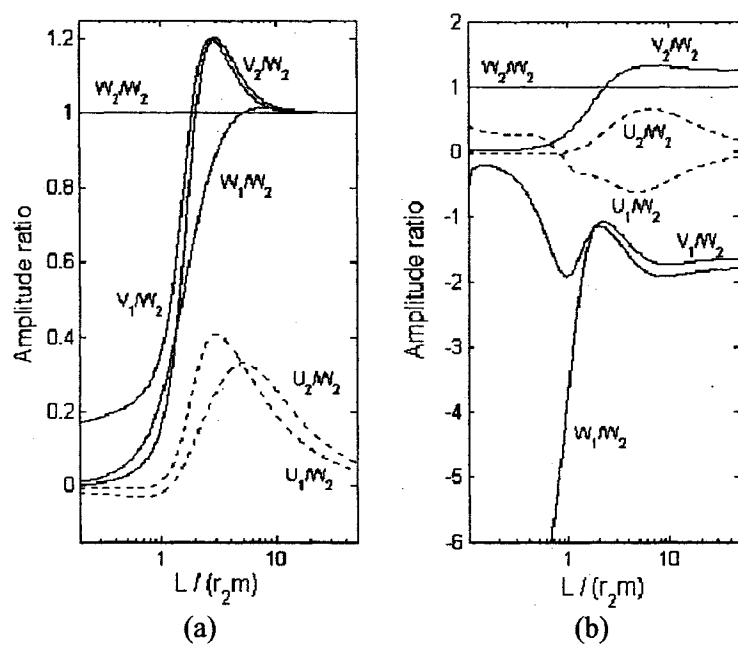
Fig.8.10 Amplitude ratios associated with frequencies (a) B_1 and (b) B_2 shown in

Fig .8.7(b) for example 3.
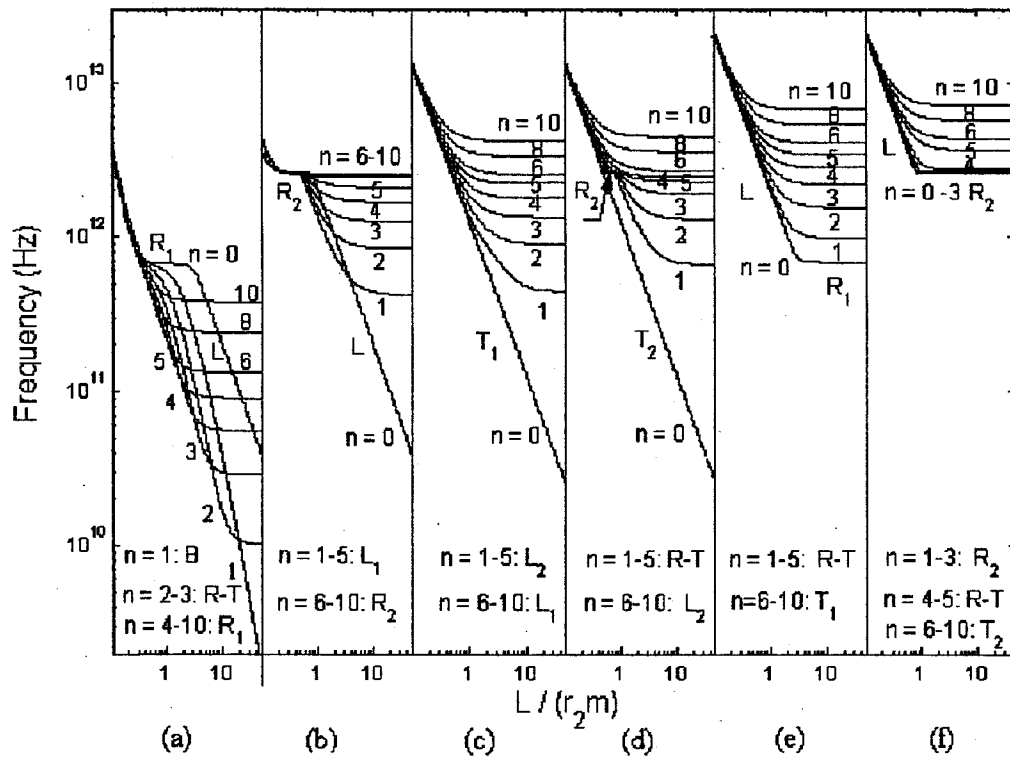
Fig.8.11 Dependence of six frequencies on $L/(r_2 m)$ for example 1 in Table 7.1. For a given n ($n \geq 1$), the lowest frequency, the second lowest frequency, ..., and the highest frequency are shown in (a), (b), ... and (f), respectively.

(R: radial mode, L: longitudinal mode, T: torsional mode, B: bending mode and $R-T$: radial and torsional combined mode)
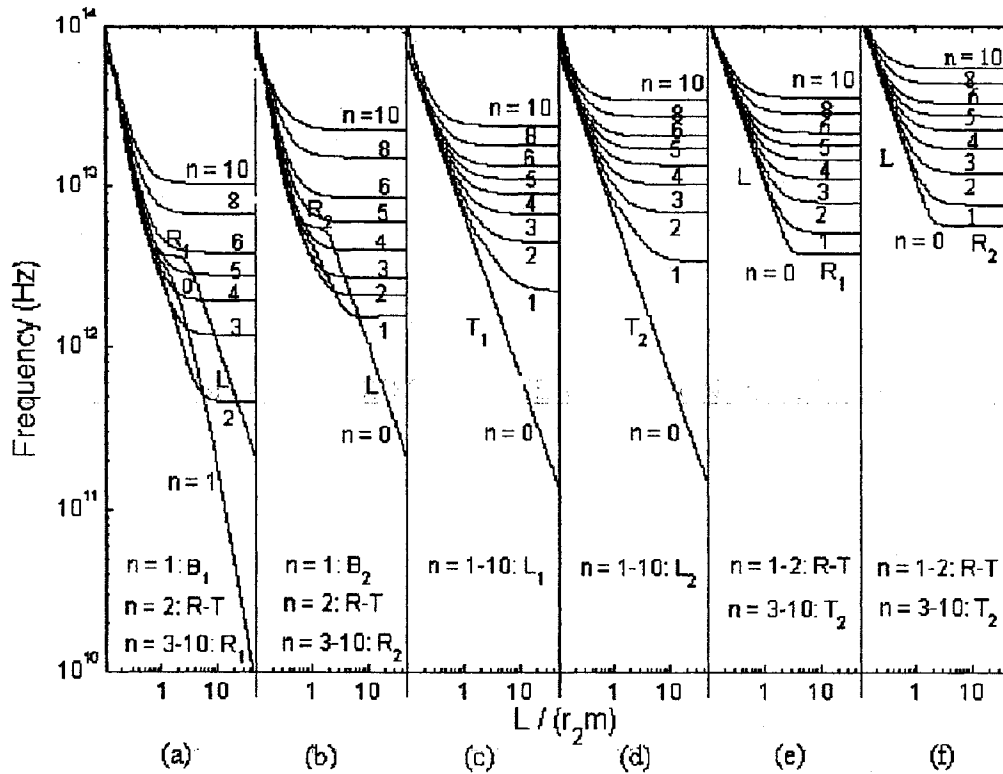
Fig.8.12   Dependence of six frequencies on $L/(r_2 m)$ for example 3 in Table 7.1. For a

given n ($n \geq 1$), the lowest frequency, the second lowest frequency, ..., and

the highest frequency are shown in (a), (b), ... and (f), respectively.

(R : radial mode, L : longitudinal mode, T : torsional mode, B : bending mode

and $R - T$: radial and torsional combined mode)
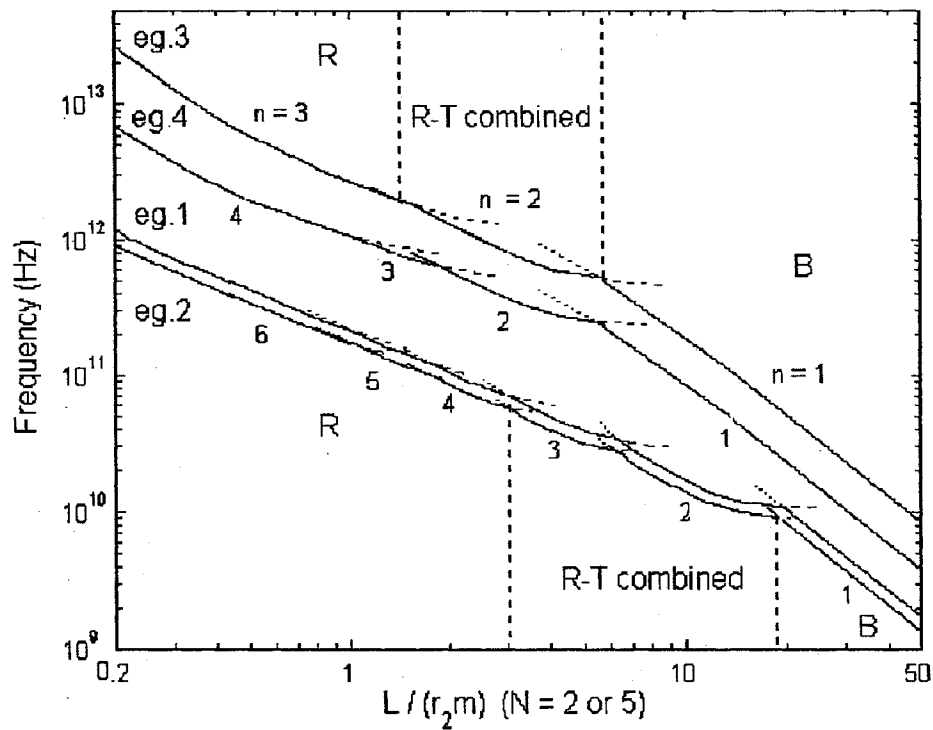
Fig. 8.13 The lowest frequency and associated modes for examples 1 to 4 in Table 7.1

Chapter 9

Simplification of the Multiple-shell Model for CNTs

9.1 Single-shell Model for MWNTs

9.1.1 Introduction

Elastic shell models have been effectively used to study mechanical deformation of CNTs [13, 119], especially free vibration of SWNTs [124-126, 132] and MWNTs [132, 134-136], and static buckling of CNTs under axial compression [32, 120, 127-129], bending [48, 120], radial pressure [123, 130, 133], or combined loadings [131]. Previous work has shown that vibrational frequencies or critical buckling load predicted by simple isotropic elastic shell models are generally in good agreement with available experiments or atomistic simulations of SWNTs [120, 131, 136] and MWNTs [130, 132-134] of as many as twenty layers [130, 159]. In particular, because elastic shell models are relatively simple and cost-effective as compared to difficult nano-scale experiments and formidable atomistic simulations, they have the potential to offer simple general formulas in some important cases, identify major factors affecting mechanical behavior of CNTs, and explain or predict new physical phenomena.

On the other hand, based on the multiple-shell model [127-129], the elastic buckling or free vibration of an $N-$ wall CNT is governed by N coupled buckling equations (2.2) or $3N$ dynamic equations (5.1), respectively. Obviously, the computation of critical buckling load and especially, vibrational frequencies is still challenging when the number of layer N is sufficiently large. Thus, it is of practical interest to further simplify the calculation and improve the efficiency of the shell model (if possible) in buckling and vibrational analyses for MWNTs of many layers. Previously, the single-layer shell model was proposed to characterize mechanical behaviors of MWNTs, which models an N-wall CNT as a single-layer shell with thickness Nh, and the bending stiffness proportional to $(Nh)^3$ (where h is effective thickness of SWNTs). As pointed out by Ru [127-129], this oversimplified single-shell model substantially overestimates the

162

critical buckling strain of MWNTs due to complete ignorance of interlayer slipping. On the other hand, based on theoretical study, Ru [129] showed that for axially compressed buckling, a thin $N-$wall CNT defined by the innermost radius-to-thickness ratio $\lambda > 4$, can be approximately treated as a single-layer shell with the effective bending stiffness ND and the thickness Nh. Furthermore, some numerical results [130] (also see Chapter 3) suggest that this single-shell model is also valid for buckling of thin MWNTs under radial pressure. Thus, as long as thin MWNTs are concerned, it is expected that the calculations and analyses could be greatly simplified by replacing the multiple-shell model [127-129] with the single-shell model.

This section offers a complementary work to the earlier studies on thin MWNTs by (i) presenting a theoretical derivation of the single-shell model for buckling of thin MWNTs under radial pressure and (ii) demonstrating the effectiveness of the single-shell model for axially compressed buckling of thin MWNTs with specific examples. Subsequently, based on the single-shell model for thin MWNTs, an approximate method is suggested for buckling of thick and (almost) solid MWNTs. As will be shown below, this approximation can efficiently reduce the problem of a MWNT of many layers (which is usually thick or solid) to a relatively simple problem for a multi-layer elastic shell of fewer layers. Finally, the single-shell model is further extended to the lowest frequency R-mode of thin MWNTs. The accuracy of the single-shell model is examined systematically as compared to the multiple-shell model in calculating the lowest R-mode frequency of thin MWNTs.

9.1.2 Elastic Buckling of Thin MWNTs

Here, let us first consider elastic buckling of thin MWNTs under external pressure. For buckling of an $N-$wall CNT under an external pressure Eqs.(2.2) reduce to the following N equations.

$$DV_1^8 w_1 = V_1^4 p_{12} + \frac{F_\theta^{(1)}}{r_1^2} \frac{\partial^2}{\partial \theta^2} V_1^4 w_1 - \frac{Eh}{r_1^2} \frac{\partial^4 w_1}{\partial x^4},$$

$$DV_2^8 w_2 = \nabla_2^4 \left[p_{23} - \frac{r_1}{r_2} p_{12} \right] + \frac{F_\theta^2}{r_2^2} \frac{\partial^2}{\partial \theta^2} \nabla_2^4 w_2 - \frac{Eh}{r_2^2} \frac{\partial^4 w_2}{\partial x^4},$$

$$\cdots\cdots$$

$$D\nabla_N^8 w_N = -\frac{r_{N-1}}{r_N} \nabla_N^4 p_{(N-1)N} + \frac{F_\theta^{(N)}}{r_N^2} \frac{\partial^2}{\partial \theta^2} \nabla_N^4 w_N - \frac{Eh}{r_N^2} \frac{\partial^4 w_N}{\partial x^4}. \tag{9.1}$$

Following [129], for a thin N − wall CNT, the radial deflections w_1, w_2, $\cdots, w_N$ can be approximately described by a single deflection function w and the radii r_1, r_2, $\cdots r_N$ can be replaced by the average radius r_{ave} of the thin N − wall CNT. Moreover, it is seen in [130] (also see Chapter 3) that an external pressure P acting on a thin N − wall CNT is almost equally shared by the N − concentric tubes. Thus in Eqs.(9.1), we have

$F_\theta^{(1)} \approx F_\theta^{(2)} \approx \cdots \approx F_\theta^{(N)} \approx -\dfrac{P \cdot r_{ave}}{N}$. Bearing all these in mind and adding the N

equations in (9.1), one can derive the following single equation governing the elastic buckling of the thin N − wall CNT subjected to an external pressure P.

$$(ND)\nabla^8 w = \frac{P}{r_{ave}} \cdot \frac{\partial^2}{\partial \theta^2} \nabla^4 w - \frac{E(Nh)}{r_{ave}^2} \frac{\partial^4 w}{\partial x^4} \tag{9.2}$$

Comparison between Eq. (9.2) and Eq. (2.1) with $p(x,\theta) = 0$ and $F_x = 0$ shows that indeed, a thin N − wall CNT can be modeled approximately as a singlelayer elastic shell with effective bending stiffness ND, effective thickness Nh and radius r_{ave}. Especially, Eq. (9.2) is equivalent to the following equation

$$D\nabla^8 w = \frac{P/N}{r_{ave}} \cdot \frac{\partial^2}{\partial \theta^2} \nabla^4 w - \frac{Eh}{r_{ave}^2} \frac{\partial^4 w}{\partial x^4} \tag{9.3}$$

indicating that the critical buckling pressure of a thin N - wall CNT is approximately N times that of a SWNT with the average radius r_{ave} of the thin N - wall CNT. This analytical result is consistent with the numerical results given in Chapter 3. Therefore, it is believed that the above single-shell model is adequate for elastic buckling of a thin MWNT under radial pressure.

As mentioned before, an analogous result is obtained analytically for axially compressed buckling of thin MWNTs in [129]. Here we shall further compare the single-shell model with the multiple-shell model for axially compressed buckling of thin MWNTs. To this end, two thin MWNTs, i.e., examples 1 and 2 shown in Table 4.1 are considered. The buckling behaviors predicted by the single-shell model are presented in Figs.9.1 and 9.2 for the two examples, respectively. Comparison between Fig.9.1 and Fig.4.2, and Fig.9.2 and Fig.4.3 indicates that the single-shell model is in good agreement with the multiple-shell model for axially compressed buckling of the two thin MWNTs considered here. In fact, both the critical axial stress and the associated wave-numbers (m,n) are almost the same for the two thin MWNTs and their equivalent singlelayer shells. For example, the critical axial stress for example 1 in Table 4.1 given by the single-shell model is 4.480 GPa (see Fig.9.1), which is very close to the exact value 4.481 GPa shown in Fig. 4.2. Similarly, the critical axial stress for example 2 in Table 4.1 given by the single-shell model is 2.166 GPa (see Fig. 9.2), very close to the exact value 2.172 GPa presented in Fig. 4.3. This offers a numerical confirmation of the analytical results of [129] for axially compressed buckling of thin MWNTs. Thus, as stated in [129] (also see Section 4.2), the critical axial stress of a thin MWNT is approximately equal to the critical axial stress of a SWNT of the average radius of the MWNT.

9.1.3 Elastic Buckling of Thick (or Solid) MWNTs

In many cases, synthesized MWNTs are thick or (almost) solid (the innermost radius-to-thickness ratio $\lambda \leq 1$) with large number of layers. The calculation for elastic buckling of these MWNTs is usually complicated and cannot be directly simplified by the single-shell model. Here, based on the single-shell model for thin MWNTs, an

approximate method is suggested to substitute a MWNT of many layers (usually thick or almost solid MWNTs) by a multilayer elastic shell of fewer thin layers (defined by the radius-to-thickness ratio around or larger than 4). This simplified method could further improve the effectiveness of the multiple-shell model [127-129] especially when the number N of nested tubes is very large, (such as 16-wall or 20-wall CNTs).

To illustrate this approximate method and demonstrate its effectiveness and accuracy, let us apply it to example 5 of Table 3.1 (a thick 8-wall CNT of the innermost radius $3\,nm$) under pure external pressure and example 4 of Table 4.1 (a thick 8-wall of the innermost radius 2.7) subjected to combined axial stress and external pressure. Then, we shall compare the results given by the approximate method with the exact data shown in Chapter 3 and 4 for the same examples. Based on the single-layer shell model for a thin MWNT, let us treat the outermost three layers of the first example (example 5 of Table 3.1) as a single-layer shell with bending stiffness $3D$ and thickness $3h$ (the layer IV in Fig. 9.3). Obviously, the radius-to-thickness ratio of the layer IV is larger than 5 and thus meets the condition set for thin MWNTs. Next, the next two tubes are treated as another single-layer shell with bending stiffness $2D$ and thickness $2h$ (the layer III), with the radius-to-thickness ratio larger than 6. Further, the next two tubes will be treated as another single-layer shell with bending stiffness $2D$ and thickness $2h$ (the layer II), with the radius-to-thickness ratio larger than 5. Finally, the innermost layer is now the layer I. Thus, the original eight-layer shell is reduced to a four-layer shell, as shown in Fig. 9.3.

Then Eq. (2.2) can now be used to each of the four new layers, with: $D_1=D$, $D_2=2D$, $D_3=2D$, $D_4=3D$, $h_1=h$, $h_2=2h$, $h_3=2h$ and $h_4=3h$, where D_k and h_k ($k=1$, 2, 3 and 4) are effective bending stiffness and thickness of the k-th new layer. The radius and the deflection of each new layer should be understood as its average radius and the deflection of its midline. In addition, the net pressure distribution stays unchanged, and thus the net pressure for every new layer can be obtained directly from the data shown in Fig. 3.3 for the 8-wall CNT, example 5 of Table 3.1. On the other hand, the vdW interaction pressure on the layer III due to the layer IV is determined by the spacing change between the layer 6 and the layer 5, and is equal to $c(w_6 - w_5)$. Assume that the change of interlayer spacing due to buckling is approximately uniform between

the midline of the layer IV and the midline of the layer III, thus we have $(w_{IV} - w_{III}) =$ $(w_6 - w_5) \times$ (the number of the layers between the two middle lines). Thus, the vdW pressure on the layer III due to the layer IV is $c(w_{IV} - w_{III}) / 2.5$. Similar modification should be made to the vdW interaction pressure between other new layers. Here, the interaction pressure between any two adjacent layers within each new layer is an "internal force" for the new layer and this is not accounted as an external pressure. In such a way, four equations for the new four-layer shell are given by

$$DV_I^8 w_I = cV_I^4 \left[\frac{2}{3}(w_{II} - w_I) \right] + \frac{F_\theta^I}{r_I^2} \frac{\partial^2}{\partial \theta^2} V_2^4 w_I - \frac{Eh}{r_I^2} \frac{\partial^4 w_I}{\partial x^4},$$

$$(2D)V_{II}^8 w_{II} = cV_{II}^4 \left[\frac{1}{2}(w_{III} - w_{II}) - \frac{r_I}{r_{II}^2} \cdot \frac{2}{3}(w_{II} - w_I) \right] + \frac{F_\theta^{II}}{r_{II}^2} \frac{\partial^2}{\partial \theta^2} V_2^4 w_{II} - \frac{E(2h)}{r_{II}^2} \frac{\partial^4 w_{II}}{\partial x^4},$$

$$(2D)V_{III}^8 w_{III} = cV_{III}^4 \left[\frac{2}{5}(w_{IV} - w_{III}) - \frac{r_{II}}{r_{III}^2} \cdot \frac{1}{2}(w_{III} - w_{II}) \right] + \frac{F_\theta^{III}}{r_{III}^2} \frac{\partial^2}{\partial \theta^2} V_2^4 w_{III} - \frac{E(2h)}{r_{III}^2} \frac{\partial^4 w_{III}}{\partial x^4},$$

$$(3D)V_{IV}^8 w_{IV} = -cV_{IV}^4 \left[\frac{r_{III}}{r_{IV}} \cdot \frac{2}{5}(w_{IV} - w_{III}) \right] + \frac{F_\theta^{IV}}{r_{IV}^2} \frac{\partial^2}{\partial \theta^2} V_2^4 w_{IV} - \frac{E(3h)}{r_{IV}^2} \frac{\partial^4 w_{IV}}{\partial x^4}. \qquad (9.4)$$

where r_i ($i = $ I, II, III and IV) is average radius of each new layer and w_i ($i = $ I, II, III and IV) is the deflection of the middle line of each new layer. The critical value P_{cr}/c (P_{cr} is the critical buckling pressure) based on this approximate method for the 8-wall CNT of the innermost radius $3 \, nm$ is $6.9858 \times 10^{-4} \, nm$ for free end, and $1.1 \times 10^{-3} \, nm$ for simply supported end, in good agreement with the exact results ($6.3738 \times 10^{-4} \, nm$ for free end, and $10^{-3} \, nm$ for simply supported end, as shown in Table 3.3 for example 5 of Table 3.1), with a relative error less than 10%. Similar agreement can be reached for buckling of example 7 of Table 3.1 (an almost solid 8-wall CNT of the innermost radius $0.65 \, nm$) under radial pressure.

For example 4 of Table 4.1 (an almost solid 8-wall CNT of the innermost radius $2.7 \, nm$) under pure axial stress or axial stress combined with an external pressure, a

similar new four-layer shell model can be obtained, as shown in Fig. 9.3, to replace the original 8-layer shell model. Following the similar procedure demonstrated above, the critical buckling stresses $9.99\,GPa$, $8.39\,GPa$, $2.01\,GPa$, $1.03\,GPa$ and $0.21\,GPa$ are obtained for the 8-wall CNT, when the external pressure-to-axial stress ratio $\beta = 0$, 0.01, 0.05, 0.1 and 0.5, respectively. These results agree well with the value $9.91\,GPa$, $7.74\,GPa$, $1.91\,GPa$, $0.99\,GPa$ and $0.20\,GPa$ calculated by the exact eight-layer model with the same value of β. The relative errors of the approximate method are less than 10%.

In view of the above comparison results, it is believed that the approximate method suggested here can be used to reduce the number of layers of MWNTs with acceptable relative errors (typically less than or around 10%). This approximate method has already been used in Chapters 3 and 4 to calculate the critical values of buckling loads for an almost solid 20-wall CNT (example 8 of Table 3.1) under radial pressures (see Table 3.3) and a 16-wall CNT (example 7 of Table 4.1) under pure axial stress (see Table 4.3). In particular, based on the approximate method the critical buckling pressure obtained for a specific group of 20-wall CNTs (of the innermost radius $1.5\,nm$) under both external and internal pressures, is in reasonably agreement with the experiment result [130].

9.1.4 The Lowest Vibrational Frequency of Thin MWNTs

It is shown in Section 7.3.2 that, as long as the lowest frequency (in-phase $R-$) mode is concerned, a thin DWNT, i.e., example 1 of Table 7.1, vibrates like a singlelayer shell with $w_1 = w_2$, $u_1 = u_2$ and $v_1 = v_2$ (see Fig. 7.4(b)) due to the strong effect of the interlayer vdW interaction. Thus, for the lowest frequency mode, it is also expected that a thin MWNT can be approximately treated as a singlelayer elastic shell with the average radius of the MWNT. Based on this assumption, in Eqs.(5.1) the $3N$ deflections u_k, v_k, and w_k ($k = 1,2,\cdots,N$) for the N individual tubes can be approximately replaced by three deflection functions u, v, and w, respectively and the radius r_k ($k = 1,2,\cdots,N$) of the N tubes can be replaced by the average radius r_{ave}. Consequently, the $3N$ equations in (5.1) reduce to just three equations describing free vibration of a singlelayer shell of

radius r_{ave}, bending stiffness D, in-plane stiffness Eh, mass density ρh and Poisson's ratio v. It is easy to see from Flugge Equations (5.1) that this elastic shell is equivalent to a singlelayer shell with the radius r_{ave}, bending stiffness ND, in-plane stiffness $E \cdot (Nh)$, mass density $\rho \cdot (Nh)$ and Poisson's ratio v, which is consistent with the single-layer shell model used for buckling analysis of thin MWNTs. The relative errors of the lowest frequencies given by the single-layer shell model for the thin MWNTs considered here are shown graphically in Fig.9.4 as compared to those predicted by the multiple-shell model with $L/(r_N \cdot m)$ ranging from 0.1 up to 100 and n varying between 0 and 10. As seen from Fig.9.4, for the thin 8-wall CNTs ($N = 8$) with the innermost radius-to-thickness ratio $\lambda = 4$ the relative error is lower than 20% for any given n and $L/(r_N m)$. In particular for $n > 2$, 4, 6, 8 and 10 the relative errors are less than 10% when $L/(r_N m) > 20$, 4, 2, 1 and 0.6, respectively. For the thinner 8-wall CNTs with $\lambda = 6$ the whole group of curves is well below 15% and especially, when λ reaches 8.5 the relatively errors of the single-shell model are less than 10%. The variation of relative errors with λ as well as n and $L/(r_N m)$ is qualitatively similar for 5-wall CNTs ($N = 5$) and DWNTs ($N = 2$), as shown in Fig.9.4. However, when number of layers N decreases from 8 to 5 and to 2 the relative errors associated with identical λ (or those close to each other) declines significantly. Particularly, to keep the relative errors less than 10% the critical value of λ for 8, 5 and 2-wall CNTs decreases from 8.5 to 7.6 and to 5, respectively. These results confirm numerically that when the lowest frequency mode is concerned a sufficiently thin $N-$wall CNT (e.g., DWNT with $\lambda \geq 5$, 5-wall CNT with $\lambda \geq 7.6$ and 8-wall CNTs with $\lambda \geq 8.5$) behaves like a single-layer elastic shell of its average radius, bending stiffness ND, in-plane stiffness $E \cdot (Nh)$, mass density $\rho \cdot (Nh)$ and Poisson's ratio v, and the lowest frequency can be well estimated by the single-layer shell model.

9.2 Simplified Shell Equations for CNTs

9.2.1 Introduction

So far, most of the existing elastic shell models for CNTs are based on the simplest Donnell equations of cylindrical shells. It is known that Donnell equations are based on several simplifications [116, 137-138, 141-142, 148]: 1) the contribution of two in-plane displacements to the changes in bending curvature is negligible; 2) the contribution of transverse shear forces to the equilibrium in the circumferential direction is negligible; 3) the in-plane inertia is negligible; and 4) the pre-stresses (for buckling problems only) are neglected in the two in-plane equations. The major advantage of Donnell equations over other more accurate shell equations (such as exact Flugge equations of cylindrical shells [137] which do not rely on any of the above four assumptions) is the remarkably simple mathematical form of Donnell equations, especially due to an uncoupled single equation for the radial deflection. Since the radial deflection is the dominant displacement component for many problems, such as buckling and radial vibration of elastic shells, this advantage largely simplifies technical complexity of elastic shell analysis in many important cases. Here, it is emphasized that this advantage of Donnell equations is even more crucial when elastic shell models are applied to MWNTs of large number of layers [129, 130-131]. On the other hand, although Donnell equations are prove to be an excellent approximate model and almost indistinguishable from exact shell models in many important cases, they indeed led to substantial errors in some cases of practical significance [139, 140, 143, 144, 175]. Hence, in view of unusual geometrical and material characteristics of CNTs, it is necessary to clarify the conditions under which Donnell equations or other simplified elastic shell models are applicable for CNTs.

This section gives a systematic study of applicability and limitations of simplified elastic shell equations for CNTs. Here, beside the Donnell model, a simplified Flugge model is also examined, which is derived from the exact Flugge equations [139] based on the last two assumptions of Donnell equations listed above and leads to an uncoupled single equation for the radial deflection [116, 139-144]. Various problems of static buckling and free vibration will be discussed with Donnell model (model I), simplified Flugge model (model II) and exact Flugge equations (model III). As will be seen below,

the simplified Flugge model (model II), which retains mathematical simplicity of Donnell model (model I), enjoys improved accuracy and enlarged range of applicability as compared to Donnell model, and thus is recommended for static and dynamic problems of CNTs.

9.2.2 The Shell Equations for CNTs

Most of existing elastic shell models for CNTs are based on the simplest Donnell equations of cylindrical shells. So, let us begin with a discussion of the assumptions of Donnell equations.

9.2.2.1 Donnell Equation (Model I)

For almost all important problems of CNTs discussed so far in the literature, tangential external loadings along axial or circumferential direction of CNTs are absent. For example, for MWNTs, because interlayer friction is usually so small that adjacent concentric tubes can almost freely slide to each other, it is assumed [127-129, 130-136] that the interlayer friction is negligible between any two adjacent tubes. In the absence of any tangential external force, dynamics of the radial deflection $w(x,\theta,t)$ of an elastic cylindrical shell of radius r is uncoupled with other two in-plane displacements, u (axial displacement) and v (circumferential displacement), and is governed by the Donnell equation as follows [127-129, 130-131].

$$DV^8 w = V^4 p(x,\theta) + F_x \frac{\partial^2}{\partial x^2} V^4 w + \frac{F_\theta}{R^2} \frac{\partial^2}{\partial \theta^2} V^4 w - \frac{Eh}{R^2} \frac{\partial^4 w}{\partial x^4} - \rho h \frac{\partial^2}{\partial t^2} V^4 w \qquad (9.5)$$

Here, different from Eq. (1.11), we only consider SWNTs subjected to axial and radial compression. Thus $F_{x\theta}$ disappears in Eq.(9.5). Once the radial deflection w is determined from (9.5), other two in-plane displacements u (axial displacement) and v (circumferential displacement) can be determined from other two (axial and circumferential) equations, see e.g. eqs. (6.33c) of [116], or eqs. (6.13a, 6.13b) of [141]. Eq. (9.5) and the other two equations (the latter will not be used in this section) are called

"Donnell equations", while the single equation (9.5) is also often called "Donnell equation".

The single uncoupled Donnell equation (9.5) has been widely used in many problems of cylindrical shells, due to its mathematical simplicity compared to other more accurate shell equations, such as exact Flugge's coupled three equations for the displacement components (u, v, w) (see eqs.(7a-c) of [137] or eqs. (11-13) of [139] for static case). The Donnell equations are based on four assumptions [116, 137-138, 141-142, 148]: 1) the contribution of two in-plane displacements to the bending curvature is negligible; 2) the contribution of transverse shear forces to the equilibrium in the circumferential direction is negligible; 3) the in-plane inertia is negligible; and 4) the pre-stresses (for buckling problems only) are neglected in two in-plane equations. The last two assumptions imply that the pre-stresses, $(F_x, F_\theta$ and $F_{x\theta})$, and in-plane inertias

$(\rho h \dfrac{\partial^2 u}{\partial t^2}$ and $\rho h \dfrac{\partial^2 v}{\partial t^2})$ are eliminated from two in-plane equations, and thus the two in-plane equations have the same form as their static counterparts without any pre-stresses. In particular, this means that Donnell equation (9.5) could give satisfactory results only

when the in-plane inertia $(\rho h \dfrac{\partial^2 u}{\partial t^2}$ and $\rho h \dfrac{\partial^2 v}{\partial t^2})$ is less important than the radial inertia

$(\rho h \dfrac{\partial^2 w}{\partial t^2})$. In addition, as long as the assumption 3) is concerned, it is noticed that the pres-stresses $(F_x, F_\theta$ and $F_{x\theta})$ do occur in each of all three equilibrium equations of more accurate shell models (such as Flugge equations, see eqs. (5a-5c) of [137], or eqs. (10-13) of [148]). Hence, the assumption 3) is indeed a simplifying approximation for buckling of elastic cylindrical shells and could lead to an error as compared to exact shell models such as Flugge equations.

9.2.2.2 Simplified Flugge Equation (Model II)

It was shown by Kempner [139, 141, 143-144] that, in the absence of the in-plane inertias and pre-stresses in two in-plane equations, an uncoupled single equation for the radial deflection can be derived from exact Flugge equations of cylindrical shells by a procedure similar to the derivation of Donnell equation. In the presence of all pre-presses

and radial inertia, after neglecting powers of $\dfrac{h^2}{12r^2}$ (or $\dfrac{(1-v^2)D}{Eh}\cdot\dfrac{1}{r^2}$ when D is a

material parameter independent of the thickness h) compared to unity, this single

equation can be written as (see Eqs. (6.34a-c) of [141], or [139-141, 143-144]):

$$D\cdot\nabla^4(\nabla^2+\frac{1}{r^2})^2 w+\frac{2D\cdot(1-v)}{r^6}\left(\frac{\partial^6 w}{\partial x^2\partial\theta^4}+\frac{\partial^4 w}{\partial x^2\partial\theta^2}-r^4\frac{\partial^6 w}{\partial x^6}\right)$$

$$=\nabla^4 p(x,\theta)+F_x\frac{\partial^2}{\partial x^2}\nabla^4 w+2\frac{F_{x\theta}}{r}\frac{\partial^2}{\partial x\partial\theta}(\nabla^4 w+\frac{\nabla^2 w}{r^2})+\frac{F_\theta}{r^2}\nabla^4(\frac{\partial^2 w}{\partial\theta^2}+w) \quad (9.6)$$

$$-\frac{Eh}{r^2}\frac{\partial^4 w}{\partial x^4}-\rho h\frac{\partial^2}{\partial t^2}\nabla^4 w$$

where the pre-stress terms are referred to Eq.(6.36) of [116].

In other words, the simplified Flugge single equation (9.6) is based on Donnell's assumptions 3) and 4) only (partially for the latter, because the pre-stress terms of (9.6) are approximate in nature), but not on the assumptions 1) and 2). On the other hand, it is seen from (9.5) and (9.6) that although the simplified Flugge equation (9.6) is slightly more complicated than the Donnell equation (9.5), it essentially retains mathematical simplicity of Donnell equation (9.5). Hence, it is of great interest to examine the range of applicability of the simplified Flugge equation (9.6) for CNTs, with a comparison to the Donnell equation (9.5). In connection with this, it should be stated that, in spite of known comparison between Donnell equations and exact Flugge equations [141, 143-144, 175], no detailed comparison has been made between exact Flugge model and the simplified Flugge model (9.6) for buckling and dynamic problems of elastic shells. Here, we would mention that an interesting equation has been suggested by Morley [143], which is obtained by neglecting some terms in the simplified Flugge equation (9.6) and has an elegant form very close to Donnell equation (9.5). As commented by Donnell [116], "the choice of coefficients in Morley's solution merely to give the desirable results in certain particular applications, rather than deriving them from basic principle as was done in Flugge's and our own (Donnell) solutions, makes their accuracy somewhat questionable in applications to unchecked problems." Hence, in the present work, we shall focus on the simplified (II).

9.2.2.3   Exact Flugge Equations (Model III)

Exact Flugge equations will be used in this section as standard elastic shell model. For static buckling of CNTs, because the general formulas of exact Flugge equations for various buckling problems are available in Flugge's book [137], the exact Flugge equations in the presence of the pre-stresses, which are somewhat lengthy, will not be cited here (see eqs. (7a-c) of [137]). For free vibration of CNTs, on the other hand, the exact Flugge equations of cylindrical shells are relatively simple because of the absence of the pre-stresses, and are given by (see [138] and [139])

$$r^2 \frac{\partial^2 u}{\partial x^2} + \frac{1}{2}(1-v)\frac{\partial^2 u}{\partial \theta^2} + \frac{r}{2}(1+v)\frac{\partial^2 v}{\partial x \partial \theta} - vr\frac{\partial w}{\partial x} + (1-v^2)\frac{D}{Ehr^2}\left[\begin{array}{c} \frac{1}{2}(1-v)\frac{\partial^2 u}{\partial \theta^2} + r^3\frac{\partial^3 w}{\partial x^3} \\ -\frac{r}{2}(1-v)\frac{\partial^3 w}{\partial x \partial \theta^2} \end{array}\right]$$

$$= \frac{\rho h}{Eh}(1-v^2)r^2 \frac{\partial^2 u}{\partial t^2},$$

$$\frac{r}{2}(1+v)\frac{\partial^2 u}{\partial x \partial \theta} + \frac{r^2}{2}(1-v)\frac{\partial^2 v}{\partial x^2} + \frac{\partial^2 v}{\partial \theta^2} - \frac{\partial w}{\partial \theta} + (1-v^2)\frac{D}{Ehr^2}\left[\begin{array}{c} \frac{3r^2}{2}(1-v)\frac{\partial^2 v}{\partial x^2} + \\ \frac{r^2}{2}(3-v)\frac{\partial^3 w}{\partial x^2 \partial \theta} \end{array}\right]$$

$$= \frac{\rho h}{Eh}(1-v^2)r^2 \frac{\partial^2 v}{\partial t^2},$$

$$vr\frac{\partial u}{\partial x} + \frac{\partial v}{\partial \theta} - w - (1-v^2)\frac{D}{Eh}r^2 \cdot \nabla^4 w + (1-v^2)\frac{D}{Ehr^2}\left[\begin{array}{c} -r^3\frac{\partial^3 u}{\partial x^3} + \frac{r}{2}(1-v)\frac{\partial^3 u}{\partial x \partial \theta^2} \\ -\frac{r^2}{2}(3-v)\frac{\partial^3 v}{\partial x^2 \partial \theta} - w - 2\frac{\partial^2 w}{\partial \theta^2} \end{array}\right]$$

$$= \frac{\rho h}{Eh}(1-v^2)r^2 \frac{\partial^2 w}{\partial t^2}$$

(9.7)

Here, it is emphasized that, even for static problems without any pre-stresses (for which assumptions 3) and 4) are valid), Eq.(9.6) is not exactly the same as the exact Eqs. (9.7) because some powers of $\dfrac{h^2}{12r^2}$ (or $\dfrac{(1-v^2)D}{Eh}\cdot\dfrac{1}{r^2}$ when D is a material parameter independent of the thickness h) have been neglected in Eq. (9.6) compared to unity. To our knowledge, no detailed comparison has been made between the simplified Flugge equation (9.6) (model II) and the exact Flugge equations (9.7) (model III) for buckling and dynamic problems. In particular, in view of unusual geometric and materials characteristics of CNTs, it is relevant to compare the simplified shell models (9.5) and (9.6) with exact Flugge equations (9.7).

9.2.3 Elastic Buckling of CNTs

First, let us examine static buckling of SWNTs. Since agreements between Donnell shell model (9.5) and available experiments or MD simulations have been demonstrated previously for various static buckling problems of CNTs [32, 120, 130-131], we shall focus on comparison between Donnell model (9.5), simplified Flugge model (9.6) and exact Flugge model (9.7). Here, we shall still consider simply-supported boundary conditions for cylindrical shells given by

$$w = 0, v = 0, F_x = 0 \quad \text{and} \quad M_x = 0 \tag{9.8}$$

Thus, for all three models I, II and III, the buckling modes are given by

$$u(x,\theta) = U\cos\frac{m\pi}{L}x\cdot\cos n\theta$$

$$v(x,\theta) = V\sin\frac{m\pi}{L}x\cdot\sin n\theta$$

$$w(x,\theta) = W\sin\frac{m\pi}{L}x\cdot\cos n\theta \tag{9.9}$$

Substitution of (9.9) into equations (9.5), (9.6) or (9.7) leads to homogeneous equations for the coefficient W or U, V and W. Thus, eigen-equation derived by existence condition of non-zero solution determines the buckling strain, as function of the wave numbers m and n. Finally, the critical strain for buckling is decided as the minimum buckling strain. Here, strictly speaking, m must be a non-zero integer for simply supported end conditions. However, it is easily understood that buckling of axially uniform modes, which do not strictly meet simply-supported end conditions, can be studied by the eigen-equation based on (9.8) by taking $m = 0$.

9.2.3.1 Axial Compression

Let us first discuss buckling of SWNT (of typical diameter 1.3 nm) under axial compression. It is shown [120] that the Donnell equation (9.5) (model I) gives good estimate of the critical stress, while the numbers m and n cannot be determined uniquely by Donnell model (I). On the other hand, the predicted axial wave-length of buckling mode, based on an empirical assumption [120] that the axial wave-length is equal to the circumferential wave-length, is found to be in good agreement with available MD simulations. It is well known [116] that, because linear theories of shell buckling admit a large number of different buckling modes which correspond to almost the same buckling stresses, they usually cannot predict the actual buckling mode without aid of any empirical assumption like that mentioned above. Thus, one cannot expect that simplified or exact Flugge model could give an accurate theoretical prediction for the wave-lengths of buckling mode of SWNTs without any empirical assumption. Therefore, our focus here is to compare three shell models and examine whether simplified Flugge equation (9.6) is in better agreement with exact Flugge equations than Donnell equation (9.5).

Because two key parameters for buckling modes are the circumferential wave number n and the dimensionless axial wave-length (normalized by the diameter $2r$) $L/(rm)$, the dependency of the buckling strain on $(L/(rm), n)$ is shown in Figs.9.5-9.7 for the model I, II and III, respectively. It is seen from Figs.9.5-9.7 that although all three models give similar results for n larger than 4 or $L/(rm)$ below unity, simplified Flugge model (II) is in much better agreement with exact Flugge model (III) than Donnell model

(I) for $n = 1$, 2 or 3 and $L/(r.m)$ larger than unity. In fact, it is found from the data shown in Figs.9.5-9.7 that the relative errors of the simplified Flugge model (II) is about less than 10% for n larger than 2 or $L/(rm)$ below 2, while the relative error of Donnell model (I) is about less than 10% only for n larger than 4 or $L/(rm)$ below 1. The critical strain given by the three models for several typical cases is shown in Table 9.1. In particular, because long SWNTs of larger aspect ratio exhibit beam-like buckling ($n = 1$), the critical strain given by elastic beam-model (Euler formula) is also shown in Table 9.1 for larger values of $L/(rm)$. It is seen from Table 9.1 that the simplified Flugge model (II) has much better accuracy than Donnell model (I) especially when $n = 2$ or 3 which corresponds to the minimum buckling strain in many important cases. In addition, simplified Flugge model (II) is a better approximate model than Donnell model (I) for very long shells for which the buckling mode corresponds to $n = 1$ (beam-mode). Indeed, in this case, Donnell equation (9.5) lead to an error in the order of magnitude, while simplified Flugge equation (9.6) differs than exact Flugge model (III) or the beam-model by a factor of two. This conclusion for very long SWNTs shows that simplified Flugge model (II) is significantly better than Donnell model (I) even in extreme cases.

9.2.3.2 Radial Pressure

It has been shown [130] that the Donnell model (I) gives satisfactory estimate of the critical pressure of CNTs. Here, our goal is to compare three shell models and examine whether simplified Flugge equation (9.6) is in better agreement with exact Flugge equations than Donnell equation (9.5). The dependency of buckling pressure on $(L/(rm), n)$ (where, by the definition of buckling under radial pressure, n is not smaller than 2) is qualitatively similar for all three models I, II and III, and thus is shown only for the exact Flugge model (III) in Fig.9.8. In addition, the relative errors of the model I and II compared to the exact model III are shown in Figs. 9.9 and 9.10, respectively. Particularly, the critical pressure given by three models (I, II and III) are shown in Table 9.2 for several typical cases. It is seen from Figs.9.9 to 9.10 and Table 9.2 that simplified Flugge model gives much smaller relative errors than Donnell model for $n = 2$ and $L/(rm)$ larger than one, while relative errors of both models (I and II) are not much

larger than 10 % for n larger than 2. On one hand, for $L/(rm)$ smaller than one, the minimum buckling pressure is decided by $n > 2$ (Fig.9.8) in which both model (I) and model (II) are applicable with relative errors not much larger than 10%. On the other hand, for larger $L/(rm)$ (it is the case when SWNTs are long or moderately long), the minimum buckling pressure is decided by $n = 2$ and thus the simplified Flugge model (II) is much better than Donnell Model (I). Hence, it is concluded that, in any case, simplified Flugge model (II) is a better approximate model than Donnell model (I) for buckling of CNTs under radial pressure.

9.2.4 Free Vibration of CNTs

Next, we shall compare simplified Flugge equation to Donell equation and exact Flugge equations in studying free vibration of CNTs.

9.2.4.1 Free Vibration of SWNTs

Let us first clarify the range of applicability of Donnell model (I) and simplified Flugge model (II) for free vibration of CNTs, in terms of the dimensionless axial wave-length $L/(rm)$ and the circumferential wave-number n. The vibration modes of a simply supported shell ($m > 0$) are given by (ω is the angular frequency)

$$u(x,\theta,t) = U \cos\frac{m\pi x}{L}\cos n\theta \cdot e^{i\omega t}$$

$$v(x,\theta,t) = V \sin\frac{m\pi x}{L}\sin\theta \cdot e^{i\omega t}$$

$$w(x,\theta,t) = W \sin\frac{m\pi x}{L}\cdot\cos n\theta \cdot e^{i\omega t} \tag{9.10}$$

where m should be a non-zero integer for simply supported end conditions. Substitution of (9.10) into equations (9.5), (9.6) or (9.7) leads to homogeneous equations, the existence condition for whose non-zero solution determine resonant frequencies as function of the numbers m and n.

Here, the frequencies given by the exact model (III) are shown in Fig. 9.11 for the SWNT of radius $r = 0.65\,nm$, while the relative errors of the frequencies given by two simplified models (I) and (II) compared to the exact model (III), are shown in Figs.9.12 and 13, respectively. Similar results for the radius $r = 5\,nm$, are given in Figs.9.14 to 9.16. It is seen from Figs. 9.11 to 9.16 that the relative errors of the simplified Flugge model (II) are about 10% or less provided that n is larger than one or $L/(rm)$ is smaller than two, while the relative errors of Donnell model (I) are about 10% or less provided that n is larger than 3 or $L/(rm)$ is less than one. Hence, the simplified Flugge model (II) is a much better approximate shell model than Donnell model I. In particular, it is seen from Figs. 9.11 and 9.14 that the critical aspect ratio $(L/(2r))$ at which the vibrational mode corresponding to the minimum frequency transfers from $n = 2$ to $n = 1$ (beam-mode) is about 5 for SWNT of radius $0.65\,nm$, and is larger than 10 for SWNT of radius $5\,nm$. In addition, for long simply supported shells, the vibrational mode corresponding to the minimum frequency is characterized by $m = 1$ and $n = 1$ (beam-model). In this case, it is seen from Figs. 9.12 to 9.13 and Figs. 9.15 to 9.16 that Donnell model (I) leads to errors in the order of magnitude, while simplified Flugge model (II) is comparable to exact Flugge model (III) (with relative errors 40%). These conclusions are qualitatively consistent with those drawn for static buckling discussed in section 9.2.3. It is emphasized that the improved accuracy of simplified Flugge model over Donnell model is significant for CNTs because the low-frequency vibrational modes often have circumferential wave number $n = 2$ or 3. Therefore, these results are important for further application of simplified shell models to CNTs, especially to MWNTs of large number of layers.

Here, it should be stressed that one essential shortcoming of simplified shell models (I) and (II) is that they give only one frequency ($R-$ mode vibration) for each combination (m, n), while the exact shell model (III) gives three frequencies for given m and n which represent $R-$, $L-$ and $T-$mode vibrations, respectively. Therefore, the simplified shell models (I) and (II) cannot be used to discuss $L-$ and $T-$vibration modes. In spite of this, because $R-$vibration is dominant in many important problems and the corresponding frequency is usually lower than the frequencies of $L-$ and $T-$modes, the $R-$modes are of major concern. An example of SWNTs of radius 5nm

are given in Fig. 9.17 for three frequencies given by the exact model (III), and single frequency given by the simplified model (I) and (II), respectively, which indicates that the $R-$mode frequency is lower than other two $(L-$ and $T-$mode) frequencies for almost all given $(L/(rm)$, $n)$ except $n = 0$ which means axisymmetric vibrational modes.

9.2.4.2   Beam-like Modes of SWNTs

The above results indicate that large errors of simplified shell models (I) and (II) could occur when $n = 1$ and $L/(rm)$ is much larger than one or two. It is the case when low-frequency vibrational modes of long SWNTs are concerned. Here, to compare the three models in this special case, let us discuss beam-like vibration of simply-supported SWNTs of larger aspect ratio whose lowest frequency corresponds to $n = 1$ and $m = 1$ [106, 163-164, 176-177]. All three shell models, together with the elastic beam-model [106, 163], are shown in Fig.9.18 for SWNTs of radius 0.65 nm, as function of the aspect ratio $(L/(2r))$. In addition, detailed comparison is shown in Table 9.3 for several relevant cases. It is found that, for special case of beam-like vibration of CNTs, simplified Flugge model (II), in which the effect of in-plane inertia is neglected [178-179], leads to as large as 40-50% relative errors as compared to exact Flugge model (III), while Donnell model (I) leads to errors in the order of magnitude.

9.2.4.3   Axially Uniform Vibration Modes of SWNTs

The results shown above do not include the special case of axially uniform vibrational modes with $m = 0$, which cannot strictly meet the simply-supported end conditions. However, it is easily understood that axially uniform vibrational modes can be studied by the eigen-equation based on the modes (9.9) by taking $m = 0$. The frequencies given by the exact model (III) and the simplified model (I) and (II), are shown in Table 9.4 for axially uniform modes $(m = 0)$ of SWNTs of radius $r = 0.65nm$ and $5 nm$. Since the case of $(m = 0, n = 1)$ represents a pure rigid-body motion, it is not included in Table 9.4. It is seen that the frequency for $n = 0$ (radial breathing mode) is higher than all other frequencies given in Table 9.4. On the other hand, for $n \geq 2$, the

frequencies shown in Table 9.4 monotonically increase with the circumferential wave-number n.

9.2.4.4   Radial Vibration Modes of MWNTs

The above results show that the simplified Flugge equation (9.6) retains the major mathematical simplicity of Donnell equation (9.5) and enjoy improved accuracy and wider range of applicability as compared to Donnell equation (9.5). Here, based on the multiple-shell model, we shall further use the simplified Flugge equation (9.6) to calculate the frequencies of $R-$mode of MWNTs, where the radial deflection is, indeed, predominant over circumferential and longitudinal deflections. In particular, the accuracy of this approximation will be examined, in detail, by comparing the simplified Flugge equation (9.6) to the exact Flugge equations (9.7). Applying Eq. (9.6) to each concentric tube of an N-wall CNT yields N dynamic equations for $R-$modes of the MWNT.

Proceeding in a similar way shown in Chapter 5 with $w_k(x,\theta,t) = W_k \sin\dfrac{m\pi x}{L}\cos n\theta \cdot e^{i\omega t}$

($k = 1,2\cdots,N$), one can obtain N frequencies for each pair of $L/(r_N \cdot m)$ and n. For 5-wall CNTs of the innermost radius $5nm$ and $0.65nm$, the results obtained by the multiple-shell model based on simplified single equation (9.6) (dotted lines) are displayed in Figs.9.19 and 9.20, respectively with comparison to the $R-$mode frequencies predicted by the multiple-shell model based on exact Flugge equations (5.1) (solid lines). With these results, the maximum relative errors of the simplified model (9.6) are calculated for each R-mode frequency of the two examples in Tables 9.5 and 9.6, respectively with n varying from 0 to 10.

(1) Large-radius 5-wall CNT (the innermost radius $5nm$)

Let us first take a look at a large-radius 5-wall CNT of the innermost radius $5\,nm$. In Fig.9.19 the multiple-shell model based on the exact Flugge equations shows that (i) for $n = 0$ or $n \geq 9$ the large-radius 5-wall CNT basically exhibits five $R-$modes all over the domain of $L/(r_5 \cdot m)$ considered here. The associated frequencies are labeled as R_1 to R_5 (dark solid lines), respectively. (ii) On the other hand, when $n = 1$ to 8, among the five possible $R-$modes, only two to four mainly exist over the domain of

$0.1 \leq L/(r_5 m) \leq 50$, e.g., the R – modes associated with frequencies R_3 to R_5 at $n = 1$, R_4 to R_5 at $n = 2$, R_1 to R_2 at $n = 4$, R_1 to R_3 at $n = 6$ and R_1 to R_4 at $n = 8$, while others can only be obtained in the domain of small $L/(r_5 \cdot m)$ (say $L/(r_5 m) \leq 0.5$ to 1.6).

It is evident in Fig.9.19 that the simplified model (9.6) is adequate for all the R – modes of the large-radius 5-wall CNT. The relative errors are less than 5% for the R – modes existing over the domain of $0.1 \leq L/(r_5 m) \leq 50$ and less than 10% for those only available when $L/(r_5 m) \leq 0.5$ to 1.6 (see Table 9.5). In particular, when $n = 0$ or $n \geq 9$ all the five frequencies given by the simplified model (9.6) (dotted lines) are in excellent agreement with the R – mode frequencies predicted by the exact model throughout the domain of $0.1 \leq L/(r_5 m) \leq 50$.

(2) Small-radius 5-wall CNT (the innermost radius 0.65nm)

For a small-radius 5-wall CNT of the innermost radius $0.65\,nm$ the qualitatively similar results can be obtained in Fig.9.20. (i) When $n = 0$ or $n \geq 3$ the simplified Flugge equation (9.6) offers a good approximation for all the five R – modes of the small-radius 5-wall CNT over the domain of $0.1 \leq L/(r_5 m) \leq 50$. As shown in Table 9.6, the relative errors are not more than 8% at $n = 3$ and less than 4% at $n = 0$ or $n > 3$. (ii) In addition, when $n = 1$ or 2 the five R – modes of example 4 only exist when $L/(r_5 m)$ is small (say $L/(r_5 m) < 0.9$ to 1.3). For these R – modes, the relative errors of the simplified model (9.6) shown in Table 9.6, are less than 10% when $L/(r_5 m) < 0.9$ to 1.3. It follows from the above results that the simplified single Flugge equation (9.6) agrees well with the exact Flugge equations in calculating all the R – mode frequencies of MWNTs with relative errors less than 10%. In general, it enjoys wider range of applicability for small-radius MWNTs of the innermost radius $0.65\,nm$ than for large-radius MWNTs of the innermost radius $5\,nm$.
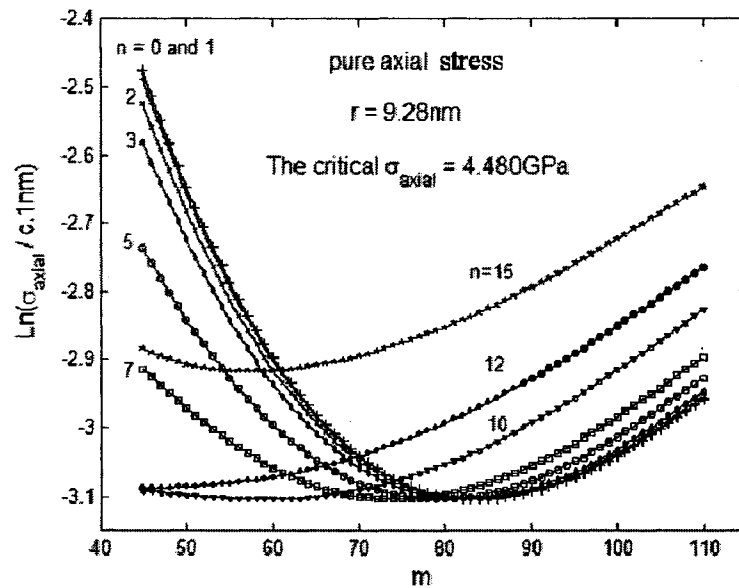
Fig. 9.1 The dependency of axial stress on the wave-numbers (m,n)

(singlelayer shell equivalent to example 1 in Table 4.1)
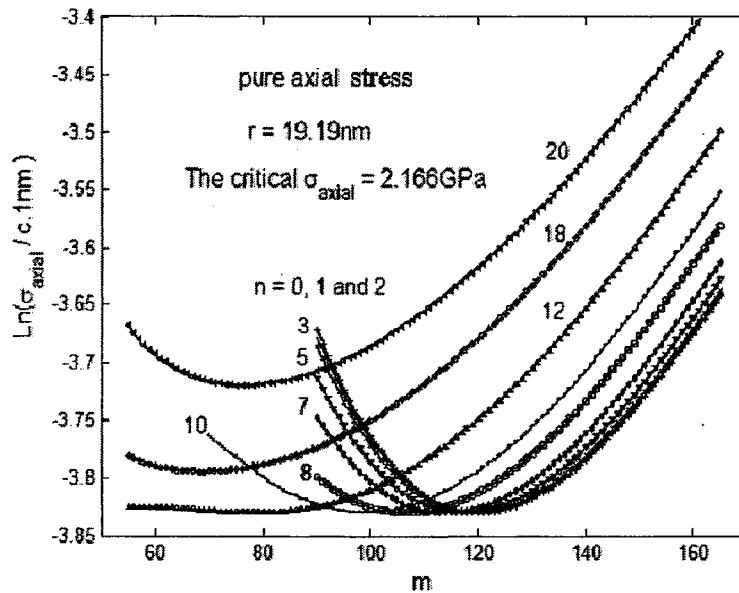
Fig. 9.2 The dependency of axial stress on the wave-numbers (m,n)

(singlelayer shell equivalent to example 2 in Table 4.1)
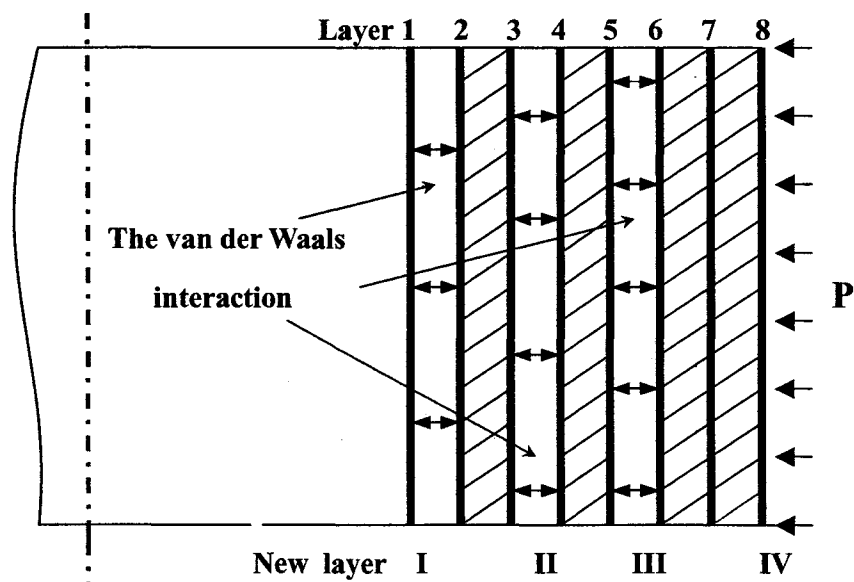
Fig. 9.3 The approximate method which substitutes an 8-wall MWNT by a 4-layer
elastic shell.
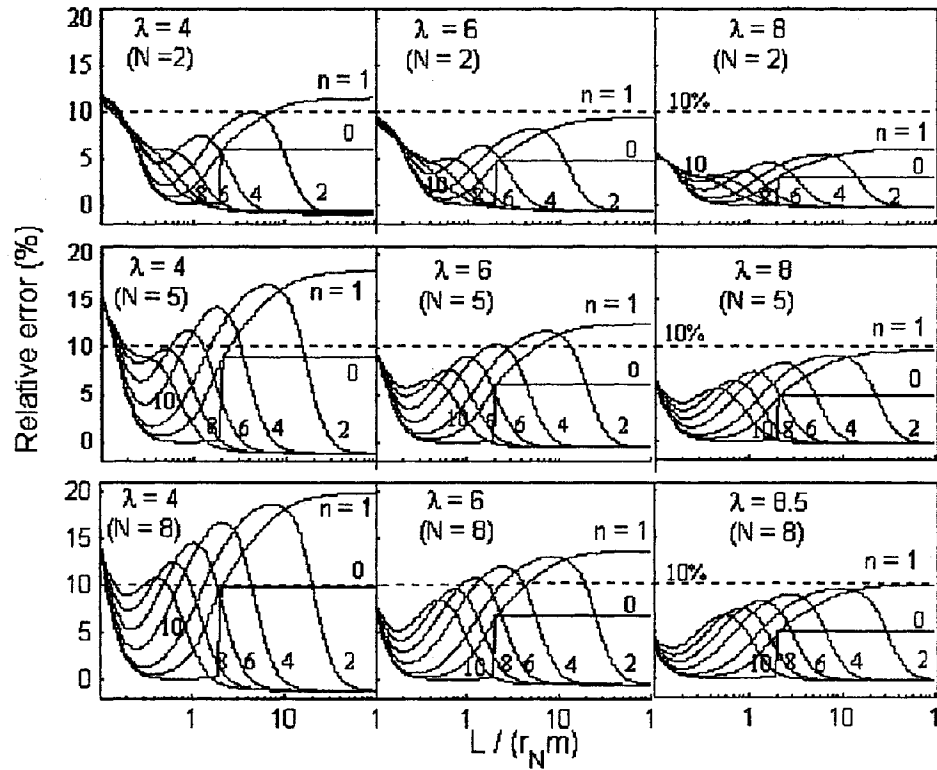
Fig.9.4 The relative errors of the lowest frequency of the in-phase R − mode obtained by the singlelayer shell model based on exact Flugge equations for thin N -wall CNTs with $N = 2$, 5 and 8, and various λ's ($\lambda = r_i / Nh$ and $h = 0.34nm$).
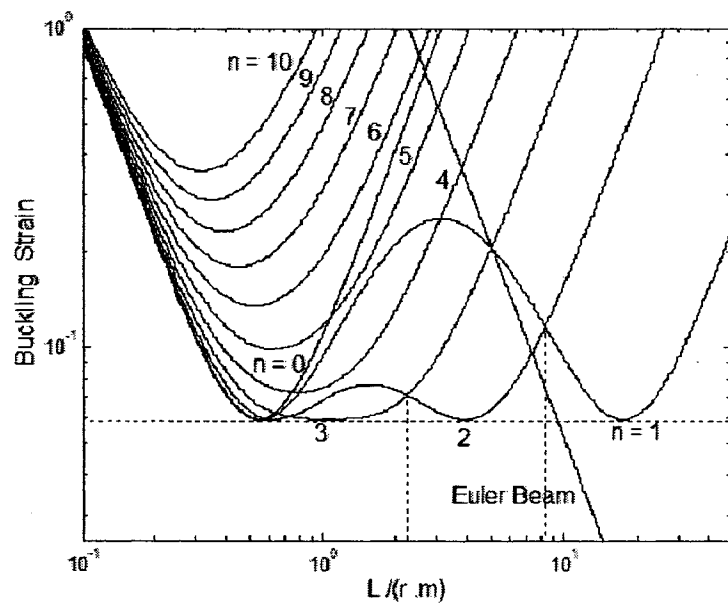
Fig. 9.5 The buckling strain given by Donnell model (I) for the SWNT

of radius 0.65 nm under axial compression.
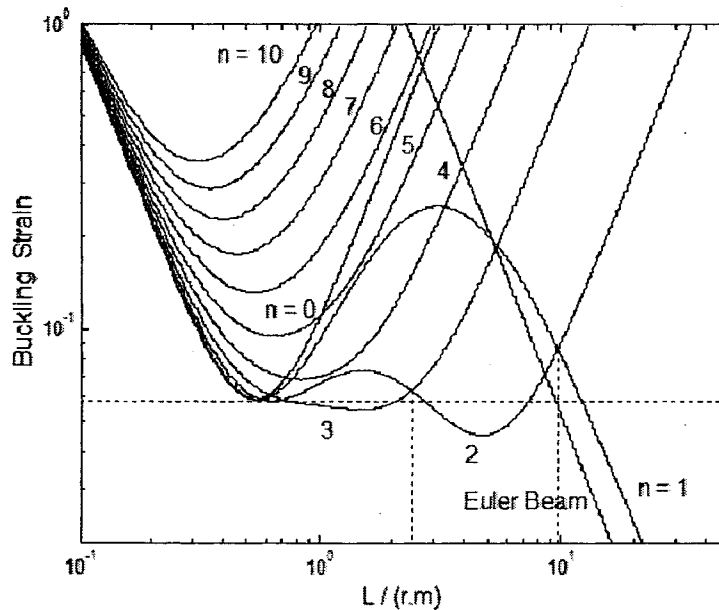
Fig. 9.6 The buckling strain given by simplified Flugge model (II) for

the SWNT of radius 0.65 nm under axial compression.
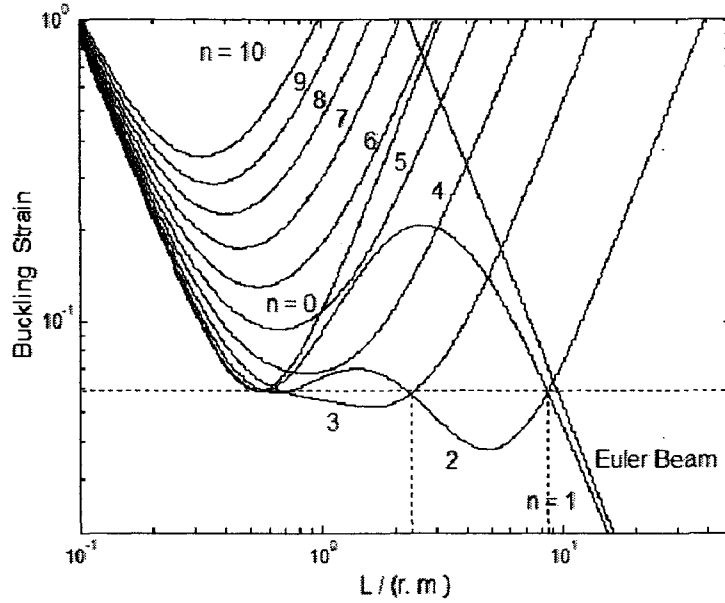
Fig.9.7 The buckling strain given by exact Flugge model (III) for

the SWNT of radius 0.65 nm under axial compression.
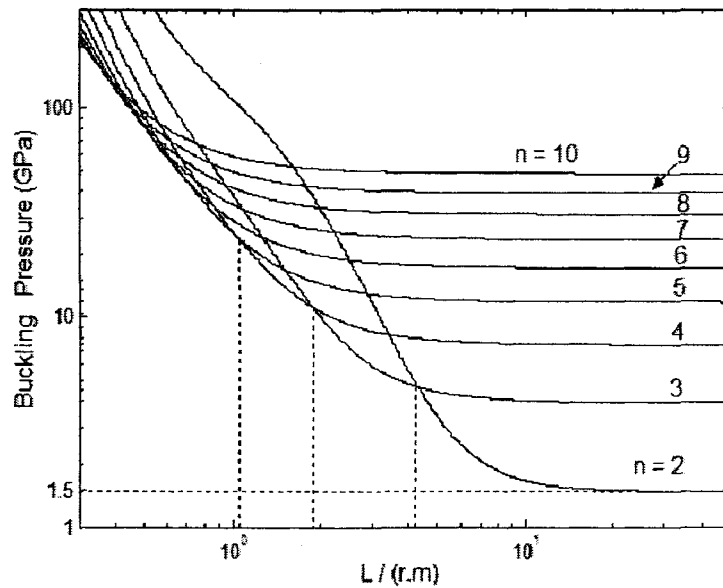
Fig.9.8 The buckling pressure given by exact Flugge model (III) for

the SWNT of radius 0.65 nm under radial pressure.
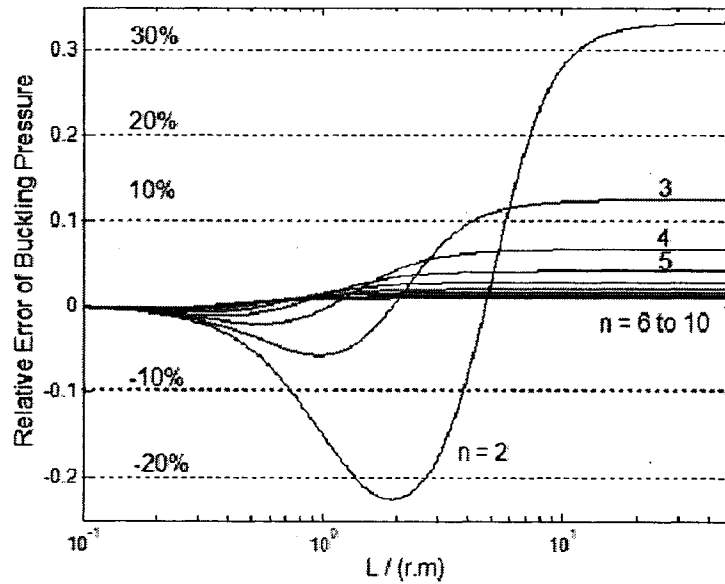
Fig.9.9 The relative error of buckling pressure predicted by Donnell model (I)

for the SWNT of radius 0.65 *nm* under radial pressure.
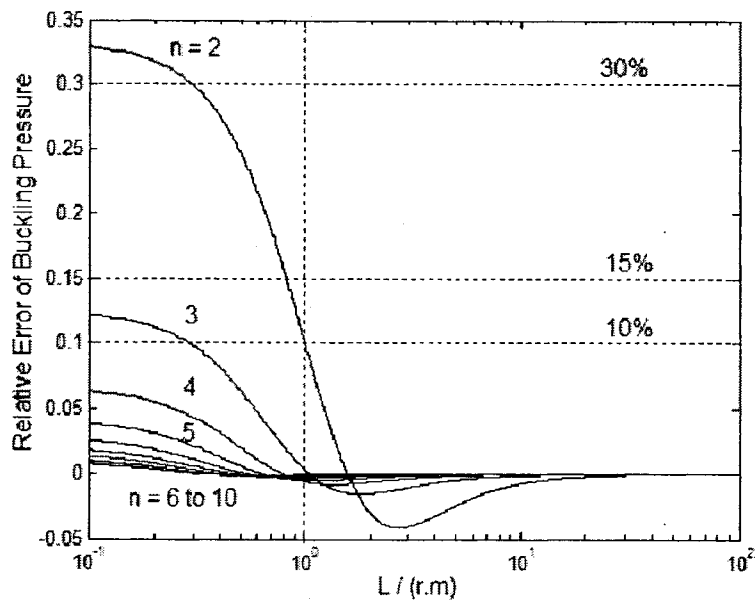
Fig.9.10 The relative error of buckling pressure predicted by simplified Flugge

model (II) for the SWNT of radius 0.65 *nm* under radial pressure.
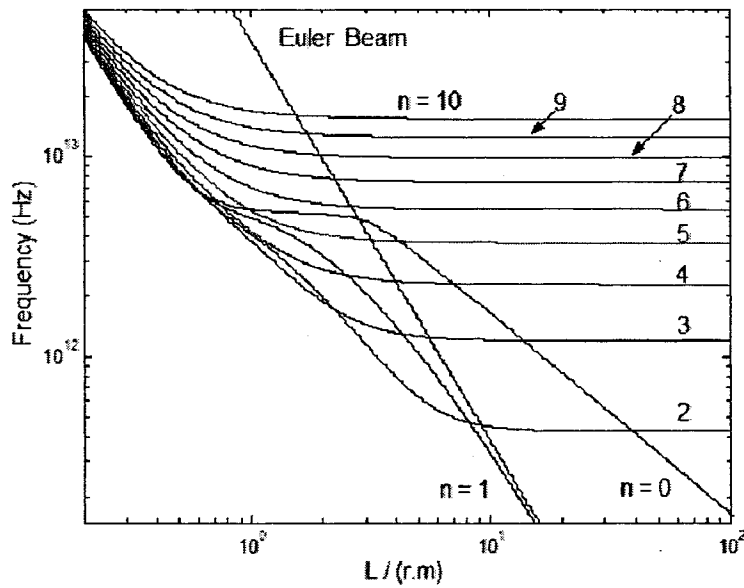
Fig.9.11 The frequency of radial vibration given by exact Flugge

model (III) for the SWNT of radius $0.65\,nm$.
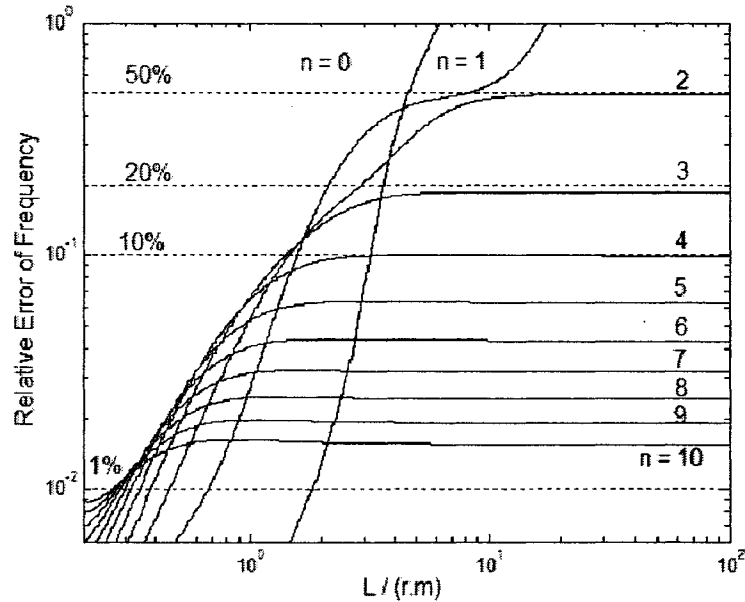
Fig.9.12 The relative error of radial vibration frequency predicted

by Donnell model (I) for the SWNT of radius $0.65\,nm$.
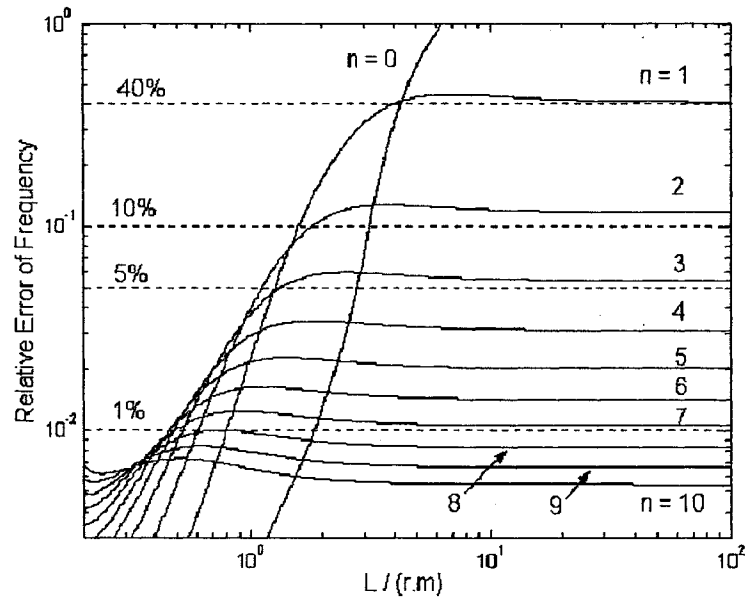
Fig.9.13 The relative error of radial vibration frequency predicted by

simplified Flugge model (II) for the SWNT of radius $0.65\,nm$.
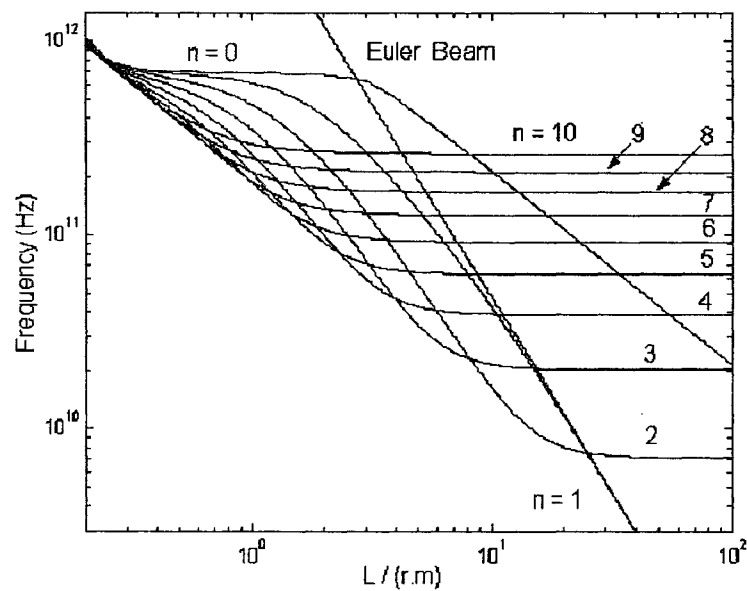
Fig.9.14 The frequency of radial vibration given by exact Flugge

model (III) for the SWNT of radius $5\,nm$.
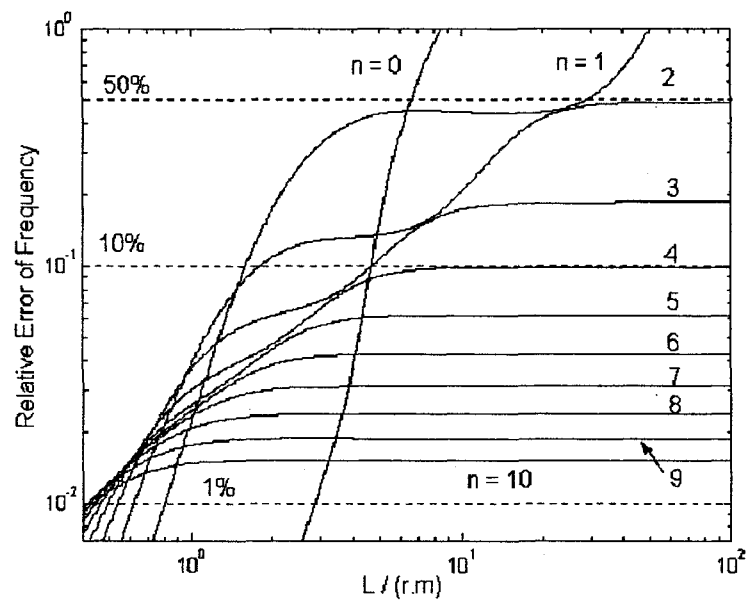
Fig.9.15 The relative error of radial vibration frequency predicted

by Donnell model (I) for the SWNT of radius $5\,nm$.
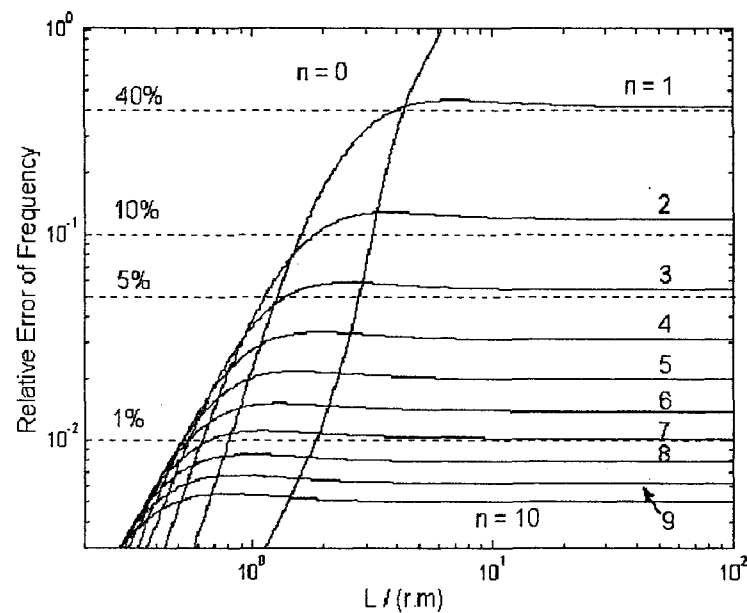
Fig.9.16 The relative error of radial vibration frequency predicted by

simplified Flugge model (II) for the SWNT of radius $5\,nm$.
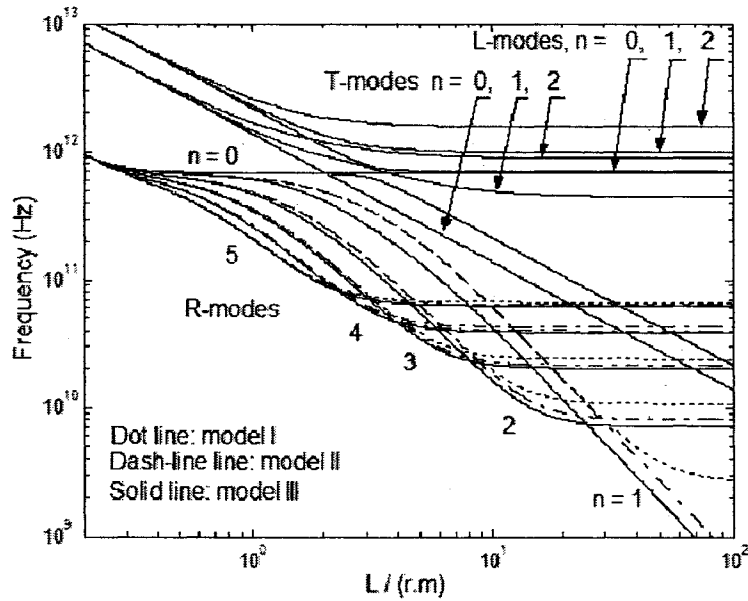
Fig. 9.17 The vibration frequencies given by three different shell

models for the SWNT of radius $5\,nm$.
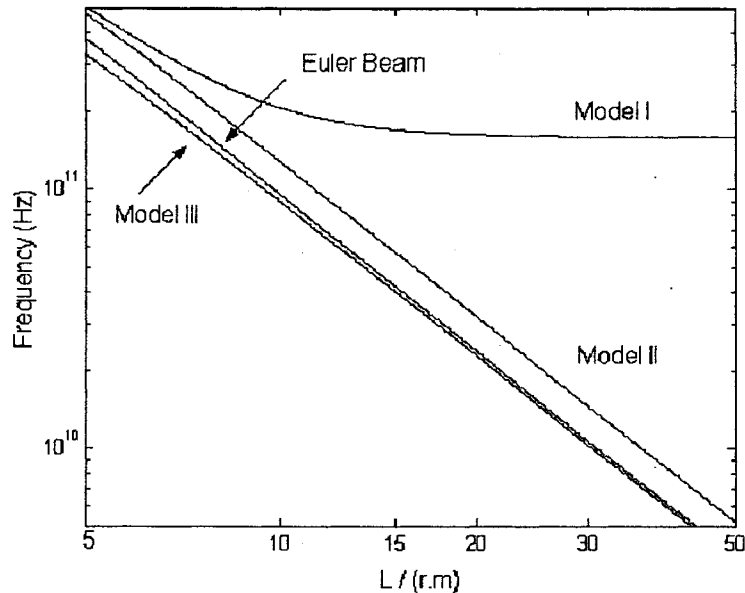
Fig.9.18 Comparison of beam-like vibrational frequencies given by

different models for the SWNT of radius $0.65\,nm$.
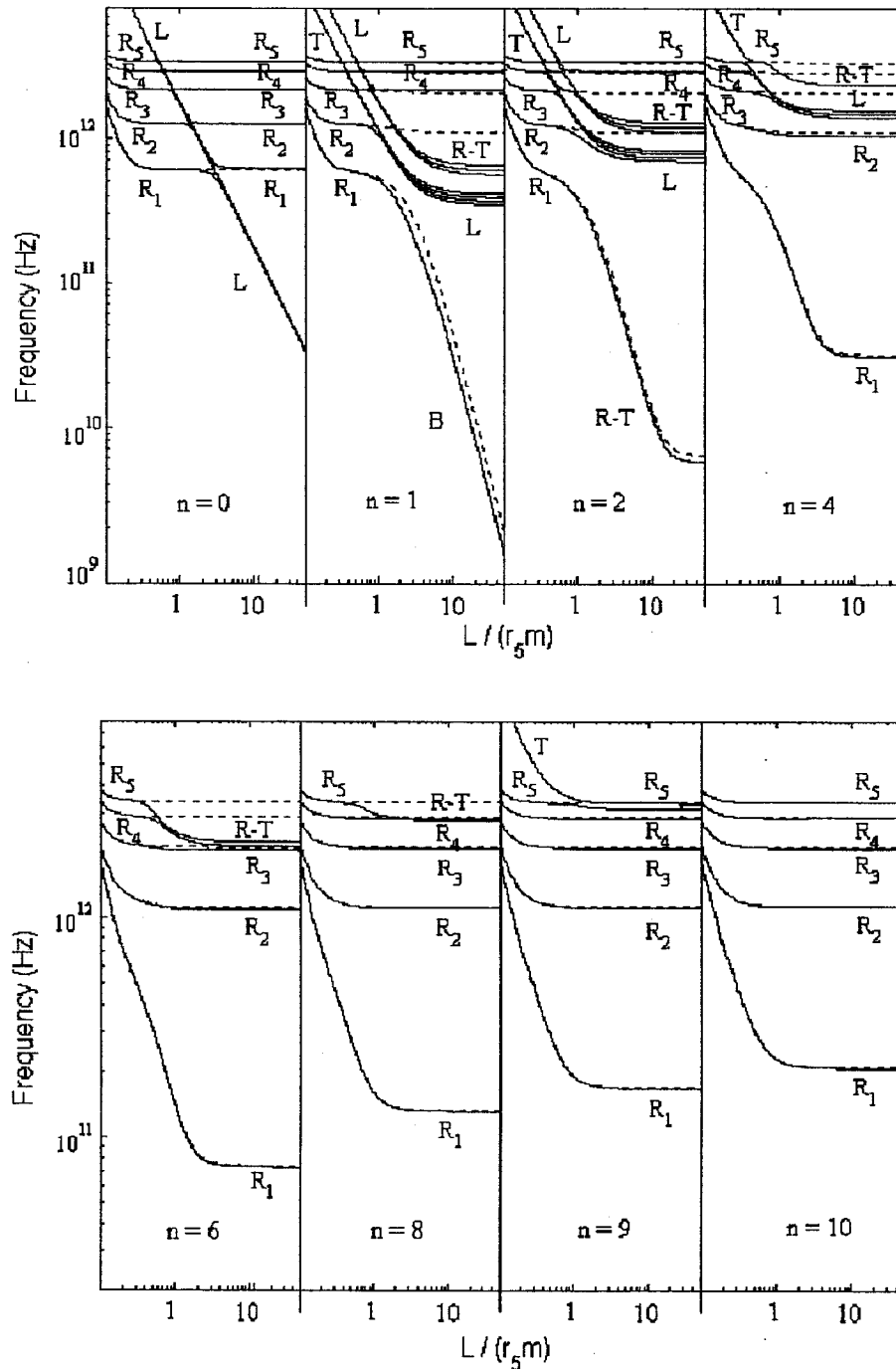
Fig. 9.19 R-mode frequencies of a large-radius 5-wall CNT (the innermost radius $5nm$) given by the five-shell model based on simplified Flugge equation (9.6) (dotted lines) and exact Flugge equations (9.7) (dark solid lines) with $0 \leq n \leq 10$.
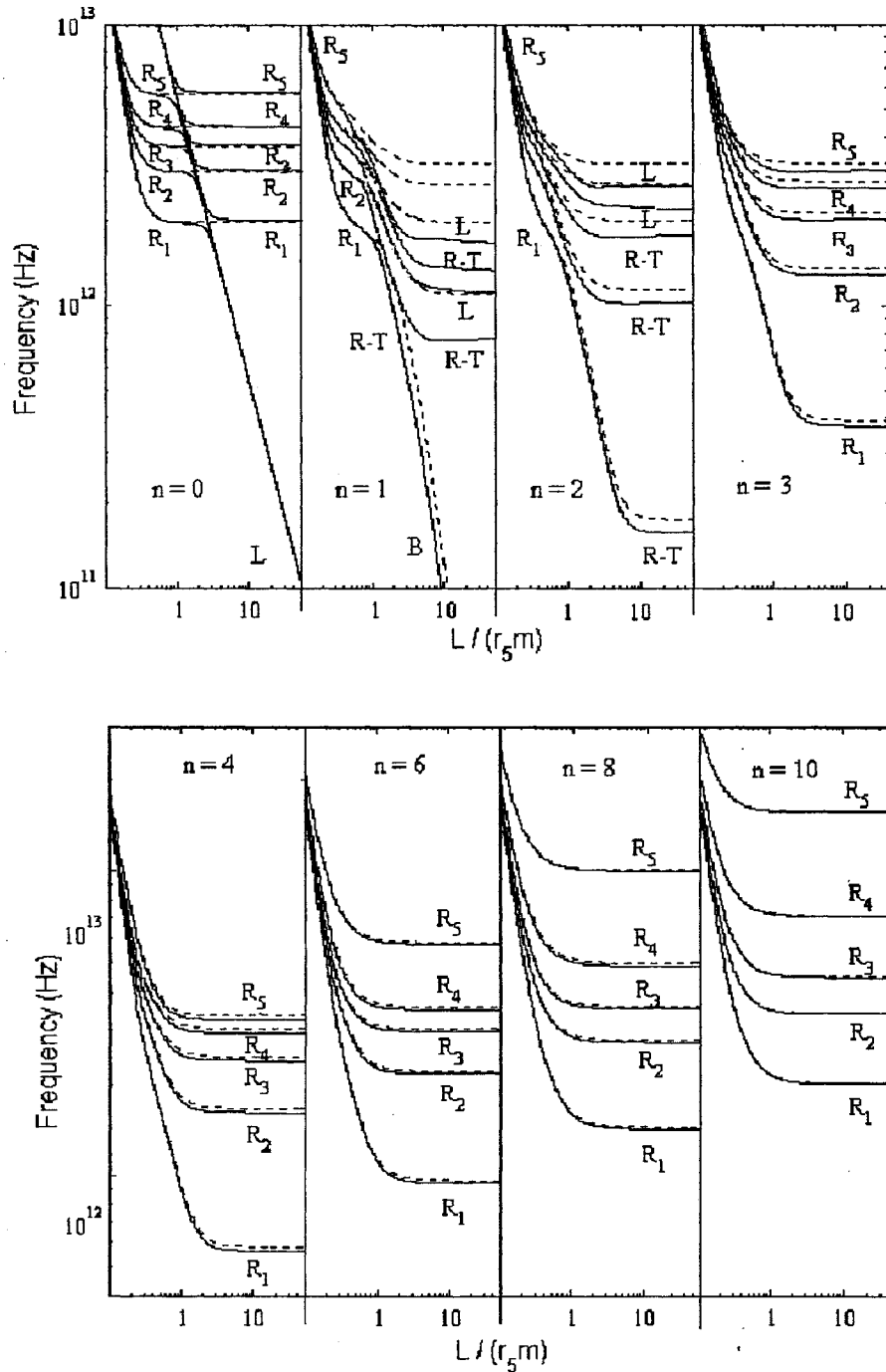
Fig.9.20 R -mode frequencies of a small-radius 5-wall CNT (the innermost radius 0.65nm) given by the five-shell model based on simplified Flugge equation (9.6) (dotted lines) and exact Flugge equations (9.7) (dark solid lines) with $0 \le n \le 10$.

Table. 9.1 The comparison of minimum buckling strains, predicted by different models for the SWNT of radius $0.65\,nm$ under axial compression.

Model / $L/(rm)$	Shell Model						Beam Model
	Model I		Model II		Model III		
0.7	$n=2$	0.0602	$n=3$	0.0592	$n=3$	0.0585	
1	$n=3$	0.0597		0.0565		0.0551	
2		0.0661		0.0574		0.0538	
3	$n=2$	0.0632	$n=2$	0.0552	$n=2$	0.0478	
4		0.0596		0.0470		0.0395	
5		0.0639		0.0455		0.0377	
6		0.0742		0.0488		0.0400	
7		0.0892		0.0556		0.0453	
8		0.1083		0.0652		0.0529	
9	$n=1$	0.1060	$n=1$	0.0969	$n=1$	0.0540	0.0651
10		0.0926		0.0818		0.0447	0.0527
20		0.0613		0.0235		0.0120	0.0132
50		0.2305		0.0039		0.0020	0.0021

Table. 9.2 The comparison of critical buckling pressure, predicted by different models for the SWNTs of radius $0.65\ nm$ or $5\,nm$ under radial pressure.

Radius (nm)	Buckling Modes		Aspect Ratio	Critical Buckling Pressure (GPa)		
	m	n		Model I	Model II	Model III
0.65	1	4	0.7	15.58	15.16	15.28
		3	1.5	6.29	5.84	5.90
		2	5	2.15	1.67	1.68
			10	2.00	1.13	1.51
			20	1.97	1.48	1.48
	0	2		1.97	1.48	1.48
5.00	1	7	0.7	0.077	0.077	0.076
		5	1.5	0.035	0.033	0.034
		3	5	10.90×10^{-3}	9.90×10^{-3}	9.90×10^{-3}
		2	10	5.05×10^{-3}	4.19×10^{-3}	4.20×10^{-3}
			20	4.38×10^{-3}	3.31×10^{-3}	3.30×10^{-3}
	0	2		4.32×10^{-3}	3.31×10^{-3}	3.24×10^{-3}

Table. 9.3 The comparison of beam-like vibration frequencies ($n = 1$), predicted by different models for the SWNTs of radius $0.65\,nm$ or $5\,nm$.

Radius (nm)	$L/(rm)$	Frequency (Hz)			
		Model I	Model II	Model III	Beam model
0.65	0.5	8.21×10^{12}	8.18×10^{12}	8.16×10^{12}	
	1	5.09×10^{12}	5.08×10^{12}	4.97×10^{12}	
	5	1.51×10^{12}	1.50×10^{12}	1.04×10^{12}	1.53×10^{12}
	10	5.06×10^{11}	4.76×10^{11}	3.29×10^{11}	3.82×10^{11}
	50	1.59×10^{11}	2.08×10^{10}	1.47×10^{10}	1.53×10^{10}
	100	1.58×10^{11}	5.22×10^{9}	3.68×10^{9}	3.82×10^{9}
5	0.5	6.80×10^{11}	6.80×10^{11}	6.78×10^{11}	
	1	6.26×10^{11}	6.25×10^{11}	6.11×10^{11}	
	5	1.94×10^{11}	1.94×10^{11}	1.30×10^{11}	1.93×10^{11}
	10	6.19×10^{10}	6.18×10^{10}	4.28×10^{10}	4.81×10^{10}
	50	3.80×10^{9}	2.71×10^{9}	1.91×10^{9}	1.93×10^{9}
	100	2.80×10^{9}	6.78×10^{8}	4.79×10^{8}	4.81×10^{8}

Table. 9.4 The comparison of vibration frequencies when $m = 0$, predicted by different models for the SWNTs of radius $0.65\,nm$ or $5\,nm$.

Radius (nm)	n	Frequency (Hz)		
		Model I	Model II	Model III
0.65	0	5.31×10^{12}	5.31×10^{12}	5.30×10^{12}
	2	6.31×10^{11}	4.73×10^{11}	4.23×10^{11}
	3	1.42×10^{12}	1.26×10^{12}	1.20×10^{12}
	4	2.52×10^{12}	2.37×10^{12}	2.29×10^{12}
	5	3.94×10^{12}	3.78×10^{12}	3.71×10^{12}
5.00	0	6.90×10^{11}	6.90×10^{11}	6.90×10^{11}
	2	1.07×10^{10}	7.99×10^{9}	7.15×10^{9}
	3	2.40×10^{10}	2.13×10^{10}	2.02×10^{10}
	4	4.26×10^{10}	4.00×10^{10}	3.88×10^{10}
	5	6.66×10^{10}	6.39×10^{10}	6.27×10^{10}

Table 9.5 The maximum relative errors of R-mode frequencies predicted by the simplified Flugge equation for a five-wall CNT of the innermost radius $5nm$ when $0 \le n \le 10$ and $0.1 \le \tau \le 50$ or in specified range of τ, where $\tau = L/(r_5 m)$.

n	0	1	2	4	6	8	9	10
R_1	-2.0%	<10% $\tau<1.4$	<10% $\tau<1.6$	3.0%	1.5%	0.9%	0.7%	0.6%
R_2	-0.5%	<10% $\tau<0.9$	<10% $\tau<1$	5.0%	1.7%	0.9%	0.7%	0.6%
R_3	-0.2%	4.6%	<10% $\tau<0.6$	10% $\tau<0.7-0.8$	3.0%	1.2%	0.8%	0.7%
R_4	-0.1%	2.4%	-2.8%	<10% $\tau<0.4-0.5$	<10% $\tau<0.6-0.7$	2.8%	1.2%	0.8%
R_5	-0.1%	1.7%	-1.9%	<10% $\tau<0.8-0.9$	<10% $\tau<0.4-0.5$	<10% $\tau<0.9$	2.0%	1.0%

Table. 9.6 The maximum relative errors of R-mode frequencies predicted by the simplified Flugge equation for a five-wall CNT of the innermost radius $0.65nm$ when $0 \le n \le 10$ and $0.1 \le \tau \le 50$ or in specified range of τ, where $\tau = L/(r_5 m)$.

n	0	1	2	3	4	6	8	10
R_1	-1.8%	<10% $\tau<1.3$	<10% $\tau<1.3$	6.0%	3.4%	1.5%	0.9%	0.6%
R_2	-1.2%	10% $\tau<1.1$	<10% $\tau<1.1$	6.0%	3.5%	1.6%	0.9%	0.6%
R_3	-1.0%	<10% $\tau<1$	<10% $\tau<1$	6.0%	3.6%	1.6%	0.9%	0.6%
R_4	-1.3%	<10% $\tau<0.9$	<10% $\tau<0.9$	7.0%	3.8%	1.6%	0.9%	0.6%
R_5	-1.8%	<10% $\tau<0.9$	<10% $\tau<0.9$	8.0%	3.6%	1.6%	0.9%	0.6%

Chapter 10

Conclusions and Future Plans

10.1 Conclusions

In this thesis, a multiple-shell model has been utilized to conduct comprehensive studies on elastic buckling and free vibration of MWNTs, most of which still remain challenging for nano-scale experiments and atomistic simulations. Here each of the concentric tubes of a MWNT is modeled as an individual elastic shell, coupled with adjacent tubes via the interlayer vdW interaction without interlayer friction [127-129]. Thus, different from the oversimplified single-shell model previously used for MWNTs, the multiple-shell model enables us to examine the effect of the interlayer vdW interaction and the interlayer sliding on mechanical behavior of MWNTs. In particular, it is found that the multiple-shell model is in good agreement with available experiments and atomistic modeling for buckling and free vibration of MWNTs [130-136]. The major conclusions based on the multiple-shell model are summarized in the following sections.

10.1.1 Buckling Behavior of MWNTs

(1) Buckling of MWNTs under External Pressure

(i) The critical external pressure of simply supported MWNTs is always associated with minimum half axial wave number $m=1$, while the corresponding circumferential wave number n varies between 2 and 4 for MWNTs studied here. Especially, the critical pressure for a thin N-wall CNT is approximately N times that of a SWNT of the average radius of the MWNT.

(ii) Introducing an internal pressure to externally pressured MWNTs with internal-to-external pressure ratio reaching a critical value results in sudden change in buckling mode of MWNTs with circumferential wave number n jumping from a small number to a relatively large number (e.g., n increases from 2 to 9, 6 and 11 for examples 1, 2 and 3 in Table 3.1). At the same time, an abrupt up-shift of the

198

critical external pressure arises for thick or thin MWNTs but only a small change of the critical external pressure occurs for (almost) solid MWNTs.

(iii) In particular, the critical pressure $1.32 GPa$ predicted by the multiple-shell model for a 20-wall CNT under both internal and external pressures is found to be in good agreement with known experimental result $1.48 GPa$ [75], showing an evidence for the relevance of the multiple-shell model for MWNTs.

(2) Axially Compressed Buckling of Pressured MWNTs

(i) For simply supported MWNTs under pure axial compression, there always is more than one combination (m, n) of the half axial wave number and circumferential wave number of the buckling mode which corresponds to the same minimum axial stress. Especially, the critical axial stress of a thin MWNT is approximately equal to that of a SWNT of the average radius of the MWNT.

(ii) Applying an internal pressure to axially compressed CNTs increases the critical axial stress of non-axisymmetric buckling modes, while it has no effect on the axisymmetirc mode $(n = 0)$. In former case, the effect of an internal pressure is strong for thin MWNTs, moderate for thick MWNTs, and negligible for (almost) solid MWNTs. In particular, the effect of the internal pressure on critical axial stress predicted by the present model for SWNTs of radius $1.3 nm$ appears to be in qualitative agreement with Ni et al.'s MD simulation results [87].

(iii) For MWNTs subject to both axial force and external pressure, the buckling mode can be determined uniquely. The critical buckling condition, expressed as the axial stress-external pressure relation, is strongly nonlinear due to the very small radius-to-thickness ratio of MWNTs as compared to that of conventional thin shells which exhibit the well-known linear critical buckling condition.

10.1.2 Vibrational Behavior of MWNTs

(1) Radial Breathing Modes (RBMs) of MWNTs

(i) In the absence of an external pressure, the RBMs of MWNTs predicted by the

present multiple-shell model agree very well with the results of atomistic models [24, 74] and experiments [71], demonstrating the effectiveness of the present shell model to free vibration of MWNTs.

(ii)   In the presence of an external pressure, the interlayer vdW interaction coefficients between outmost few layers of MWNTs increase significantly due to the pressure-induced reduction of interlayer spacing. As a result, RBM frequencies of MWNTs almost linearly up-shift with increasing external pressure. The most significant pressure effect occurs for the highest frequency mode of large-radius MWNTs (the innermost radius $> 1\,nm$) or an intermediate-frequency mode of small-radius MWNTs (the innermost radius $< 1\,nm$), where the outermost tubes are involved substantially and most adjacent tubes vibrate counter-phase with significant change in the interlayer spacing.

(2) General Vibrational Properties of MWNTs

(i)   During vibration, the motions of all the nested tubes of a MWNT are generally coupled with each other via the interlayer vdW interaction. This effect of the interlayer vdW intreracton is most significant for radial (R) modes of the large-radius MWNTs (e.g., the innermost radius $5\,nm$) with low stiffness of the individual tubes, and moderate for the small-radius MWNTs (e. g., the innermost radius $0.65\,nm$) with higher stiffness of the individual tubes when the circumferential wave number n is nonzero but relatively small (e.g., $3 < n < 7$), while it becomes negligible for torsional (T) and longitudinal (L) modes regardless the radius of MWNTs.

(ii)   As a result, T– and L– modes of MWNTs are essentially the vibrations of individual tubes, while R–modes of the large-radius MWNTs or the small-radius MWNTs with small nonzero n are characterized by collective radial vibrations of all the nested tubes, where the in-phase mode is always associated with the lowest R–mode frequency, the counter-phase mode is associated with the highest R–mode frequency, and mixed modes have intermediate frequencies.

(3) Special Vibrational Modes of MWNTs

(i)   For axisymmetric vibration ($n = 0$), $L-$ and $R-$modes of MWNTs are strongly coupled with each other in the $L-R$ transition zone due to the Poisson-ratio effect. In particular, different from non-axisymmetric $L-$modes of MWNTs (with large n), which are basically uncoupled L-vibration of individual tubes, axisymmetric $L-$modes of MWNTs are usually collective vibrations of nested tubes due to the Poisson-ratio effect, interlayer vdW interaction and especially, the almost identical $L-$mode frequency of individual tubes.

(ii)   For beam-like vibration ($n = 1$), the multiple-(Euler) beam model agrees well with the multiple-shell model for almost coaxial $B-$mode of MWNTs and the non-coaxial $B-$modes of small-radius MWNTs (e.g., 2-5 wall CNTs of outermost radius less than $2\,nm$), with relatively errors less than 10%. However, the relative errors between the two models are up to 30 to 50% for high-order non-coaxial modes of large-radius MWNTs, due to significant non-beam-like cross-sectional deformation caused by the interlayer vdW interaction. Therefore, the multiple-beam model is more relevant for small-radius MWNTs than large-radius MWNTs.

(iii) The lowest frequency of simply supported MWNTs is always associated with the minimum axial half wave number $m = 1$. When the length-to-outermost radius ratio increases, the lowest frequency of MWNTs decreases monotonically and the associated mode shifts from a $R-$mode with larger n (say, $n = 3-6$), to a $R-T$ combined mode with smaller n (say, $n = 2-3$), and finally, to a beam-like coaxial $B-$mode with $n = 1$.

10.1.3 Simplification of the Multiple-shell Model

(1) The Single-shell Model for Thin MWNTs

(i)   For elastic buckling and the lowest frequency vibration, a thin N-wall CNT is approximately equivalent to a singlelayer elastic shell whose effective bending stiffness and thickness are N times the effective bending stiffness and thickness of SWNTs and the radius is equal to the average radius of the thin N-wall CNT.

(ii)   Based on the single-shell model for thin MWNTs, an approximate method is suggested for buckling of thick or (almost) solid MWNTs, which can effectively reduce the problem of MWNTs of many layers to the problem of a multilayer elastic shell of fewer layers.

(2) The Accuracy and Applicability of Simplified Flugge Equations

For general cases of static buckling and free vibration of SWNTs, the relative errors of the simplified Flugge model (compared to the three exact Flugge equations) are generally less than 10% for n larger than 1 or 2, or for $L/(r.m)$ smaller than two, while the relative errors of Donnell model are less than 10% only for n larger than 3 or 4, or for $L/(r.m)$ smaller than one. This conclusion is significant because the critical buckling mode and low-frequency vibrational modes often have circumferential wave number $n = 2$ or 3. Hence, simplified Flugge model has a significantly enlarged range of applicability compared to Donnell model, and covers almost all important cases of major concern. Here, we would emphasize that simplified shell models, characterized by a single uncoupled equation for radial deflection, will be particularly useful for MWNTs of large number of layers. On the other hand, such simplified shell models are applicable only for radial deformation of cylindrical shells with simpler end conditions (such as simply-supported ends).

All these results convincingly show that the multiple-shell model can be used to describe overall mechanical behavior of CNTs with characteristic length much larger than the c-c bond length (about 0.14 nm) of CNTs. On the other hand, we would like to comment that elastic shell model would be questionable for highly localized deformation with very small characteristic length comparable to the c-c bond length of CNTs, such as cracks or local buckling of very small wave-length. Thus the elastic shell model are usually limited to reversible elastic deformation and do not account for fracture and failure [180-181].

10. 2 Future Plans

In the current thesis, the multiple-shell model has been used for characterization of elastic buckling and free vibration of MWNTs. Indeed, because nano-scale experiments are usually difficult and atomistic simulations still remain expensive and formidable for MWNTs, the multiple-shell model [127-129] does offer an alternative method for study of MWNTs. In particular, the comparison between the present shell model and available experiments and atomistic simulations convincingly demonstrates the effectiveness and accuracy of the present shell model for CNTs [130-136]. Thus, it is anticipated that the multiple-shell model can be further utilized for characterization of the mechanical behavior of MWNTs. In particular, the further work could include:

(1) **The Effect of Dimensional Factors on Buckling of MWNTs:** It is known that MWNTs are distinguished from SWNTs due to multilayer structure and associated interlayer vdW interaction. Especially, synthesized MWNTs usually have wide distribution of radius and the number of layers, and will be used in practical application with different aspect ratios. Thus, the effect of these dimensional factors on buckling properties is important for MWNTs as building blocks in nano-devices. Very recently, the effect of geometry of CNTs has already been discussed based on MD simulation [89-90]. However, since MD simulation is computationally expensive, these studies [89-90] are limited to CNTs of not more than four layers. Using the cost-effective multiple-shell model [127-129], one is able to conduct a comprehensive study on this issue by considering MWNTs of the innermost radius ranging from the order of $1nm$ to the order of 10 nm, the number of layers varying from two to several dozens and aspect ratio increasing from the order of 1 to the order of 100.

(2) **The Buckling Analysis of MWNTs under Torsional Load:** In the present work, elastic buckling of MWNT under axial force and radial pressure has been discussed in detail. Another loading condition, which is of practical interest, is torsional load. Recently, following the present multiple-shell model [127-129], torsional buckling of DWNTs embedded in an elastic medium has been investigated analytically [182], while torsional strength of individual SWNTs and MWNTs has

been calculated based on an atomistic modeling [183]. However, systematical study on torsional buckling of MWNTs has not been reported in the literature. Based on the multiple-shell model [127-129], numerical work can be done to further discuss the buckling behavior of MWNTs under torsional load and examine the effect of geometric size of MWNTs and especially, the interlayer vdW interaction on torsional buckling of MWNTs.

(3) **The Pressure Effect on Free Vibration of MWNTs:** It has been shown [134] that applying an external pressure to MWNTs can effectively increase the vdW interaction coefficient between the outmost few layers due to the pressure-induced reduction of interlayer spacing. Thus, for RBMs of MWNTs whose circumferential wave number n and half axial wave number m are zero, an external pressure could significantly up-shift the frequency of RBMs of MWNTs [134]. On the other hand, for free vibration of MWNTs with nonzero n and m, the pressure-induced compression of individual tubes also reduces the structural stiffness of MWNTs, which decreases vibrational frequencies of MWNTs. Thus, the pressure dependence of vibrational frequency of MWNTs in general cases provides a useful probe for complete study on the structure-mechanical property relationship of MWNTs, which is obviously a key issue for MWNTs as an engineering material.

(4) **The Effect of Boundary Conditions on Mechanical Behavior of MWNTs:** In the present work, the simply supported boundary condition is assumed for MWNTs in both buckling and vibrational analysis. However, for MWNTs used in nanocomposites or nanomachines, nested tubes or two ends of one individual tube could have different boundary conditions. For example, the outer tube of a double wall CNT embedded in a polymer matrix can be modeled as a shell with two fixed ends while the two ends of its inner tube may be free or simply supported. Since the combinations of the different boundary conditions on the two ends of MWNTs could significantly affect the performance of MWNTs as reinforcement of nanocomposites or structure elements in nanodevices it is relevance to investigate the effect of boundary condition on mechanical behavior, such as buckling and free vibration of MWNTs

(5) **The Curvature Effect on Mechanical Behavior of MWCNTs**: There is clear evidence that, usually, neglecting curvature effect on the interlayer vdW interaction coefficient c will not result in substantial errors. Thus the radius-independent vdW interaction coefficient is used in the multiple-shell model. However, recent study [184] showed that for MWNTs of very small radius, the curvature effect does play a significant role in determining the interlayer vdW interaction coefficient c. Thus, it is expected that the mechanical behavior of MWNTs could be affected by curvature effect-induced variation in the interlayer vdW interaction coefficient. In this future work, effort will be devoted to a complete study of the curvature effect on buckling and free vibration of MWNTs by using radius-dependent interlayer vdW interaction coefficient c.

In view of above statements, the multiple-shell model can be further used to study the mechanical behavior of MWNTs, especially those of many layers. In particular, the results obtained base on the present model could considerably improve the understanding on mechanics of MWNTs, which may not be easy for other techniques and serve as guidance for further study in experiments and atomistic simulations.

References

[1] H. W. Kroto, J. R. Heath, S. C. O'Brien, R. F. Curl and R. E. Smalley, C_{60} : Buckminsterfullerene, Nature 318, (1985) 162-163.

[2] S. Iijima, Helical microtubules of graphitic carbon, Nature, Vol. 354 (1991) 56-58.

[3] T. W. Ebbesen and P. M. Ajayan, Large-scale synthesis of carbon nanotubes, Nature, Vol. 358 (1992) 220-2.

[4] S. Iijima and T. Ichihashi, Single-shell carbon nanotubules of 1-nm diameter. Nature, Vol. 363 (1993) 603-5.

[5] D. S. Bethune and C. H. Kiang, Cobalt-catalysed growth of carbon nanotubes with single-atomic-layer walls. Nature, Vol. 363 (1993) 605-7.

[6] B. I. Yakobson and E. S. Richard, Fullerene nanotubes: $C_{1,000,000}$ and Beyond, American Scientist, Vol. 85 (1997) 324-37.

[7] M. S. Dresselhaus, G. Dressehaus and R. Saito, Physics of carbon nanotubes, Carbon, Vol. 33 (1995) 883-91.

[8] W. E. Thomas, Carbon Nanotubes, Physics Today, Vol. 49 (1996) 26-32.

[9] P. Ball, Roll up for the revolution. Nature, Vol. 414 (2001) 142-4.

[10] E. T. Thostenson, Z. F. Ren and Tsu. W. Chou, Advances in the science and technology of carbon nanotubes and their composites: a review, Composite science and technology , Vol.61 (2001), 1899-1912.

[11] R. H. Baughman, A. A. Zakhidov, and W. A. de Heer, Carbon nanotube-route toward applications. Science, Vol. 297 (2002) 787-92.

[12] K. T. Lau, and D. Hui, The revolutionary creation of new advance materials-carbon nanotube composite. Composites B, Vol. 33 (2002) 263-77.

[13] D. Qian, G. J. Wagner, W.K. Liu, M.F. Yu, and R.S. Ruoff, Mechanics of carbon nanotubes. Applied Mechanics Reviews, Vol. 55 (2002) 495-533.

[14] M. S. Dresselhaus and P. C. Eklund, Phonons in carbon nanotubes, Advance in Physics 49 (2000) 705-814.

[15] M.F. Yu, B. I. Yakoboson, and R. S. Roff, Controlled sliding and pullout of nested shells in individual multiwalled carbon nanotubes, Journal of Physical Chemistry B, Vol. 104 (2000) 8764-7.

[16] J. C. Charlier and J. P. Michenaud, Energetics of multilayered carbon tubules. Physical Review Letters, Vol. 70 (1993) 1858-61.

[17] A. N. Kolmogorov and V. H. Crespi, Smoothest Bearings: Interlayer Sliding in Multiwalled Carbon Nanotubes. Physical Review Letters, Vol. 85 (2000) 4772-30.

[18] J. Cumings and A. Zettel, Low friction nanotube linear bearing realized from carbon nanotubes. Science, Vol. 289 (2000) 602-4.

[19] L. A. Cirifalco and R. S. Lad, Energy of cohesion, compressibility, and the potential energy functions of the graphite system, The Journal of Chemical Physics, Vol. 25 (1956) 693-6.

[20] L. A. Cirifalco, M. Hodak, and R. S. Lee, Carbon nanotubes, buckyballs, ropes and a universal graphitic potential. Physical review B, Vol. 62 (2000) 13104-10.

[21] M. Hodak and L. A. Cirifalco, Fullerenes inside carbon nanotubes and multi-walled carbon nanotubes: optimum and maximum sizes. Chemical Physics Letter, Vol. 350 (2001) 405-11.

[22] Y. Satio, T. Yoshikawa, S. Bandow, M. Tomita, and T. Hayashi, Interlayer spacings in carbon nanotubes, Physical Review B, Vol. 48 (1993) 1907-9.

[23] C. H. Kiang, M. Endo, P. M. Ajayan, G. Dresselhaus and M. S. Dresselhaus, Size effects in carbon nanotubes. Physical Review Letters, Vol. 81 (1998) 1869-72.

REFERENCES

[24] V. N. Popov and L. Henrard, Breathinglike phonon modes of multiwalled carbon nanotubes. Physical Review B, Vol. 65 (2002) 235415-1 – 6.

[25] E. W. Wong, P. E. Sheehan, and C. M. Lieber, Nanobeam mechanics: elasticity, strength, and toughness of nanorods and nanotubes. Science, Vol.277 (1997) 1971-5.

[26] J. P. Salvetat, J. M. Bonard, N. H. Thmoson, A. J. Kulik, L. Forro, W. Benoit and L. Zuppiroli, Mechanical properties of carbon nanotubes. Applied Physics A, Vol. 69 (1999) 255-60.

[27] B. Vigolo, A. Penicaud, C. Coulon, C. Sauder, R. Pailler, C. Journet, P. Bernier and Pooulin, Macroscopic fibers and ribbons of oriented carbon nanotubes. Science, Vol. 290 (2000) 1331-4.

[28] M. F. Yu, B. S. Files, S. Arepalli, and R. S. Roff, Tensile loading of ropes of single wall carbon nanotubes and their mechanical properties, Physical Review Letters, Vol. 84 (2000) 5552-5.

[29] M. F. Yu, O. Lourie, M. J. Dyer, K. Moloni, T. F. Kelly, and R. S. Ruoff, Strength and breaking mechanism of multiwalled carbon nanotubes under tensile load, Science, Vol. 287 (2000) 637-40.

[30] C. Y. Li and T. W. Chou, A structural mechanics approach for the analysis of carbon nanotubes, International journal of solid and structure, Vol. 40 (2003) 2487-99.

[31] D. H. Robertson, D. W. Brenner, and J. W. Mintmire, Energetics of nanoscale graphitic tubules, Physical Review B, Vol. 45 (1992) 12592-5.

[32] B. I. Yakobson, C. J. Brabec, and J. Bernholc, Nanomechanics of carbon tubes: Instability beyond linear response, Physical Review Letters, Vol. 76 (1996) 2511-4.

[33] J. P. Lu, Elastic properties of carbon nanotubes and nanoropes, Physical Review Letters, Vol.79 (1997) 1297-300.

[34] E. Hernandez, C. Goze, P. Bernier and A, Rubio, Elastic Properties of C and $B_xC_xN_z$ composite nanotubes. Physical Review Letters, Vol. 80 (1998) 4502-5.

[35] G. H. Gao, T. Cagin, and W. A. Goddard, Energetics, structure, mechanical and vibrational properties of single-walled carbon nanotubes, Nanotechnology, Vol. 9 (1998) 184-91.

[36] D. Sanchez-Portal, D. Artacho, J. M. Soler, A. Rubio, and P. Ordejon, ab initio structural, elastic, and vibrational properties of carbon nanotubes. Physical Review B, Vol. 59 (1999) 12678-88.

[37] V. N. Popov, V. E. Van Doren and M. Balkanski, Elastic properties of single-wall carbon nanotubes. Physical Review B, Vol. 61 (2000) 3078-84.

[38] K. N. Kudin, G. E. Scuseria and B. I. Yakobson, CF, BN, and C nanoshell elasticity from ab initio computations. Physical Review B, Vol. 64 (2001) 235406-1—10.

[39] M. M. J. Treacy, T. W. Ebbesen and J. M. Gibson, Exceptionally high young's modulus observed for individual carbon nanotubes, Nature, Vol. 381 (6584) 678-680.

[40] R. S. Ruoff and D. C. Lorents, Mechanical and thermal properties of carbon nanotubes, Carbon, Vol. 33 (1995), 925-30.

[41] A. Krishnan, E. Dujardin, T. W. Ebbesen, P. N. Yianilos and M. M. J. Treacy, Young's modulus of single-walled nanotubes. Physical Review B, Vol. 58 (1998) 14013-9.

[42] N. Yao and V. Lordi, Young's modulus of single-walled carbon nanotubes, Journal of Applied Physics, Vol.84 (1998) 1939-43.

[43] B. I. Yakobson, M. P. Campbell, C. J. Brabec, and J. Bernholc, High strain rate fracture and c-chain unraveling in carbon nanotubes, Computational Materials Science, Vol. 8 (1997) 341-8.

[44] T. Belytshko, S. P. Xiao, G. C. Schatz, abd R.S. Ruoff, Simulation of the fracture of nanotubes (submitted for publication).

[45] P. M. Morse and H. Feshbach, Methods of Theoretical Physics, (McGraw Hill, New York, 1953).

[46] M. S. Dresselhaus, G. Dresselhaus and P. C. Eklund, Science of Fullerenes and carbon nanotubes (Academic, New York, 1996).

[47] S. Iijima, C. Brabec, A. Maiti and J. Bernholc, Structural flexibility of carbon nanotubes. Journal of Chemical Physics, Vol. 104 (1995) 2089-92.

[48] M.R. Falvo, G. J. Clary, R. M. Taylor, V. Chi, F. P. Brooks Jr, S. Washburn and R. Superfine, Bending and buckling of carbon nanotubes under large strain. Nature, Vol. 389 (1997) 582-4.

[49] H. K. Walter, S. D. Georg and J. B. Werner, Reversible bending of carbon nanotubes using a transmission electron microscope. Applied Physics Letters, Vol. 73 (1998) 1961-3.

[50] O. Lourie, D. M. Cox and H. D. Wagner, Buckling and collapse of embedded carbon nanotubes. Physical Review Letters, Vo.81 (1998) 1638-42.

[51] C. Bower, R. Rosen, L. Jin, J. Han and O. Zhou, Deformation of carbon nanotubes in nanotube-polymer composite. Applied Physics Letters, Vol. 74 (1999) 3317-9.

[52] P. Poncharal, Z. L. Wang, D. Ugarte and W. A. de Heer, Electrostatic Deflections and Electromechanical Resonance. Science, Vol. 287 (1999) 1513-6.

[53] R. S. Ruoff, J. Tersoff, D. C. Lorents, S. Subramoney and B. Chan, Radial deformation of carbon nanotubes by van der Waals force. Nature, Vol. 364 (1993) 514-26.

[54] T. Hertel, R. E. Walkup and P. Avouris, Deformation of carbon nanotubes by surface van der Waals forces. Physical Review B, Vol.58 (1998) 13870-3.

[55] P. Avouris, T. Hertel, R. Martel, T. Schmidt, H. R. Shea and R. E. Walkup, Carbon nanotubes: Nanomechaincs, manipulation, and electronic devices. Applied Surface Science, Vol. 141 (1999) 201-9.

[56] P. G. Collins and P. Avouris, Nanotubes for electronics. Scientific American, Vol. 283 (December, 2000) 62-9.

[57] W. J. Liang, M. Bockrath, D. Bozovic, J. H. Hafner, M. Tinkham and H. Park, Fabry-Perot interference in a nanotube electron waveguide. Nature, Vol. 411 (2001) 665-9.

[58] S. P. Frank, P. Pocharal, Z. L. Wang and W. A. de Heer, Carbon nanotube quantum resistors. Science, Vol. 280 (1998) 1744-6.

[59] M. Kocial, A. Yu. Kasumov, S. Guéron, I. I. Khodos, Yu. B. Gorbatov, V. T. Volkov, L. Vaccarini and H. Bouchiat, Superconductivity in Ropes of Single-Walled Carbon Nanotubes. Physics Review Letters, Vol. 86 (2001) 2416- 9.

[60] P. Sheng, N. Wang and Z. K. Tang, Superconductivity in 4 Angstrom single-walled carbon nanotubes. Science, Vol. 292 (2001) 2462-5.

[61] D. Qian, E. C. Dikey, R. Abdrews and T. Rantell, Load transfer and deformation mechanism in carbon nanotube-polystyrene composite. Applied Physics letter, Vol.76 (2000) 2868-70.

[62] P. J. F. Harris, Carbon nanotubes and related structure, new materials for the twenty-first century. UK: Cambridage University Press, 2000.

[63] P. Kim and C. M. Lieber, Nanotube Nanotweezers. Science, Vol. 286 (1999) 2148-50.

[64] H. J. Dai, J. H. Hafner, A. G. Rinzler, D. T. Colbert and R. E. Smalley, Nanotubes as nanoprobes in scanning probe microscopy. Nature, Vol. 384 (1996) 147-50.

[65] P. Sharke, Hybrid Nems, Mechanical Engineering, Vol. 123 (February 2001) 42-5.

211

[66] A. Majumdar, Not without engineering. Mechanical Engineering, Vol. 123 (March 2001) 46-9.

[67] K. Maney, Nanotech is near: Celebrate or take cover?. Scientists explore new frontier of promising microscopic technology, USA Today (October 24, 2000).

[68] J. F. Waters, L. Riester, M. Jouzi, P. R. Guduru and J. M. Xu, Buckling instability in multiwalled carbon nanotubes under uniaxial compression. Physics Review Letter, Vol. 85 (2004) 1787-9.

[69] E.T. Thostenson and T.W. Chou, Nanotube buckling in aligned multi-wall carbon nanotube composites. Carbon, Vol.42 (2004) 3015-8.

[70] A. M. Rao, E. Richter, S. Bandow, B. Chase, P.C. Eklund, K. A. Williams, S. Fang, K. R. Subbaswamy, M. Menon, A. Thess, R. E. Smalley, G. Dresselhaus, G. and M. S. Dresselhaus, Diameter-slective Raman scattering from vibration modes in carbon nanotubes. Science, Vol. 275 (1997) 187-91.

[71] X. L. Zhao, Y. Ando, L. C. Qin, H. Kataura, Y. Maniwa and R. Saito, Radial breathing modes of multiwalled carbon nanotubes. Chemical Physics Letters, Vol. 36 (2002) 169-74.

[72] H. Jantoljak, J. P. Salvetat, L. Forro and C. Thomsen, Low energy Raman-active phonons of multipwalled carbon nanotubes. Applied Physics A, Vol. 67 (1998) 113-6.

[73] S. Bandow, M. Takizawa, K. Hirahara, M. Yudasaka and S. Iijima, Raman scattering study of double-wall carbon nanotubes derived from the chains of fullerenes in single-wall carbon nanotubes. Chemical Physics Letters, Vol. 337 (2001) 48-54.

[74] J. M. Benoit, J. P. Buisson, O. Chayvet, C. Godon and S. Lefrant, Low frequency Raman studies of multiwalled carbon nanotubes: Experiments and theory. Physical Review. B, Vol. 66 (2002) 073417-1—4.

[75] D.S. Tang, Z.X. Bao, L.J. Wang, L.C. Chen, L.F. Sun, Z.Q. Liu, W.Y. Zhou, and S.S. Xie. The electrical behavior of carbon nanotubes under high pressure. Journal of Physics and Chemistry Solid, Vol. 61 (2000) 1175-8.

[76] D. S. Tang, L. C. Chen, L. J. Wang, L. F. Sun, Z. Q. Liu, G. Wang, W. Y. Zhou and S. S. Xie, Behavior of carbon nanotubes under high pressure and high temperature. Journal of Material Research, Vol. 15 (2000) 560-3.

[77] U. D. Venkateswaran, A. M. Rao, E. Richter, M. Menon, A. Rinzler, R. E. Smalley, and P. C. Eklund, Probing the single-wall carbon nanotube bundle: Raman scattering under high pressure. Physical Review B, Vol. 59 (1999) 10928-34.

[78] U. D. Venkateswaran, E. A. Brandsen, U. Schlecht, P. C. Eklund, A. M. Rao, E. Richter, L. Loa, K. Syassen and P. C. Eklund, High pressure studies of the Raman-active phonons in carbon nanotubes. Physical State Solid (b), Vol. 223 (2001) 225-36.

[79] U. D. Venkateswaran, D. L. Masica, G. U. Sumanasekera, C. A. Furtado, U. J. Kim and P. C. Eklund, Diameter dependent wall deformation during the compression of a carbon nanotube bundle. Physical Review B, Vol. 68 (2003) 241406-1 – 4.

[80] C. Thomsen, S. Reich, H. Jantoljak, L. Loa, K. Syassen, M. Burghard and G. S. Duesberg, Raman spectroscopy on single- and multi-walled nanotubes under high pressure. Applied Physics A, Vol. 69 (1999) 309-12.

[81] C. Thomsen and S. Reich, The pressure dependence of the high-energy Raman modes in empty and filled multiwalled carbon nanotubes, Physics State and Solid (b), Vol. 225 (2001) R18-19.

[82] J. Sandler, M. S. P. Shaffer, A. H. Windle, M. P. Halsall, M. A. Montes-Moran, C. A. Cooper and R. J. Young, Variations in the Raman peak shift as a function of hydrostatic pressure for various carbon nanostructures: A simple geometric effect. Physical Review B, Vol. 67 (2003) 35417-1– 8.

[83] M. J. Peters, L. E. Mcneil, J. P. Lu and D. Kahan, Structure phase transition in carbon nanotube bundles under pressure. Physics Review B, Vol. 61 (2000) 5939-45.

[84] R. Gaal, J. P. Salvetat and L. Forro, Pressure dependence of the resistivity of single-wall carbon nanotube ropes. Physical Review B, Vol. 61 (2000) 7320-3.

[85] S. Rols, I. N. Goncharenko, R. Almairac, J. L. Sauvajol and I. Mirebeau, Polygonization of single-wall carbon nanotube bundles under high pressure. Physical Review B, Vol. 64 (2001) 153401-4.

[86] D. H. Roberson, D. W. Brenner and J. W. Mintmire, Energetic of nanoscale graphitic tubules, Carbon, Vol. 33 (1992) 925-30.

[87] B. Ni, S. B. Sinnott, P. T. Mikulski and J. A. Harrison, Compression of carbon nanotubes filled with C_{60}, CH_4, or Ne: predictions from molecular dynamics simulations. Physical Review Letters, Vol. 88 (2000) 205505-1–4.

[88] D. Srivastava, M. Menon and K. Cho, Nanoplasticity of single-wall carbon nanotubes under uniaxial compression. Physical Review Letters, Vol. 83 (1999) 2973-6.

[89] C. Y. Li and T. W. Chou, Modeling of elastic buckling of carbon nanotubes by molecular structural mechanics approach. Mechanics of Materials, Vol. 36 (2004) 1047-55.

[90] K. M. Liew, C. H. Wong, X. Q. He, M. J. Tan and S. A. Meguid, Nanomechanics of single and multiwalled carbon nanotubes. Physical Review B, Vol. 69 (2004) 115429-1—8.

[91] R. Saito, T. Takeya, T. Kimura, G. Dresselhaus and M. S. Dresselhaus, Raman intensity of single-wall carbon nanotubes. Physical Review B, Vol. 57 (1998) 4145-53.

[92] S. Bandow, S. Asaka and Y. Satio, Effect of the growth temperature on the diameter distribution and chirality of single-wall carbon nanotubes. Physical Review Letters, Vol. 80 (1998) 3779-82.

[93] J. Kürti, G. Kresse. and H. Kuzmany, First-principles calculations of the radial breathing mode of single-wall carbon nanotubes. Physical Review B, Vol. 58 (1998) R8869-72.

[94] D. Kahn and J. P. Liu, Vibrational modes of carbon nanotubes and nanoropes. Physical Review B, Vol. 60 (1999) 6535-40.

[95] L. Henrard, E. Hernandez, P. Bernier and A. Rubio, van der Waals interaction in nanotube bundles: Consequences on vibrational modes. Physical Review B, Vol. 60 (1999) R8521-4.

[96] V. N. Popov and L. Henrard, Evidence for the existence of two breathinglike phonon modes in infinite bundles of single-walled carbon nanotubes. Physical Review B, Vol. 63 (2001) 233407-1—14.

[97] L. Henrard, V. N. Popov and A. Rubio, Influence of packing on the vibrational properties of infinite and finite bundles of carbon nanotubes. Physical Review B, Vol. 64 (2001) 205403-1—9.

[98] S. Ldfrant, Raman and SERS studies of carbon nanotube systems. Current Applied Physics, Vol . 2 (2002) 479-82.

[99] S. Ldfrant, J. P. Buisson, J. Schreiber, O. Chauvet, M. Baibarac nad I. Baltog, Study of interaction in carbon nanotubes systems by using Raman and SERS spectroscopy. Synthetic Metals, Vol. 139 (2003) 783-5.

[100] S. Timoshenko, Vibration problem in engineering. Wiley, New York, 1974.

[101] J. F. Doyle, Wave propagation in structure. Sprinter-Velag, Berlin, 1989.

[102] J. P. Salvetat, A. J. Kulik, J. M. Bonnard, G. A. D. Briggs, T. Stocki, K. Meitenier, S. Bonnamy, F. Beguin, N. A. Burnham and L. Forro, Elastic Modulus of Ordered and Disordered multiwalled carbon nanotubes. Advanced Materials, Vol. 11 (1999) 161-5.

[103] J. M. Gere, Mechanics of materials, 5th edition. Brooke/Cole, (2001).

[104] A. Garg, J. Han and S. Sinnott, Interactions of Carbon-Nanotubule Proximal Probe Tips with Diamond and Graphene. Physical Review Letters, Vol. 81 (1998) 2260-3.

[105] C. Q. Ru, Column buckling of multiwalled carbon nanotubes with interlayer radial displacement. Physical Review B, Vol. 62 (2000) 16962-6.

[106] J. Yoon, C. Q. Ru, and A. Mioduchowski, Noncoaxial resonance of an isolated multiwall carbon nanotube, Physical Review B, Vol. 66 (2002) 233402-1—4.

[107] A.Y. Kasumov, H. Bouchiat, B. Reulet, O. Stephan, I. I. Khhodos, Y. B. Gorbratov and C. Colliex, Conductivity and atomic structure of isolated multiwalled carbon nanotubes. Europhysics Letters, Vol. 43 (1998) 89-94.

[108] A. Hassanien, A. Mrzel, M. Tokumoto and D. Tomanek, Imaging the interlayer interactions of multiwall carbon nanotubes using scanning tunneling microscopy and spectroscopy. Applied Physics Letters, Vol. 79 (2001) 4210-3.

[109] Y. Miyamoto, S. Satio and D. Tomanek, Electronic interwall interactions and charge redistribution in multiwall nanotubes. Physical Review B, Vol. 65 (2001) 041402-1—041402-4.

[110] P. G. Collins, M. Hersam, M. Aronld, R. Martel and P. Avouris, Current saturation and electrical breakdown in multiwalled carbon nanotubes. Physical Review Letters, Vol. 86 (2001) 3128-31.

[111] M. F. Lin, F. L. Shyu and R. B. Chen, Optical properties of well-aligned multiwalled carbon nanotube bundles. Physical Review B, Vol.61 (2000) 14114-8.

[112] Z. Jin, X. Sun, G. Xu, S. H. Goh and W. Ji, Nonlinear optical properties of some polymer/multi-walled carbon nanotube composites. Chemical Physics Letters, Vol. 318 (2000) 505-10.

[113] C. Y. Li and T. W. Chou, Vibrational behaviors of multiwalled-carbon-nanotube-based nanotubemechanical resonators, Applied Physics Letters, Vol. 84 (2003) 121-3.

[114] E. S. Snow, P. M. Campbell and J. P. Novak, Single-wall carbon nanotube atomic force microscope probes. Applied Physics Letters, Vol. 80 (2002) 2002-5.

[115] M. Ishikawa, M. Yoshimura and K. Ueda, A study of friction by carbon nanotube tip. Applied Surface Science, Vol. 188 (2002) 456- 9.

[116] L. H. Donnell, Beams, Plates and Shells, McGraw-Hill, New York (1976).

[117] S. Timoshenko and S. Woinowsky-Krieger, Theory of Plates and Shells, McGraw-Hill, New York (1976).

[118] C. R. Calladine, Theory of Shell Structures, Cambridage University Press, Cambridge, UK (1983).

[119] C. Q. Ru, Elastic models for carbon nanotubes, Encylopedia of Nanoscience and Nanotechnology. Vol.2 (2004) 731-744.

[120] C. Q. Ru, Effective bending stiffness of carbon nanotubes. Physical Review B, Vol. 62 (2000) 9973-76.

[121] C. F. Cornwell and L. T. Wille, Elastic properties of single-walled carbon nanotubes in compression. Solid State Community, Vol. 101 (1997) 555-8.

[122] T. Ozaki, Y. Iwasa and T. Mitani, Stiffness of Single-Walled Carbon Nanotubes under Large Strain. Physical Review Letters, Vol. 84 (2000) 1712-5.

[123] C. Q. Ru, Elastic buckling of single-walled carbon nanotube ropes under high pressure. Physical Review B, Vol. 62 (2000) 10 405-8.

[124] D. Kahn and K. W. Kim, Quiantized vibrational modes of nanospheres and nanotubes in the elastic continuum model. Journal of Applied Physics, Vol. 89 (2001) 5107-11.

[125] A. Raichura, M. Dutta, and M. A. Stroscio, Quantized acoustic vibrations of single-wall carbon nanotube. Journal of Applied Physics, Vol. 94 (2003) 4060-5.

[126] C. E. Bottani, A. L. Bassi, M. G. Beghi, A, Podesta, P. Milani, A. Zakhidov, R. Baugham, D. A. Walters, and R. E. Smalley, Dynamic light scattering from acoustic

217

modes in single-walled carbon nanotubes. Physical Review B, Vol. 67 (2003) 155407-1—6.

[127] C. Q. Ru, The effect of van der Waals force on axial buckling of a double-walled. Journal of Applied Physics, Vol. 87 (2000) 7227-31.

[128] C. Q. Ru, Axially compressed buckling of a doublewalled carbon nanotube embedded in an elastic medium. Journal of Mechanical Physics Solids, Vol. 49 (2001) 1265-79.

[129] C. Q. Ru, Degraded buckling strain of multiwalled carbon nanotubes. Journal of Applied Physics, Vol. 89 (2001) 3426-33.

[130] C. Y. Wang, C. Q. Ru and A. Mioduchowski, Elastic buckling of multiwall carbon nanotubes under high pressure. Journal of Nanoscience and Nanotechnology, Vol. 3 (Special Issue on Nanotubes) (2003) 199-208.

[131] C. Y. Wang, C. Q. Ru and A. Mioduchowski, Axially compressed buckling of pressured multiwall carbon nanotubes. International Journal of Solids and Structures, Vol. 40 (2003) 3893-911.

[132] C. Y. Wang, C. Q. Ru and A. Mioduchowski, Applicability and limitations of simplified elastic shell equations for carbon nanotubes. Journal of Applied Mechanics, Vol. 71 (2004) 622-31.

[133] C.Y. Wang, C.Q. Ru and A. Mioduchowski, Critical External Pressure of Empty or Filled Multiwall Carbon Nanotubes. Journal of Computational and Technological Nanoscience, Vol. 1 (2004) 412-6.

[134] C. Y. Wang, C. Q. Ru, and A. Mioduchowski, Pressure effect on radial breathing modes of multiwall carbon nanotubes. Journal of Applied Physics,Vol. 97 (2005) 024310-1—10.

[135] C.Y. Wang, C.Q. Ru and A. Mioduchowski, Free Vibration of Multiwall Carbon Nanotubes. Journal of Applied Physics, Vol. 97 (2005) 114323-1—11.

218

REFERENCES

[136] C.Y. Wang, C.Q. Ru and A. Mioduchowski, Axisymmetric and beam-like vibrations of Multiwall carbon nanotubes. Physical Review B, Vol.72 (2005) 75414-1—10.

[137] Flugge, W., Stresses in shells. Springer-Verlag. Berlin (1960).

[138] Markus, S., The mechanics of vibration of cylindrical shells. Elsevier Amsterdam (1998).

[139] J. Kempner, N.Y. Brooklyn, Remarks on Donnell's equation. Journal of Applied Mechanics (ASME), Vol. 77 (1955) 117-18.

[140] N.J. Hoff, N.Y. Brooklyn, The accuracy of Donnell's equation. Journal of Applied Mechanics (ASME) 22, No. 2 (1955) 329-34.

[141] H. Kraus, Thin elastic shells: an introduction to the theoretical foundations and the analysis of their static and dynamic behavior. Wiley. New York (1967).

[142] W. Soedel, Vibrations of shells and plates. Marcel Dekker. New York (1993).

[143] L.S.D. Morley, An improvement on Donnell's approximation for thin-walled circular cylinders. Quart. Journal of Mechanics and Applied Mathematics XII, (1959) 88-99.

[144] D.S. Weaver and T.E. Unny, On the dynamic stability of fluid-conveying pipes. Journal of Applied Mechanics (ASME), Vol. 40 (1973) 49-52.

[145] Kazaoui, S. Nanotechnology Research Institute, Ibaraki, Japan (private communications).

[146] R. Satio, R. Matsuo, T. Kimura, G. Dresselhaus and M. S Dresselhaus, Anomalous potential barrier of double-wall carbon nanotube. Chemical Physics Letters, Vol. 348 (2001) 187-93.

[147] O. Gulseren, T. Yildirim, and S. Ciraci, Systematic ab initio study of curvature effects in carbon nanotubes. Physical Review B, Vol. 65 (2002) 153405-8.

[148] S. P. Timoshenko and J. M. Gere, Theory of Elastic Stability. McGraw-Hill. New York (1961).

[149] Bon O.Brush, Bo O.Almroth. Buckling of bars, plates, and shells. McGraw-Hill. New York (1975).

[150] S. Kazaoui, N. Minami, H. Yamawaki, K. Aoki, H. Kataura and Y. Achiba, Pressure dependence of the optical absorption spectra of single-walled carbon nanotube films. Physical Review B, Vol. 62 (2001) 1643-6.

[151] M. J. Lopez, A. Rubio, J. A. Alonso, L. C. Qin and S. Iijima, Novel Polygonized Single-Wall Carbon Nanotube Bundles. Physical Review Letters, Vol. 86 (2001) 3056-9.

[152] M. Popov, M. Kyotani, R. J. Nemanich and Y. Koga, Superhard phase composed of single-wall carbon nanotubes. Physical Review B, Vol. 65 (2002) 033408-11.

[153] H. D. Wagner, O. Lourie, Y. Feldman and R. Tenne, Stress-induced fragmentation of multiwall carbon nanotubes in a polymer. Applied Physics Letter, Vol.72 (1998) 188-90.

[154] Q. Zhao, J. R. Wood and H. D. Wagner, Stress fields around defects and fibers in a polymer using carbon nanotubes as sensors. Applied Physics Letters, Vol. 78 (2001) 1748-50.

[155] M. R. Falvo, R. M. Taylor, A. Helser, F. P. Brooks, S. Washburn and R. Superfine, Nanometre-scale rolling and sliding of carbon nanotubes. Nature, Vol. 397 (1999) 236-8.

[156] M. R. Falvo, J. Steele, R. M. Taylor and R. Superfine, Gearlike rolling motion mediated by commensurate contact: Carbon nanotubes on HOPG. Physical Review B, Vol. 62 (2000) R10665-7.

[157] M. F. Yu, B. I. Yakobson and R. S. Ruoff, Controlled Sliding and Pullout of Nested Shells in Individual Multiwalled Carbon Nanotubes, Journal of Physical Chemistry B, Vol. 104 (2000) 8764-7.

[158] K. Miura, T. Takagi, S. Kamiya, T. Sahashi and M. Yamauchi, Natural rolling of zigzag multiwalled carbon nanotubes on graphite. Nano letters, Vol. 1 (2001) 161-3.

[159] C.Y. Wang and A. Mioduchowski, The effect of dimensional factors on buckling behaviour of multiwall carbon nanotubes (in preparation).

[160] J. Yu, R. K. Kalia, and P. Vashishta, Phonons in graphitic tubules: A tight-binding molecular dynamics study. Journal of Chemical Physics, Vol. 103 (1995) 6697-705.

[161] R. A. Jishi, L. Venkataura, M. S. Dresselhaus, and G. Dresselhaus, Phonon modes in carbon nanotubules. Chemical Physics Letters, Vol. 209 (1993) 77-82.

[162] K. Sohlberg, B. G. Sumpter, R. E. Tuzun, and D. W. Noid, Continuum methods of mechanics as a simplified approach to structural engineering of nanostructures. Nanotechnology, Vol. 9 (1998) 30-36.

[163] J. Yoon, C.Q. Ru and A. Miduchowski, Vibration of embedded multiwall carbon nanotubes, Composites Science and Technology, Vol. 63 (2003) 1533-42.

[164] J. Yoon, C. Q. Ru and A. Mioduchowski, Timoshenko-beam effects on transverse wave propagation in carbon nanotube, Composites: B 35, (2004) 87-93.

[165] G. D. Mahan, Oscillations of a thin hollow cylinder: Carbon nanotubes. Physical Review B, Vol. 65 (2002) 235402-1--7.

[166] H. Suzuura and T. Ando, Phonons and electron-phonon scattering in carbon nanotubes. Physical Review B, Vol. 65 (2002) 235412-1—5.

[167] L. Chico and R. Perez-Alvarez. Continuum model for long-wavelength optical phonons in cylinders. Physical Review B, Vol. 69 (2004) 035419-1—6.

[168] M. G. Xia, S. L. Zhang, E. H. Zhang, S. M. Zhao, and X. J. Zuo, Vibrational spectra of double-wall carbon nanotubes. Physical Review B, Vol. 69 (2004) 233407-1—3.

[169] M. G. Xia, S. L. Zhang, X. J. Zuo, E. H. Zhang, S. M. Zhao, J, Li, L. Zhang, Y. C. Liu, and R. Liang, Assignment of the chrialities of double-walled carbon nanotubes using two radial breathing modes. Physical Review B, Vol. 70 (2004) 205428-1—8.

[170] A. M. Rao, J. Chen, E. Richer, U. Schlecht, P. C. Eklund, R. C. Haddon, U. D. Venkateswaran, Y. K. Kwon and D. Tomanek. Effect of van der Waals interaction on the Raman modes in single walled carbon nanotubes. Physical Review Letters, Vol. 86 (2001) 3895-9.

[171] H. Sakata, G. Dresselhaus, M. S. Dresselhaus and M. Endo, Effect of uniaxial stress on the Raman spectra of graphite fibers. Applied Physics, Vol. 63 (1987) 2769-72.

[172] Q. Zheng and Q. Jiang, Multiwalled carbon nanotubes as gigahertz oscillators, Physical Review Letter, Vol. 88 (2002) 45503-1—3.

[173] C.Y. Li and T. W, Chou, Single-walled carbon nanotubes as ultrahigh frequency nanomechanical resonators, Physical Review B, Vol. 68 (2003) 073405-1—3.

[174] H. J. De Los Santos, Introduction to Microelectromechanical Microwave Systems ~Artech House Publishers, London (1999).

[175] C.L. Dym, On the buckling of cylinders in axial compression. Journal of Applied Mechanics (ASME), Vol. 40 (1973) 565-8.

[176] J.E. Greenspon, Vibrations of a thick-walled cylindrical shell — comparison of the exact theory with approximate theories. Journal of the Acoustical Society of America, Vol. 32 (1960) 571-8.

[177] K. Forsberg, Axisymmetric and beam-type vibrations of thin cylindrical shell. AIAA Journal 7, No2 (1969) 221-7.

[178] L. K. Shayo and C. H. Ellen, Theoretical studies of internal flow-induced insensitivities of cantilever pipes. Journal of Sound and Vibration, Vol. 56 (1978) 463-74.

[179] M.EL-Raheb and C.D. Babcock, Some approximations in the linear dynamic equations of thin cylinders. Journal of Sound and Vibration , Vol.76 (1981) 543-59.

[180] P. Zhang, Y. Huang, H. Gao and K.C. Hwang, Fracture nucleation in single-wall carbon nanotubes under tension. Journal of Applied Mechanics (ASME), Vol. 69 (2002) 454-8.

[181] T. Belytschko, S. P. Xiao, G. C. Schatz and R. S. Ruoff, Atomistic simulations of nanotube fracture, Physical Review B, Vol. 65 (2002) 235430-1—8.

[182] Q. Han and G. Lu, Torsional buckling of a double-walled carbon nanotube embedded in an elastic medium, European Journal of Mechanics A/ Solid, Vol. 22 (2003) 875-83.

[183] E. Ertekin and D. C. Chrzan, Ideal torsional strengths and stiffnesses of carbon nanotubes, Physical Review B, Vol.72 (2005) 45425-1—5.

[184] X. Q. He, S. Kitipornchai and K. M. Liew, Buckling analysis of multi-walled carbon nanotubes: a continuum model accounting for van der Waals interaction. Journal of the Mechanics and Physics of Solid, Vol. 53 (2005) 303-26.